TECHNISCHE UNIVERSITÄT MÜNCHEN
MAX-PLANCK-INSTITUT FÜR PHYSIK

Development and characterisation of silicon photomultipliers with bulk-integrated quench resistors for future applications in particle and astroparticle physics

Christian Jendrysik

Vollständiger Abdruck der von der Fakultät für Physik
der Technischen Universität München zur Erlangung des akademischen Grades eines

Doktors der Naturwissenschaften

genehmigten Dissertation.

Vorsitzender: Univ.-Prof. Dr. Martin Beneke

Prüfer der Dissertation:

1. Hon.-Prof. Dr. Siegfried Bethke
2. Univ.-Prof. Jonathan J. Finley, Ph.D.

Die Dissertation wurde am 21.05.2014 bei der Technischen Universität München
eingereicht und durch die Fakultät für Physik am 14.07.2014 angenommen.

Abstract

This thesis deals with the development and characterisation of a novel silicon photomultiplier concept for applications in particle and astroparticle physics (e.g. Cherenkov telescopes, calorimeter). Silicon photomultipliers are a new type of detectors with single photon counting capability consisting of an array of parallel-connected avalanche photo diodes operated in Geiger-mode. For conventional devices, the required individual quench resistors for the Geiger-mode operation are realised with high ohmic polysilicon on the surface. Together with the connecting metal grid, this acts as an obstacle for light and thus is limiting the photon detection efficiency of the sensor. In the SiMPl detector approach (Silicon MultiPixel light detector), which is the focus of this thesis, the quench resistor is integrated to the highly resistive silicon bulk material resulting in a free and unstructured entrance window. Hence, high fill factors can be realised which improve the efficiency of these detectors. In addition, a reduction of process steps offers the prospect of lower costs in mass production.

Simulations demonstrated the feasibility of the concept and allowed to specify device dimensions and process parameters. With a first prototype production, a proof of concept was possible by measuring a working quench mechanism. Due to technological problems, a comprehensive characterisation of the first prototype was not possible.

In an improved second prototype production, the major technological problems of the first iteration were solved and allowed a first complete characterisation of the device. Apart from a high dark count rate the detectors showed promising results. Particularly noteworthy is the photon detection efficiency value of 35% for a wavelength of 400 nm, given that no optimised entrance window and antireflective coatings were implemented within the framework of this thesis. Comprehensive simulations in 2-D, and first real 3-D studies regarding the cell geometry, were performed in order to analyse the device characteristics and to verify and improve the predictability by comparison to measurements. In addition, a new method to determine the operating range of a SiPM, based on the measurement of the dark current and the dark count rate, was developed.

For a third prototype iteration, simulation-based optimisations with respect to technological parameters were performed within the scope of this thesis, in order to improve the detector quality. First preliminary results of test wafers with various annealing scenarios indicate that a low dark count rate SiMPl detector for room temperature operation without early edge breakdown is feasible.

Finally, conceptual studies for the next SiPM generation were performed with a focus on the compatibility of the SiPM approach with optical trenches as well as the potential of single cell readout for applications in particle tracking. The results suggest that both, optical isolation as well as the reading of individual cells, can be achieved by small changes in technology. This opens a wide range of possible applications for those devices.

Zusammenfassung

Thema dieser Arbeit war die Entwicklung und Charakterisierung eines neuartigen Silizium-Photomulitplierkonzepts für Anwendungen in der Teilchen- und Astroteilchenphysik (u.a. Cherenkov Teleskope, Kalorimeter). Bei Silizium-Photomultipliern handelt es sich um eine neue Art von Detektoren, die die Fähigkeit besitzen einzelne Photonen zu zählen. Die Bauteile bestehen aus einer Matrix von Lawinenphotodioden im Geiger-Modus, die alle parallel ausgelesen werden. Bei konventionellen Bauelementen befinden sich die für den Betrieb im Geiger-Modus erforderlichen einzelnen Löschwiderstände aus Polysilizium auf der Oberfläche und stellen, zusammen mit dem erforderlichen Metallgitter für die Kontakte, ein Hindernis für einfallendes Licht dar. Hierdurch wird die maximale Photonendetektionseffizienz dieser Sensoren limitiert. Um dies zu umgehen wurde in dem im Rahmen dieser Arbeit untersuchten SiMPl-Detektorkonzept (Silicon MultiPixel light detector) der Löschwiderstand in das Silizium-Bulk-Material integriert. Dadurch entsteht ein freies und unstrukturiertes Eintrittsfenster, was zu hohen Füllfaktor führt. Darüber hinaus kann die Anzahl der Prozessschritte verringert werden, was niedrigere Kosten in der Massenherstellung verspricht.

In Simulationsstudien konnte die Machbarkeit des Konzeptes gezeigt sowie Prozessparameter und Bauteilabmessungen spezifiziert werden. Mit einem ersten Prototyp konnte ein funktionierender Löschmechanismus gemessen, und damit der Machbarkeitsnachweis erbracht werden. Aufgrund technologischer Probleme konnte mit diesem ersten Prototyp jedoch keine umfassende Charakterisierung der Bauteile durchgeführt werden.

In einer deutlich verbesserten zweiten Prototypenproduktion konnten die größeren technologischen Probleme gelöst, und eine komplette Charakterisierung der Detektoren durchgeführt werden. Abgesehen von einer hohen Dunkelrate zeigten die Sensoren vielversprechende Ergebnisse. Besonders hervorzuheben ist eine Photonendetektionseffizienz von ca. 35% im Bereich von 400 nm angesichts der Tatsache, dass weder ein optimiertes Eintrittsfenster noch spezielle Antireflexionsbeschichtungen im Rahmen dieser Arbeit implementiert wurden. Des Weiteren wurden umfassende Simulationen in 2-D, und hinsichtlich der Zellgeometrie auch erstmals in 3-D, durchgeführt, um die Bauteilcharakteristiken zu analysieren und die Vorhersagbarkeit der Simulationen durch Abgleich mit Messungen zu überprüfen und zu verbessern. Außerdem wurde im Rahmen dieser Arbeit eine auf Dunkelstrom- und Dunkelratenmessung basierende Methode entwickelt, mit der sich der Betriebsbereich eines SiPMs bestimmen lässt.

Für einen dritten Prototypen wurde, mit Hilfe von Simulationen, darüber hinaus versucht die Detektorqualität durch Optimierung der Technologieparameter weiter zu verbessern. Erste Auswertungen von Teststrukturen mit verschiedenen Ausheilszenarien zeigten, dass ein SiMPl-Detektor mit niedriger Dunkelrate, und ohne vorzeitigem Randdurchbruch, bei Raumtemperatur machbar ist.

Abschließend wurden Konzeptstudien für die nächste SiPM-Generation durchgeführt, die sich auf die Kompatibilität mit optischen Trenngräben und das potentielle Auslesen einzelner Zellen, für den Einsatz als Vertexdetektoren, konzentrierten. Die Ergebnisse legen nahe, dass durch geringe technologische Veränderungen sowohl optische Isolation als auch das Auslesen

individueller Zellen erreichbar ist. Damit eröffnet sich den Detektoren ein breites Spektrum an Anwendungsmöglichkeiten.

Contents

1. Detectors for physics at the high energy and cosmic frontier 1
1.1. Future electron-positron linear colliders 1
1.1.1. The physics motivation 2
1.1.2. The International Linear Collider 5
1.1.3. The Compact LInear Collider 6
1.1.4. Detector systems for future linear colliders 8
1.1.4.1. Calorimeter 9
1.1.4.2. Vertex detector 10
1.2. Cherenkov telescopes for astroparticle physics at the terascale 11
1.2.1. The physics motivation for gamma ray astronomy 12
1.2.2. Low light level cameras for future Cherenkov telescopes 14
1.3. Rare events search with liquid noble gases 16
1.3.1. Neutrinoless double beta decay 18
1.3.2. Dark matter 21
1.3.3. Low background photosensors 23
1.4. Structure of this thesis 24

2. Photon detection with semiconductors 25
2.1. Light-matter interaction 25
2.1.1. Photoelectric effect 25
2.1.2. Compton scattering 27
2.1.3. Pair production 27
2.2. Semiconductor properties 28
2.2.1. Band structure 28
2.2.2. Doping 29
2.2.3. Optical absorption 31
2.2.4. Non radiative recombination 32
2.2.5. pn-junction 33
2.2.6. Impact ionisation and avalanche breakdown 35
2.3. Semiconductor photon detectors 37
2.3.1. Avalanche photo diodes 38
2.3.2. Geiger-mode avalanche photo diodes 39
2.3.3. Silicon photomultiplier 40

3. Methods 47
3.1. Simulation tools 47
3.1.1. Process simulation 47
3.1.2. Device simulation 48
3.1.3. Monte Carlo methods 49

3.2. Characterisation of SiPMs 52
  3.2.1. Static measurements 52
    3.2.1.1. Current-voltage measurements 52
    3.2.1.2. Capacitance-voltage measurements 55
  3.2.2. Dynamic measurements 55
    3.2.2.1. Gain 55
    3.2.2.2. Amplitude and charge spectra 56
    3.2.2.3. Noise 59
    3.2.2.4. Dynamic range 60
    3.2.2.5. Dark counts 61
    3.2.2.6. Recovery time 62
    3.2.2.7. Optical cross talk 62
    3.2.2.8. Afterpulsing 64
    3.2.2.9. Photon detection efficiency 67
  3.2.3. Photon emission microscopy 70

4. SiPM with bulk-integrated quench resistor **73**
4.1. Concept 74
4.2. Simulations for feasibility study 77
4.3. Advantages and drawbacks 79

5. Results **83**
5.1. First prototype 83
  5.1.1. Characterisation of SiMPl 1 86
5.2. Second Prototype 91
  5.2.1. Detailed simulation of SiMPl 2 92
    5.2.1.1. Stationary simulations 93
    5.2.1.2. Transient simulations 95
    5.2.1.3. Geometrical considerations 97
    5.2.1.4. Model comparison and parameter variations 98
  5.2.2. Static characterisation of SiMPl 2 104
  5.2.3. Dynamic characterisation of SiMPl 2 107
    5.2.3.1. Gain and capacitance 107
    5.2.3.2. Breakdown voltage 109
    5.2.3.3. Amplitude spectrum 111
    5.2.3.4. Dark count rate 112
    5.2.3.5. Optical cross talk 115
    5.2.3.6. Afterpulsing 119
    5.2.3.7. Recovery time and quench resistor 120
    5.2.3.8. Determination of SiPM operating range 126
    5.2.3.9. Photon detection efficiency 129
    5.2.3.10. Process window for operating devices and validation of simulations 137
5.3. Third prototype 138
  5.3.1. Improvement of technology 139
  5.3.2. Studies for devices with small cell size 145

6. Future concepts **149**
6.1. Single cell readout . . . 149
6.1.1. Particle detection . . . 150
6.1.2. Photon detection . . . 152
6.2. Optical cross talk suppression . . . 155
6.3. Low temperature devices . . . 157

7. Summary and outlook **161**

A. Derivation of PDE **167**

B. pin-diode data **169**

C. Wafer positioning **171**

Bibliography **173**

List of Figures **187**

List of Tables **191**

List of Abbreviations **193**

List of Publications **195**

Acknowledgements **197**

1. Detectors for physics at the high energy and cosmic frontier

In the twentieth century particle physics started to explore two major fields of interest. Telescopes and satellites allowed to observe details of cosmic objects like supernova remnants and blazars. Due to these observations, the knowledge about the evolution of the universe improved. On the other side of the size scale, the structure of the microcosm was revealed with collider experiments down to the spectrum of elementary particles which finally led to the formulation of the standard model (SM) [1–3]. This theoretical model of particle physics was accepted for many decades, since it describes the observed particle spectra as well as the electromagnetic, the weak and the strong fundamental force. The discovery of a Higgs-like boson (predicted by Higgs in 1964) at the Large Hadron Collider (LHC) in 2012 [4,5] – maybe one of the greatest discoveries in the last decades – was another milestone in the fundamental understanding of nature.

Nevertheless, the standard model has some unresolved issues, i.e. to explain observed phenomena like dark matter, which existence is confirmed by rotational speeds of galaxies and gravitational lensing effects by galaxy clusters. Amongst other aims of future experiments in particle and astroparticle physics, one is the common vision to clarify the mysterious nature of dark matter. In order to achieve these goals, increasingly powerful and precise instruments as well as novel measurement methods have to be realised.

1.1. Future electron-positron linear colliders

After the commissioning of the LHC and its promising first years of operation which led to the discovery of a new Higgs-compatible boson at approximately 125 GeV by the ATLAS and CMS experiments in 2012 [4, 5], it is of highest priority to precisely characterise the nature of this new particle. In order to enable the precise measurements, a new lepton collider at the energy frontier is planned to be built. A ring collider has the advantage of an efficient operation, since the acceleration process is realised in many cycles which reduces the number of required accelerating structures. Furthermore, a high collision rate (high luminosity) for improving the measurement accuracies can be realised by refocussing and colliding those particles which did not interact in previous collisions. However, high-energetic particles which are forced on a curved path by magnetic fields emit synchrotron radiation. The resulting energy loss, which is inversely proportional to the fourth power of the particle mass, limits the maximum energy of the particle (Large Electron-Positron Collider: $\sqrt{s_{max}} \approx 200$ GeV). τ leptons have high mass (1777 MeV) but only a lifetime of $2.9 \cdot 10^{-13}$ s. Muons, with a mass of 106 MeV, would also allow circular acceleration, but their lifetime of $2.2 \cdot 10^{-6}$ s sets challenging requirements on the instrument, which prevent the realisation of a muon collider up to now. Therefore, due to the small electron mass of 0.51 MeV, only an e^+e^- linear collider (LC) can be used to reach energies in the TeV range.

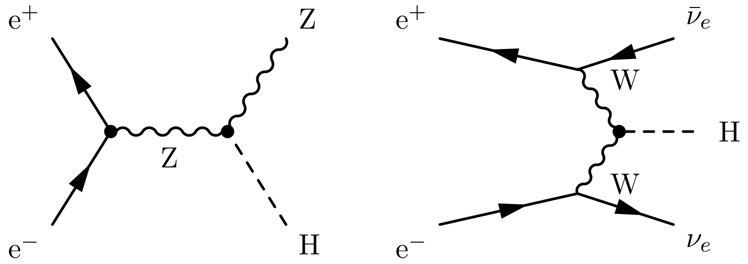

Figure 1.1: The two main Higgs boson production processes at a linear collider (see Fig. 1.2). Left shows the Higgs-strahlung whereas the WW fusion process is illustrated on the right.

Significant features of the clean experimental environment resulting from e^+e^- collisions in a LC are the precisely known and adjustable centre-of-mass energy $\sqrt{s}$, which is not distributed among the hadron constituents like in the LHC, as well as the initial-state polarisations [6]. Furthermore, in comparison to the quantum chromodynamics (QCD) backgrounds in a hadron collider, the backgrounds in a LC are many orders of magnitude lower. Thus, a trigger-free readout and full event reconstruction is possible. As a result of this experimental environment, a future LC will allow to study the physics at the TeV scale with outstanding precision. Moreover, it will fundamentally contribute to determine the properties of newly discovered particles at the LHC with highest precision and the search for new physics. For this purpose, the complementarity of the two collider systems has been established over many years [7]. A successful example of such a complementary cooperation was the confirmation of the gauge structure of the standard model and the precise measurements of its parameters which was a result of analyses from e^+e^- and hadron colliders as well as deep-inelastic lepton-nucleon scattering [6].

1.1.1. The physics motivation

With the discovery of the new particle, compatible with a light Higgs boson, the prospects for the realisation of a future LC are significantly enforced. However, the physics program of a future LC has the ability to cover a wide range of particle physics [6]:

- precise characterisation of the Higgs sector,
- determination of properties and interactions of top quarks, gauge bosons and new particles with outstanding precision,
- search for new physics.

Thus, the future linear colliders are essential tools which will advance our understanding of nature. In the following sections, a brief overview of the individual items will be given. A complete and detailed discussion can be found in Refs. [6, 8]

Driven by the discovery of a new Higgs-like boson, one of the main goals of a new linear collider will be the investigation of Higgs physics. The Higgs mechanism describes the Electroweak Symmetry Breaking (EWSB) in the SM model and is the fundamental basis of the generation of the masses of all elementary particles. Future linear accelerators provide the unique opportunity to study the new boson model-independent. Due to the clean experimental environment all relevant decay channels of the particle can be investigated.

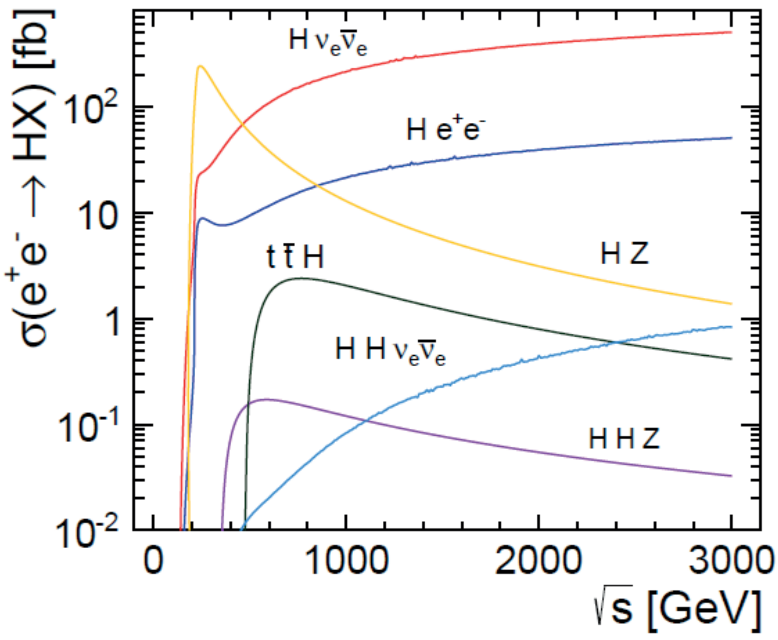

Figure 1.2: Cross-section for different production mechanisms for a 125 GeV Higgs boson [10].

The main Higgs boson production channels in e^+e^- collisions are Higgs-strahlung and vector boson fusion (see Fig. 1.1). At low energies the process $e^+e^- \to HZ$ dominates, whereas with increasing centre-of-mass energy the WW fusion process $e^+e^- \to H\nu_e\bar{\nu}_e$ becomes increasingly important and dominates at $\sqrt{s} \approx 500$ GeV, as can be seen in the cross-sections for different production mechanisms in Fig. 1.2. With the Higgs-strahlung process a model-independent investigation of the Higgs boson coupling (g_{HZZ}) is possible via an event selection based on two oppositely charged leptons in the final state with an invariant mass corresponding to the Z boson. Thus, an absolute measurement of the Higgs-strahlung cross section is possible including potential invisible final states of the Higgs boson. The branching fraction of the Higgs boson can be absolutely determined by identifying all final states of the Higgs and Z boson decay. The strength of the Higgs self-coupling can be measured via $e^+e^- \to HH\nu_e\bar{\nu}_e$ and $e^+e^- \to HHZ$ processes [9]. The resulting precise determination of couplings to gauge bosons and fermions, including the direct measurement of the top quark Yukawa coupling via $e^+e^- \to t\bar{t}H$, can be used to test the mass-proportional coupling of the Higgs boson to different particles, predicted by the Higgs mechanism. Deviations, revealed by the high precision measurements would indicate new physics beyond the standard model.

Furthermore, with a linear collider the investigation of the CP-properties in the Higgs and top quark sector becomes feasible. For example, the threshold behaviour of the $e^+e^- \to t\bar{t}H$ process allows not only to determine the CP-nature of the Higgs boson but potentially also the measurement of the CP-mixing in this sector [6]. The large number of Higgs bosons resulting from ZZ and WW fusion processes even at lowest considered LC energies can be used to measure the relative couplings of the Higgs boson to W and Z bosons with high precision and thus enables the verification of the SM prediction $g_{HWW}/g_{HZZ} = \cos^2\theta_W$, with θ_W the weak mixing angle.

Besides the study of the Higgs boson, future LC also provide the possibility to investigate the top quark sector. The top quark is the most massive fundamental fermion, most strongly coupled to EWSB and is expected to have the strongest interaction with the Higgs boson. High precision measurements of the properties and interactions of the top quark can have sensitivity to physics at mass scales much above EWSB. Especially modern theory generally does not accept that the SM Higgs boson alone can be a stable solution to the dynamics of EWSB [11]. Therefore, due to its strong coupling it is very important for testing the SM and search for new physics.

The top quark sector has been mainly studied at the Tevatron and LHC. Up to now there is no indication for new physics in the production process except the anomaly in the forward-backward asymmetry. Although there can be an asymmetry in the production due to interference between box and tree diagrams, or interference between initial and final state QCD radiation [12], CDF and D0 have measured values which well exceed the SM prediction [13]. The current measurements of $\mathrm{p\bar{p}}$ at the LHC are not inconsistent with the SM but still not decisive. The clean environment in a LC allows to achieve accuracies of ca. 5%.

At a future LC the top quark mass received from $\mathrm{t\bar{t}}$ measurements will be unique since it will enable a high-precision measurement of a threshold mass, for which the relation to a well-defined top quark mass is precisely known. From a threshold scan with approximately 100 fb^{-1} a statistical precision of about 34 MeV for the mass will be achievable, resulting in an overall precision for m_t of better than 100 MeV [14].

Concerning the search for new physics, the contribution of a future LC can be divided into three parts:

- improve LHC measurements of new physics phenomena due to the clean experimental environment and high precision
- direct discoveries complementary to the LHC especially in the search for colour-neutral states (including the full nature of the Higgs sector)
- indirect discoveries through high precision measurements of observables with known particles and their deviations from the SM prediction.

One example for the first item is the search for new electroweak matter states which are difficult to be found directly at the LHC because of the small event rates in comparison to the background. A well known theory in this field is supersymmetry which provides a calculable framework for the studies. A LC with sufficient energy could produce non-coloured particles, charginos, neutralinos and sleptons with low background for a direct discovery with a general discovery reach of $\sqrt{s}/2$. The high precision allows the measurement of masses, couplings to SM particles, and assignment of spins which have to be experimentally tested in order to check the predictions of supersymmetry.

Another indication of physics beyond the SM is the well-established assumption that the universe must contain a certain fraction of dark matter (27%), which cannot be composed of SM particles. With R-parity conservation in supersymmetric theories, the chargless massive stable χ as the lightest neutralino is an ideal candidate for a weakly interacting, electrically neutral particle (weakly interacting massive particle, WIMP). A direct production of dark matter could be possible by $\mathrm{e}^-\mathrm{e}^+ \rightarrow \chi\chi\gamma$ interactions. The LC can provide information on the strength and chiral structure of these interactions as well as the mass of the WIMP. Furthermore, the annihilation and co-annihilation of dark matter particles could be investigated.

Even with a light Higgs boson mass there are EWSB formulations where the light Higgs boson is just a part of a larger spectrum of strongly interacting particles. This in turn would be manifested in observable effects of the strong dynamics like gauge boson couplings. In particular, the scattering of WW/ZZ and WW final state processes are of interest. These measurements require studies of angular correlations among the decay products of the W/Z bosons and further need separation of the W and Z final states decaying to quarks. Since this leads to a need for excellent jet-energy resolution, it has driven the design of the LC detector concepts and has been shown to be feasible.

For reasons of completeness it should be mentioned that also the asymmetry in the baryonic sector requires new dynamics like extra sources of CP-violation as well as the discovery of neutrino oscillation is not covered by the standard model with massless neutrinos.

Due to relatively low radiation, linear colliders allow different detector designs compared to the LHC. They offer an experimental environment for high precision measurements with low QCD backgrounds, but the demanding physics are still challenging for readout and sensor technologies. For precision mass measurements, a jet energy resolution of $\frac{\sigma_{Ejet}}{E_{jet}} \leq 3\%$ is essential, since many physics processes of interest appear as multi-jet events. An efficient electron and muon identification is required for studies of leptons from W and Z decays as well as accurate momentum measurements over the largest possible solid angle. A high granularity calorimeter and a highly efficient tracking system would allow to meet the jet mass resolution requirements (see Sec. 1.1.4).

The two options, developed for a future e^+e^- LC are the International Linear Collider (ILC) which uses superconducting radio frequency cavities to provide the accelerating power and the Compact LInear Collider (CLIC) which uses a separate drive beam. Both accelerators are briefly described below.

1.1.2. The International Linear Collider

The ILC, shown in Fig. 1.3, will be a 31 kilometre-long accelerator made up of several subsystems. To realise a compact bunch, necessary to obtain the high density for sufficient collisions, two damping rings with a circumference of 6.7 km will be integrated. In each ring, the bunches traverse a series of wigglers, which compresses the bunches by means of circling about 10000 times before leaving the damping ring. The two main linear accelerators for electrons and positrons accelerate the bunches from their injected energy of 15 GeV to the final beam energy of 250 GeV (for 500 GeV centre-of-mass beam energy) towards the collision point. Each one of them has a length of 11 km and consists of approximately 17000 superconducting radio frequency cavities (1.3 GHz) made of pure niobium. They are cooled down to -271 °C using liquid helium. The average acceleration gradient of the machine is 31.5 MeV/m. A functional requirement is that the main accelerator preserves the small bunch emittance to achieve the high luminosity around $2 \cdot 10^{34}$ cm^{-2}s^{-1}. The beam delivery system has to focus the beam to the required size and minimise the background in the detectors by removing those particles which are not within the acceptable ranges of energy and spatial spread (beam-halo). The whole process of e^+e^- production, damping, and acceleration will repeat with a frequency of 5 Hz. Every 200 ms, a group of electron and positron bunches with a total length of 0.73 ms (bunch train), will collide. With 1312 bunches per pulse, a bunch crossing occurs every 554 ns. Table 1.1 lists some basic design parameters for the ILC. In a first step the centre-of-mass energy $\sqrt{s}$ will be 500 GeV and can later be increased by an upgrade to 1 TeV. The advantage of this concept is its fully developed technology.

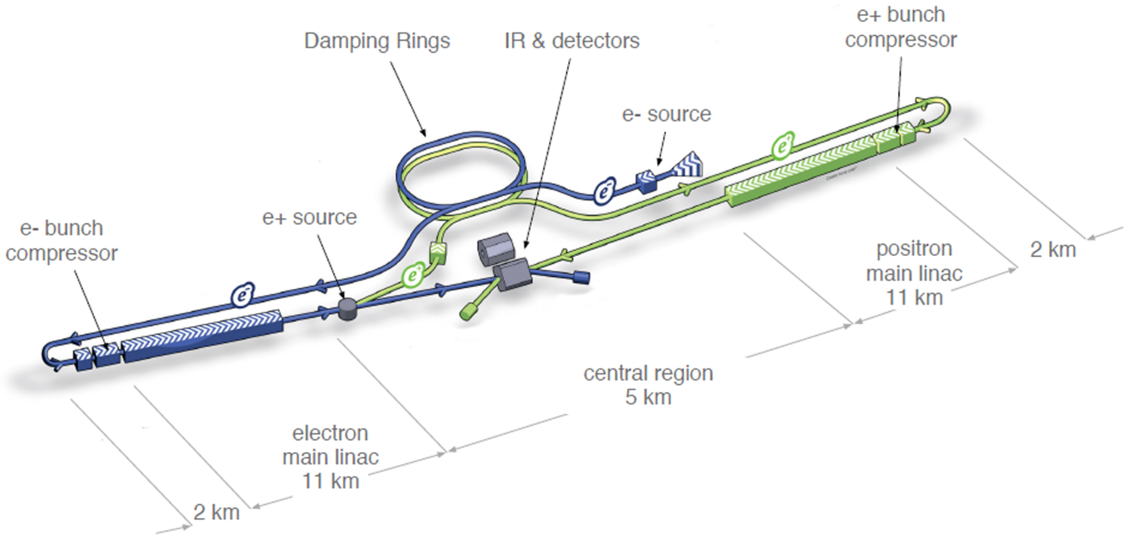

Figure 1.3: The International Linear Collider with its major subsystems. The beam collision angle is set to 14 mrad to reduce beam induced backgrounds at the interaction point. Image from [15].

Parameter $\sqrt{s}$	500 GeV	1 TeV	Unit
Peak luminosity	$1.8 \cdot 10^{34}$	$4.9 \cdot 10^{34}$	$\mathrm{cm}^{-2}\mathrm{s}^{-1}$
Pulse rate	5.0	4.0	Hz
Number of bunches per pulse	1312	2450	
Bunch population	$2 \cdot 10^{10}$	$1.74 \cdot 10^{10}$	
Bunch separation	554	366	ns
Typical beam size at IP (horizontal)	474	335	nm
Typical beam size at IP (vertical)	5.9	3.7	nm

Table 1.1: Basic design and beam parameters for the ILC [15]. IP stands for interaction point.

It therefore will provide the possibility for the realisation of a Higgs boson and top quark factory on a short timescale [6, 15].

A detailed description of the machine can be found in Ref. [16].

1.1.3. The Compact LInear Collider

A more ambitious approach is chosen for the high energy collider option CLIC, where a separate drive beam is used to provide the accelerating power. This concept would allow a new region in the multi-TeV scale beyond today's particle accelerators. The nominal centre-of-mass energy is planned to be $\sqrt{s} = 3$ TeV. Fig. 1.4 illustrates a schematic of the CLIC experiment. To achieve this high energy in a realistic and cost efficient way the accelerating gradient has to be in the order of 100 MeV/m, which is not achievable by superconducting radio frequency cavities. In addition to a better investigation of the electroweak symmetry breaking (EWSB) by measuring the Higgs self-coupling (see also Sec. 1.1.1), a multi-TeV

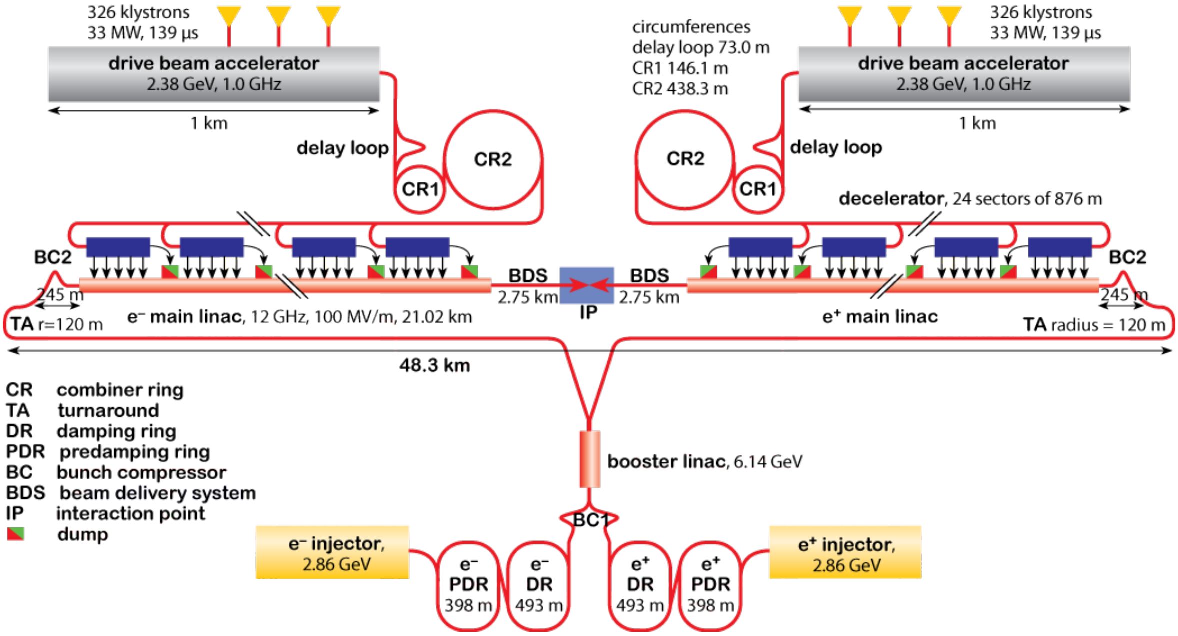

Figure 1.4: The layout scheme of the Compact LInear Collider (CLIC). Image from [17].

Parameter		Unit
Peak luminosity (at $\sqrt{s} = 3$ TeV)	5.9×10^{34}	$\mathrm{cm}^{-2}\mathrm{s}^{-1}$
Pulse rate	50	Hz
Number of bunches per pulse	312	
Bunch population	3.72×10^{9}	
Bunch separation	0.5	ns
Typical beam size at IP (horizontal)	40	nm
Typical beam size at IP (vertical)	1	nm

Table 1.2: Basic design and beam parameters for CLIC [19]. IP stands for interaction point.

centre-of-mass energy collider would significantly surpass the discovery range of the LHC for physics beyond the standard model.

In order to achieve the high accelerating gradient of 100 MeV/m, CLIC is based on a novel two-beam-acceleration concept. The required wave structures of roughly 12 GHz radio frequency (RF) are generated by a high current electron beam (drive beam) running in parallel to the main beam. The drive beam is decelerated in special power extraction and transfer structures (PETS) which are passive microwave devices. The beam power of the drive beam is extracted, converted to radio frequency power, collected and transferred to the main accelerator system. The two-beam-acceleration concept leads to a total LC length of only 48 km. A detailed explanation of the working principle can be found in [11, 18, 19] and the references therein. A summary of some specific parameters for CLIC is given in Table 1.2. The choice of parameters results from a trade-off between high luminosity and costs. CLIC is designed in its final upgrade for a peak luminosity of roughly $6 \cdot 10^{34}$ $\mathrm{cm}^{-2}\mathrm{s}^{-1}$. Like the ILC, it is also operated in a pulsed mode. Bunch trains of 156 ns length will collide with a frequency of 50 Hz. The number of 312 bunches per pulse leads to a bunch crossing separation of 0.5 ns, which is favourable for high luminosity. Short intervals between bunches

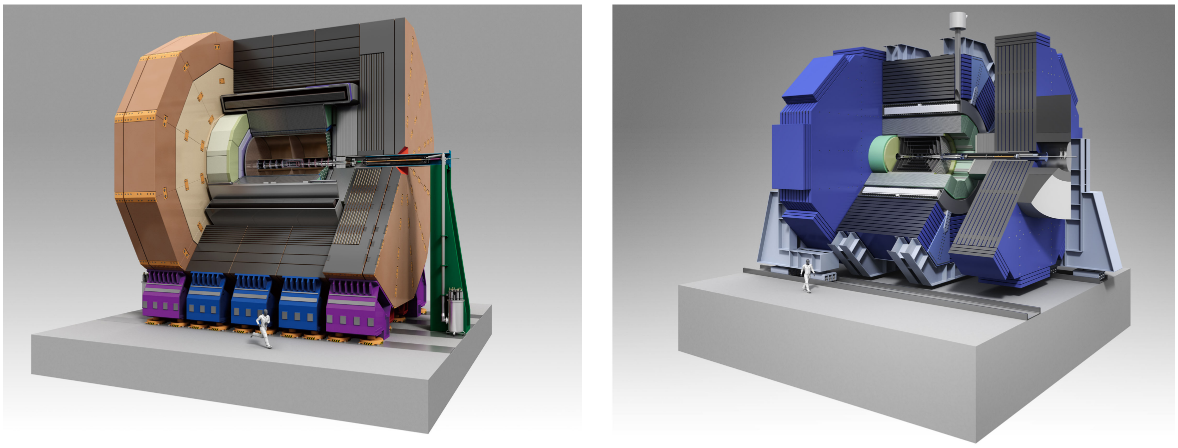

Figure 1.5: View of ILD [15] (left) and SiD [22] (right) detector concepts for ILC.

are also advantageous for improving the RF-to-beam efficiency. On the other hand, the detector design and the event reconstruction for a bunch separation of only 0.5 ns become a challenging task.

Although, the CLIC Test Facility [20] already demonstrated the feasibility of large parts of the novel CLIC technology, still a lot of problems, i.e. power consumption and stability, have to be solved for the realisation of a multi-TeV linear collider [19].

1.1.4. Detector systems for future linear colliders

The physics goals of a future LC, mentioned in the previous section, define the challenging requirements on the detector systems. Particularly demanding areas in the reconstruction of events are the impact parameter resolution, the track momentum measurement and the jet flavour identification as well as jet energy resolution. The two validated detector concepts for addressing these issues at the ILC are the International Large Detector (ILD) and the Silicon Detector (SiD) [21]. Both proposals, which are illustrated in Fig 1.5, are based on a common detector structure but use complementary technologies for the different sub-systems. Modified ILD and SiD proposals of the ILC have been adopted by the CLIC project, in order to meet the even more demanding detector specifications for this ambitious concept of a multi-TeV collider.

The vertex detector uses a multilayer barrel layout with silicon pixels surrounding the beam pipe and is the innermost detector sub-system. It is the main tool for heavy flavour identification by measuring charged particles coming from a secondary vertex. Particle tracking at small angles is ensured by forward and backward silicon pixel disks. The vertex detector is followed by the main tracker, which measures the momentum of charged particles by reconstructing their tracks. For ILD it is based on a gaseous Time Projection Chamber surrounded by silicon strip layers, whereas SiD proposes an all-silicon approach using silicon strip sensors. Outside of the tracker detector the energy of charged and neutral particles is measured by the electromagnetic and hadronic calorimeters. Both concepts are completed by a muon identification system.

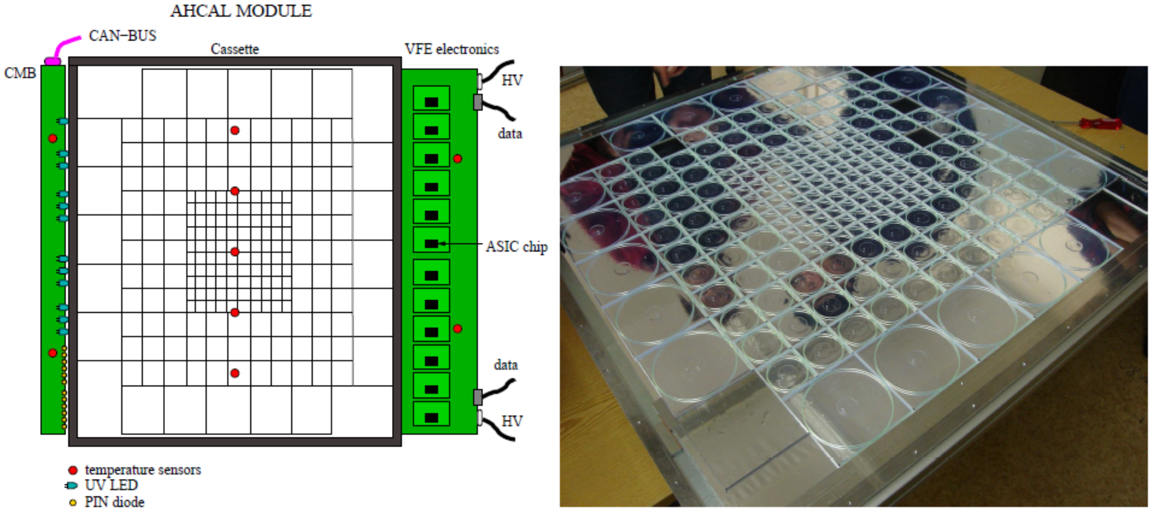

Figure 1.6: Tile layout of a scintillator module of the first generation CALICE prototype (left). On the right hand side, a photograph of the scintillation tiles in a module is shown. Images from [24].

1.1.4.1. Calorimeter

The design of calorimeters for future linear collider experiments is driven by the requirement of multi-jet final states reconstruction with highest accuracy. The aim for a separation of W and Z hadronic decays results in a required invariant mass resolution of $\sigma_m/m \approx 2.7\%$. To meet this specification the particle flow approach (PFA, [23]) was developed; an algorithm which uses the combination of tracking and calorimetry for measuring the energy of charged and neutral particles for event reconstruction, respectively. Roughly 60% of all particles in jets are charged and can be identified in the tracker, whereas photons (30%) are reconstructed in the electromagnetic and neutral hadrons in the hadronic calorimeter. For an accurate determination of neutral hadron showers, the energy depositions from other particles have to be identified and removed. The mis-assignment of overlapping showers leads to a decrease in energy resolution. The best performance can be achieved by using a calorimeter with high granularity in longitudinal and transversal directions, since it allows to assign the signal of an individual cell to the correct shower [24]. Good particle flow reconstruction requires both electromagnetic and hadron calorimeter inside the solenoid.

The analogue hadron calorimeter (AHCAL) prototype [24], constructed by the CALICE[1] collaboration, is inspired by the ILD concept. It consists of a steel/scintillator sandwich structure of 1 m^3 containing 7608 scintillator tiles and has a total depth of 5.3 nuclear interaction lengths. The layout of one module as well as a picture of the scintillation tiles are shown in Fig. 1.6. In order to resolve the substructure of the shower the longitudinal segmentation has to be in the order of the radiation lengths whereas the transverse structuring is in the order of the Molière radius. Simulations indicated that a 3×3 cm^2 dimension is sufficient for the separation of two particles [25]. The AHCAL is based on the well-established and robust scintillator technique which can be realised at reasonable costs but requires compact photodetectors to meet the high granularity condition. Further requirements are a low power consumption due to the large number of photodetectors, the possibility to be operated

---

[1] CAlorimeter for the LInear Collider Experiment

in magnetic fields as well as the ability to resolve the bunch separation of the future LC. Promising candidates to achieve the high granularity of the active layers are silicon photomultiplier (SiPMs), arrays of avalanche photo diodes in Geiger-mode (see Sec. 2.3.3). In the first prototype of CALICE, for the first time the individual scintillation tiles (thickness of 5 mm) are read out by SiPMs. The scintillation light is mediated to the green region via wavelength shifting fibres, which are coupled to the SiPMs, in order to meet the peak detection efficiency of the utilised photodetectors. For the minimisation of the non-linearity of the SiPM signal (dynamic range, see Sec. 3.2.2.4), devices with a large number of cells are preferred, whereas a maximum photon detection efficiency plays a minor role. Test beam operation demonstrated the feasibility of this detector concept [24].

For a second generation of an AHCAL, new scintillation tiles with the same size but a different thickness of 3 mm are produced [26]. The key features are fully integrated electronics and a realistic mechanical design with respect to a future LC detector. Technological development of the SiPMs with high sensitivity in the blue regime also allows readout of the tiles without wavelength shifting fibres, which simplifies the production drastically, and additionally gives the possibility of recording the time structure of the hadronic shower in calorimeters [26, 27].

1.1.4.2. Vertex detector

Since the PFA approach requires excellent tracking, the vertex tracking detector for the reconstruction of the track and momentum of charged particles is a key element of future LC experiments. Especially the reconstruction of decay vertices of short lived particles, in order to identify heavy quarks (flavour tagging), is of interest for the physics program of a future LC. The desired performance level of a future vertex detector implicates strict specifications [21]. The material budget has to be very low (0.1% X_0/layer, where X_0 is the radiation length) to reduce multiple Coulomb scattering, and hence the uncertainties in the track reconstruction. Thus, a low power consumption of the sensor and the readout electronics is required, since no active cooling is allowed inside the acceptance region. The single point resolution σ_{point} close to the interaction point should be better than 5 µm, which implies a cell size of 17 µm according to [28]

$$\sigma_{point} = \frac{\text{Cell size}}{\sqrt{12}}. \tag{1.1}$$

At the same time highest possible fill factors for a maximisation of the efficiency should be achieved. The pixel occupancy should be low (expected dark count rate: innermost layer $6 \cdot 10^{-8}$ hits/µm^2/bunch crossing; forward tracking detector: $2 \cdot 10^{-10}$ hits/µm^2/bunch crossing). Due to the short separation of the bunch crossings (ca. 300 ns for ILC) fast detectors are needed to distinguish between several bunches. Since the detector is located inside of the solenoid insensitivity to magnetic fields is important. Additionally, the required radiation tolerance is given by the beam-induced background. For the ILC a maximum total ionising dose of up to 1 kGy/year and a neutron equivalent fluence of roughly 10^{11} $\mathrm{n_{eq}/cm^2}$/year is expected, whereas for CLIC these values change to 200 Gy/year and 10^{10} $\mathrm{n_{eq}/cm^2}$/year. Also an affordable cost should be taken into account, since a huge number of devices is necessary to cover the large area of the detector.

Currently, the technology options are CMOS Pixel Sensors, Fine Pixel CCDs and Depleted Field Effect Transistors (DEPFET) [21]. More recently, the use of Geiger-mode avalanche diode arrays was proposed, due to their excellent timing in the sub-ns regime and their fast

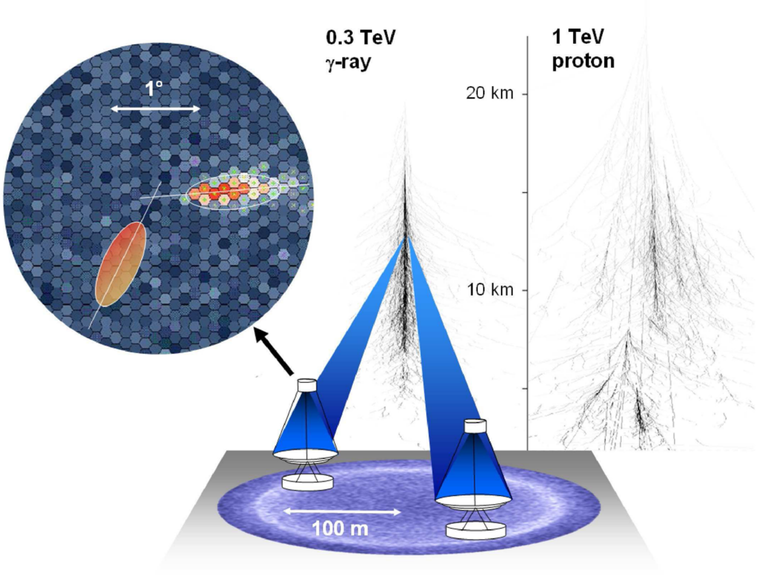

Figure 1.7: Sketch of imaging atmospheric Cherenkov technique based on extensive electromagnetic air showers (300 GeV). The upper left shows the combined camera image of the two telescopes for the detected Cherenkov light and allows reconstruction of the source position. In comparison the shower for a 1 TeV proton is also plotted. Image from [30].

readout. Additionally, these devices result in a high signal and have the advantage of a high sensitivity [29]. With development of the technology and dedicated electronics this approach has the potential for an excellent tracking detector.

1.2. Cherenkov telescopes for astroparticle physics at the terascale

New detectors are also required in a different field of physics at the energy frontier. For a deeper understanding of the universe and its evolution, the cosmos is studied in all fields of radiation; charged particles, also called cosmic rays, neutrinos and of course the full electromagnetic spectrum from radio waves to the gamma regime. In contrast to observations in the visible range, which has been started centuries ago, gamma ray astronomy is a rather new field in astrophysics since it was originally only possible with space-based instruments. The absorption in the earth's atmosphere prohibits the direct observation of photons in the gamma regime from the ground. However, the detection of very high energetic photons requires large calorimeters to absorb enough of the photon-induced energy and is therefore limited by its size and weight in satellite missions. Also the low flux at these energies in the order of 10^{-11} photons per cm^2-second excludes observation in space [30]. However, this part of the energy spectrum contains information about objects like supernovae remnants, active galactic nuclei and blazars, and can also be used to study dark matter which potentially annihilates into gamma-rays [31]. Since gammas are not electrically charged, unlike other astroparticles, they are not affected by magnetic fields. Therefore, observation of distant cosmic events by straight extrapolation to the source is possible.

Very high energetic gamma rays permit observation in an indirect way with ground based telescopes by using secondary Cherenkov light flashes from extended air showers in the upper atmosphere (Imaging Atmospheric Cherenkov Technique, IACT). Photons in the gamma regime with high enough energy induce these electromagnetic air showers, leading to the creation of photons, electrons and positrons, when they interact with the upper atmosphere via bremsstrahlung and pair production. Thus, the initial γ-ray cascades in strongly forward boosted electron positron pairs until the threshold for ionisation is higher than that of bremsstrahlung. Since the generated secondary electrons and positrons move nearly with the speed of light in vacuum, Cherenkov light is emitted at an angle Θ with respect to the direction of the entering primary particle, which is defined by

$$\cos(\Theta) = \frac{1}{\beta n}, \tag{1.2}$$

and depends only on the refractive index n of the medium and the speed of the particle $\beta = v/c$ in units of the vacuum speed of light. Assuming an altitude of 20 km and a Cherenkov angle of ca. 0.33°, the light cone on the ground is in the order of 100 m. Compared to satellites the effective area of the IACT is huge (10^5 m^2) since the whole atmosphere is used as calorimeter and allows to extend observations to energies larger than 100 GeV. On the other hand, the light intensity on the ground is low. The Cherenkov emission is collected with a parabolic mirror and a fast imaging camera system of low light photon detectors, since the signal lasts only for a few ns. From the signal the energy and the source position of the γ-ray can be re-calculated. Fig. 1.7 compares the γ- and proton-induced air showers and illustrates the basic working principle of ground-based Cherenkov telescopes.

Most showers detected by the telescopes are caused by hadrons, which result in different images (more diffuse and extended, see Fig. 1.7) and can thus be discriminated; only one in 10^4 events is caused by a very high energy gamma ray shower.

1.2.1. The physics motivation for gamma ray astronomy

The most energetic objects are emitting in the γ-ray band and recently, the large area telescope of the Fermi satellite has identified more than 2500 sources (see also Fig. 1.8) [32]. Up to now the origin of very high energy γ-rays is not fully understood, since only charged particles can be accelerated and afterwards emit high energetic photons. In addition to photons there are also ionising particles, cosmic rays, which mainly consist of hadrons. Energies of more than 10^{20} eV have been measured for these particles and up to now it is still unclear where they originate from and how they are accelerated.

Interactions of the cosmic rays with the magnetic fields or ambient gas results in the generation of gamma radiation. By investigating the time variation and energy spectrum of the very high energy gamma rays, conclusions about the primary cosmic rays and their production processes can be made. The fundamental processes in cosmic γ-ray generation are [30]:

- synchrotron radiation by leptons with a spiral trajectory in a magnetic field
- energy transfer from relativistic electrons to photons (inverse Compton scattering)
- bremsstrahlung is emitted by deflection of leptons in the electric field of a nuclei in the interstellar medium
- annihilation of matter and antimatter generates photons with an energy of $2m_i$ in their rest frame

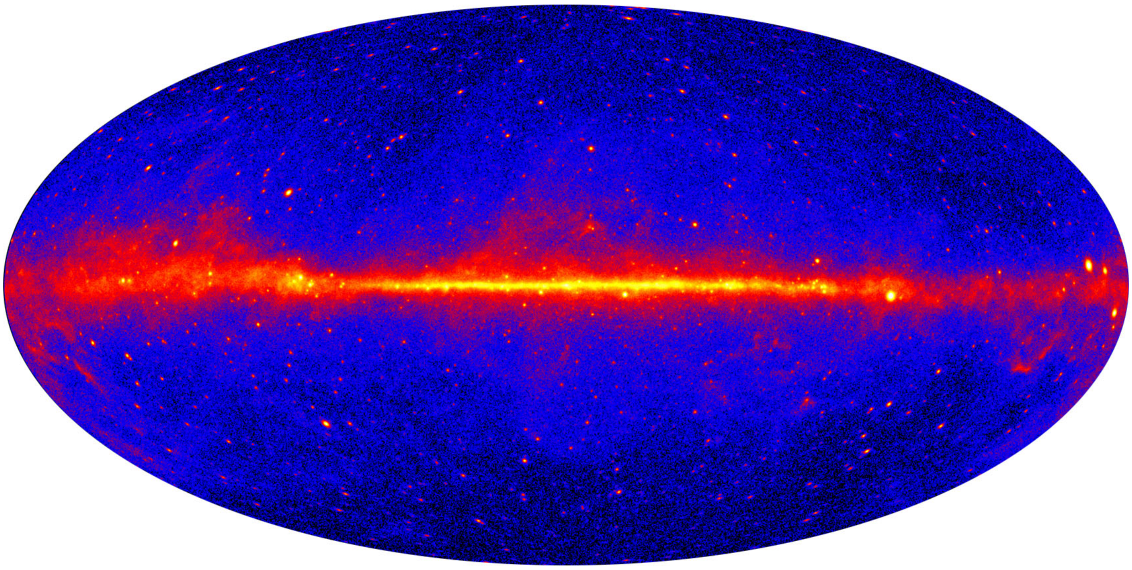

Figure 1.8: Full five year map of the Large Area Telescope on board of the Fermi Gamma-ray Space Telescope in Hammer-Aitoff projection with more than 2500 galactic and extragalactic sources identified. Image from [33].

- collisions of protons with other hadrons results in generation of pions with a finite life time. Gamma rays are produced by the decay of neutral pions (main decay channel)

Therefore, the identification and investigation of gamma ray sources in the universe can lead to a better understanding in the physics behind these objects. Concerning the galactic sources supernova remnants and pulsar wind nebulae are in the focus of interest. Although the acceleration of particles to high energies has been demonstrated with the current generation of IACTs it is still an open question if the observed γ-ray emission has leptonic or hadronic origin.

Magnetic fields of pulsars are known to act as particle accelerators. The exact process is not yet fully understood. In order to understand the emission process in pulsars, studies at high energies are required, since they reveal information about the electrodynamics within their magnetospheres.

The galactic centre is one of the prime targets of future γ-ray astronomy, since it represents the nearest supermassive black hole. Information about particle acceleration and production of γ-rays close to black holes as well as the propagation of particles in the molecular cloud can be revealed by high resolution observations.

X-ray binaries and microquasars consist of binary systems of a compact object, like a neutron star or a black hole, and a massive star. The fact that the physical processes in some microquasars in our galaxy, which produce relativistic jets, are close to the situation in extragalactic supermassive black holes, makes them interesting candidates for studying the emission mechanisms of gamma rays. Also the interaction of microquasars with their surroundings can be revealed by improved angular separation in observations.

Extragalactic sources like active galactic nuclei (AGN) have been one of the first objects discovered by IACT (e.g. Markarian 421, [34]). However, the emission of gamma rays is still not fully understood. AGN consist of an accreting supermassive black hole, which shows emissions of relativistic jets. If this jet points toward the earth, the AGN is called blazar and very high energy gamma rays can be observed. A deeper understanding of the composition of the jets and how they originate is still missing. A fast oscillation of the gamma flux indicates a generation close to the black hole. Simultaneous observations of AGNs in multiple wavelengths with high temporal and spectral resolution will help to reveal the nature of these cosmic objects.

Gamma ray bursts are the most luminous light sources in the known universe and are thus detectable over large distances. They are characterised by a short time scale for the peak luminosity and are followed by a distinct afterglow. Intensive studies with IACT can reveal the intrinsic spectrum and the particle acceleration mechanism of gamma ray bursts and also might reveal if they can explain the highest energy particles in the universe.

Galaxy clusters, the largest gravitationally bound objects, contain all the cosmic rays produced inside. Via the observation of γ-ray emission, a measurement of the non-thermal energy output of the galaxies is feasible. Although no signal of gamma rays from galaxy clusters have been measured yet, their emission is predicted below current instrument sensitivities. Thus, future telescopes should be able to detect gamma ray emission.

Dark matter annihilation into γ-rays can be an additional source of non-thermal radiation from galaxy clusters which will be observable by future large area telescopes. Slow dark matter particle annihilation may lead to an almost mono-energetic photon emission, which will be noticed in a spectral line. However, dark matter can also be detected close the centres of galaxies, where the accumulation of particles should result in a detectable signal due to the increased annihilation rate at high densities. Again the galactic centre is a promising region because of the predicted high density of dark matter. Improvements in sensitivity and angular resolution will help to distinguish between conventional gamma ray sources and diffuse background from potential dark matter signals. Complementary to the possible results of the LHC and underground experiments, ground-based gamma ray telescopes will contribute to verify the nature of dark matter in the universe.

A more detailed discussion about the astroparticle physics motivation for novel gamma ray telescopes can be found in Ref. [35].

1.2.2. Low light level cameras for future Cherenkov telescopes

The currently leading instruments in ground-based gamma-ray astronomy are the High Energy Stereoscopic System (H.E.S.S.) in Namibia [36], the Major Atmospheric Gamma-Ray Imaging Cherenkov Telescopes (MAGIC) on La Palma, Canary islands [37], and the Very Energetic Radiation Imaging Telescope Array System (VERITAS) in Arizona, USA [38]. Over the last few years they have studied more than a hundred γ-sources. The energy range of today's instruments covers the regime from tens of GeV to tens of TeV. For example, the two MAGIC telescopes, optimised for large mirror surface and optimised light collection have achieved a minimum energy threshold of 25 GeV. However, the small flux of gamma-rays in the energy range above 10 TeV requires detection areas in the order of several km^2 to allow discoveries within standard observation times of 50 h. Thus, there is a need for large telescope arrays.

The next generation in IACT telescopes, the Cherenkov Telescope Array (CTA, [35]), is in its design phase. Its sensitivity will be at least one order of magnitude higher than the instruments mentioned above. Thus, CTA will reveal detailed information about the high energy universe with unprecedented precision and increase the number of identified sources by a factor of ten. The complete array will consist of roughly 100 telescopes of different size

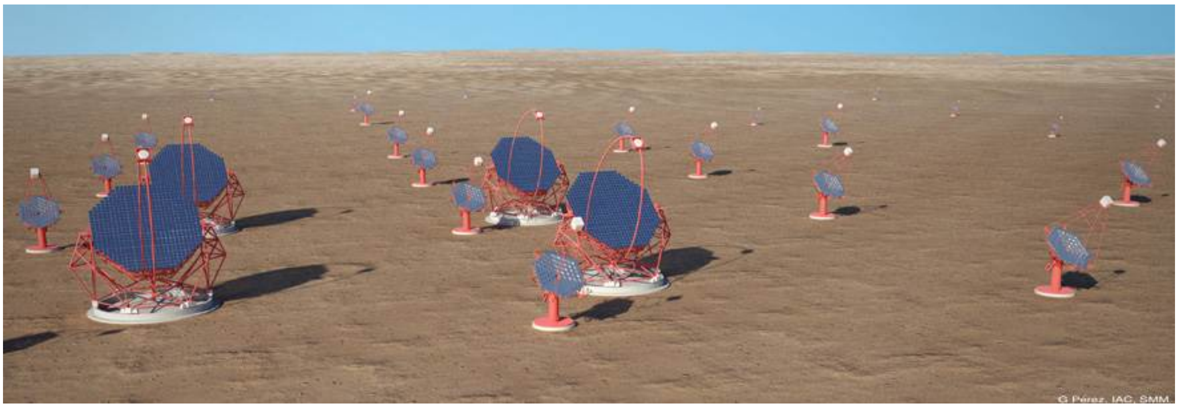

Figure 1.9: Possible layout for the Cherenkov Telescope Array with different telescope sizes. Image from [39].

to cover various energy ranges. The least energetic showers below 50 GeV will be detected by the large size telescopes (ca. 24 m dish), whereas the medium range from 50 GeV to 10 TeV and the high energy above 10 TeV is covered by the middle size (ca. 12 m dish) and small size (ca. 5 m dish) instruments, respectively. A schematic view of the potential layout is shown in Fig. 1.9. In order to achieve full sky observation, one array for the northern and one for southern hemisphere is planned. Due to the large number of telescopes with camera resolutions of ca. 2000 pixels, there is a need for a large amount of photon detectors.

The camera systems of IACT telescopes requires ultra fast and low light level detectors in order to decrease the energy threshold. The minimum detection energy is determined by the light collection which is related to the maximum mirror size and the photon detection efficiency of the detectors. Thus, an improvement of the detector PDE by 50% corresponds to an increase of the effective mirror area by the same amount, assuming a constant PDE [40]. An important fact is that the intensity spectrum of the Cherenkov light is proportional to $1/\lambda^2$, where λ is the wavelength. Thus, most of the light is emitted in the ultraviolet and blue regime as can be seen in Fig. 1.10. Wavelengths below 300 nm are strongly absorbed by the ozone in the atmosphere and therefore do not reach the ground. The preferred peak sensitivity of potential photon detectors can thus be determined to be at around 350 nm. On the other hand the main contribution from night sky background is in the wavelength regime from 550 nm and above. To minimise the noise contribution from the background, the sensitivity of the camera in this regime should be as low as possible. Fortunately, this can be realised by introducing appropriate optical filters.

Since the time distribution of the faint Cherenkov signal is only in the range of 5–10 ns, fast detectors are required. In order to reduce the energy threshold of the instrument, the photon detection efficiency has to be as high as possible. Crucial for improved long-term observations of gamma ray sources, even during bright moonlight periods, is a device which is able to resist high light levels. Up to now, this is a limiting factor of observation time due to the use of vacuum photomultiplier tubes (PMTs). Further preferable requirements are small aging effects, a low power consumption, compact dimensions and also reduced costs, due to the large amount of detectors per camera.

Silicon photomultiplier (SiPM) tend to become a promising alternative technology to photomultiplier tubes, since they meet many of the requirements for future photon detectors for IACT telescopes (see Sec. 2.3.3). In this context, the First G-APD Cherenkov Telescope

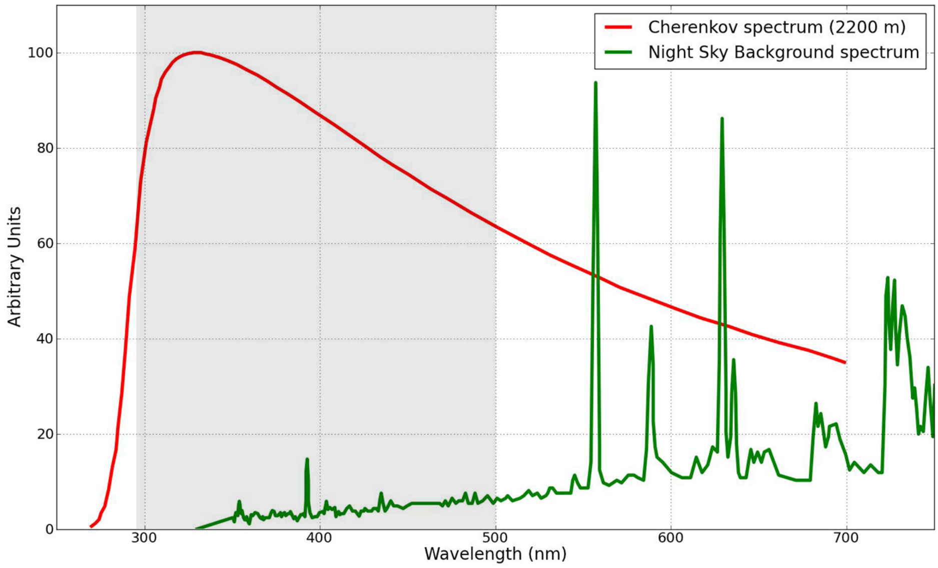

Figure 1.10: Cherenkov and night sky background spectra for IACTs. The red curve is the Cherenkov spectrum from extensive air showers observed at 2200 metres above sea level. The green curve is the night sky background at the telescope site in La Palma, Canary islands. The background emission varies with the location whereas the Cherenkov spectrum changes with energy and impact distance of the air shower. The sensitivity of a photon detector should be adjusted to the wavelength regime indicated by the highlighted area. Image adapted from [41].

(FACT) plays a pioneering role, by replacing the common PMT-based camera with one made of SiPMs. First results are very promising, since they report observations at strong moonlight and long-term stability with a timing resolution of about 600 ps [42, 43]. Due to the limitations in the present performance studies coming from other components of the test telescope, also the full evaluation of the improvements due to the usage of those novel photosensors is limited. Nevertheless, in order to further optimise the performance, technological development of these novel photon detector candidates is important.

1.3. Rare events search with liquid noble gases

By utilising large-volume detectors in deep underground laboratories, scientist are trying to address answers to fundamental questions in modern particle physics. Some of those puzzles, which will be briefly discussed within the scope of this thesis, are the nature of the neutrinos and dark matter. The underlying physical processes for answering these open questions have either extraordinary long half-lives (neutrinoless double beta decay) or very small cross-sections (elastic scattering of dark matter off atomic nuclei). The resulting low detection rate requires experimental environments with lowest possible backgrounds of natural radioactivity and cosmic rays. For this purpose, new large detectors with an optimised shielding, ultra-high radiopurity of all components and an effective event discrimination, in order to distinguish the background from the signal, have to be developed.

The passive shielding against background events from cosmic rays is realised by the rock coverage of underground laboratories, which reduces the flux of cosmic ray induced muons as well as the number of neutrons generated by muon spallation processes in the detector surrounding material. Additional neutron background can originate from the presence of natural radionuclides ^{238}U and ^{232}Th (by fission and (α,n) reactions) in the surrounding rock and concrete as well as in the shielding material itself. Especially for dark matter experiments, the understanding of all neutron background sources is crucial, since they generally cannot distinguish between nuclear recoils caused by dark matter and those by neutron backgrounds. Therefore, an additional shielding is often realised by a surrounding water tank to moderate ambient neutrons and gamma radiation as well as to identify remaining cosmic muons (Cherenkov muon veto). The uranium and thorium series, in combination with the decay of potassium (^{40}K), also contribute to the gamma ray photon background in deep underground experiments. Those photon backgrounds can be shielded by high-Z materials like lead[2] or copper, which in turn have to be produced with a very high level of radiopurity.

As a detector for rare events searches liquid noble gases are well suited medium, since they offer several advantages [44]:

- high purity levels achievable by chemical purification from radioactive contaminants like ^{40}K
- efficient scintillators with a high light yield (order of few 10.000 photons per MeV of deposited energy)
- transparency to own scintillation light (low self-absorption due to impurities like oxygen, water, nitrogen)
- simultaneous detection of scintillation and ionisation signals for particle identification (two-phase detectors), which allows additional background discrimination
- the possibility of an easy scaling to very large volumes (up to multi-ton scale) allows the use of the central part of those detectors which is free from outer radioactivity due to the self-shielding by the peripheral part

However, because of practical reasons, not all noble gases are suitable detector materials in rare events searches. Cooling of helium and neon is rather expensive. In addition, their dominant emission at wavelengths below 90 nm, as depicted in Fig. 1.11, requires windowless photodetectors, since there is no transparent window material for these wavelengths [45]. Krypton has a natural radioactivity due to a non-negligible amount of ^{85}Kr (β emitter, half-life: 10.75 a) and would be affected by an increased background with respect to rare events searches. As a result, most current experiments focus on argon or xenon as detector material. Argon has a low price but a natural atmospheric radioactivity due to ^{39}Ar with an activity of 1 Bq/kg (β emitter, half-life 269 a), which would require purification for very large detector volumes. Due to its natural rarity, the price for xenon is much higher than for other noble gases. However, xenon has a much heavier nucleus than argon, which is of advantage in dark matter searches (see 1.3.2). Additionally, the higher density of liquid xenon improves the self-shielding. Detailed descriptions of the properties of liquid xenon and liquid argon can be found in Refs. [46] and [44], respectively.

The scintillation light in the range of 60–200 nm (see Fig. 1.11), the cryogenic operation temperature and the requirement for lowest backgrounds and energy thresholds sets challenging requirements to the photodetectors in those experiments.

---

[2] The isotope ^{210}Pb, which is a source of photon background, cannot be removed. Therefore, the inner shielding is usually realised by high-purity copper.

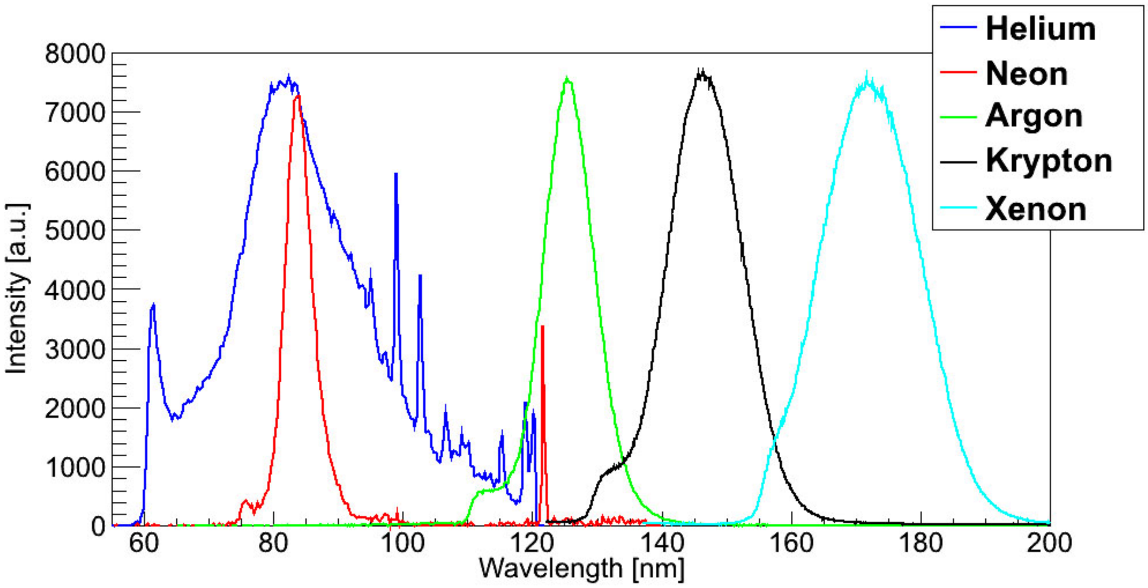

Figure 1.11: Emission spectra of noble gases in gaseous state and room temperature. Excitation was realised with electrons. Similar spectra are obtained in liquid state of aggregation. Image from [44].

1.3.1. Neutrinoless double beta decay

The observation of neutrino oscillations proofed that neutrinos are massive particles. However, these observations do not allow to measure the absolute mass of these elementary particles, since they are only sensitive to the mass squared differences of the neutrino mass eigenstates. One possible way to address the absolute neutrino mass scale could be the neutrinoless double beta decay ($0\nu\beta\beta$). This even rarer hypothetical version of the standard double beta decay ($2\nu\beta\beta$)

$$(Z) \rightarrow (Z+2) + 2e^- + 2\bar{\nu}_e, \tag{1.3}$$

where Z is the atomic number, violates the lepton number conservation and can only occur if neutrinos are their own anti-particles (Majorana particles). The schemes of both double beta decay versions are illustrated in Fig. 1.12. The existence of Majorana neutrinos could explain the small neutrino masses, without an unnaturally small Yukawa coupling to the Higgs field (like for Dirac particles), as well as improve the understanding of the matter-antimatter asymmetry in the universe.

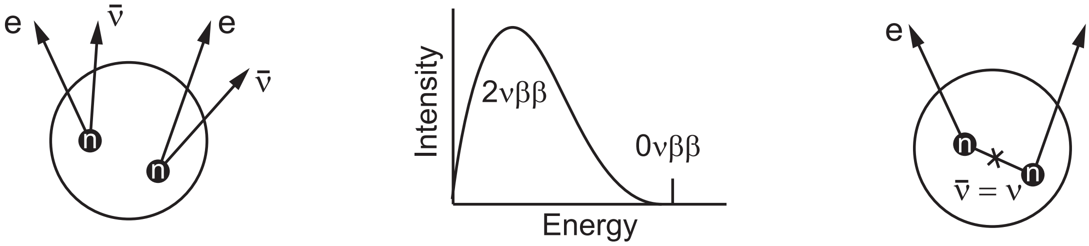

Figure 1.12: Schemes of standard (left) and neutrinoless (right) double beta decays of two neutrons. The expected sum energy spectrum for both cases is plotted in the middle.

Candidate isotope		Q value	Isotopic abundance
Parent nuclide	Daughter nuclide	(MeV)	(%)
^{48}Ca	^{48}Ti	4.272	0.187
^{76}Ge	^{76}Se	2.039	7.8
^{82}Se	^{82}Kr	2.995	9.2
^{96}Zr	^{96}Mo	3.350	2.8
^{100}Mo	^{100}Ru	3.034	9.6
^{116}Cd	^{116}Sn	2.814	7.5
^{130}Te	^{130}Xe	2.527	33.8
^{136}Xe	^{136}Ba	2.458	8.9
^{150}Nd	^{150}Sm	3.371	5.6

Table 1.3: Candidate isotopes of experimental interest for neutrinoless double beta decay [48]. High Q values are desired since they have faster decay rates (phase space) and the amount of radioactive backgrounds is smaller. A large natural abundance is of advantage, since it lowers the costs for the experiment.

The neutrinoless decay can be experimentally distinguished by the energy spectrum of the resulting electrons. In contrast to the common $2\nu\beta\beta$ decay with a broad spectrum of electron energies, the electrons of the neutrinoless decay would have a fixed energy of [47]

$$E_e = \frac{1}{2}[M(Z) - M(Z+2)], \tag{1.4}$$

with the parent and the daughter nuclei masses $M(Z)$ and $M(Z+2)$, respectively, resulting in a sharp line in the energy spectrum.

Double beta decays can be observed only in a few isotopes for which the single beta decay is energetically forbidden. A list of candidates with a Q value larger than 2 MeV is given in Table 1.3. Various experiments are trying to make use of the different isotopes.

In the GERDA experiment [49], high purity germanium detectors are surrounded by liquid argon which acts as cryogenic cooling liquid and passive shielding. The detector material is isotropically enriched with the $0\nu\beta\beta$ candidate $^{76}_{32}$Ge. As previously mentioned, the main challenge of those detectors is to achieve a high exposure (mass × time) with lowest possible background event rates in the energy range of interest (Q = 2039 keV). As a result of phase I (total exposure of 21.6 kg year), the lower limit for the ^{76}Ge half-life was set to $T^{0\nu}_{1/2} > 2.1 \cdot 10^{25}$ a [50], with a determined background of roughly $2 \cdot 10^{-2}$ events/(kg keV year) [49]. However, the background suppression is limited by the remaining radioactivity of the specially fabricated materials used in the experimental setup. A further reduction is only possible via identification of background events (active background suppression).

The $0\nu\beta\beta$ decay deposits the energy only in one detector segment which makes a suppression of background by identification of coincidence events possible. The main source of background for the GERDA experiment is the surrounding material. Photons in the gamma region, originating from natural decay chains, deposit energy in the detectors (predominantly via Compton scattering). There is a high probability that these photons deposit only a part of the energy in the germanium detector itself. After escaping the detector they deposit their energy in the ambient liquid argon shielding. Additionally, α and β radiation from surface contaminations (^{226}Ra, ^{42}K) partially results in energy depositions in the liquid noble gas. By detecting the resulting scintillation light (peak wavelength at 128 nm), those events can be

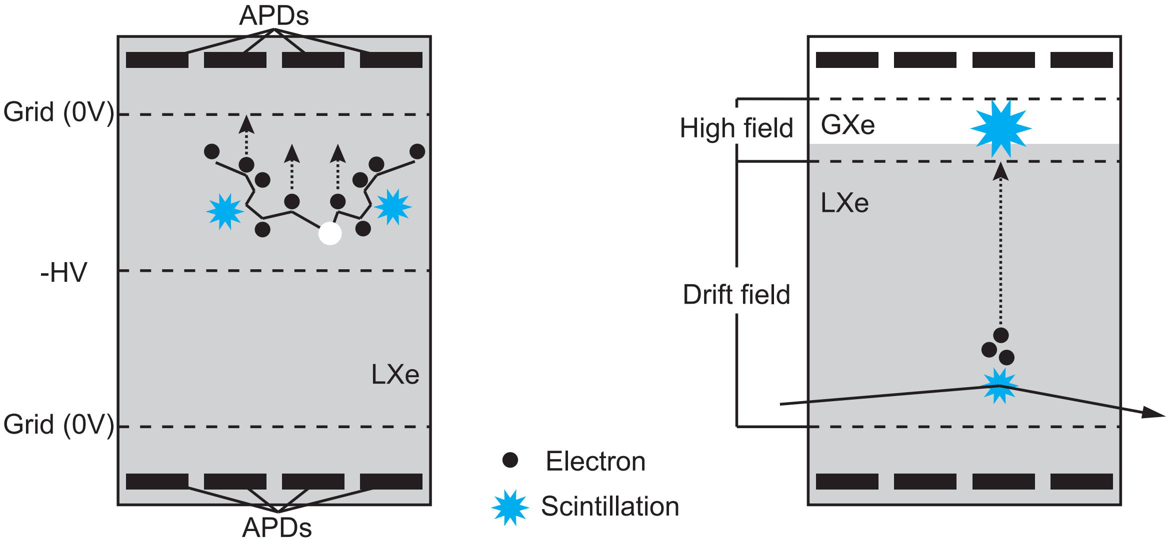

Figure 1.13: Measurement concept for single (left) and dual phase (right) xenon TPCs. Energy deposition in the liquid xenon (LXe) results in ionisation and scintillation which is detected by the APDs and the wire grids (shown for $0\nu\beta\beta$ decay) and allows 3-D reconstruction and measurement of the energy. In the dual phase (shown for dark matter interaction) the ionisation is measured as a second scintillation proportional to the generated electrons. More details are given in the text.

identified as background (liquid argon veto). However, when selecting the photon detectors it has to be considered that they may also contribute to the background (see Sec. 1.3.3). The upgrade is planned for phase II of the experiment, which will have an exposure of 100 kg yr, in order to further reduce the background to a value of 10^{-3} events/(kg keV year) [49].

Since the double beta decay was also observed for the isotope ^{136}Xe [51], new approaches like EXO-200 [52] try to use liquid xenon single phase experiments (operation at $T \approx 167$ K) for the observation of the neutrinoless double beta decay. The time projection chamber (TPC) concept in EXO-200 is a combination of measuring the ionisation and the scintillation signal (see Fig. 1.13 left) of an event. The EXO-200 project is a prototype for an 1–10 ton sized experiment utilising the same readout concept. The TPC is filled with liquid xenon (about 200 kg), enriched to about 80% in the isotope ^{136}Xe. By measuring the scintillation light, the start time signal is provided. The emitted light at 175 nm is recorded by large area photo diodes located behind the anodes. For maximisation of the detection yield, all other surfaces are covered with reflective material. The generated electrons drift towards the anode grids due to the applied electric field and induce a signal. With this information, it is possible to reconstruct the full 3-D distribution of the ionisation. This is important since it allows to distinguish between beta-like events, where the energy is deposited in a single point, and gamma-like events with multiple scattering and thus multisite ionisation. Furthermore, the position also allows to define a volume of reduced background due to the self-shielding of the liquid noble gas which in turn improves the signal to background ratio. α decay events can be identified by their high light-to-ionisation ratio.

A comprehensive overview of double beta decay experiments can be found in Ref. [53].

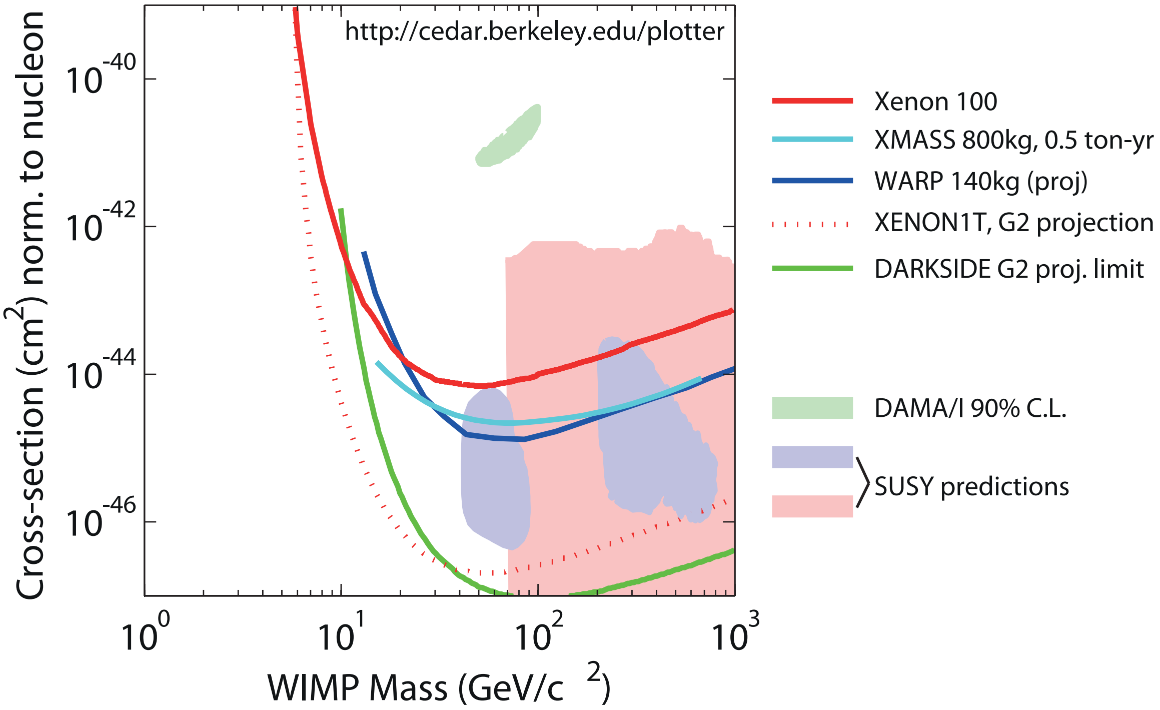

Figure 1.14: WIMP cross section limit versus particle mass for different experiments. XENON100 [54], DarkSide [55], XENON1T [56], WArP [57], XMASS [58]. The filled areas are expected confidence limits for WIMPs from SUSY [59, 60] and DAMA [54].

1.3.2. Dark matter

A common topic of particle and astroparticle physics is to reveal the exact nature of dark matter which makes up roughly 69% of the matter in the universe. Among the hypothetical candidate particles, there is the weakly interactive massive particle (WIMP) which is a neutral particle with a mass in the GeV–TeV range weakly interacting with ordinary matter. These WIMPs might be related to the lightest supersymmetric particles (neutralinos) and were not specifically introduced as a solution to the dark matter problem. Thus, they could also solve further open issues of the standard model what makes them one of the favoured dark matter candidates.

If most of the dark matter in the universe is due to WIMPs, it should be possible to directly detect them by interactions with normal matter. Elastic WIMP-nucleon scattering in a target material should result in nuclear recoils with energies in the keV range [61]. With dedicated detectors, measurements of the small energy transfer to the nuclei allows to observe WIMPs. However, the cross section is very small and thus the event rate of these experiments is also expected to be very low. Xenon has a high atomic number of $Z = 54$ which is preferable for WIMP searches, since the energy transfer to the nucleus is maximised if the mass of the nucleus is in the range of the expected WIMP mass. Assuming a 100 GeV WIMP, rates of about 0.1 and 0.01 events per year per kg are expected for xenon and argon, respectively [61]. Fig. 1.14 compares the cross section sensitivity limits for different experiments as a function of the WIMP mass. The XENON1T and the DarkSide-G2 experiments claim a sensitivity down to cross sections of $\sigma \approx 10^{-47}$ cm^2 for a mass around 100 GeV. This will allow to

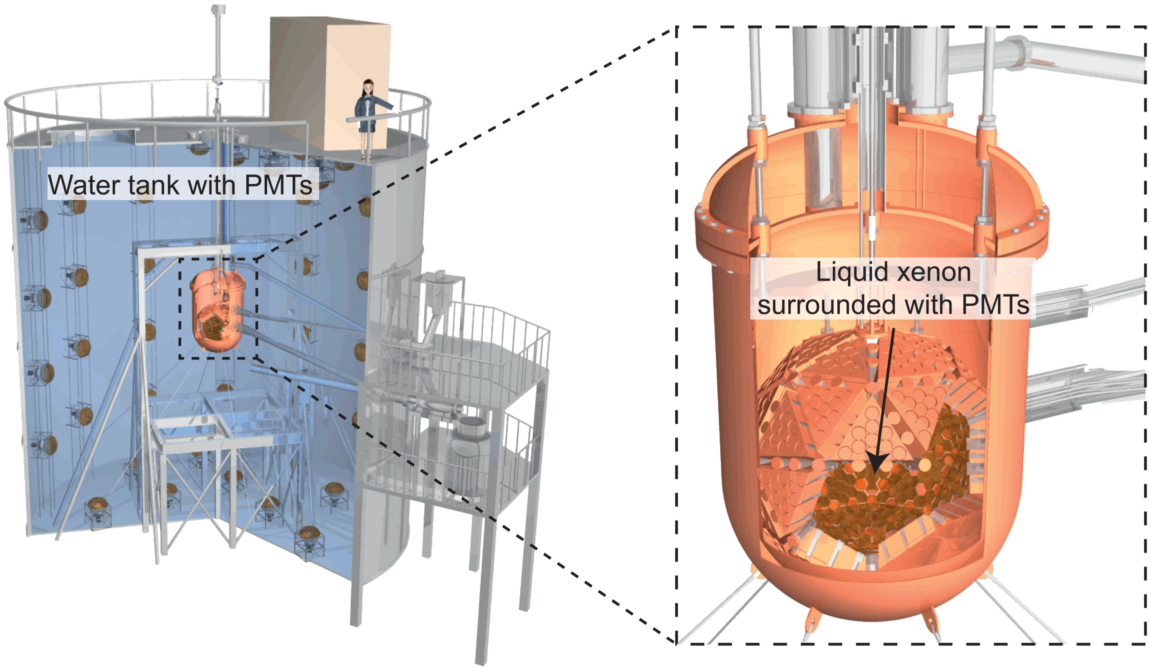

Figure 1.15: Schematic view of the XMASS detector. For shielding against cosmic muons the experiment is placed in a water tank with PMT readout (left). In the liquid xenon detector (right) the xenon is completely surrounded by PMTs to measure the scintillation light distribution. Images adapted from [71].

investigate a wide range of the predictions by latest calculations based on supersymmetry models [59]. Furthermore, it gives the possibility to confirm or disprove the results of other experiments (e.g. DAMA). Similar to the $0\nu\beta\beta$ decay experiments, the low event rate makes the suppression of the background an extremely important issue. Even more challenging is the detection at low energies and without an expected peak signal like for the beta decay. A background reduction via shielding, radiopure construction and active event discrimination is essential for those experiments.

The interaction of WIMPs with the normal matter of a target material and the resulting energy deposition can produce three types of excitation: ionisation (electrons), heat (phonons) and scintillation (photons). In general, the detection can be based on the measurement of only one excitation channel (i.e. annual modulation of scintillation measured with PMTs, DAMA/LIBRA [62]). However, most detectors use the information of two excitation channels in order to distinguish between nuclear and electronic recoils:

- heat and light (CRESST-II [63], ROSEBUD [64])
- heat and charge (SuperCDMS [65], EDELWEISS-II [66])
- charge and light (XENON [67], ZEPLIN-III [68], LUX [69], ArDM [70])

Hence, the predominant background from gamma rays and β decays can be excluded by calculating the ratios of the excitation channel signals.

Liquid noble gas detectors can benefit from their high light yield. Scintillation light is produced by formation of excited dimers of Ar_2^* and Xe_2^* via i.e. $Xe_2^* \rightarrow 2Xe + h\nu$. Moreover, the easily scalable size of the experiment is a further advantage. It allows to build very large detectors in order to improve the sensitivity and to utilise the self-shielding capability of the target material. The inner volume of the detector is shielded from the external radioactivity by the peripheral liquid due to the high atomic number and the large density. Self-shielding for background reduction thus requires the capability of reconstructing the event position in the detector. In the single phase detector XMASS [72] (see Fig. 1.15) no electric field is necessary and no ionisation signal is extracted, since the detection is only based on the scintillation light which is measured by PMTs surrounding the liquid xenon. The event localisation relies solely on the distribution of the scintillation light.

Other experiments like XENON are dual phase detectors based on TPC concepts (see Fig. 1.13 right), where the ionisation signal (electron-ion pairs: $\mathrm{Xe}^+ + \mathrm{e}^-$) can be additionally determined by an electric field across the volume. The generated electrons in the liquid (LXe) drift due to the electric field towards the gaseous xenon (GXe). In the subsequent high field region the carriers are accelerated which results in an excitation of the gas atoms and produces a second scintillation signal. The scintillation light of the primary interaction of the WIMP in the liquid is compared to the scintillation signal generated in the gas phase, which is proportional to the number of ionisation electrons. From the time difference of the two signals in combination with the distribution of the signal in the upper photodetector array, the xyz position can be reconstructed. Most of the external background interacts in the outer layers and can be excluded. With the ratio between the two scintillation signals, an additional background rejection (rejection factor 10^4 [73]) is possible by a discrimination between electronic and nuclear recoils (ionisation-to-light ratio).

Liquid argon detectors (WArP [74], ArDM, DarkSide [75]) use the same measurement principles but offer an additional discrimination tool. By pulse shape discrimination of the primary scintillation electronic recoils can be distinguished from nuclear ones. This is important in order to suppress the large background arising from atmospheric ^{39}Ar.

A review of current dark matter experiments can be found in Refs. [73, 76].

1.3.3. Low background photosensors

The emitted scintillation light of noble gases in the vacuum[3] UV region (argon: 128 nm, xenon: 175 nm) can be shifted by wavelength shifting materials to 280–480 nm, depending on the material [77]. Therefore, sensors with a peak sensitivity in the UV to blue regime, highest possible detection efficiencies, a potential for operation at cryogenic temperatures and a high radiopurity are required to detect the faint light signals.

The conventional way to detect the scintillation light in liquid noble gases is by PMTs, since they offer a high sensitivity and large areas. Although the development of low radioactivity PMTs has been an area of active research, their significant contribution to the background (neutron and gamma), due to their high amount of radioactive impurities, is still a drawback for rare events searches [78, 79]. Large area avalanche photo diodes, as used in the EXO detector, have the advantage of being made of materials that suggest a low contribution to the radioactive background of the experiment and are already used in the EXO experiment for the neutrinoless double beta decay. However, the requirement for single photon sensitivity currently prevents their utilisation in dark matter experiments.

Silicon photomultipliers could be a promising alternative in rare events search. They also offer a low radioactivity of the sensor material with the benefit of the capability of single

---

[3] Photons in this wavelength regime are strongly absorbed by molecular oxygen but can propagate through vacuum.

photon detection with a high efficiency. Currently, their high dark count rates (even at cryogenic temperatures) set a limit to the energy threshold of the experiment which prevents their use in dark matter detectors. Moreover, today's SiPMs usually have a small size and it is a challenging task to realise large area SiPMs with low dark count rates. However, the technological development to improve these devices with respect to dark count rate and UV sensitivity is an ongoing process with good perspectives [80].

1.4. Structure of this thesis

This thesis presents the development, characterisation and optimisation of a novel SiPM approach, in order to increase the photon detection efficiency and simplify the fabrication process. Chapter 2 gives a short introduction to photon-matter interaction, semiconductor properties and detector concepts. The characteristics of SiPMs are described in Chapter 3 together with their measurement methods. In Chapter 4 the new SiPM concept of the semiconductor laboratory of the Max-Planck-Society and its advantages and drawbacks are presented followed by the discussion of the prototype results in Chapter 5. First feasibility studies for the next SiPM generations are described in Chapter 6. Chapter 7 concludes the thesis with a summary and a short outlook.

2. Photon detection with semiconductors

The conceptual design of photon detectors requires deep understanding of a fundamental process in nature — the interaction of matter and light. Moreover, it is necessary to understand what processes subsequently take place in the detector. This is particularly important if it is necessary to tailor the sensor properties for certain applications. In this chapter the basic principles of light-matter interaction are discussed, followed by an introduction to properties of semiconductors which offer, amongst others, the possibility to build small and robust low cost devices with low voltage operation and high efficiencies. Afterwards, the different types of semiconductor photon detectors and their working principles are presented and discussed.

2.1. Light-matter interaction

Light detection with solid state devices is based on the generation of charged secondary particles (electron-hole pairs) by the interaction of photons with matter. The signal formation of such a detector results from the subsequent charge collection. In difference to charged particles, photons are not moderated in a medium but removed from the linear propagating beam. If the initial intensity of a light beam is I_0, the intensity is attenuated exponentially within a distance x in a medium according to the *Beer-Lambert law*:

$$I = I_0 \cdot \mathrm{e}^{-\mu x}, \tag{2.1}$$

with the material dependent absorption coefficient μ, as a function of the photon energy. Thus, Eq. (2.1) gives a quantitative information about the average depth of penetration for photons of different wavelengths.

Due to the fact that the electromagnetic spectrum covers many orders of magnitudes from radio waves (wavelengths of a few metres) to gamma rays (wavelengths below 10 pm), the predominant way of interaction changes, and therefore the value of μ as well, which is the sum of the absorption coefficients of all possible interaction mechanisms.

In principle it can be distinguished between two different basic processes: complete absorption (photoelectric effect, pair production) or scattering (Compton effect) of a photon. In the following, these effects, shown in Fig. 2.1, are discussed in more detail with respect to solid states.

2.1.1. Photoelectric effect

The photoelectric effect describes the emission of electrons, often called photoelectrons (phe), by complete absorption of incident photons. In solids, it can be distinguished between the external photoelectric effect, where the electrons are emitted from the surface to the vacuum (usually for metals) and the internal photoelectric effect (in semiconductors), where electrons are excited from the valance band to the conduction band (see Sec. 2.3). Both processes are shown in Fig. 2.1a and b. Photoemission is only allowed if the energy of the incident photon

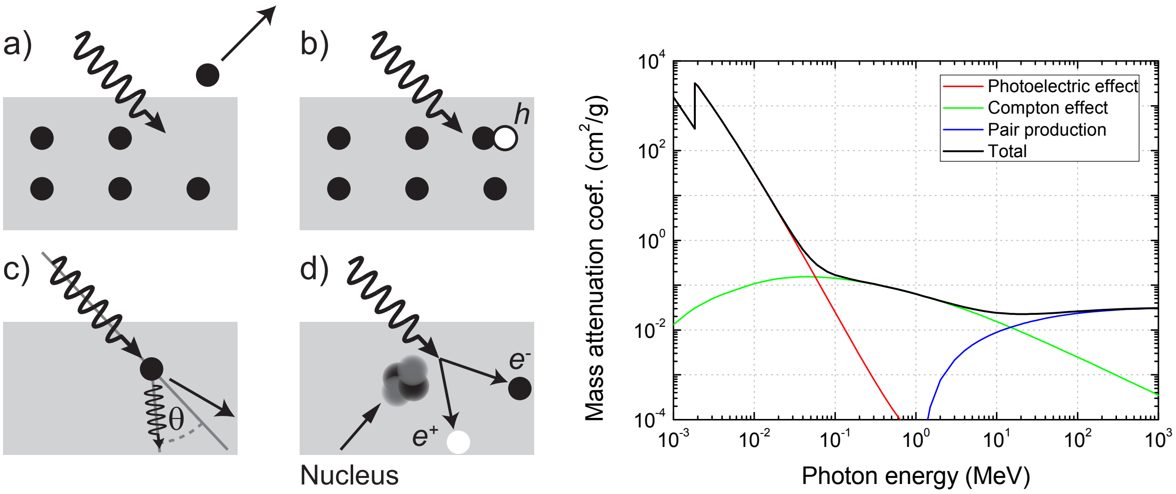

Figure 2.1: Light-matter interactions in solid states. a) external photoelectric effect, b) internal photoelectric effect, c) Compton effect, d) pair production. On the right hand side, the mass attenuation coefficient for the different interactions is plotted as a function of the photon energy. Data from [81].

Material	Band gap energy E_g (eV)
Silicon	1.12
Germanium	0.66
Gallium Arsenide	1.42
Indium Antimonide	0.17
Indium Arsenide	0.35
Indium Phosphide	1.34

Table 2.1: Transition energies for different semiconductors at 300 K.

is above a certain threshold. In other words, the wavelength of the photon has to be below the threshold wavelength λ_t, which is given by

$$\lambda(\mu m) \leq \lambda_t \approx 1.24/\Delta E, \tag{2.2}$$

with ΔE the transition energy of energy levels in eV.

For the external photoelectric effect, ΔE is given by the material-specific work function W, which is in the order of several eV. For the internal effect, the transition energy is defined by the energy band gap E_g of the semiconductor material (see Sec. 2.2). For comparison, Table 2.1 shows some transition energies for different semiconductors. Depending on the desired detection wavelength the appropriate material should be selected with Eq. (2.2). After the absorption, the kinetic energy of the emitted photoelectrons is

$$E = h\nu - \Delta E, \tag{2.3}$$

with h the Planck constant and ν the frequency of the incident photon. The probability of the photoelectric effect is proportional to Z^{4-5}, with Z the atomic number [82].

Since the kinetic energy of the electron is approximately the energy of the incident photon, for photons with $h\nu \gg \Delta E$, it would allow the measurement of the photon energy. Due to the high kinetic energy the electron creates secondary electron-hole pairs by impact ionisation. The detectors in this work are semiconductor sensors designed for the detection of scintillation or Cherenkov light. Thus, the wavelengths of interest are in the visible to ultraviolet range (ca. 350 nm - 500 nm) with ΔE in the order of $h\nu$ and the photoelectric effect is the dominant interaction mechanism.

2.1.2. Compton scattering

In Compton scattering (see Fig. 2.1c) photons are scattered inelastically at quasi-free electrons in a solid state body. A part of their energy is transferred to the participating electron. The binding energy inside the material can be neglected compared to the photon energy as a first approximation. The scattered energies of electron (E'_e) and photon (E'_γ) can be calculated with four-momentum conservation:

$$E'_e = h(\nu - \nu') = h\nu \left[1 - \frac{1}{1 + \frac{h\nu}{m_e c^2}\left(1 - \cos(\theta)\right)}\right] \tag{2.4}$$

and

$$E'_\gamma = h\nu' = \frac{h\nu}{1 + \frac{h\nu}{m_e c^2}\left(1 - \cos(\theta)\right)}, \tag{2.5}$$

with c the speed of light in vacuum, θ the scattering angle, m_e the electron mass, and ν' the frequency of the scattered photon.

The differential cross-section of Compton scattering is defined by the *Klein-Nishina formula* [83], and the maximum energy transfer between electron and photon is reached for an angle of $\theta = 180°$. Compton scattering depends on the number electrons, available as scattering partners, and therefore scales linearly with Z [82]. It is the dominant interaction within a photon energy range of $50 - 2000$ keV. Thus, it can be neglected for the measurements in this thesis.

2.1.3. Pair production

Pair production describes the transformation of energy into matter by generation of an elementary particle and its antiparticle. For example, if the energy of a photon exceeds twice the rest energy of an electron, the photon can be converted into an electron-positron pair (see Fig. 2.1d):

$$\gamma \rightarrow e^- + e^+$$

with

$$E_\gamma > 2m_e c^2 \approx 1.02 \text{ MeV} \tag{2.6}$$

Due to conservation of momentum, this process is only possible in the presence of a nucleus. The probability of pair production increases with increasing energy and is proportional to the atomic number ($\propto Z^2$) [82]. For photon energies of more than 3 MeV, the pair production is the dominant process in light-matter interaction. Since there is no pair production in the measurement of scintillation and Cherenkov light it can also be neglected.

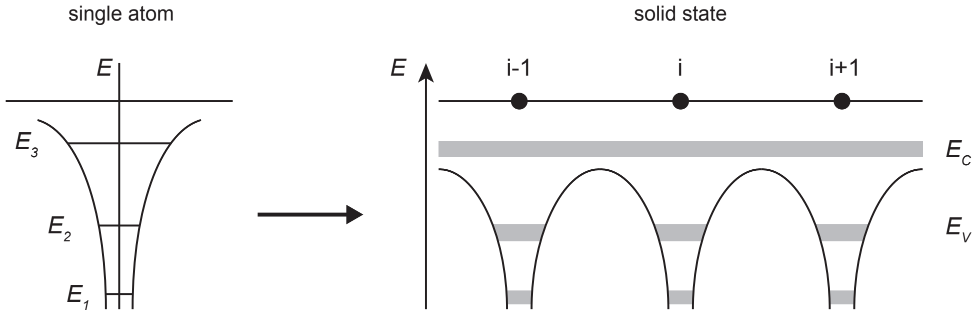

Figure 2.2: The discrete energy levels of a single atom (left) and the situation in a solid state body (right) with the formation of energy bands due to the overlap of the N wave functions (tight binding model). The width of the band is a function of the distance to the next neighbours. The closer the distance the bigger the width.

2.2. Semiconductor properties

Depending on the wavelength and the amount of light, various methods for detection have been developed over the last decades. Semiconductor detectors play an increasingly important role in optoelectronics. Especially in the detection of single photons, semiconductor technology offered new possibilities and led to promising instrumentation. In order to understand the working principle of semiconductor detectors, this section provides a brief overview of the main properties of semiconductors, mainly based on Refs. [84–87].

2.2.1. Band structure

The wave function of an electron in a solid state differs from a plane wave by a lattice periodic modulation. Thus, the eigenfunction of the Schrödinger equation for electrons in a crystal can be written as

$$\psi_k(\mathbf{r}) = u_k(\mathbf{r})\, \mathrm{e}^{-i\mathbf{k}\cdot\mathbf{r}}, \tag{2.7}$$

the product of a plane wave $\mathrm{e}^{-i\mathbf{k}\cdot\mathbf{r}}$ with a modulation function $u_k(\mathbf{r})$ representing the periodicity of the crystal lattice. Those *Bloch functions* describe free movement of electrons in a perfectly periodic crystal.

Furthermore, the interaction of the lattice atoms in solid states results in a transition from discrete energy levels for a single atom to energy band structures. The tight binding model is one approach to calculate these band structures of solid states. It is based on tightly bound electrons to the individual atoms in the crystal lattice and takes into account the perturbation potential of the neighbouring atoms. It is similar to the LCAO (linear combination of atomic orbitals) method where two atoms form a binding and a non-binding molecular orbit. With the interaction of N atoms and $N \gg 1$ in solid states, the energy levels are smeared out and can be assumed as a continuum (see Fig. 2.2). As a result the energy is a function of the wave vector, with the width of the band depending on the strength of the overlap of the wave functions. In addition, these bands are separated by band gaps which do not contain allowed energy states. If there are no allowed energy states in all directions of the momentum space $\mathbf{k}$, this region is called absolute band gap (E_g).

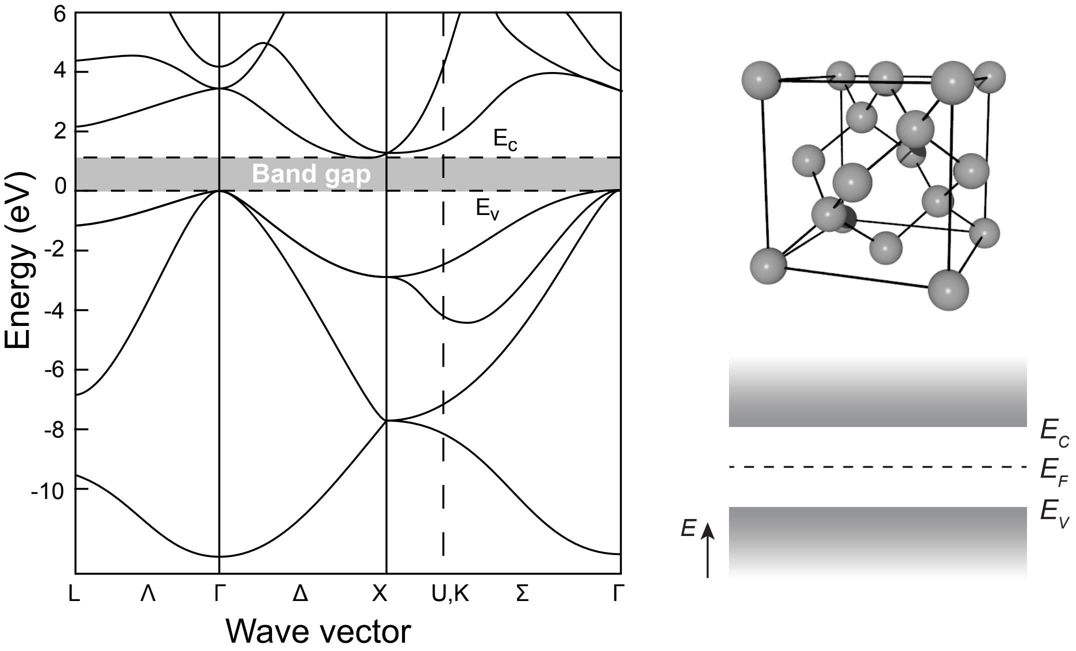

Figure 2.3: Band structure (after [88]) and unit cell of silicon. The maximum of the valence band and the minimum of the conduction band are not at the same position in k-space (indirect semiconductor). The right side shows the diamond crystal structure of the silicon unit cell and below the conduction and valence band with the Fermi energy in real space.

The bands are filled with electrons up to the Fermi energy E_F according to the Pauli exclusion principle. The topmost completely filled band is called the valence band and the first partially filled or unoccupied one conduction band. E_C is the energy level at the bottom of the conduction band and E_V at the top of the valence band. A completely filled band does not contribute to carrier transport, since no free states are available. Materials with the Fermi level within an absolute band gap are semiconductors or isolators, depending on the size of E_g. In metals the Fermi level is within the conduction band, which means this band is partially filled. Holes are introduced as imaginary equivalent particles to describe the interactions of the electrons within an almost completely filled band. Instead of calculating with a large number of electrons, a small number of holes is considered.

Silicon, a group IV material, shows a pronounced sp^3 hybridisation which results in a diamond crystal structure (see Fig. 2.3). The sp^3 hybrid orbitals lead to two energy bands in which the lower one is filled with the four valence electrons while the upper one is empty. The resulting band structure of silicon is also shown in Fig. 2.3. As can be seen, the minimum of the conduction band and the maximum of the valence band are not at the same position in k-space. Therefore, silicon is an indirect semiconductor with a minimum energy band gap of $E_g = 1.12$ eV at room temperature, whereas the direct band gap at the Γ-point in k-space is $E_\Gamma = 3.4$ eV.

2.2.2. Doping

An advantage of semiconductors is that their electrical properties can be altered. By introducing impurity atoms into the crystal lattice, additional charge carriers can be provided.

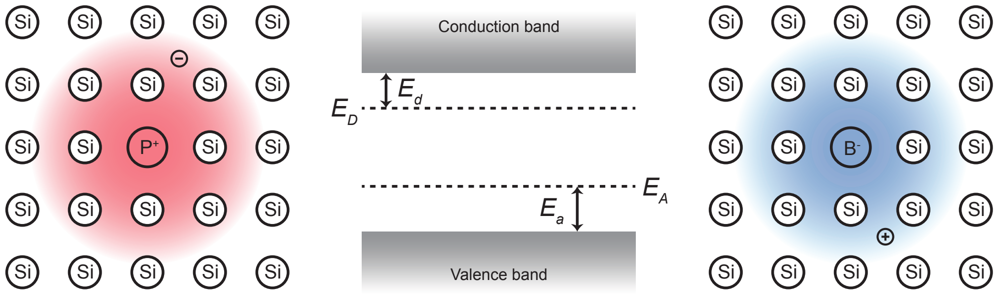

Figure 2.4: Principle of doping in semiconductors. The left side shows the donor impurity and energy level, whereas on the right hand side the same is plotted for acceptors (after [87]).

	Donors				Acceptors			
	P	As	Sb	Bi	B	Al	Ga	In
$E_{d,a}$ (meV)	45	54	43	69	45	72	74	157

Table 2.2: Ionisation energies E_D and E_A for donors and acceptors in silicon. In comparison, the intrinsic band gap of silicon is $E_g = 1.12$ eV [84].

Electrically active impurities, which supply electrons for the conduction band, are called *donors*. Typical donor materials for Si are elements from group V like phosphorus and arsenic. If a Si atom in the crystal is replaced by a donor, only four of the valance electrons are used for the covalent binding. The fifth electron can be separated from the atomic nucleus with a small amount of energy (see Fig. 2.4). Therefore, the energy level of the donor E_D is located in the meV range below the conduction band. Table 2.2 shows the ionising energies for different materials in silicon. Semiconductors with high donor concentrations are called *n-type* semiconductors.

By replacing the Si atom with a group III element like boron, one electron is missing for the tetrahedral binding. Thus, this atom can easily accept an electron which is afterwards missing in its crystal environment. This missing electron can be described by an additional hole in the valence band and impurities with those characteristics are called *acceptors*. The energy states of the acceptors E_A are located in the meV range above the valence band (see also Fig. 2.4 and Table 2.2). If the acceptor concentration is dominating, the semiconductor is called *p-type*. Since the energy levels in both cases of doping are in the order of the thermal energy at room temperature (≈ 25 meV), the doping states can be easily thermally ionised.

In a doped semiconductor an electron in the conduction band can originate either from the valence band or from a donor atom. Respectively, a hole in the valence band corresponds to an electron in the conduction band or an ionised acceptor atom. With the law of mass action

$$n_i = \sqrt{n_c p_v} = 2\left(\frac{k_B T}{2\pi\hbar}\right)^{3/4}(m_e^* m_h^*)^{3/4}\,\mathrm{e}^{-E_g/2k_BT} = const. \tag{2.8}$$

the position of the Fermi level can be calculated. Here, n_c is the electron density in conduction band, p_v the hole density in valence band, k_B the Boltzmann constant, T the absolute temperature, and m_e^*, m_h^* the effective mass of electrons and holes, respectively. In contrast to

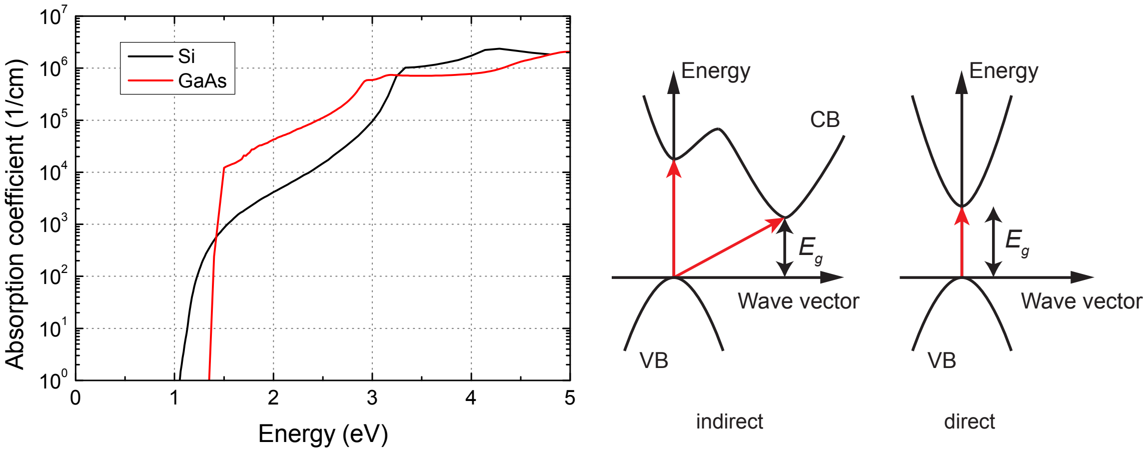

Figure 2.5: Absorption spectrum of direct and indirect semiconductors. Gallium arsenide (GaAs) with a direct band gap shows a strong increase once the photon energy reaches E_g, whereas the indirect band gap in silicon leads to a slower increase in the absorption coefficient values. The difference in principle in the absorption mechanism between the two materials is shown on the right. Data after Ref. [89].

intrinsic semiconductors ($n_c = p_v$) the influence of the dopants has to be taken into account, which leads to the charge neutrality condition

$$n_c + n_A^- = p_v + n_D^+ \tag{2.9}$$

where n_D^+ and n_A^- are the densities of ionised donors and acceptors. At room temperature all dopants can be assumed to be ionised and the charge carrier density is equal to the doping density of the material.

2.2.3. Optical absorption

As mentioned in Sec. 2.1.1, the internal photoelectric effect is the dominant process for semiconductors in the wavelength range of visible light. When a semiconductor is illuminated with photons an electron from the valence band can be excited to the conduction band by absorption of a photon with energy $\hbar\omega$ and wave vector $\mathbf{k}_\gamma$. For those interband transitions the conservation of energy and momentum

$$\begin{aligned} E_g &= \hbar\omega \pm \hbar\omega_q \quad \text{with } \hbar\omega = \frac{h}{2\pi}2\pi\nu & (2.10) \\ \hbar\Delta\mathbf{k} &= \hbar(\mathbf{k}_\gamma \pm \mathbf{q}) & (2.11) \end{aligned}$$

must be met. Here $\Delta\mathbf{k}$ is the difference of the wave vectors of the participating states in the valence and conduction band and $\mathbf{q}$ and $\hbar\omega_q$ are the wave vector and the energy of a phonon, respectively. Since the wave vector of photons ($k_\gamma = \omega/c$) is very small, also Δk has to be very small for transitions with exclusive photon participation. The result is a quasi vertical transition in the dispersion relation $E(\mathbf{k})$. All other transitions with a larger Δk can only occur with the assistance of phonons, since usually $|\mathbf{q}| \gg |\mathbf{k}_\gamma|$ is the case.

In Fig. 2.5, the absorption spectrum of a direct (gallium arsenide) and indirect (silicon) semiconductor is plotted. In a direct semiconductor the minimum of the conduction band

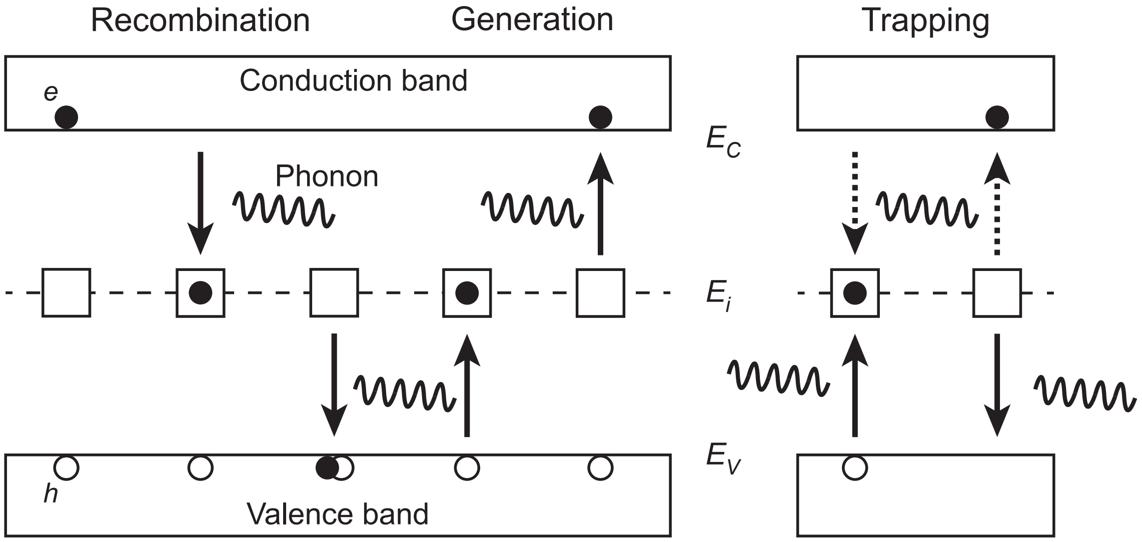

Figure 2.6: Shockley-Read-Hall process and trapping. The left side shows the SRH process where an electron recombines with a hole in the valence band via a mid-gap defect state, while the last two steps show the generation of an electron-hole pair via the defect state. All shown processes involve phonon absorption or emission. E_i indicates the intrinsic Fermi level. The right hand shows the process of trapping charge carriers. An electron from the conduction band is captured by the defect and emitted afterwards or the electron comes from the valence band what corresponds to the trapping of a hole.

in k-space is at the same position as the maximum of the valence band and absorption is possible, once the photon energy exceeds the band gap energy, without participation of phonons. Thus, the absorption is strongly increasing at an energy corresponding to E_g. In indirect semiconductors, the band extrema have a difference of $\Delta\mathbf{k}$ and therefore the emission or absorption of a phonon is necessary for band transitions, according to Eq. (2.11). Due to the reduced probability of a three particle interaction, the absorption coefficient of indirect semiconductors is strongly reduced and shows a slow increase as long as the energy is below the value which allows direct band transitions. For silicon at room temperature, this is the case for an energy of $\hbar\omega = 3.4$ eV.

2.2.4. Non radiative recombination

In an ideal semiconductor, there are no allowed energy levels within the absolute band gap. In reality, chemical impurities can lead to deep band gap states as well as the doping process itself can cause defects such as vacancies or interstitials. At these states, the electron is localised in a finite space around the defect unlike the electron states in conduction and valence band, which generally correspond to free motion in space. On the one hand, electrons and holes can be trapped and emitted afterwards by these defect states, as shown on the right hand side in Fig. 2.6. On the other hand, these defects allow the recombination and generation of electrons and holes by emission or absorption of phonons. Most important are defect states near the mid-gap, since they give the possibility for two energy steps of $E_g/2$.

This non radiative recombination is the dominant recombination process in indirect band gap materials like silicon and is known as Shockley-Read-Hall (SRH) process. Considering only the trap states in the mid-gap, the net transition rate for SRH[1] is

$$U_{SRH} = \frac{n_c p_v - n_i^2}{\tau_p \left(n_c + n_i\right) + \tau_n \left(p_v + n_i\right)}, \tag{2.12}$$

where τ_n and τ_p are the electron and hole lifetimes, respectively and n_i is the intrinsic charge carrier density. The minority carrier lifetimes are given by

$$\tau_p = \frac{1}{\sigma_p v_{th} N_t} \tag{2.13a}$$

$$\tau_n = \frac{1}{\sigma_n v_{th} N_t}, \tag{2.13b}$$

with the trap density N_t, the thermal velocity $v_{th} = \sqrt{2k_BT/\pi m}$, and σ_n and σ_p the electron and hole capture cross sections, respectively.

SRH describes the carrier generation in space charge regions and is therefore of interest for avalanche photodetectors because they represent a potential source of noise. In the depletion region, where $pn \ll n_i^2$, the generation of charge carriers dominates and is proportional to the density of traps N_t. This thermal generation of charge carriers affects the dark noise (thermal noise) and afterpulsing probability of photon detectors (see Sec. 3.2.2.8).

2.2.5. pn-junction

In order to collect the electron-hole pairs produced by the absorption of photons, an electrical field is required. For low light levels it is also necessary, that the charge carrier density in the sensitive volume is as small as possible, since the number of generated electron-hole pairs is small, too. A common way to achieve this is to use the built-in electric field of a pn-junction together with an applied voltage in reverse bias.

Fig. 2.7 shows a schematic view of an unbiased abrupt junction of p- and n-type material. Since in thermal equilibrium $dE_F/dx = 0$ must be valid, the Fermi level has to be uniform throughout the structure. This results in a bending of conduction and valence band at the junction region. A diffusion current arises because of the difference in electron and hole densities across the junction leaving behind negatively charged acceptors in the p-region and positively charged donors in the n-region. This, in turn, results in a space charge region $\varrho(x)$, which extends with d_n on the n-side and d_p on the p-side with no free carriers remaining (also called depletion region). An electric field is generated, leading to a drift current which counterbalances the diffusion current in thermal equilibrium. The potential difference between n- and p-type is called built-in voltage V_{bi}. With the Poisson equation

$$\frac{d^2\Phi}{dx^2} = -\frac{\varrho(x)}{\varepsilon_r \varepsilon_0} \quad \text{with} \begin{cases} \varrho(x) = +en_D & 0 < x < d_n \\ \varrho(x) = -en_A & -d_p < x < 0 \end{cases} \tag{2.14}$$

---

[1] The complete equation is $U_{SRH} = \dfrac{\sigma_n \sigma_p v_{th} N_t (n_c p_v - n_i^2)}{\sigma_n \left(n_c + n_i \exp\left(\frac{E_t - E_i}{k_B T}\right)\right) + \sigma_p \left(p_v + n_i \exp\left(\frac{E_i - E_t}{k_B T}\right)\right)}$

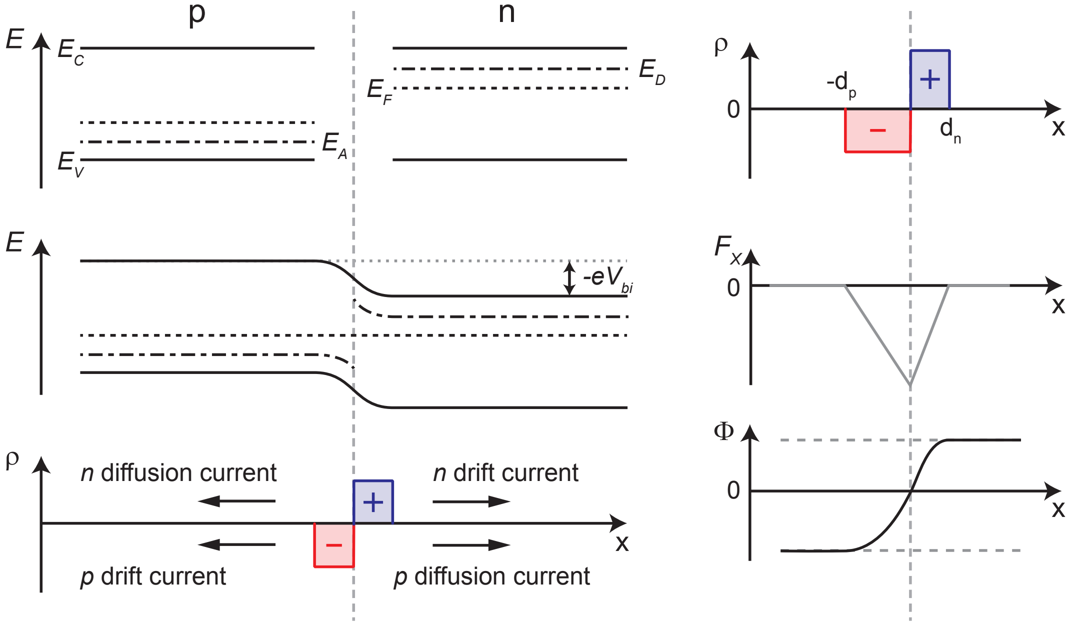

Figure 2.7: Schematic overview of an abrupt pn-junction. The left hand side shows the p- and n-type material with the characteristic energy levels and the situation after connecting. Also the different currents and the space charge region is shown. On the right hand side the derivation of the electric field and the potential from the space charge region $\varrho(x)$ via the Poisson equation is plotted. The electric field peaks at the junction and has a linearly form, the potential drop in the depletion region has a quadratic form (after [87]).

the electric field F and the potential Φ as a function of x can be calculated. Together with the boundary condition of charge neutrality $n_D d_n = n_A d_p$, the width of the depletion region is

$$W = d_n + d_p = \sqrt{\frac{2\varepsilon_r \varepsilon_0 V_{bi}}{e} \left(\frac{n_A + n_D}{n_A n_D} \right)}, \tag{2.15}$$

with ε_r the relative permittivity, ε_0 the vacuum permittivity, and n_A and n_D the doping densities of acceptors and donors.

With an external potential applied across the junction the equilibrium is no longer present and a net current will flow. Due to the low charge density the whole voltage V drops over the space charge region:

$$\Delta\Phi = V_{bi} - V. \tag{2.16}$$

The width of the space charge region is therefore altered $\propto \sqrt{(1 - V/V_{bi})}$, since V_{bi} in Eq. (2.15) is replaced by $V_{bi} - V$. In forward bias, the p-side is at positive potential with respect to the n-side and $V > 0$. At reverse bias the situation is vice versa, which gives $V < 0$. Hence, the depletion region and the band deflection is reduced in forward biasing and increased in reverse biasing.

With respect to the different contributions of drift and diffusion currents the *Shockley diode equation*[2] can be derived:

$$I(V) = I_S \left(\mathrm{e}^{\frac{eV}{k_B T}} - 1 \right). \tag{2.17}$$

The saturation current I_S is defined by

$$I_S = \frac{eD_p p_n}{L_p} + \frac{eD_n n_p}{L_n}, \tag{2.18}$$

with the diffusion coefficient D_p, L_p the diffusion length, and p_n the density of holes in n-type material. Here, the diffusion length $L_p = \sqrt{D_p \tau_p}$ is given by the square root of the diffusion coefficient and the recombination lifetime τ_p of holes in n-type material[3]. D_n, L_n, and n_p correspond to same parameters for electrons in p-type material.

The depletion region of a pn-junction represents a parallel plate capacitor with the depletion width W as the plate distance. The depletion-layer capacitance is thus given by

$$C_D = \frac{dQ}{dV} = \frac{\varepsilon_0 \varepsilon_r A}{W}, \tag{2.19}$$

where dQ is the change of depletion charge on each side upon an incremental voltage step dV, and A is the area of the junction.

2.2.6. Impact ionisation and avalanche breakdown

At high electric fields, like in pn-junctions with high reverse bias voltage, impact ionisation becomes a dominant process. Here, an electron in the conduction band, with high kinetic energy, gained from the electric field, scatters with an electron in the valence band via Coulomb interaction and excites it to the conduction band (see Fig. 2.8). For this process, the minimal energy for the initial electron cannot be less than the band gap energy [90, 91]. Since the conservation of energy and momentum must be satisfied, and with the assumption of the simplest parabolic dispersion for electrons and holes, the threshold energy for electrons can be calculated [90, 92]:

$$E_{th} = E_g \left(1 + \frac{m_e^*}{m_e^* + m_h^*} \right). \tag{2.20}$$

However, for a real semiconductor the band structure at high energies can never be described by this simple approximation. As shown in Fig. 2.3, several valleys in the conduction and valence band have to be taken into account for silicon. For room temperature it is shown that the minimum value of E_{th} is close to the energy gap E_g and can vary with the direction of motion [90, 91].

The multiplication of impact ionisation can be calculated with the approximation of ionisation rates [91]. In this approach, impact ionisation is characterised by ionisation rates $\alpha_i(F)$ for electrons and $\beta_i(F)$ for holes. They are defined as probabilities of ionisation per

---

[2] By taking into account the generation-recombination current in the space charge region caused by energy levels within the band gap, Eq. (2.17) is adapted with an ideality factor n to:

$$I(V) = I_S \left[\exp\left(\frac{eV}{nk_B T} \right) - 1 \right] \quad \text{with } n \in [1, 2].$$

[3] The lifetime of minority charge carriers is an inverse sum of different contributions from SRH, surface, ...: $\tau^{-1} = \tau_1^{-1} + \tau_2^{-1} + ...$

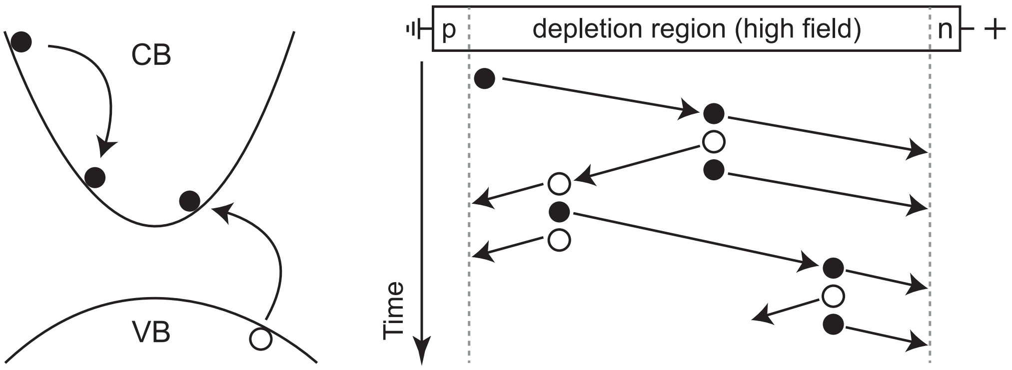

Figure 2.8: Impact ionisation in semiconductors. The left side shows the process of ionisation in a schematic band diagram. An electron in the conduction band with $E > E_g$ scatters with an electron in the valence band and produces two new free carriers, an electron-hole pair. In the plot on the right hand side an electron is injected into the high field region (depletion region) from the left. After a certain distance it creates an electron-hole pair. Electrons will move to the right and can create new free carriers. Holes will move to the left and can also create electron-hole pairs.

unit length and and are assumed to be functions of the electric field F. These assumptions are valid for devices with depletion widths $W \geq 100$ nm. Theoretical results for α_i and β_i have been a topic of many investigations with absolutely non-unique results [93]. However, in good approximation the field dependency can be described by the empirical expressions

$$\alpha_i(F) = \alpha_0^\infty \exp(-b_n/F) \tag{2.21a}$$

$$\beta_i(F) = \beta_0^\infty \exp(-b_p/F), \tag{2.21b}$$

with α_0^∞, β_0^∞ and $b_{n,p}$ being the ionisation coefficients [94]. Fig. 2.9 shows the ionisation rates for silicon at room temperature as a function of the inverse electric field.

While traversing a distance dx, an electron will create an average of $\alpha_i dx$ electron-hole pairs. Thus, the increase of the electron current density j_n due to electron multiplication will be

$$\left.\frac{dj_n}{dx}\right|_n = \alpha_i j_n dx. \tag{2.22}$$

In addition, the electron current density will also increase due to hole multiplications

$$\left.\frac{dj_n}{dx}\right|_p = \beta_i j_p dx. \tag{2.23}$$

Hence,

$$\frac{dj_n}{dx} = \alpha_i j_n + \beta_i j_p. \tag{2.24}$$

For the hole current density it is analogously

$$\frac{dj_p}{dx} = -\beta_i j_p - \alpha_i j_n \tag{2.25}$$

and

$$\frac{dj_p}{dx} = -\frac{dj_n}{dx}, \tag{2.26}$$

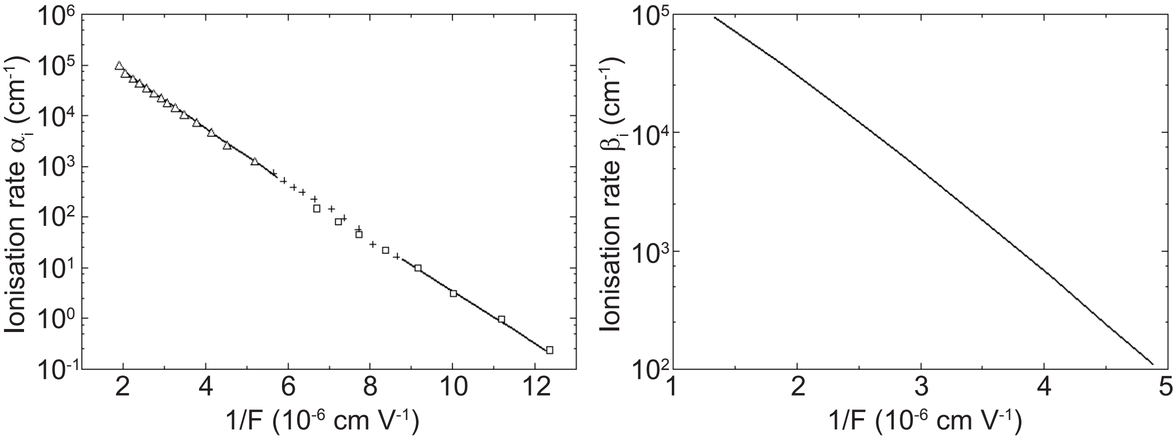

Figure 2.9: Ionisation rates of silicon for electrons (left, adapted from [95]) and holes (right, adapted from [96]) as a function of the inverse electric field $1/F$. The values for electrons are roughly one order of magnitude higher than those for the holes.

while the total current density is

$$j = j_n + j_p. \tag{2.27}$$

The multiplication factor M can be calculated using Eqs. (2.24) - (2.27) and results in

$$M_n = \frac{1}{1 - \int_0^L \alpha_i \exp\left(-\int_0^x (\alpha_i - \beta_i)dx'\right) dx} \tag{2.28}$$

for electrons and

$$M_p = \frac{1}{1 - \int_0^L \beta_i \exp\left(-\int_x^L (\beta_i - \alpha_i)dx'\right) dx} \tag{2.29}$$

for holes, where L is the width of the avalanche region. Both components must be added if electrons and holes are injected into the high field region.

If the bias voltage exceed the breakdown voltage V_{bd}, avalanche breakdown occurs. This corresponds to $M \to \infty$ or $\int_0^L ...dx = 1$. Once this condition is fulfilled, there is no need for external carriers to support the avalanche and the breakdown becomes self-sustaining. The current flow can be limited with an external series resistor. This limited Geiger-mode is the operating range of Silicon photomultipliers.

During the avalanche breakdown, photon emission can occur due to hot-carrier luminescence [97]. The emitted photons propagate in the semiconductor material and can be reabsorbed if their energy is above E_g. This can lead to parasitic effects in SiPMs by triggering avalanches in neighbouring cells (see Sec. 3.2.2.7).

2.3. Semiconductor photon detectors

A common pn-junction already forms the simplest type of a photon detector — a solar cell. If a photon is absorbed in the depletion region, the generated electron and hole are separated by the internal electric field. Also electrons and holes which are generated in the neutral regions within a distance of the diffusion lengths are able to enter the depletion region and contribute to the photo current I_{ph}. This leads to a positive charging of the p-side and a

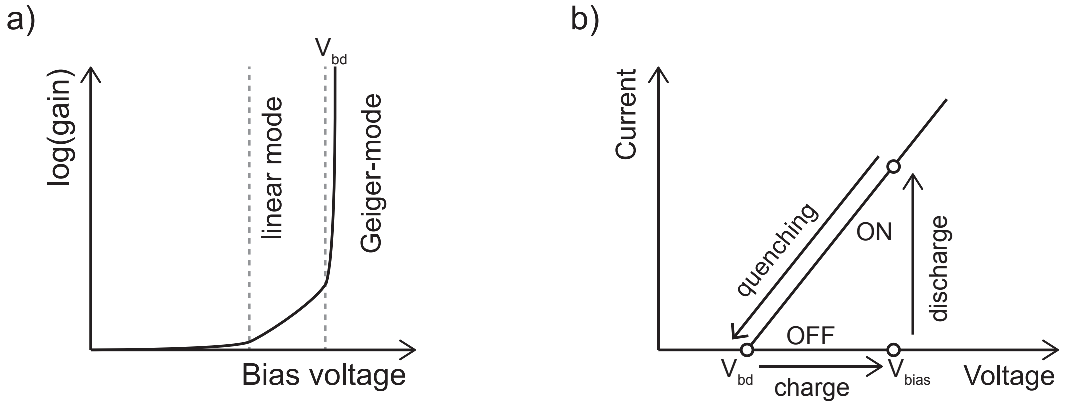

Figure 2.10: Different operating principles of photo diodes. a) shows the gain of the diode in logarithmic scale. By increasing the bias voltage the gain is increasing. Below V_{bd} the signal is proportional to the incident light; above, the gain becomes divergent. b) shows the loop of an APD in Geiger-mode. The device is biased above V_{bd}. Once the cell is fired, a current flows which is decreased by a voltage drop at a series resistance. When the avalanche is stopped the cell starts to recharge.

negative charging of the n-side and results in a positive voltage[4] over the junction, which can be tapped.

By applying a voltage in reverse bias, the saturation current I_S is increased by the photo current, which is proportional to the intensity of the incident light and the width of the depletion region [86].

For low light levels the superimposition of I_{ph} and I_S is dominated by the thermally generated dark current which leads to a low signal-to-noise ratio (SNR) and prevents the detection of the signal. In avalanche photo diodes impact ionisation can be used as an internal amplification to increase the SNR of the detector system.

2.3.1. Avalanche photo diodes

An avalanche photo diode (APD) is operated in the proportional or linear mode of the multiplication by impact ionisation in semiconductors. This means neither $M_n = 1$ nor $M_p = 1$ (Eqs. (2.28) and (2.29)) and the signal is still proportional to the amount of incident light. APDs have a high detection efficiency, a large dynamic range and the internal gain is in the order of 10 to 500 [98]. The voltage in reverse bias (V_{bias}) is slightly below the breakdown voltage V_{bd}, as can be seen in Fig. 2.10. In this regime the ionisation rates of holes are usually much smaller than those for electrons and so the multiplication is dominated by the electron contribution.

A limiting factor of this operational mode is the low gain of the proportional mode which, in turn, requires low noise amplifiers. In large area APDs the background by thermal generation of electron-hole pairs in the depletion region can superimpose the signal of the photo current and still some 20 photons are necessary for detectable output pulses [99]. Especially at voltages just below V_{bd}, hole multiplication sets in and makes the process unstable. Due to the statistical nature of the multiplication process, additional noise (*Excess Noise Factor*) is

---

[4] The open circuit voltage of a solar cell is $V_{oc} = \frac{nk_BT}{e} ln\left(1 + \frac{I_{ph}}{I_S}\right)$

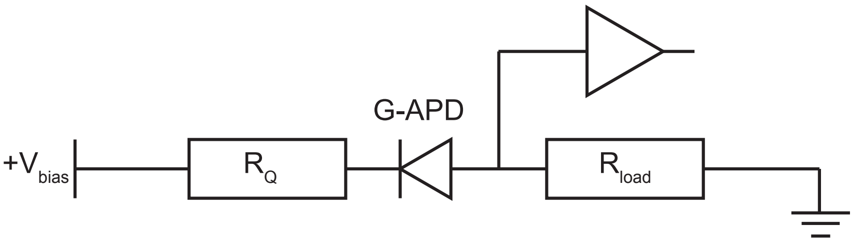

Figure 2.11: Basic passive quenching circuit with current-mode readout (after [101]). The output signal is measured via the input resistance of the front-end electronics R_{load}, which is usually in the order of 50 Ω.

caused by the variance of the avalanche gain distribution. The excess noise factor of APDs generally depends on the gain, the point of charge generation and the ratio of α_i and β_i, and can easily rise to values of up to 1000 [91, 100]. This prevents a separation of individual photoelectron peaks and thus limits the resolution.

2.3.2. Geiger-mode avalanche photo diodes

In order to avoid most of the gain instability problems and to get high amplification, the device has to be operated in the so-called limited Geiger-mode by increasing V_{bias} above the breakdown voltage. These devices are known as Geiger-mode avalanche photo diodes (G-APD) or single photon avalanche diodes (SPAD). Provided a low leakage current, in a small active volume no free carriers are present for a prolonged time which could trigger an avalanche breakdown. In this metastable condition, once an electron-hole pair is created in the depletion region (by photon absorption or thermal generation) an avalanche breakdown occurs. Since electrons and holes participate in the multiplication process, the avalanche in a Geiger discharge is divergent and the amount of charge is determined by the depletion-layer capacitance of the diode and the voltage above breakdown.

A quenching mechanism is required to limit the avalanche current and to stop the breakdown process. In passive quenching circuits the discharge is stopped by a voltage drop at a high-impedance series resistor R_Q (quench resistor) caused by the avalanche current (see Fig. 2.11). As the voltage at the diode is reduced to approximately V_{bd} [101], and since the avalanche is a statistical process, there is a certain probability that none of the carriers crossing the junction may impact ionise and the avalanche is quenched. Afterwards the cell needs a certain amount of time (τ) to recharge via R_Q in order to reach the initial bias voltage (see Sec. 2.3.3 for detailed discussion).

There is also the possibility of quenching the breakdown with dedicated electronics (active quenching). It is triggered by the breakdown event and lowers the bias voltage below V_{bd} for a certain period of time. Thus, the avalanche is quenched. Afterwards, the voltage rises again up to the bias voltage. Active quenching allows much faster recovery times than passive quenching [101].

G-APDs only need simple pre-amplifiers for readout because of their high internal gain ($\mathcal{O}(10^6)$), which also allows the detection of single photons. Due to the fast development of the avalanche process (sub-ns, [102]) they also provide the possibility for advanced timing measurements. Yet, the capability of single photon detection brings some drawbacks. The

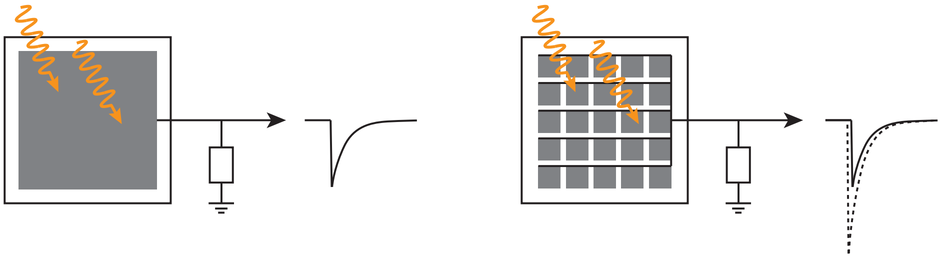

Figure 2.12: G-APD versus SiPM. On the left side, a single G-APD is shown with the event of one or two simultaneously incident photons. The signal is the same for both events due to the binary mode of the device. By combining multiple small G-APDs in an array with a common output (right), the signal of each simultaneously fired cell (solid line) adds up to the output signal (dashed line) and allows single photon counting.

information about the number of incident photons initiating the breakdown is lost because of the quasi-digital output caused by the divergent nature of multiplication in Geiger-mode. Thus, it cannot be distinguished whether a discharge is caused by thermal generation or by photon absorption. Due to the thermal generation of charge carriers in semiconductors, G-APDs can only have small areas without cooling. In addition, delayed *false* breakdowns can be triggered by charge carriers, which are trapped in the avalanche region during the initial discharge (afterpulsing, see Sec. 3.2.2). Furthermore, after the discharge of a diode there is a certain dead time in which the diode is not or less sensitive for subsequent photons (recovery time).

2.3.3. Silicon photomultiplier

The idea to overcome the drawbacks of the small active area and the loss of photon counting capability is to divide the area of a large single G-APD into an array of small individual equivalent cells, connected in parallel. The basic concept is shown in Fig. 2.12. The signal of each individual cell adds up to the output signal due to the common readout and thus the signal is proportional to the number of simultaneously fired cells. This, in turn, allows photon counting measurements. If two or more photons hit the same cell, the signal does not differ from the one of a single photon for a single G-APD. However, as long as the number of photons is smaller than the number of available cells it can be assumed, that on average only one photon per cell impinges. This inherent limitation of the device is called *dynamic range* and is discussed in Sec. 3.2.2.4 as one of the requirements for novel photodetectors.

After first G-APD matrices were developed in the former USSR [103, 104], many groups started to work on these devices, resulting in many different names:

- Silicon Photomultiplier (SiPM)
- Solid State Photomultiplier (SSPM)
- Avalanche Micro-Pixel Photo Diode (AMPD)
- Multi Pixel Photon Counter (MPPC)
- . . .

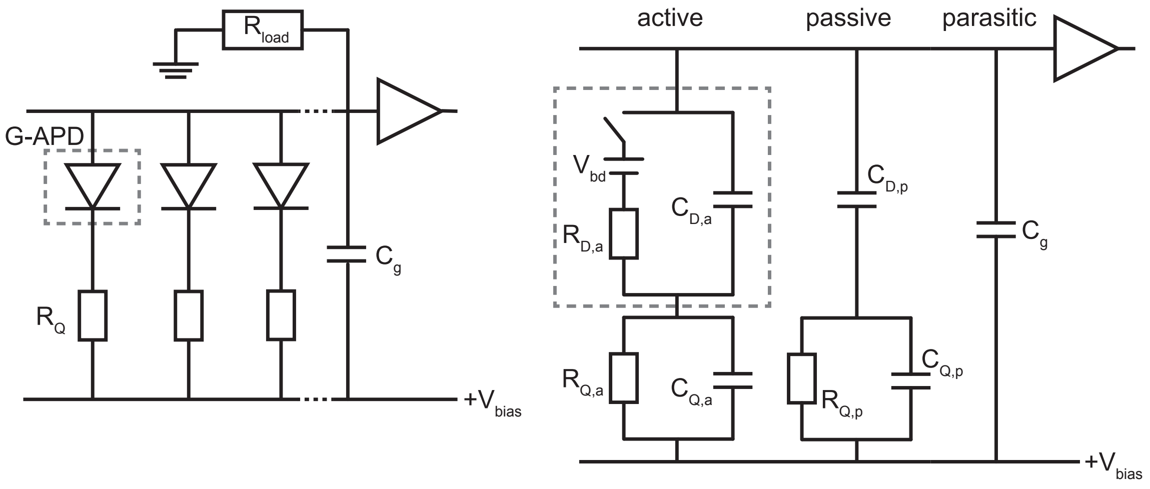

Figure 2.13: Structure and equivalent circuit of a SiPM. A Silicon Photomultiplier is an array of G-APDs connected in parallel, each with an individual quench resistor (left). The G-APD itself can be taken as a parallel circuit of a capacitor C_D and a resistor R_D (right). The triggering of an avalanche corresponds to closing the switch causing the voltage at the junction to drop to V_{bd}. The quench resistor limits the current and stops the breakdown. The discharge of the coupling capacitance results in the fast output signal. The passive resistors contribute with a factor of $1/(N - N_f)$, with N the number of cells, whereas capacitances contribute with $(N - N_f)$, according to Eq. (2.30). The metal grid for contacting the individual G-APDs results in an additional capacitance C_g. R_{load} is only shown on the left hand side. Image after [105].

Although the term Silicon photomultiplier is, strictly speaking, wrong since actually photoelectrons are multiplied, it was adopted by the community and is used throughout this thesis.

The general passive quenching circuit of a SiPM on the left hand side in Fig. 2.13 illustrates the basic idea of connecting all G-APDs of the array in parallel, each with an individual quench resistor R_Q in series. The additional capacitance C_g in the circuit equals the sum of all parasitic capacitances, such as the metal grid, required for contacting the individual cells. The right hand side of Fig. 2.13 shows the full SiPM equivalent circuit. While the G-APD can be replaced by the diode resistance R_D and the diode capacitance C_D in parallel, the resistor R_Q contributes to the signal with a parallel stray capacitance C_Q. An array of N cells can be divided into an active part of N_f fired cells, a passive part with $N_p = N - N_f$ non-fired cells, and the parasitic part C_g. The values of capacitors and resistors in the respective parts are thus given by [105]:

$$\begin{aligned} C_{D,a} &= C_D N_f & C_{D,p} &= C_D N_p \\ C_{Q,a} &= C_Q N_f & C_{Q,p} &= C_Q N_p \\ R_{Q,a} &= R_Q/N_f & R_{Q,p} &= R_Q/N_p \\ R_{D,a} &= R_D/N_f \end{aligned} \tag{2.30}$$

wherein in the following only the case of a single fired cell ($N_f = 1$) is discussed.

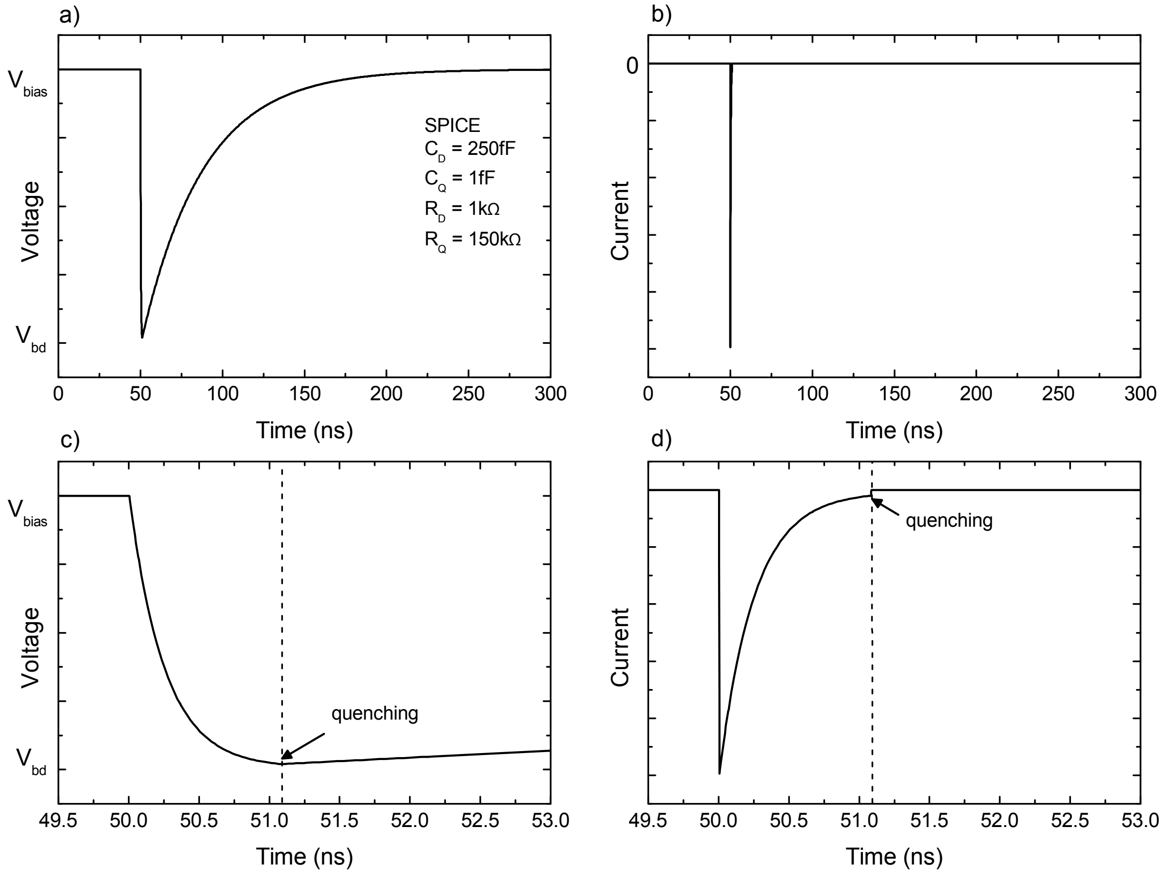

Figure 2.14: Typical time behaviour of diode voltage and current of a SiPM micro-cell in limited Geiger-mode. When the avalanche is triggered at 50 ns the voltage over the diode drops from V_{bias} to V_{bd} with a short current pulse (a) and b)). By taking a closer look at the time of the breakdown, it can be observed that the avalanche is quenched and the cell begins to recover if the current through the diode is below the latching current level (c) and d)). More details are explained in the text.

For a non-fired cell, which corresponds to an open switch, the full bias voltage drops across the depletion region of the G-APD (C_D). Thus, the electric field can be approximated by

$$F \approx \frac{V_{bias}}{W}, \tag{2.31}$$

where W is the width of the depletion region. After triggering an avalanche, which corresponds to closing the switch, the capacitances are discharged and the initially large diode current drops towards an asymptotic value

$$I_f = \frac{V_{bias} - V_{bd}}{R_Q + R_D} \approx \frac{V_{ob}}{R_Q}, \tag{2.32}$$

given by the overbias voltage V_{ob} and the quenching resistance R_Q, while the voltage at the diode drops to

$$V_f = V_{bd} + R_D I_f \approx V_{bd}. \tag{2.33}$$

The typical voltage and current characteristic of a SiPM diode during an avalanche breakdown is plotted in Fig. 2.14. If the current I_f is well below the latching current limit of ca. 100 µA there is a probability that the avalanche is quenched and the cell starts to recover to the initial bias voltage. A current level of $I_f = 20\,\mu\text{A}$ can be taken as a rule of thumb for a safe quenching condition [101]. This is also shown in Fig. 2.14. Once the current through the diode has fallen below the quenching current limit (here 20 µA), the avalanche is quenched by opening the switch and the cell starts to recover via R_Q. The time for quenching the avalanche increases by approaching the latching current level with I_f. If I_f is above this level (high overbias), the avalanche keeps self-sustaining and is no longer quenched by statistical fluctuations [101]. Since C_D is recharged through R_Q, the time for recovery is mainly determined by the values of the diode capacitance and quenching resistance

$$\tau_{rec} = R_Q\, C_D. \tag{2.34}$$

During the recovery, the cell is not fully sensitive for subsequent photons but it is worth mentioning that the non-fired cells of the array remain fully sensitive during this period. However, Eq. (2.34) already illustrates that for a fast recovery time of the cell small values for R_Q and C_D are necessary. In turn, to maximise the detection efficiency, the avalanche also has to be quenched for high overbias voltages ($V_{ob} \geq 10\%$ of V_{bd}) which corresponds to the need for a high resistance, as shown in Eq. (2.32). Therefore, there is always a trade-off between recovery time and maximum overbias for all G-APDs or SiPMs with passive quenching.

By measuring the charge or amplitude of the individual output pulses the information of the detected photon number can be obtained from the resulting histogram. The number of fired cells is often also called photon equivalent (p.e.). Taking into account the cell to cell variations and the Poisson distribution of the incident light, the ideal[5] charge histogram $N(Q)$ for photon detection can be described by a convolution of multiple normalised Gaussian with the Poisson distribution:

$$N(Q) = \sum_{k=0}^{N} \underbrace{\frac{\bar{n}_{pe}^{k}}{k!}\, \mathrm{e}^{-\bar{n}_{ph}}}_{\text{Poisson}} \cdot \underbrace{\frac{1}{\sqrt{2\pi\left(\sigma_{ped}^2 + k\sigma_{gain}^2\right)}}\, \exp\left[-\frac{(Q - k\cdot Q_{cell} - Q_{ped})^2}{2\left(\sigma_{ped}^2 + k\sigma_{gain}^2\right)}\right]}_{\text{norm. Gaussian}}, \tag{2.35}$$

with N the number of cells and $\bar{n}_{pe} = \bar{n}_{ph} \cdot PDE$ the mean number of photon equivalents, which is defined by the product of the photon detection efficiency (PDE) and the mean photon number $\bar{n}_{ph}$. Q_{cell} and σ_{gain} are the average charge (gain) and the standard deviation of one cell, respectively, whereas Q_{ped} and σ_{ped} are the corresponding parameters for the electronic noise. A detailed description of these characteristics is given in the following chapter. Fig. 2.15 shows an example for an ideal charge histogram with a mean p.e. number of $\bar{n}_{pe} = 3.33$. The number of resolved fired cells depends on the standard deviation of the individual peaks.

The Silicon photomultiplier provides a way to overcome some of the drawbacks of a single G-APD. SiPMs allow photon counting on the single photon level with a low excess noise factor due to the G-APD matrix. They are compact and robust devices with low power consumption. They do not require high voltage power supply and in addition they are insensitive to magnetic fields (up to 7 T, [106]), which gives them a significant advantage compared to conventional photomultiplier tubes (PMT), as they can be used in the environment of detectors in high

---

[5] 100% detection efficiency, no correlated noise (cross talk and afterpulsing, see Sections 3.2.2.7 and 3.2.2.8)

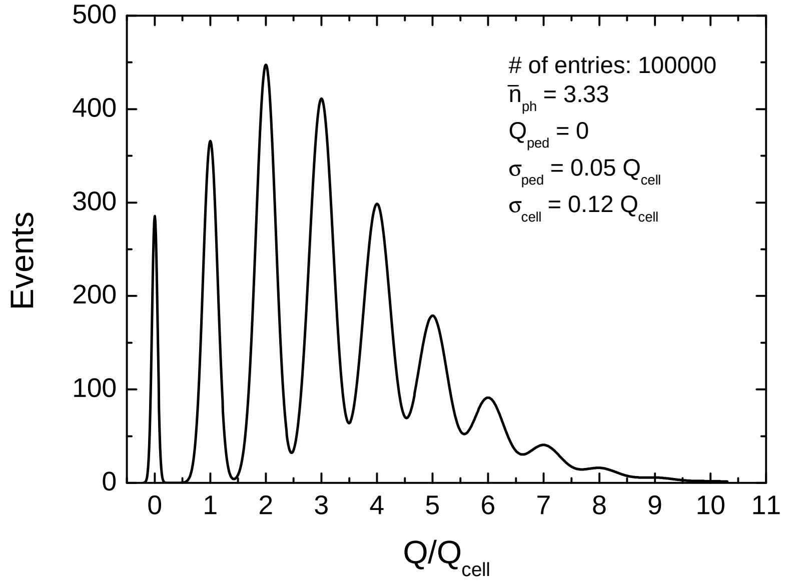

Figure 2.15: Theoretical charge spectrum for an ideal device calculated with Eq. (2.35) assuming a mean photon equivalent number of $\bar{n}_{pe} = 3.33$.

energy physics or medical applications [107]. Because of these facts the SiPM is becoming a promising candidate to replace vacuum photomultiplier tubes in future applications. A general comparison between PMTs and SiPMs is listed in Table 2.3.

Like the G-APD, SiPMs have the problem of thermally generated pulses in the order of several hundreds of kHz to MHz per square millimetre with the same signal as photon induced ones. Yet, the probability of two cells, fired simultaneously by thermal generation is negligible. Thus, they offer the possibility to set the trigger level for data acquisition on a threshold above the output signal of a single cell. Thus, the effective dark count rate can be

	PMT	SiPM
Max. detection efficiency	$\approx 40\%$	$> 65\%$
Gain	10^6	10^6
Operating voltage	$\mathcal{O}$(kV)	$\mathcal{O}$(50 V)
Excess Noise Factor	1.1 - 1.5	≈ 1 (with cross talk suppression)
Dark noise rate	$\mathcal{O}$(kHz/cm^2)	$\mathcal{O}$(100 kHz/mm^2)
Single photon counting	good	good
Robust & Compact	no	yes
Aging	yes	no
Magnetic field immunity	no	yes
Damage from high light level exposure	yes	no

Table 2.3: General comparison between SiPM and PMT.

approximately reduced by an order of magnitude. Additionally, the thermal generation and thus the dark count rate decreases by cooling the device.

Another drawback derives from the G-APD array structure. A fired cell can trigger neighbouring cells by photon emission during an avalanche breakdown (optical cross talk). This results in additional noise and leads to a deviation from the Poisson distribution.

A lot of technological effort is put into the optimisation of the fabrication process, since many of the inherent drawbacks, such as thermal noise and the suppression of cross talk, can be reduced or eliminated. Therefore, the obtained results are always reflecting the current state of the art (see also Sec. 5.3.1).

In this thesis a novel approach for the realisation of SiPMs is investigated where the quenching mechanism is integrated into the silicon bulk. The concept, its advantages, drawbacks and results of the characterisation are discussed in detail in Chapters 4 and 5.

3. Methods

The development of a new device from its first concepts to the final detector consists of several iterative steps of simulation, production and measurement. Simulating the process flow allows to reduce the time and cost of technology development. Simulations of device operation provide insights into the behaviour of semiconductor devices, necessary for new prototyping and optimisation. Afterwards, the characterisation of the prototype gives information about the quality and accuracy of the simulations and allows fine tuning of parameters.

The characterisation of the device can be separated into static and dynamic measurements. The following chapter gives a detailed description of the simulations and measurement methods used in this thesis.

3.1. Simulation tools

Process and device simulators are powerful tools in the development of new detectors. TCAD (Technology Computer Aided Design) can already provide information regarding the feasibility of the concept, possible problems and optimisation by pre-characterisation of the virtual device. The results of the process and device simulations can be used in further simulation tools like for investigation of breakdown probability in G-APDs.

3.1.1. Process simulation

TCAD tools for semiconductor processing allow the simulation of fabrication steps like implantation, diffusion, oxidation, or etching. Process parameters like implantation dose, energy, angle, annealing time and temperature, or selective etching can be specified by the user. As a result, the doping profile and the topology are obtained by using the finite element method.

In this thesis two simulation tools have been used for the process simulation of the devices. During the first part, which is related to the feasibility studies of the first two prototype iterations (SiMPl 1 and SiMPl 2), the ISE-TCAD process simulator DIOS[1]was utilised. Here, the implantation model is based on analytical implant tables only, calibrated with measurement data but not taking into account the channelling effect in semiconductors [108]. Meanwhile, the software is no longer supported by the developers, which is why also the more complex simulation tool Sentaurus Process from SYNOPSYS[2] was used later on. This tool provides the possibility of choosing between different implantation and diffusion models. A major advantage in this context is the ability of calculating implantation profiles based on Monte Carlo methods, which can describe the crystal lattice orientation-dependent channeling[3] much better than analytical models. As a drawback, the simulations are optimised for parameters

---

[1] Integrated Systems Engineering AG

[2] www.synopsys.com/TOOLS/TCAD

[3] If the ion beam meet particular crystal axes the range of the ions is much longer, since they can move along these axes due to less scattering. This effect, known as ion channeling, is highly sensitive on small deviations from perfect orientation which results in a strong variation of the implantation depth.

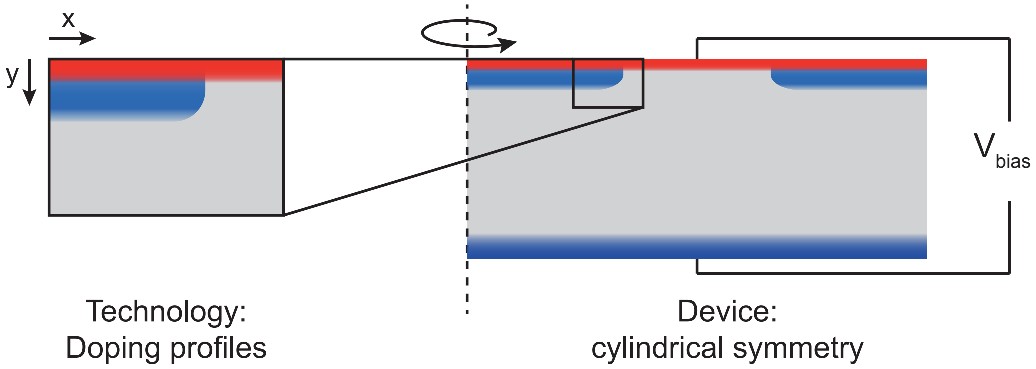

Figure 3.1: Interaction principle of technology and device simulation. Only the part between homogeneous regions, like at the edge of photo resist, is simulated. Afterwards the final device structure is assembled from the different simulation areas and completed by extrapolation. Electric contacts allow to apply external voltages to the device. To get quasi-3-D results the problem is solved in cylindrical symmetry with the cell under investigation in the centre. Drawings are not to scale.

usually used in semiconductor industries. Deviations from the optimised parameter regime can lead to significant differences between simulation and reality. Hence, measurements of the real doping profile are essential as a cross-check and fine tuning of the simulation.

In practice, usually only the parts of the device with transitions in the doping profiles, like for resist edges or changes in topology, are simulated in the process simulation which allows a fine grid resolution with still acceptable computing times. These results are afterwards used to assemble the final detector structure for device simulation which is illustrated schematically in Fig. 3.1

3.1.2. Device simulation

The basic working principle of device simulations is to numerically solve the equations for charge carrier transport and electrostatics in semiconductors with the finite element method. The equation system, which is solved, consists of the equations for electron and hole current and the electrostatic potential. The latter is defined by the Poisson equation and can be written as (see Ref. [109]):

$$\mathrm{div} \cdot (\varepsilon_0 \varepsilon_r \nabla \Phi + \mathbf{P}) = -e(p - n + n_D - n_A) - \rho_{trap} \tag{3.1}$$

where $\mathbf{P}$ is the ferroelectric polarisation and ρ_{trap} the charge density contributed by traps and fixed charges. The carrier transport is calculated with continuity equations describing charge conservation:

$$\mathrm{div}\ \mathbf{j}_n = eR_{net} + e\frac{\partial n}{\partial t} \qquad -\mathrm{div}\ \mathbf{j}_p = eR_{net} + e\frac{\partial p}{\partial t} \tag{3.2}$$

with R_{net} the net recombination rate and $\mathbf{j}_n$, $\mathbf{j}_p$ the electron and hole current densities. For transient problems, the total current density also satisfies

$$\mathrm{div}\left(\mathbf{j}_n + \mathbf{j}_p\right) = \mathrm{div}\ \mathbf{j} = 0. \tag{3.3}$$

The net recombination rate is given by different recombination and generation mechanisms like SRH, Auger recombination, optical recombination, avalanche generation, and surface recombination. For the simulation, the parameters of the particular physical models, and which of them are actually activated, can be defined by the user.

The boundary conditions are defined by the Dirichlet boundary condition

$$V = V_{bias} + V_{intern} \tag{3.4}$$

for contacts, where the potential is defined by the external voltage V_{bias}. Otherwise the ideal Neumann boundary condition

$$\varepsilon_0 \varepsilon_r \nabla \Phi + \mathbf{P} = 0 \tag{3.5}$$

has to be met, assuming a constant potential at the boundary.

As well as for the process simulation two different tools were used for device simulations. The first simulations were done with WIAS-TeSCA[4] only. After implementing Synopsys TCAD also its device simulation Sentaurus Device was used. One advantage of the second software is the possibility to log information like potential, electric field, etc. of a specific grid point, which can be a helpful tool to determine the characteristics of the device in transient simulations. Furthermore, the tool provides models of different complexity for recombination and generation as well as for temperature dependence. A big advantage of Synopsys is the capability of real 3-D simulations and therefore the investigation of the influence of different geometries. In order to realise real 3-D simulations the device structure is assembled from 2-D simulations with Sentaurus Process by sweeping the corresponding 2-D elements along a polygonal path or a reference axis in the 3-D coordinate system (for details see Ref. [110]).

3.1.3. Monte Carlo methods

Monte Carlo (MC) methods are a numerical approach based on the theory of probability to solve problems that are not analytically solvable. As mentioned in the last section the TCAD tools are based on carrier densities which implicate some drawbacks for simulation of G-APDs. Since the triggering and quenching of the avalanche breakdown is a statistical process, an appropriate avalanche breakdown model requires a MC method with a particle based model. Therefore, MC methods are used to calculate the characteristics of an avalanche breakdown and allow to investigate its trigger probability as a function of the electric field distribution.

Results on this topic have been published by Oldham and McIntyre [111, 112]. They already reported a dependence of the breakdown probability on the bias voltage which shows a saturation at a certain E-Field value as well as the influence of the position of photoelectron generation. This method is also a helpful tool to investigate the influence of potential enhancements of the electric fields at the edge regions of the sensitive areas. This edge effect can result in an unwanted early breakdown of the G-APD cells in this region, known as edge breakdown.

In the 1-D model used for this thesis, in a first step the electric field in x- and y-direction[5] as well as the potential are extracted from the 2-D grid of the device simulation (TeSCA) at different bias voltages. These informations are imported into a self-made analysis program[6]

---

[4] Weierstraß Institut für angewandte Analysis und Stochastik, Berlin: *Two-Dimensional Semi-Conductor Analysis Package*

[5] In the simulations, the x represents the lateral direction, whereas y corresponds to the depth in the silicon.

[6] written by Rainer Richter

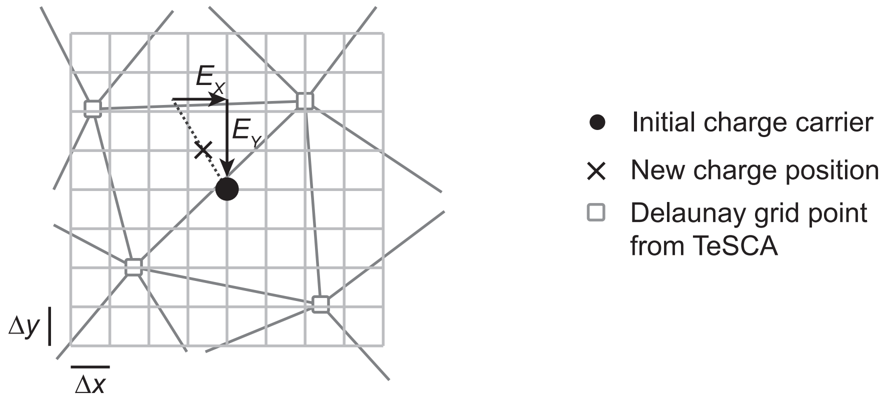

Figure 3.2: Remeshing principle for trajectory calculation (here for an electron). From the Delaunay-triangulated grid the E-Field at the current position is interpolated and the next position, defined by the first grid line crossing, is calculated. The result is shown in Fig. 3.3. The cumulative sum of the travelled distance and the absolute electric field is stored in a data file.

where the trajectory of a charged particle is calculated based on the E-Field components. The principle for this estimation is shown in Fig. 3.2. The starting position of the initial charge carrier (electron or hole) is defined by the user. The E_x and E_y values around the respective position are interpolated on a fine rectangular grid, based on the values from the Delaunay grid in TeSCA. From the starting point, the next position of the charge carrier is given by the first crossing with a grid line, which is calculated from the movement according to the electric field vectors. Afterwards, the procedure is repeated for the new calculated position until the field is below a defined threshold, where no impact ionisation takes place. Fig. 3.3 shows the results of such a trajectory calculation for the edge region of a micro-cell. The simulated structure is sketchily illustrated in the upper left of the graph. The individual trajectories are plotted in an overlay to the equipotential lines.

The travelled distance of the electron or hole is stored together with the respective absolute electric field. These data are afterwards imported to the Monte Carlo tool[7], where the ionisation coefficients along the trajectory, according to the electric field, are calculated based on the model by van Overstraeten [94] (see. Eqs. (2.21a) and (2.21b)). These coefficients determine the probability $P(\Delta d)$ of an ionisation event within a certain distance Δd, given by:

$$P(\Delta d) = 1 - \exp(-\alpha \Delta d) \approx \alpha \Delta d \qquad \text{for } \alpha \Delta d \ll 1. \tag{3.6}$$

The effect of a dead space, where no impact ionisation can take place ($E < E_{th}$), can be neglected. For avalanche regions with widths larger than 1 µm, the dead space plays no relevant role in the multiplication process [113]. New generated particles are added to the charge flow and subsequently taken into account in the further calculations. An avalanche breakdown is assumed once the number of charge carriers exceeds a predefined threshold (usually 2000 in agreement with a current calculated by Ramo's theorem [114]). If this threshold number is not reached, the event is not counted as a Geiger discharge. In order to obtain the probability of triggering an avalanche this procedure is repeated 10^4 times.

---

[7] A first version of the MC tool was written by Hans-Günther Moser

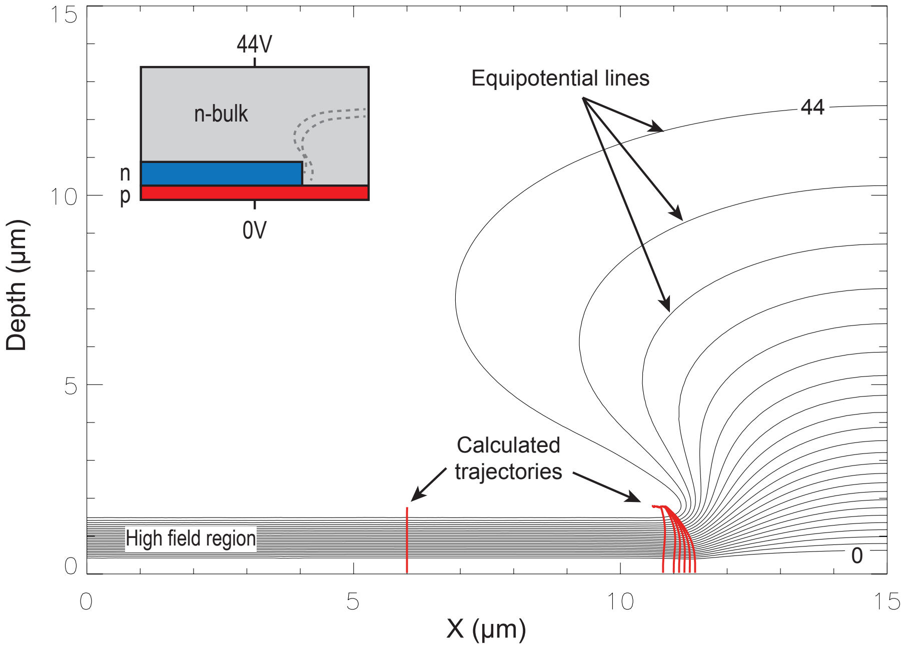

Figure 3.3: Calculation of charge trajectory (red lines) for MC simulations of the breakdown probability plotted together with the equipotential lines. The simulated structure is shown in the inset on the upper left in which a depth of zero corresponds to the surface. From the electric fields the trajectory of the charge which is generated at a defined point is calculated as shown in Fig. 3.2. Here, an electron close to the surface is generated at different positions of the micro-cell to investigate potential edge effects of the electric field at $X \approx 11$ μm.

By performing this calculation for different bias voltages, which also changes the electric field distribution in the space charge region and therefore the ionisation coefficients, it is possible to investigate the breakdown voltage of the device and the trigger efficiency as a function of the bias voltage. By including the trajectories at the edge region of the device, which can contain local electric field maxima, an investigation of early breakdown in this region is possible too.

Based on the method described in Ref. [113], a new MC avalanche simulation was realised in C++ and all presented simulation results in this thesis concerning avalanche trigger probabilities were obtained by utilising this tool. It enables to investigate the trigger probability as a function of the photon absorption depth which should allow basic conclusions on the wavelength dependence. Furthermore, it is also possible to change the number of generated particles in order to get information about the Geiger efficiency for detection of minimum ionising particles (MIPs, see Sec. 6.1.1). The number of generated charge carriers in the simulation region is calculated by distributing the e-h-pairs randomly over the individual steps Δd with an uniform probability given by

$$P(MPV, \Delta d) = MPV \cdot \Delta d \qquad \text{for } MPV \cdot \Delta d < 1, \tag{3.7}$$

where $MPV = 80$ e-h/μm is the most probable value for generation of e-h-pairs per μm by MIPs [13] (see also Fig. 3.4). The resulting distribution corresponds to the starting value for the subsequent avalanche simulation which is the same as for the single photon absorption described above.

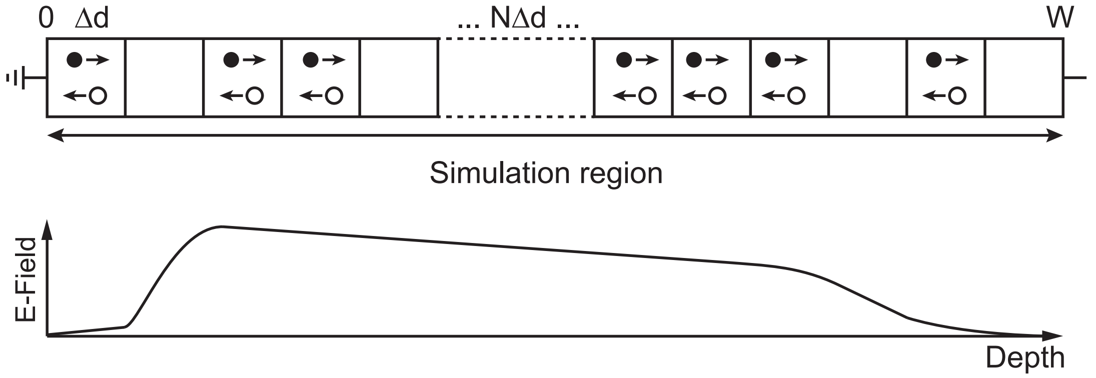

Figure 3.4: Random distribution of e-h-pairs as starting condition for MIP trigger probability simulation. The distribution is normalised to the most probable value for generation of e-h-pairs/µm by minimum ionising particles. The result is used as starting value for the MC avalanche simulation.

So far, none of the MC avalanche simulations take into account the minority carrier recombination lifetime in the non-depleted areas. The short lifetime in these highly doped regions prevents the generated charge carries from reaching the high field region. Thus, in the discussion of the results for the trigger probability as a function of the depth it has to be considered that the values in these regions are overestimated in the simulations.

3.2. Characterisation of SiPMs

In order to precisely interpret the results obtained with a detector, it is necessary to understand the characteristics of the device itself. Hence, parasitic effects interfering with the actual result can be taken into account and – ideally – eliminated. For the SiPM, the characterisation provides information about the operation range, the parasitic effects and the maximum achievable detection efficiency. It can be distinguished between two different types of measurements: static and dynamic. In the following, the characteristic properties of SiPMs are discussed and both types of the characterisation are presented in more detail.

3.2.1. Static measurements

When speaking of static measurements in the context of SiPMs, measurements of the current-voltage (IV) and capacitance-voltage (CV) characteristics are meant.

3.2.1.1. Current-voltage measurements

Using the IV measurements, first conclusions regarding the properties of the G-APDs can be made. Fig. 3.5 shows the basic setup used for the IV characterisation of the SiPMs. Initial measurements on the wafer level are possible by using a probe station. The wafer is put inside a light-tight box and the devices are connected via needles. In this way the parasitics of the measurements can be minimised. In order to additionally be able to measure bonded devices as well as commercial ones, the connection to the Source Measure Unit of a parameter analyser[8] is realised via a simple circuit board (PCB), providing conductive paths. The PCB

---

[8] Keithley 4200-SCS

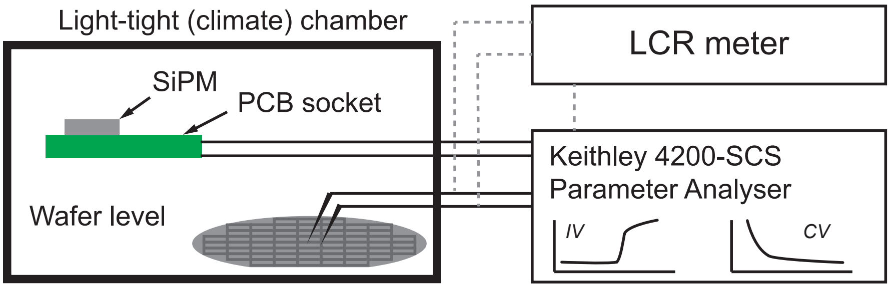

Figure 3.5: Setup for IV and CV measurements. First measurements of the IV and CV are possible in a light-tight box on the wafer level. Devices which are bonded as well as commercial devices can be stored on a simple PCB socket in a light-tight climate chamber which allows measurements at different temperatures. CV measurements, in addition, require a LCR-meter providing the AC component.

with the SiPM can be placed in a light-tight climate chamber[9], which allows measurements at different temperatures.

In the characterisation of G-APD-based devices the more important IV characteristic is obtained by applying a reverse bias voltage to the SiPM in dark conditions. A measurement of an IV curve of a Hamamatsu[10] MPPC S10362-11 with an area of 1×1 mm^2 and 100 µm cell size is plotted in Fig 3.6. The left graph shows the full IV measurement in reverse bias at three different temperatures. The part in the lower voltage range (up to 65 V) corresponds to the leakage current of the device, caused by thermal generation of e-h-pairs. Since the generation is a function of the temperature, the leakage current shows a temperature dependence. Thus, decreasing the temperature leads to a decrease in the leakage current (see Eq. (3.14)). The increase of the current with the reverse bias voltage can be explained by the increase of the depletion region volume with the voltage and the corresponding increase of generation centres. The breakdown voltage V_{bd} is characterised by a strong increase of the dark current due to the Geiger discharges and is defined as the voltage at a dark current of $I_D \approx 1$ nA. The right hand side of Fig. 3.6 shows the region of the breakdown in more detail. The individual characteristic regimes of a SiPM can be distinguished, starting with the breakdown voltage. A temperature dependence $\partial V_{bd}/\partial T$ is observed. By decreasing the temperature, the number of phonons is decreased leading to less electron-phonon scattering [84]. Thus, the ionisation rate is increasing and a lower voltage is required to trigger an avalanche breakdown. The voltage regime after V_{bd} is associated with the normal operation of the device. The disproportionate increase at higher voltages (ca. 71.8 V at 298 K) is composed by enhanced pile-up events (afterpulsing, cross talk, dark counts) as well as the transition to the non-quenching regime of the avalanche diode (cf. Sec. 5.2.3.8).

With the IV measurements in reverse bias, broken devices can be identified on wafer level by unusual behaviour. A high leakage current points to a high dark count rate of the device. Breakdown at significantly lower voltages than expected is an indication of early breakdowns at the edge of the individual cells due to local field maxima.

---

[9] CTS GmbH, T-70/100

[10] Hamamatsu Photonics K.K.

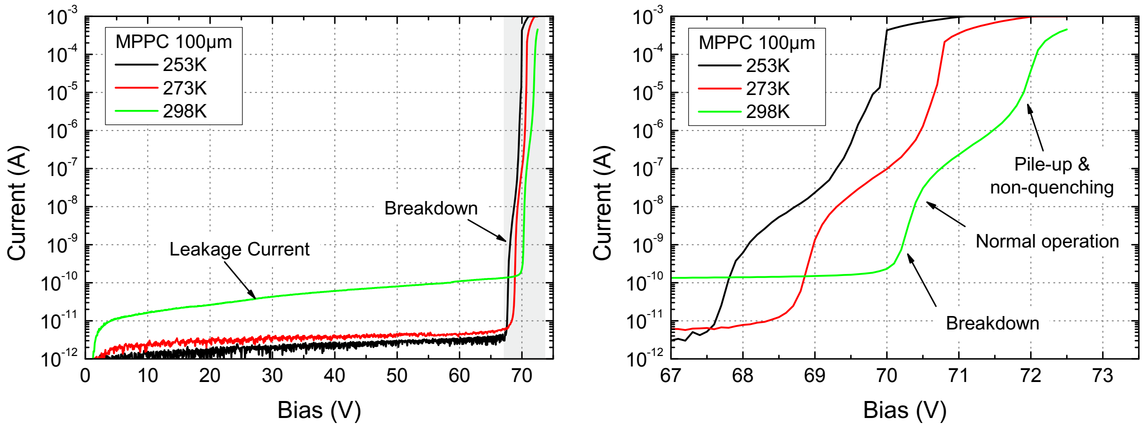

Figure 3.6: Example of an IV measurement in reverse bias of a Hamamatsu MPPC with 100 µm pitch size at three different temperatures. The left plot shows the whole IV curve of the device, thus the contribution of the leakage current is clearly visible as well as the breakdown voltage. The right graph zooms into the region of the breakdown voltage which corresponds to the operating range of the SiPM. More details are given in the text.

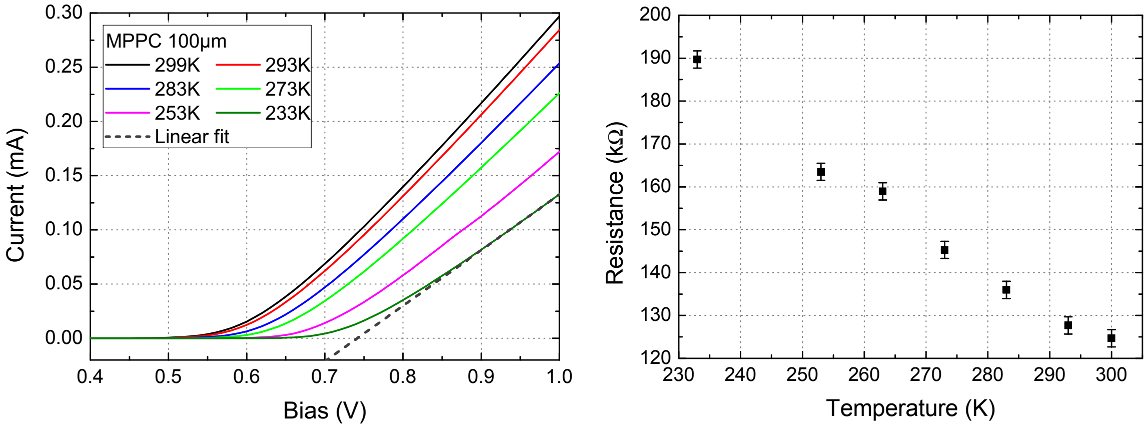

Figure 3.7: Measurement of the quenching resistor for conventional SiPMs. By applying a forward bias, the series quench resistor can be measured by fitting the linear part of the IV and using Eq. (3.8). The figure on the right shows the obtained results for the polysilicon resistor at different temperatures.

By applying a forward bias to conventional SiPMs, also the value of the quench resistor R_Q can be determined from the IV curve. At bias voltages around 1 V the IV characteristics are dominated by the series resistance of the SiPM cell and thus show a linear behaviour. By fitting this linear region, R_Q can be calculated via

$$R_Q = N_{cells} R_{meas}, \tag{3.8}$$

with N_{cells} the number of cells in the array and R_{meas} the resistance obtained from the IV measurement. Fig. 3.7 illustrates this measurement method for a MPPC with 100 µm pitch at different temperatures. Also plotted are the obtained results for the polysilicon resistor as a function of the temperature showing a negative temperature coefficient which is in good agreement to the literature [115]. The determination of the quench resistor value is required for one possible way of calculating the recovery time (see Sec. 3.2.2.6).

3.2.1.2. Capacitance-voltage measurements

The capacitance of the SiPM is determined by a capacitance-voltage (CV) measurement. The SiPM is connected to a LCR meter[11] where the capacitance and the series resistance or the conductance, respectively, are measured as a function of the reverse bias voltage. A result for two MPPCs with different pitch sizes is shown in Fig. 3.8. At low bias voltages up to 20 V the capacitance shows a decrease according to the increase of the depletion width [84]:

$$C = \frac{A\,C_0}{(1 - V_{bias}/V_{bi})^m} \qquad \text{with } m = 1/3 \ldots 1/2, \tag{3.9}$$

where A is the area of the cell and C_0 the zero volt capacitance per unit area. For voltages above 20 V a transition of the capacitance to a quasi constant plateau can be observed. This corresponds to the fact that the depletion reached an area of high doping density [84], which drastically reduces the further increase of the depletion width and thus the change of C_D (see Eq. (2.19)).

In saturation, the capacitance of both devices reaches values of 30 pF to 40 pF. The different contributions from the diode capacitances to the total capacitance, caused by different pitch sizes, are compensated by the different number of cells in parallel.

It has to be taken into account, that the measurement also includes the influence of all the parasitic capacitances of the whole network in series and parallel and therefore does not correspond to the diode capacitance C_D but the total capacitance of the SiPM. If the equivalent circuit of the device is known, the intrinsic values can be recalculated as shown in Ref. [116], giving the possibility to extract the individual capacitances of the device (see Sec. 2.3.3).

3.2.2. Dynamic measurements

The dynamic characterisation of the photon detector allows studying the device during operation and provides information on the influence of parasitic effects.

3.2.2.1. Gain

The gain G of a SiPM is determined by the charge Q, which is generated during a single avalanche breakdown. In good approximation the multiplication factor is defined by the

---

[11] Agilent HP 4284A

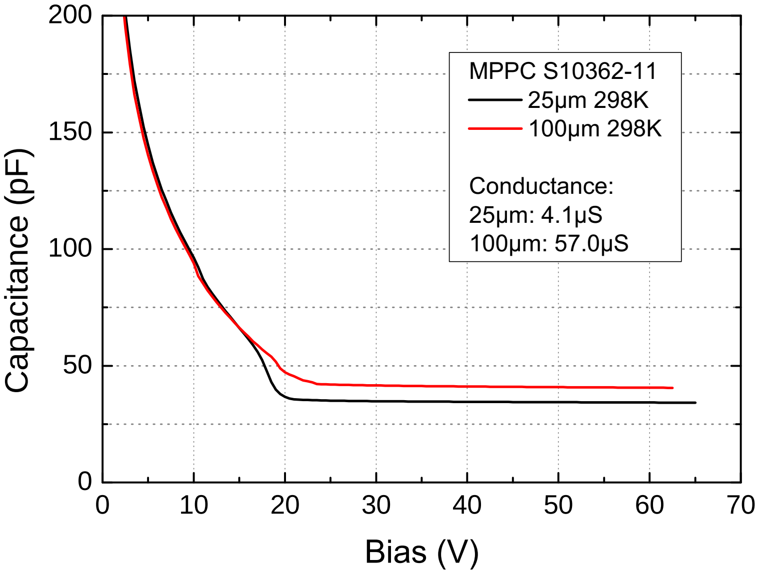

Figure 3.8: CV measurements of Hamamatsu MPPCs (S10362-11) with pitch of 25 µm and 100 µm at a frequency of 1 MHz. At operation voltage (≈ 70 V) the capacitance can be assumed constant. The conductance of the devices is given at $V_{bias} = 60$ V. Data taken at room temperature.

cell capacitance $C_{cell} = C_D + C_Q \approx C_D$ and the applied overbias voltage V_{ob}, which is the difference between the bias voltage V_{bias} and the breakdown voltage V_{bd}:

$$G = \frac{Q}{e} = \frac{C_{cell} V_{ob}}{e} = \frac{C_{cell}}{e} \left(V_{bias} - V_{bd} \right). \tag{3.10}$$

Since in first approximation the capacitance C_D can be expected to be constant in full depletion, the gain shows a linear dependence on the overbias voltage. As an example the gain of three MPPCs from Hamamatsu with different pitch is shown in Fig. 3.9. A good agreement to the expected linear behaviour can be observed. Deviations from the linearity can reveal problematic operation conditions for the device.

The measurement of the gain is related to the measurement of the charge spectrum and is therefore described in the following section.

3.2.2.2. Amplitude and charge spectra

As already mentioned in Sec. 2.3.3 and shown in Fig. 2.12, the signal output of the SiPM is the sum of all simultaneously fired cells due to the parallel readout of the whole device. Therefore, the signal amplitude A_k of k cells, fired at the same time, adds up to:

$$A = \sum_k A_k. \tag{3.11}$$

In order to get a detectable signal from the detector a custom-made pre-amplifier readout board was utilised. A photograph of the board and its circuit diagram are shown in Fig. 3.10. The amplification of the readout channel of the board was measured with a network analyser[12]

---

[12] Rohde & Schwarz ZVA8

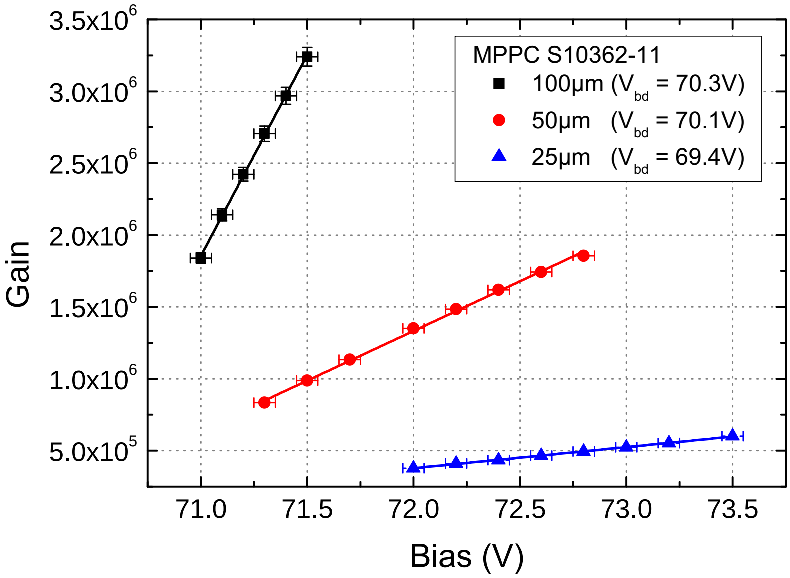

Figure 3.9: Gain of Hamamatsu MPPCs with different pitch (25/50/100 µm) as a function of the bias voltage. The data show good agreement with the linear behaviour expected from Eq. (3.10). V_{bd} is different for all the devices. The gain was calculated via a charge histogram measured with a SiPM evaluation kit from CAEN.

for frequencies between 300 kHz and 4 GHz and the result is depicted in Fig. 3.11. A gain of 29.8 dB can be measured with the MAR-8ASM+ amplifier from MiniCircuits. The -3 dB bandwidth limit is at a frequency of roughly 480 MHz. The board with the BGA614 amplifier from Infineon shows an amplification 19.3 dB from 85 MHz until 290 MHz while the -3 dB limit is at 1.3 GHz. If not stated otherwise the MAR-8ASM+ amplifier was used for the measurements in this thesis.

The amplitude spectrum is recorded with a digital oscilloscope (LeCroy WaveRunner 64Xi, 600 MHz bandwidth) defining a measurement window of ca. 20 ns with respect to the trigger event. A dark count amplitude spectrum of a MPPC with 50 µm pitch size is shown in Fig. 3.12a. The spectrum is dominated by the 1 p.e. peak, but also events with a higher number of fired cells caused by optical cross talk (see Sec. 3.2.2.7) are visible.

The charge can be measured by integrating over the time period of one pulse. With an integration window of $7\,\tau_{rec}$ (see Eq. (2.34)), the cell can be assumed to be fully recovered ($7\,\tau_{rec} \equiv 99.9\%$). The charge spectrum or the gain is measured by using the *SiPM Evaluation Kit* from CAEN[13]. It provides a power supply unit to apply the bias voltage to the detector as well as a pre-amplifier with variable gain. The bandwidth of the amplifier is 500 MHz and its amplification can be set in steps of 1 dB to a maximum of 50 dB. In addition, the unit also offers the possibility to correct for temperature instabilities, which would affect the overbias voltage due to $\partial V_{bd}/\partial T$. The detector under test can be illuminated with a pulsed light source (either a LED of 405 nm with 5 ns FWHM or a picosecond laser[14] with 445 nm) with the possibility to change the repetition rate and the intensity. The SiPM signal is measured

---

[13] CAEN Technologies: SiPM Evaluation Kit http://www.caentechnologies.com

[14] ALPHALAS GmbH

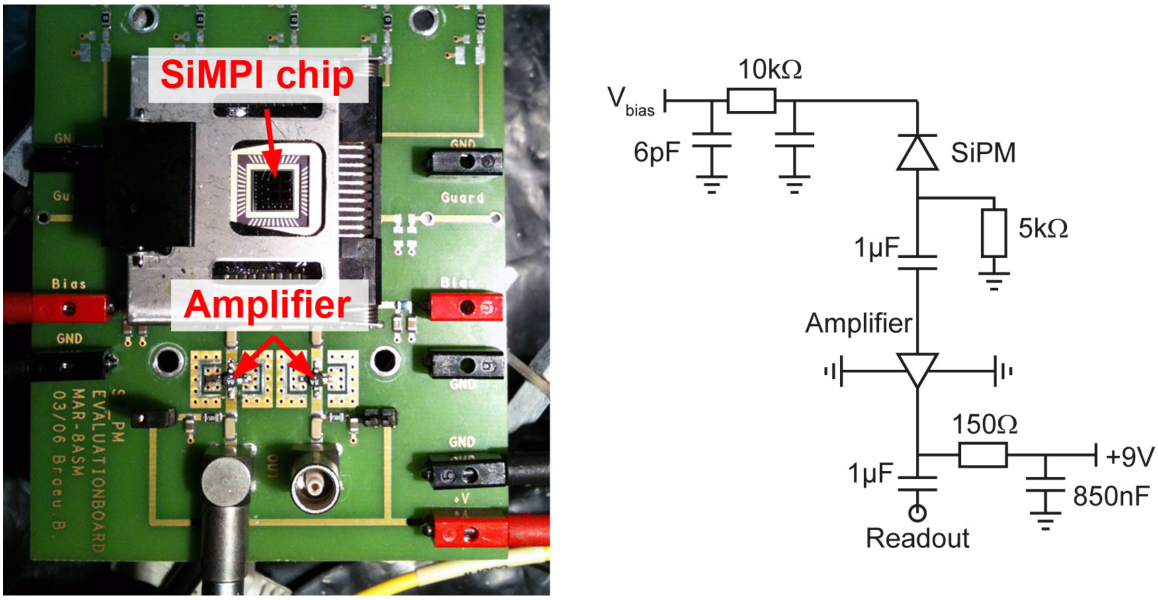

Figure 3.10: Custom-made readout board for SiPMs with MAR8-ASM+ amplifiers (photograph and circuit diagram).

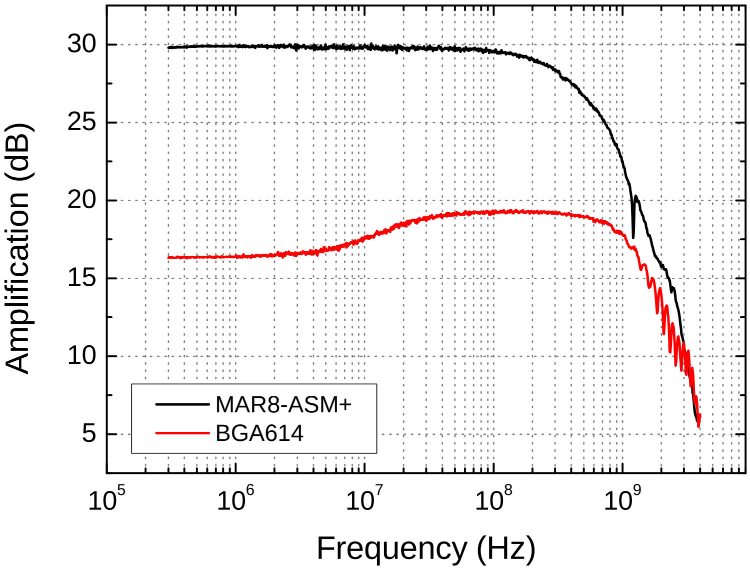

Figure 3.11: Amplification versus frequency of the readout boards with amplifiers MAR-8ASM+ and BGA 614. The measurements for MAR-8ASM+ show an amplification of 29.8 dB for a bandwidth up to 480 MHz. The BGA 614 amplifier has a maximum gain of 19.3 dB for frequencies between 85 MHz and 290 MHz.

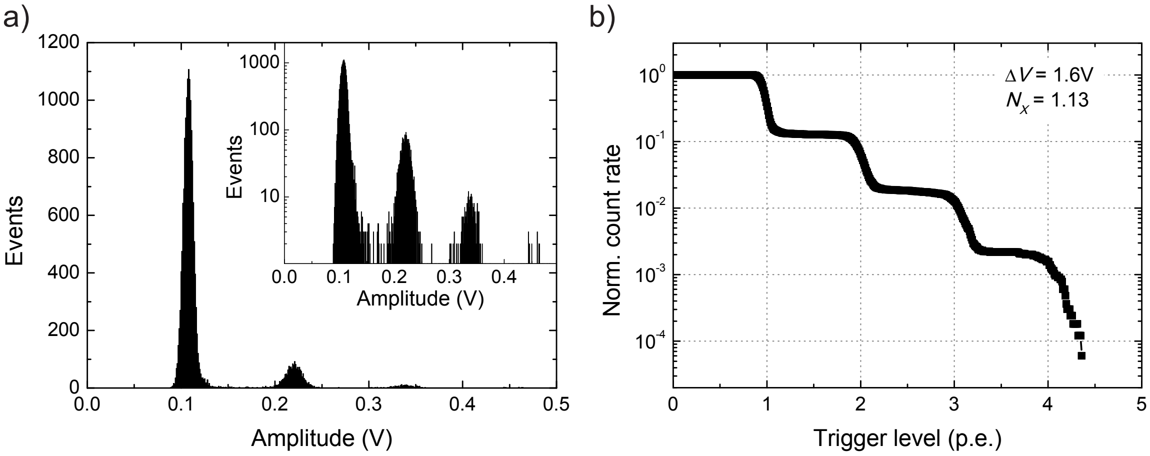

Figure 3.12: Amplitude spectrum (a)) and resulting normalized dark count rate (b)) of a Hamamatsu MPPC with 50 µm pitch. The inset in a) shows a semilogarithmic plot of the data. Integration leads to an average number N_X of fired cells per trigger event.

in coincidence with the pulsed light source. The data are sent to the related digitiser board and further processed. An algorithm calculates the baseline of the signal and the user can define, amongst others, the length of the integration window, the threshold, and the time between two signal recordings [117]. The integrated signal is assigned to an arbitrary digital unit (ADU) and stored in a histogram (1 ADU = 40 fC) resulting in a similar distribution as in Fig. 3.12a. The distance between the individual p.e. peaks corresponds to the gain of the SiPM, according to Eq. (3.10).

However, integration of the signal leads to additional broadening of the p.e. peaks due to afterpulsing and dark count events within the integration window (see below).

3.2.2.3. Noise

The single photon resolution by measuring the charge spectrum is limited, amongst others, by the noise of the electronics σ_{ped} and the gain fluctuations σ_{gain}. Thus, the resolution of the k-th peak in the spectrum (see Fig. 2.15) is

$$\sigma^2(k) = \sigma_{ped}^2 + k \cdot \sigma_{gain}^2. \tag{3.12}$$

The pedestal noise is defined by the signal fluctuation if no avalanche breakdown occurs. These fluctuation arise from leakage currents and the noise of the readout electronics and results in a pedestal peak in the amplitude or charge spectrum. The ratio of σ_{gain}/G of the 1 p.e. peak is called the *Excess Noise Factor (ENF)* of a SiPM cell. Compared to APDs in proportional mode, the ENF of a single SiPM cells is usually much smaller due to the Geiger discharge [118]. The fluctuations in the gain originate from cell-to-cell variations due to imperfections in the fabrication process of the pn-junction as well as small fluctuations in the avalanche process itself. In contrast, the ENF of the whole SiPM device can be defined by the cross talk contribution (average number of fired cells per dark count). By integration of a normalised amplitude spectrum with respect to counts and p.e. an average number N_X of fired cells per dark count event can be calculated. The result of this calculation, with the data from Fig. 3.12a, is shown in Fig. 3.12b.

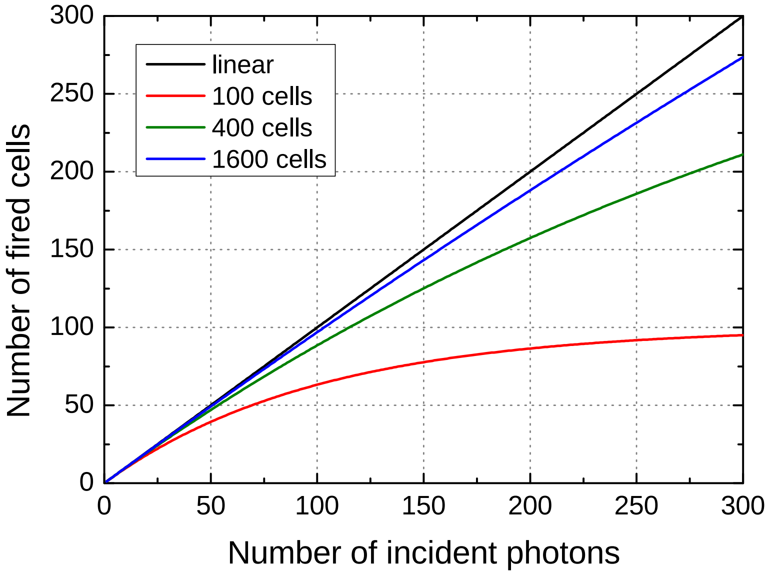

Figure 3.13: Average response of three different array sizes of SiPMs as a function of incident photons. Calculated with Eq. (3.13) for $PDE = 1$. For comparison, also the linear behaviour is shown.

The measurement of the noise is associated with the measurements of the charge spectrum and the gain.

3.2.2.4. Dynamic range

The finite number of cells in the array intrinsically limits the number of photons which can be detected simultaneously. Thus, a saturation of the SiPM response, which limits the dynamic range can be observed, as is shown in Fig. 3.13. For an ideal device, and with the assumption of an infinitely short light pulse, the SiPM response can be described analytically by

$$N = N_{cells}\left(1 - \exp\left(\frac{-PDE \cdot N_\gamma}{N_{cells}}\right)\right), \tag{3.13}$$

where N_{cells} is the total number of cells in the array, N_γ the number of incident photons and PDE the photon detection efficiency. As a result of this equation, the signal output of a SiPM deviates from linearity with increasing number of photons. If N_γ exceeds 50% of the available cells, the deviation is already more than 20%. This is due to the fact, that the probability of two or more photons hitting one cell is steadily increasing. Thus, the dynamic range is already defined by the number of cells within a device. Increasing the number of cells per area would also increase the dynamic range but in turn usually decrease the sensitive area of the device because of the insensitive regions necessary for circuits, resistors, and cross talk suppression. Therefore, the application requirements define the substructure of the SiPM. Detection of large photon numbers with good resolution requires devices with many cells, while low light levels demand high detection efficiencies and thus fewer cells with bigger size.

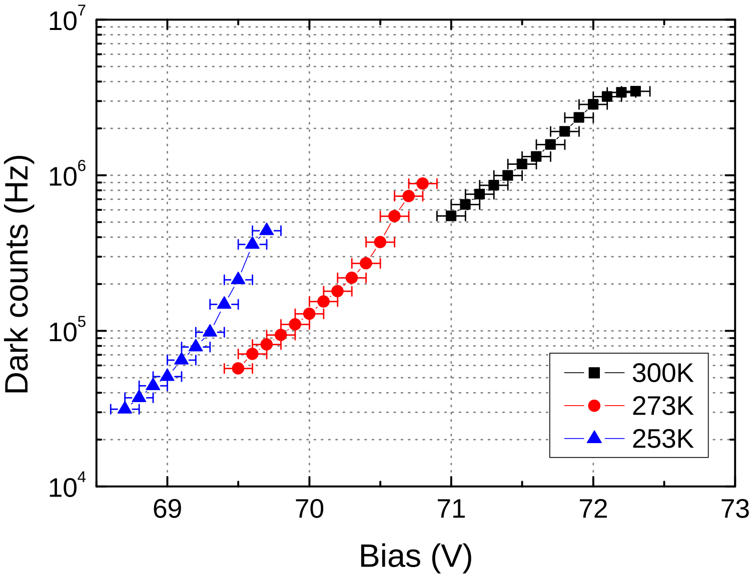

Figure 3.14: Dark count rate of a MPPC at different temperatures. The decrease of the dark count rate is clearly visible taking into account a temperature coefficient of the breakdown voltage of 55 mV/K.

3.2.2.5. Dark counts

A Geiger discharge cannot be triggered by photon absorption only, but also by thermal generation which is increased by defect states (SRH generation in Sec. 2.2.4). Since the resulting signal is the same, it cannot be distinguished from a photon induced pulse.

The dark count rate (DCR) is a function of temperature and also depends on the overbias voltage, since the probability of triggering a breakdown is proportional to V_{ob}. Thus, the dark count rate limits the maximum overbias once it approximates the recovery time due to pile-up events. Taking into account SRH, the dark current for silicon is given by

$$I \propto T^{3/2} \exp(-E_g/2k_BT). \tag{3.14}$$

Since the exponential term is the dominant part, the dark count rate can be reduced by decreasing the temperature of the device (approximately a factor of two for every 7 K). Therefore, room temperature operation requires minimisation of the trap density in the avalanche region, which is a technological challenge for the optimisation of implantation and annealing processes.

These thermal events, together with the secondary pulses (afterpulse and cross talk), result in the dark rate of a SiPM. Measuring the optical cross talk and afterpulsing allows to separate the different contributions (see below).

The dark count rate is given by the number of events per second at a threshold level of 0.5 p.e. It can be measured with a frequency counter (Agilent 53131A) with the same setup already used for the amplitude spectra. In Fig. 3.14, the DCR measurement of a MPPC is shown as an example. The decrease of the dark counts with the temperature is obvious taking into account a decrease of the breakdown voltage from 70.3 V at 300 K to 67.7 V at 253 K.

Temperature (K)	R_Q (kΩ)	C_D (fF)	τ_{rec} (ns)	$\tau_{90\%}$ (ns)	$\tau_{rec,W}$ (ns)
300	125 ± 2	448 ± 10	56 ± 2	129 ± 5	44 ± 2
273	145 ± 2	448 ± 10	65 ± 2	150 ± 5	52 ± 1
253	163 ± 2	448 ± 10	73 ± 3	168 ± 6	60 ± 2

Table 3.1: Recovery time for Hamamatsu MPPCs. τ_{rec} (and $\tau_{90\%}$) is calculated via R_Q and C_D with Eq. (2.34), whereas $\tau_{rec,W}$ results from fitting of the pulse shape.

3.2.2.6. Recovery time

The recovery of the G-APD cell in a SiPM can significantly influence the signal response. During an avalanche breakdown the bias voltage at the diode drops to the breakdown voltage (see Fig. 2.14). When the avalanche is quenched, the cell recovers to V_{bias} with a characteristic time constant τ_{rec}. For conventional SiPMs the recovery time is in first approximation defined by $\tau_{rec} = R_Q C_D$ (see Eq. (2.34)) since the equivalent circuit, as shown in Fig. 2.13, is dominated by this RC element [101,105]. During the recovery, the amount of charge generated by a subsequent avalanche breakdown, caused either by photon absorption, thermal generation or afterpulsing, is related to the current voltage $V_{ob}(\Delta t)$ at the high field region. Thus, using Eq. (2.34), the charge $\Theta(\Delta t)$ for a second discharge after time Δt can be described by

$$\Theta(\Delta t) = C_D \cdot V_{ob}(\Delta t) = C_D \cdot V_{ob} \left(1 - \exp\left(-\frac{\Delta t}{\tau_{rec}}\right)\right). \tag{3.15}$$

Therefore, 90% of the original charge are reached after a time difference of $\Delta t \approx 2.3\,\tau_{rec}$ between two subsequent avalanches, while the total recovery (99.9%) requires $\Delta t \approx 7\,\tau_{rec}$.

The recovery time for conventional SiPMs can be measured in two different ways. As mentioned in Sec. 3.2.1.1, by applying a forward bias to the device the quench resistor value R_Q can be obtained. The diode capacitance C_D can be determined by gain measurements. Thus, the time constant of a conventional SiPM cell can be calculated using Eq. (2.34). Table 3.1 lists the recovery times for a MPPC 100 at three different temperatures. The increase of the quench resistance leads to an increase in the recovery time with decreasing temperature.

A different method is to use the pulse shape and fit the slow part of the signal, which corresponds to the recovery of the cell (see Fig. 2.14a), with an exponential function $\exp(-t/\tau_{rec,W})$. This also offers the possibility to determine the time constant $\tau_{rec,W}$ via the fitting parameters. The obtained values are also listed in Table 3.1 and are in good agreement with the first method. Comparable values have been found in other studies [119].

3.2.2.7. Optical cross talk

Light emission from Si pn-junctions in reverse bias was already reported in the 1950s by Newman et al. [120]. Charge carriers, crossing the junction in an avalanche breakdown, can create photons in a broad energy range starting from 0.5 eV up to 3 eV [121]. The emission spectrum can be explained by hot carriers loosing energy via direct and indirect transitions in the conduction band, as quantum mechanical calculations suggest [122].

In average, one photon with an energy of $E \geq 1.12$ eV (band gap energy of silicon) is generated per $3 \cdot 10^5$ charge carriers crossing the junction [97]. With the high multiplication of SiPMs in the order of 10^6 approximately 30 photons are generated per Geiger discharge.

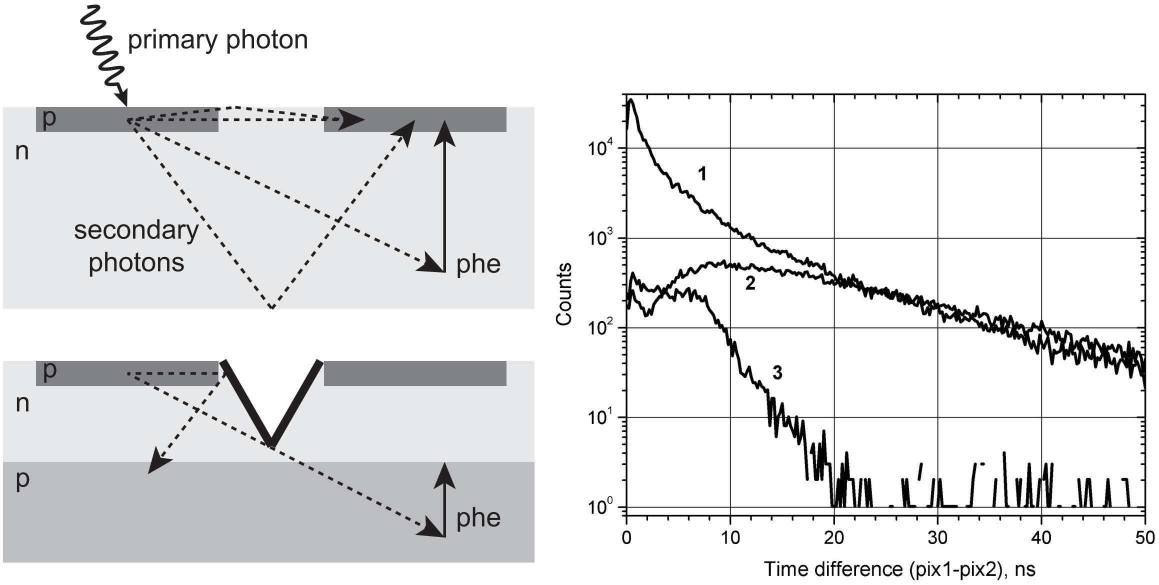

Figure 3.15: Optical cross talk: process and suppression. The left side shows the main process of OCT. The generated photons can either trigger a neighbouring cell directly or via reflections at the interfaces (fast); or they can be absorbed in the bulk material and the resulting photoelectron (phe) can migrate to the avalanche region afterwards (slow). By introducing trenches between the cells, covered with opaque material, the fast component can be suppressed. The introduction of a second pn-junction the photoelectrons are prevent to reach the avalanche region. The right hand side shows the time distribution of two neighbouring cell signals without OCT suppression (1), with trenches (2), and with trenches and second junction (3) (after [123]).

These photons can propagate in the silicon and initiate an additional breakdown event in neighbouring cells. Such an event cannot be distinguished from a second, simultaneously incident photon. Since the triggering is caused by the generated photons, this effect is called optical cross talk (OCT).

As was shown by Buzhan et al. [123], the OCT consists of a fast and a slow component (see Fig. 3.15). The fast component corresponds to the direct propagation of the photon to the high field region of a neighbouring cell, where it is absorbed. Another possibility, which is also fast, is to reach the sensitive area of a neighbouring cell via reflection at the backside of the wafer. In the slow component, the photon is absorbed in the silicon bulk underneath a nearby cell. Afterwards the photoelectron migrates to the avalanche region and might trigger a discharge. It was also shown, that the OCT can be suppressed by suitable measures. The introduction of optical trenches between the cells prevents the photon to propagate to the neighbouring cells and can therefore suppress the fast part. The slow contribution can be suppressed by an additional pn-junction in the silicon bulk material, which prevents the photoelectrons to migrate to the high field regime by an additional potential barrier.

Since the gain, and therefore the number of charge carriers, as well as the probability to trigger an avalanche are functions of the overbias voltage [111], the optical cross talk shows a dependency on V_{ob} as well. Because of this behaviour, OCT is a limiting factor of the maximum overbias which can be applied, since the dynamic range of the device is decreased by the increased occupancy of cells by cross talk events. Furthermore, fluctuations in the number of the cross talk events degrades the resolution of the SiPM.

One possibility to determine the optical cross talk of a SiPM is to plot the number of the dark count rate, measured with a frequency counter (Agilent 53131A), versus the trigger level. The Gaussian distribution of the p.e. signal amplitudes causes the count rate to decrease once the trigger level has reached the peak of the 1 p.e. signal. This repeats with every photoelectron peak in the histogram and results in a distribution known as "staircase plot" (similar to Fig. 3.12b). The OCT is thus defined as

$$OCT = \frac{DC_{1.5}}{DC_{0.5}}, \tag{3.16}$$

the ratio of the dark count rate at a trigger level of 1.5 p.e. and 0.5 p.e. For a device with good photon resolution (clearly separated peaks) these points can be found by determining the constant plateaus of the DCR staircase between the steepest points.

An additional way to measure OCT is to use the amplitude histogram and calculate the ratio of entries larger than 1.5 p.e. to all entries (see Fig. 3.12b):

$$OCT = \frac{N_{>1.5}}{N_{all}}. \tag{3.17}$$

One advantage of the latter method is the noise filter of the oscilloscope which improves the signal-to-noise ratio. In addition, by making use of the amplitude spectrum the measurement is less influenced by afterpulsing or additional dark count events. Both advantages together can result in a distinct and visible staircase even for devices with high noise rates.

3.2.2.8. Afterpulsing

During an avalanche breakdown, charge carriers can be trapped by defect states within the depletion region as shown in Sec. 2.2.4. The trapped charge is released after a characteristic time and can cause a delayed second avalanche breakdown event faking a photon signal, and thus degrading the resolution of the SiPM. This effect is called *afterpulsing.* The probability of an afterpulse at time t after an initial breakdown is given by

$$P(t) \propto \exp\left(-\frac{t}{\tau_i}\right). \tag{3.18}$$

The average trapping time τ_i is defined by the energy level of the trap. In principle, there can be different trapping centres with characteristic trapping times, though measurements indicate the existence of one slow and one fast time constant [124–126]. Since cross talk and afterpulsing are caused by the avalanche breakdown itself, these effects are often referred as *correlated noise* [119].

To determine the afterpulse probability of a SiPM device, the time difference Δt between subsequent pulses was measured using a LabVIEW program. The SiPM signal was recorded with a digitiser board (Acqiris AP235, 8bit resolution and 500 MHz bandwidth). The data were differentiated with respect to t, which results in a distinct peak in the derivative due to the fast rise time of the signal. This method allows to detect events, which would be lost with a standard threshold applied on the original data. The peak detection is realised by a threshold level for the derivative, which is set just above the noise level. If more than one peak is detected within the measurement window, the time difference between two

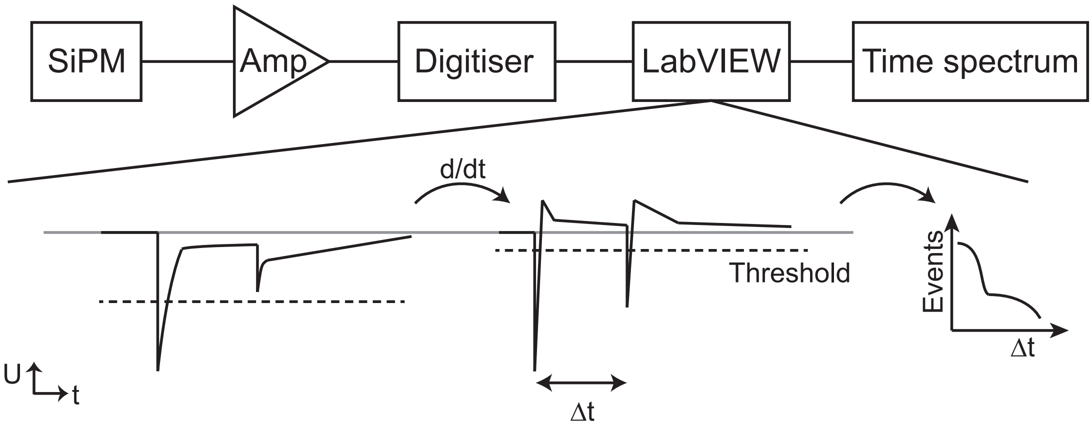

Figure 3.16: Basic readout and analysis for afterpulsing measurements of SiPMs. The signal is recorded and derived either via a digitiser board and a LabVIEW program or with a digital oscilloscope. The peaks above the noise threshold are detected and the time difference is stored in a histogram (see Fig. 3.17).

successive breakdowns is stored in a histogram. The basic readout and analysis chain is shown in Fig. 3.16. The resulting time spectrum can be fitted by a superposition of the different contributions from thermal events and afterpulses. The probability density for thermal pulses is

$$n_t = \frac{N_t}{\tau_t}\,\mathrm{e}^{-t/\tau_t} \tag{3.19}$$

and for an afterpulse event

$$n_{ap} = \frac{N_{ap}}{\tau_{ap}}\,\mathrm{e}^{-t/\tau_{ap}}, \tag{3.20}$$

respectively [124]. As already mentioned above, for afterpulsing a fast (n_{apf}) and a slow (n_{aps}) component has to be taken into account. N_t and N_{ap} are the integrated numbers of thermal and afterpulsing events. The probability of afterpulsing can then be calculated via [124]

$$P_{AP} = \frac{\int_0^\infty n_{aps} + n_{apf} dt}{\int_0^\infty n_{aps} + n_{apf} + n_t dt}, \tag{3.21}$$

the fraction of afterpulsing events in the histogram. With the fit the parameters of τ_t, τ_{apf}, and τ_{aps} can be estimated and the reduced dark count rate without afterpulsing can be determined (see Table 3.2).

Since the overbias is reduced for an avalanche breakdown during recovery (Eq. (3.15)), also the charge and thus the amplitude is reduced. Therefore, very fast afterpulse events are not detected because their amplitude is too small. If the time difference is larger than the recovery time, the afterpulse cannot be distinguished from an incident photon or thermal noise.

The time distribution of a MPPC at $T = 253$ K and $V_{ob} = 1$ V is shown in Fig. 3.17. The measurement is limited by the setup to a minimum of ca. 35 – 70 ns, depending on the signal, which also defines the fit region. The distribution is well described by the combination of afterpulses and thermal noise. With Eqs. (3.19) - (3.21) the parameters in Table 3.2 can be extracted from the fitting function.

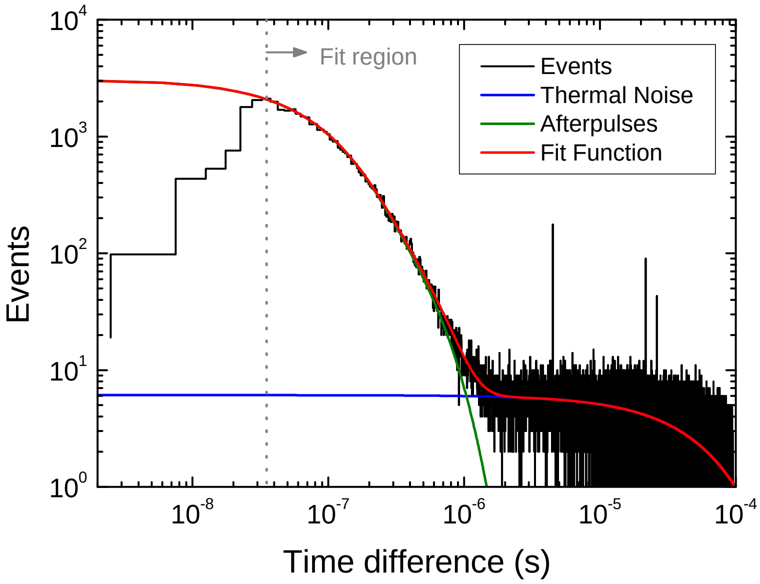

Figure 3.17: Time distribution of MPPCs with 100 µm pitch size ($V_{ob} = 1$ V, $T = 253$ K). The distribution is in good agreement with the exponential approximations. The fit region is adapted to the limits given by the measurement setup towards small time distances (here 35 ns).

τ_{apf}	τ_{aps}	τ_t	P_{AP}
(78 ± 1) ns	(239 ± 5) ns	(54.8 ± 1.0) µs	$(49 \pm 3)\%$

Table 3.2: Extracted values from afterpulsing measurement of Hamamatsu MPPC 100 µm pitch at 1 V overbias shown in Fig. 3.17.

In other studies the probability for afterpulsing is convoluted with a factor to correct for the reduced charge contribution from a non fully recovered cell [124]. In contrast, in this thesis the sole probability that an afterpulse event takes place is considered. Thus, this factor is not taken into account in the calculation of afterpulsing. Measurements with respect to the dependency on overbias and temperature as plotted in Fig. 3.18 show that the afterpulse probability is increasing with the overbias voltage and decreasing with temperature. Since the gain of the device is proportional to the overbias voltage (cf. Eq. (3.10)), increasing the overbias results in an increase of the number of charge carriers crossing the junction. Thus, the probability that a trap level is filled with a charge carrier is increasing as well. The temperature dependence could be a result of the fact that the emission time of the trapped charges increases. As shown in Ref. [127], the emission rate ϵ of traps at an energy level E_t in the space charge region is given by

$$\epsilon = \frac{1}{\tau} \propto \exp\left(\pm \frac{E_t - E_{C,V}}{k_B T}\right) . \tag{3.22}$$

Thus, the emission time is increasing for lower temperatures. This increase leads to a higher probability of detecting the afterpulse event with the measurement setup because the cell is in a progressed recovery state compared to high temperatures. The increase of the recovery

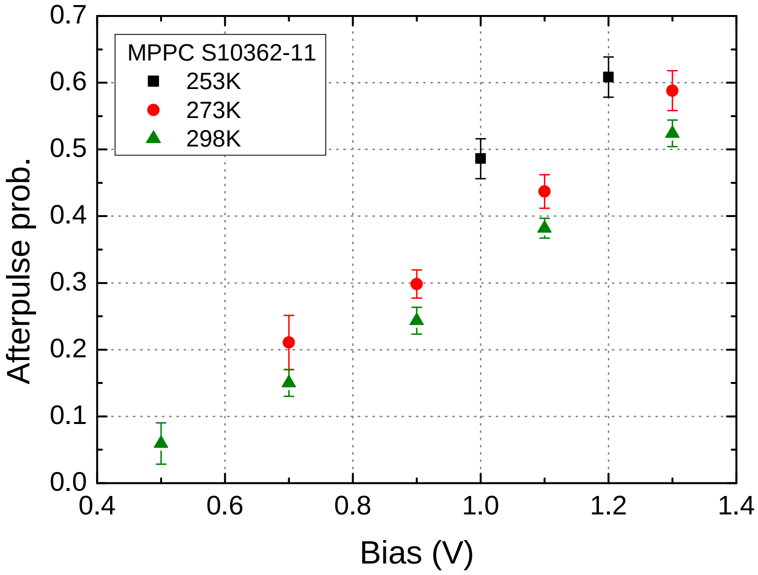

Figure 3.18: Voltage and temperature dependence of afterpulsing for MPPCs. The afterpulse probability increases with the overbias voltage because of the increasing gain. The temperature dependence can be explained by the change of the emission rate for trapped charges with temperature and the corresponding recovery status of the cell. For more details see text.

time as discussed in Sec. 3.2.1.1 does not compensate the exponential dependency of the emission rate.

3.2.2.9. Photon detection efficiency

The essential property of a photon detector is the photon detection efficiency (PDE), the probability to detect a single photon. For a silicon photomultiplier the PDE is a function of the wavelength and the overbias voltage and is determined by:

$$PDE(\lambda, V_{ob}) = QE(\lambda) \cdot FF \cdot \varepsilon_G(V_{ob}), \tag{3.23}$$

with the three contributions:

- internal quantum efficiency QE
- geometrical fill factor FF
- trigger or Geiger efficiency ε_G.

The internal quantum efficiency is the probability that a photon is absorbed and an electron-hole pair is created in the sensitive region of the device. As shown in Sec. 2.1 this is proportional to the absorption coefficient and therefore dependent on the wavelength of the incident photon. If the absorption takes place in the non-depleted highly doped top implantation or the non-depleted deep implantation, the carriers are most probably lost due to the short recombination times. Especially for detection of UV and blue light with very short penetration depths, the fabrication of shallow top layers is a technological challenge. The reflection of

Wavelength	Refraction index	Reflection
300 nm	5.01	0.62
400 nm	5.57	0.49
500 nm	4.30	0.39
600 nm	3.94	0.35

Table 3.3: Refraction index and surface reflection for silicon at different wavelengths for an incident angle of 90° [128].

light due to the difference of the refraction indices also has to be taken into account. The transmission of photons to the silicon bulk can be estimated by using the simulation tool *OpenFilters* [128], which is based on the transfer matrix method. Several coating layers with variable thickness can be added to the silicon surface. The software allows to check the transmission into silicon for different wavelengths and incident angles. The refraction index and the corresponding surface reflection of a silicon/air interface at different wavelengths are shown in Table 3.3. These reflection values can be decreased below 10% by engineering entrance windows with optimised antireflective coatings.

The fill factor is the ratio of the photon-sensitive area of the SiPM and the whole area of the array. Usually, the dead area of the device is needed for the integration of the quenching mechanism and contacts as well as the suppression of optical cross talk. Therefore, the FF value generally depends on the cell size of the array.

The trigger efficiency defines the probability, that the generated electron-hole pair triggers an avalanche breakdown while drifting through the high field region of the detector. This parameter is a function of the electric field and thus of the applied overbias voltage as well as the doping profile (depletion width) [111, 112]. A homogeneous high electric field strength is required, in order to maximise the trigger efficiency. Furthermore, ε_G depends on the position where the photon absorption takes place and on the type of the charge carrier that triggers the avalanche. In silicon, electrons have a higher trigger probability compared to holes due to their larger ionisation coefficients, what makes them the preferred charge carriers to initiate an avalanche. This fact determines the basic structure of the device. Since the penetration length of blue light is shorter than for red, devices with a PDE peak wavelength in the blue regime are built as *p-on-n* structures. Here, the photon is most probably absorbed near the surface and the electrons see the whole electric field while propagating through the space charge region (in other words, the ionisation integral is maximised). For the detection of red light *n-on-p* structures are used, thus the electrons can again exploit the whole electric field to trigger the avalanche. The different situations for both structures are illustrated in Fig. 3.19. The behaviour of the trigger efficiency can be estimated with Monte Carlo methods if the electric field in the depletion region is known. As a rule of thumb the trigger efficiency, and therefore the PDE, saturates at a relative overbias of roughly 15% of the breakdown voltage [129]. The advantage of operating the SiPM in saturation is the minimisation of the PDE temperature dependence caused by $\partial V_{bd}/\partial T$.

For the PDE measurements, the SiPM with the readout board is stored in a light-tight climate chamber. As a reference detector, a calibrated *pin*-diode[15] is used and positioned next to the SiPM (QE calibration data in Appendix B). The sensitive area of the diode is limited by an aperture to a diameter of 25 mm. As light sources pulsed lasers and LEDs

---

[15] Hamamatsu S3584-08

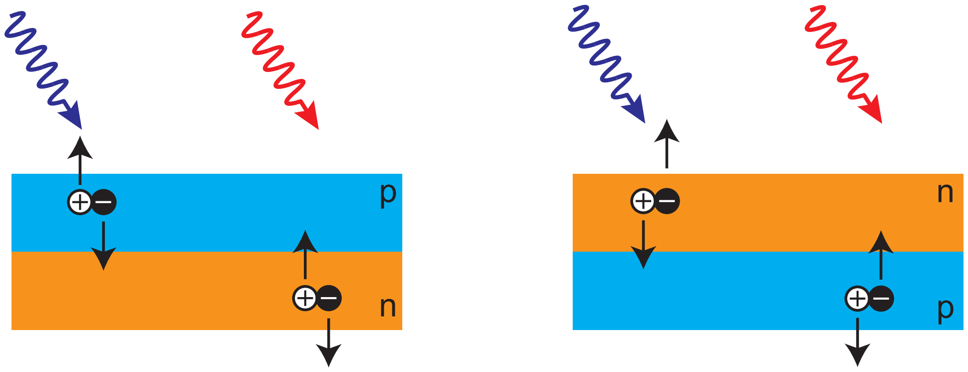

Figure 3.19: Comparison between p-on-n (left) and n-on-p (right) structures. The depth of penetration differs with the wavelength and so the device has to be optimised for specific energies. Since the ionisation coefficients for electrons are higher, it is always preferred to let the electrons drift through the entire high electric field, resulting in an optimised PDE.

from *PicoQuant* (PLS and LDH series) with pulse lengths in the order of 100 ps FWHM and wavelengths in the range of 281 - 598 nm are used. The incident light is reflected by a plate of sintered polytetrafluoroethylene granulate (known as Spectralon), a high reflective and diffuse scattering material, which guarantees an almost equal illumination of SiPM and photo diode [130]. The amplitude histogram of the DUT signal output is recorded with an oscilloscope, while the photocurrent of the reference photo diode is simultaneously measured using a picoamperemeter (*Keithley 6485 picoammeter*). Fig. 3.20 shows a schematic picture of the PDE measurement setup.

The mean number of photons for the reference diode is proportional to the photo current, while the mean number of photon equivalents, measured with the SiPM is defined by Poisson distribution. To eliminate the contribution of optical cross talk and afterpulsing the zero-p.e. peak is used via

$$P_\lambda(k) = \frac{\lambda^k}{k!}\mathrm{e}^{-\lambda} \quad \rightarrow \quad P_\lambda(0) = \mathrm{e}^{-\lambda} \quad \rightarrow \quad \lambda = -\ln\left(P_\lambda(0)\right) \tag{3.24}$$

to calculate the mean photon number λ from the Poisson distribution [124]. $P_\lambda(0)$ can be derived from the histogram. Since the intensity $\Im$ for both devices is assumed to be constant,

$$\Im_{SiPM} = \Im_{PD}, \tag{3.25}$$

the ratio of the mean photon numbers, which corresponds to the PDE of the SiPM, is then given by (see Appendix A):

$$PDE = \frac{\bar{n}_{pe}\, e\, \nu}{I_{PD}} \cdot QE_{PD} \cdot \frac{A_{PD}}{A_{SiPM}} \tag{3.26}$$

with

- $\bar{n}_{pe}$ mean number of photon equivalents,
- ν trigger frequency of the laser,
- I_{PD} photocurrent of the photo diode,

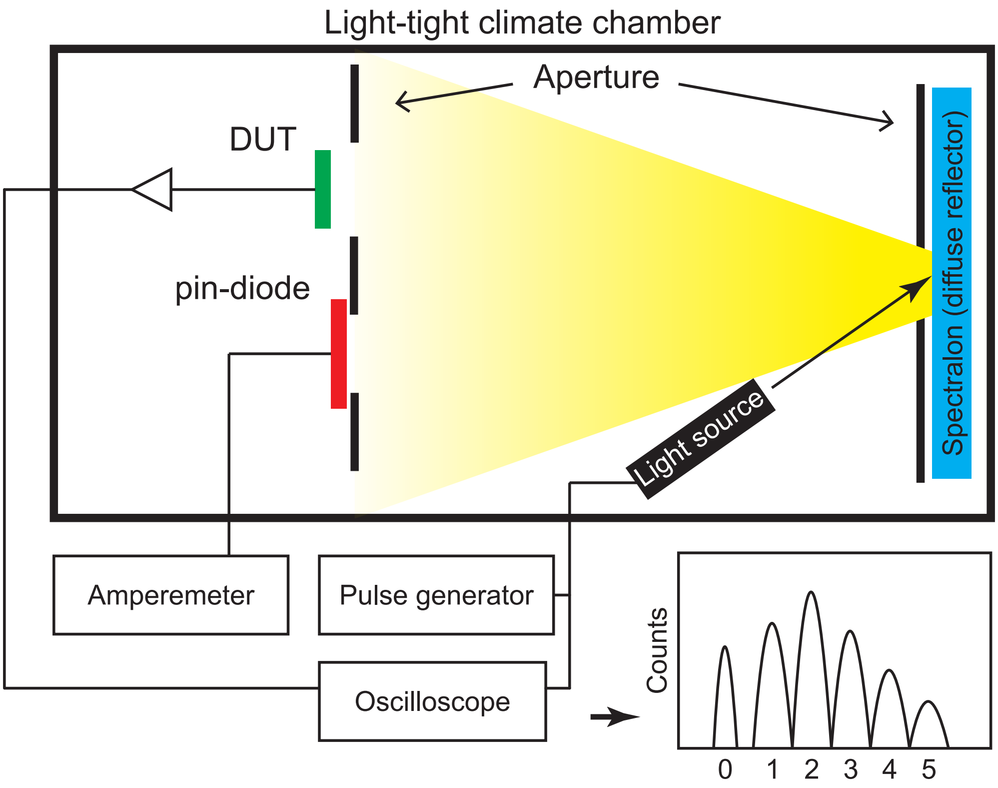

Figure 3.20: Schematic of the PDE measurement setup. The detector under test (DUT) is illuminated via a highly reflective Spectralon plate by a ps pulsed light source. A calibrated photo diode is used as reference. The histogram of the charge spectrum is recorded with an oscilloscope. The PDE is calculated by the ratio of the mean photon numbers. See text for details.

- QE_{PD} quantum efficiency of the photo diode,
- detector areas A_{PD} and A_{SiPM} of photo diode and SiPM, respectively.

In order to cross-check the setup, measurements of MPPCs with 100 µm pitch size were performed. At recommended operating voltage and a wavelength of 405 nm, they showed PDE values in the range of 35%. This is comparable to results obtained in other studies [124].

3.2.3. Photon emission microscopy

As already mentioned in Sec. 3.2.2.7, during an avalanche breakdown a broad spectrum of photons is emitted [121]. By collecting the emission with a camera this process can be used to determine the avalanche regions in the device. Therefore, emission microscopy is a helpful tool for characterisation and failure analysis of SiPMs.

For the measurements, the photon emission microscope *PHEMOS 1000* from Hamamatsu was used. The detector under test is placed under the objective of a microscope in a light-tight box. A bias voltage is applied and, as a cross-check, the signal of the detector is visualised on an oscilloscope to be sure to have a working device. The emission image is recorded with a cooled CCD camera by collecting the emitted light and integrating the signal over a certain period of time. Afterwards, the image can be corrected for the thermal noise of the

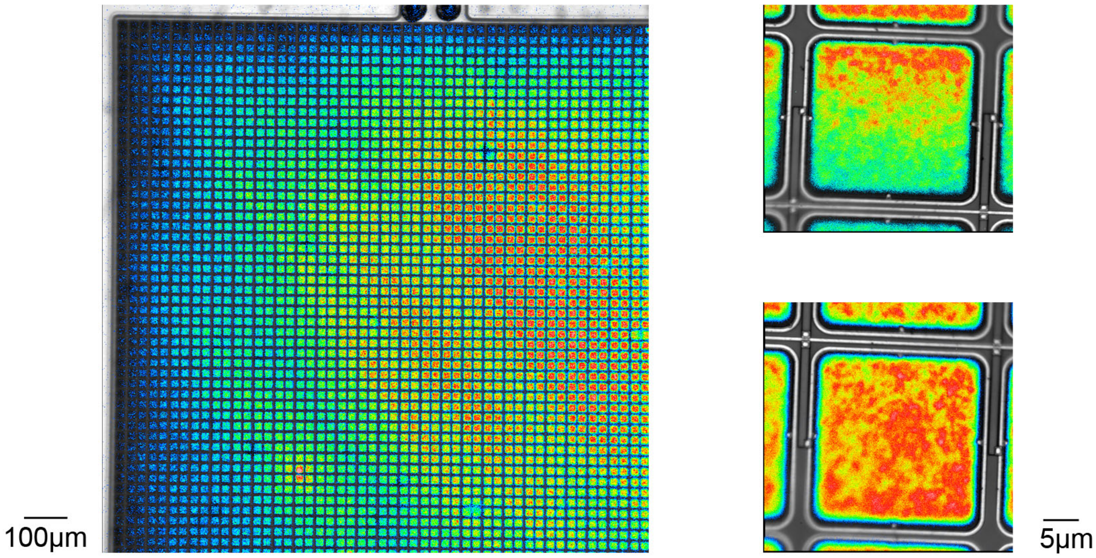

Figure 3.21: Photon emission microscope images of MPPCs with 25 µm pitch. On the left hand side the image shows the inhomogeneity of the intensity of a 1x1 mm^2 array, which can be an indication of varying electric fields and thus affecting the detection efficiency and photon resolution. The right hand side shows also variations within one cell.

camera by taking a picture under dark conditions (device without bias voltage). Different levels of magnification (5x, 20x, 100x) are available in which the required integration time increases with magnification. For localisation, the emission images can be superimposed to a high-resolution pattern image of the detector surface.

The high field regions become visible by increased light emission, as can be seen in Fig. 3.21. In the range of the breakdown voltage an early edge breakdown would be noticed by photon emission in the edge region, while the rest of the cell is still below breakdown and therefore dark. Since this is a long time measurement, neither individual avalanches nor their spatial distribution can be observed. Nevertheless, inhomogeneities within the array (Fig. 3.21 left) and within one cell (Fig. 3.21 upper right) as well as hot cells can be identified. The small inhomogeneities within one G-APD originate from the fact that an avalanche breakdown occurs only in a small volume of the cell (avalanche diameter of ca. 10 µm) [131].

4. SiPM with bulk-integrated quench resistor

As presented in Sec. 2.3.3, a network of integrated quenching resistors is required in order to stop the avalanche breakdown in the individual cells of a SiPM. In conventional devices the resistors are realised on top of the structure, as can be seen in Fig. 4.1. Additionally, each cell needs an individual connection to the common readout contact via a metallic grid. Up to now, most commercially available SiPMs are using polysilicon resistors. Their fabrication requires several steps (deposition, structuring, doping) and is therefore one of the cost drivers in the production of a SiPM. Besides, the avalanche quench condition requires resistor values in the order of several 100 kΩ [101], since the PDE saturation regime starts at an overbias of $V_{ob} \approx 0.15\,V_{bd}$. In this range the resistivity of polysilicon layers depends not only on the doping level but also on the shape and size of the polysilicon crystallines [132]. This, in turn, affects the reproducibility of the resistors and may have a negative influence on the yield of the production.

In addition, the polysilicon and the metallic grid are an obstacle for light. Since they require space within the sensitive area of the device, the fill factor and thus the maximum photon detection efficiency of the SiPM is limited.

At the semiconductor laboratory of the Max-Planck-Society a novel SiPM approach was proposed. In order to simplify the technology and to increase the fill factor, the quench resistor is integrated to the silicon bulk material [133,134]. The development and optimisation of these devices is the aim of this thesis. This chapter describes the concept of the so-called Silicon MultiPixel light (*SiMPl*) detector and its basic advantages and drawbacks.

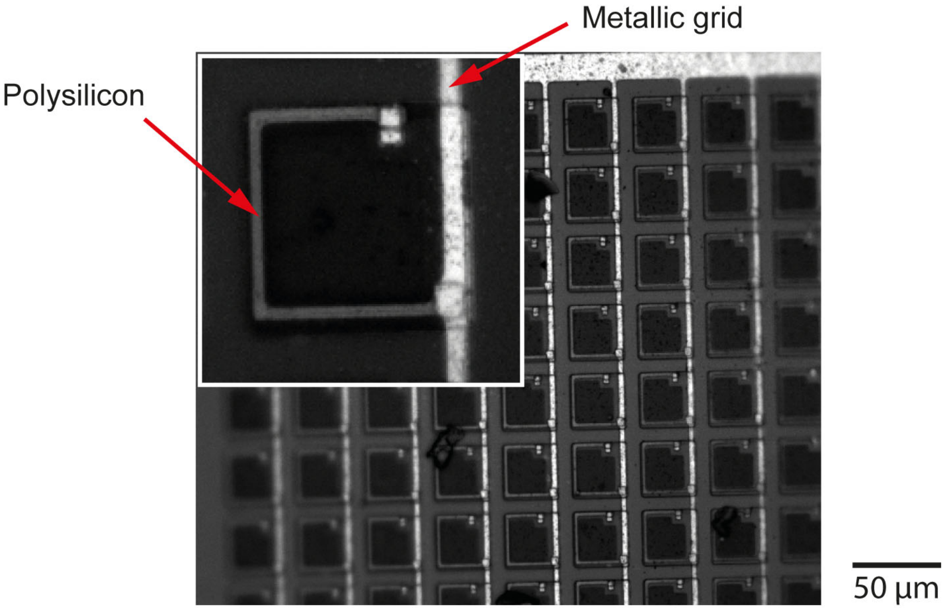

Figure 4.1: Conventional SiPM with polysilicon quenching resistor and metallic grid. The device is from Moscow Engineering Physics Institute (MEPhI) with 42 µm pitch size.

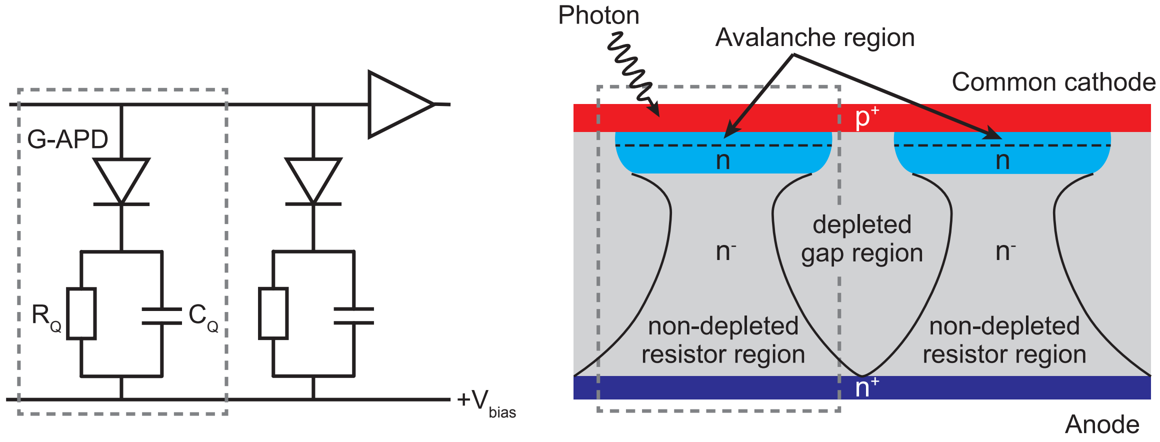

Figure 4.2: Equivalent circuit and cross-section for SiMPl. The left side shows the components of an equivalent circuit of a silicon photomultiplier micro-cell. The right hand side shows the corresponding schematic cross-section of two neighbouring cells of the SiMPl concept. The quenching resistor is integrated into the high-ohmic silicon bulk and laterally defined by the depletion expanding from the gap region. For details see text.

4.1. Concept

The idea of the SiMPl detector is to integrate the individual passive quench resistors of the G-APD array into the silicon bulk material. The equivalent circuit in Fig. 4.2 shows all the components of the SiPM cells: a G-APD with a series resistance R_Q as well as the coupling capacitance C_Q in parallel to the resistor. For comparison, the cross-section of two neighbouring cells of the SiMPl approach is plotted next to it and illustrates the corresponding parts in the design of the device.

In order to be most sensitive in the blue wavelength regime, the basic structure of the device is p-on-n, and therefore the wafer material is n-doped (cf. Sec. 3.2.2.9). A p^+ implanted *cathode* and a highly n-doped backside *anode* form the outer contacts of the device, connected to ground and V_{bias}, respectively. It should be mentioned that the nomenclature of anode and cathode is inverted in comparison with a standard diode operated in forward bias[1] (p-side: anode, n-side: cathode). The sensitive avalanche region is defined by a structured deep n-implantation, which acts as an internal anode. This pn-junction corresponds to the G-APD in the equivalent circuit on the left side in Fig. 4.2. In regions without internal anode implantations a depletion region extends into the low-doped silicon bulk due to the applied reverse bias voltage. Within the avalanche regions, the depletion stops at the deep n-implantations so that it is only present at the edges of the individual cells (gap region). In the bulk regions below the cells, a lateral (sidewards) depletion cannot be avoided (JFET behaviour, see below). The remaining non-depleted bulk volume defines the vertical quench resistor R_Q. The unstructured common p^+ cathode, together with the internal anodes, already provide the parallel connection of all cells. The non-depleted bulk material below the avalanche region implies that the voltage drop occurs only between the internal anode and the cathode. The width of the corresponding depletion region, in combination with the doping profile, defines the high electric field and thus the breakdown voltage. The fast component of

---

[1] Since the standard operation of the detector is in reverse bias, the electrons drift to the n-region and the "collection" of electrons is associated with the anode.

the signal, which determines the amplitude, is given by the discharge of the parallel coupling capacitance C_Q during the breakdown. In the SiMPl approach this capacitance is formed automatically between the internal anode and the back contact.

The depletion of the n-bulk already suggests that the resistance depends on several device parameters. The value of the resistor R_Q is theoretically defined by

$$R_Q = \rho \frac{l}{A} = \frac{1}{en\mu} \frac{l}{A}, \tag{4.1}$$

with ρ the resistivity of the bulk material, n the majority charge carrier density, μ the majority charge carrier mobility, l the depth of the bulk material, and A the cross-sectional area of the non-depleted region. As a result of the bulk integration of the resistor, the resistance is defined by the following parameters:

- the cell size, since the pitch-gap combination defines the maximum extension of A
- the thickness of the bulk material, which corresponds to l
- the resistivity of the bulk material, given by the doping level and the temperature dependent mobility
- the bias voltage, which defines the expansion of the depletion region
- the geometrical shape of the cell.

Taking this into account, Eq. (4.1) can be written in cylindrical approximation as

$$R_Q = \rho \frac{l}{A(l)} = \rho \int_0^l \frac{1}{r^2(x)\pi} \, dx. \tag{4.2}$$

Due to the lateral depletion of the bulk, the IV characteristic is less that of a standard resistor and rather behaves similar to a junction field effect transistor (JFET) in source follower mode, with the non-covered cathode in the gap region as the gate and the internal anode and the back contact as source and drain, respectively [134]. As a result, the value of R_Q is changing with the source-drain voltage during the loop of a G-APD (cf. Fig. 2.10b) and thus affecting the recovery time of the cell. The lateral depletion from the adjacent gap regions can lead to a fully depleted bulk volume directly underneath the G-APD structure resulting in a so-called pinch-off (see Fig. 4.3a).

For an optimised decoupling of the cells, a full vertical depletion is preferable. In the case of a standard wafer with a thickness of approximately 450 µm, this would require voltage values much higher than usual operating voltages of SiPMs with respect to V_{bd}. In addition, the full depletion of a standard wafer with a thickness of 450 µm is not achievable with respect to the size of the micro-cells. This would lead to a full sidewards depletion of the bulk underneath the cell and results in the previously mentioned pinch-off of the bias voltage. In this case, a part of the externally applied voltage already drops across this depleted region in the bulk. As a result, the actual potential at the internal anode, and thus the voltage drop across the high field region, is less than V_{bias}. On the other hand, the standard operating voltage for the SiPM would lead to a depletion region expanding only into a small fraction of the bulk (see Fig. 4.3, right). The resulting current from the internal anode of a fired cell to the backside spreads in the thick bulk material to regions below neighbouring cells. This current leads to a change of the potential and thus the effective bias voltage of adjacent cells is affected

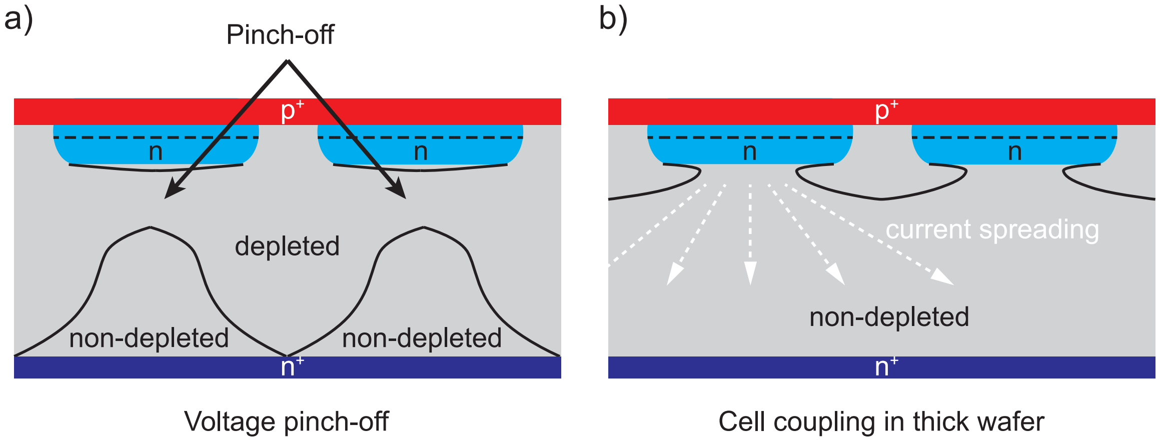

Figure 4.3: Thick wafer exclusion for SiMPl. a) shows the general situation for a device with pinch-off. The whole area below the diode is depleted too, which leads to a voltage drop before the high field region and prevents recovery of the diode. b) illustrates the situation for a thick wafer where only a small fraction of the bulk material is depleted. This would lead to a strong coupling of the cells due to the current spreading. Drawings are not to scale.

(coupling). Hence, standard material cannot be used for the production of properly working devices.

A proper adjustment of the resistors requires high-ohmic material with a smaller thickness than standard wafer material. Starting from the large parameter space mentioned above, the final adjustment of the cell dimensions (pitch/gap) depends on the thickness and the resistivity of the bulk material. On the one hand, a sufficient probability to trigger an avalanche breakdown requires a certain overbias voltage [111], without exceeding the quench condition for the G-APD given by Cova [101]. Therefore, sufficient resistor values are required. On the other hand, high resistances can be associated with an approach to the pinch-off state increasing the recovery time to several µs. Hence, a trade-off between recovery time and quench capability, as with conventional SiPMs, is necessary.

A technological challenge is to optimise the homogeneity of the electric field in the avalanche region (see Fig. 4.4), which can suffer from diffusion during annealing and local electric field maxima in the edge regions. Latter is the reason for early edge breakdown, since it reduces the breakdown voltage in the affected edge regions. Thus, these small edge regions become the dominating part of the cell resulting in an inefficiently working G-APD. The prevention of this effect is usually realised by guard ring structures for the edge region. For this purpose, various approaches have been developed within the last years (see Ref. [135]). However, the ambition of the SiMPl approach is to avoid such additional guard structures for edge breakdown suppression in order to simplify the fabrication process. In turn, this requires detailed studies of process parameters by means of TCAD simulations.

In order to meet the requirements for avalanche quenching and to avoid pinch-off, also the bulk resistor problem has to be simulated in detail due to contributions from carrier diffusion from top and bottom layer into the resistor bulk, as well as due to precise calculation of the sidewards depletion [134]. Nevertheless, the performance of the final device is always a question of experience and quality of the technology.

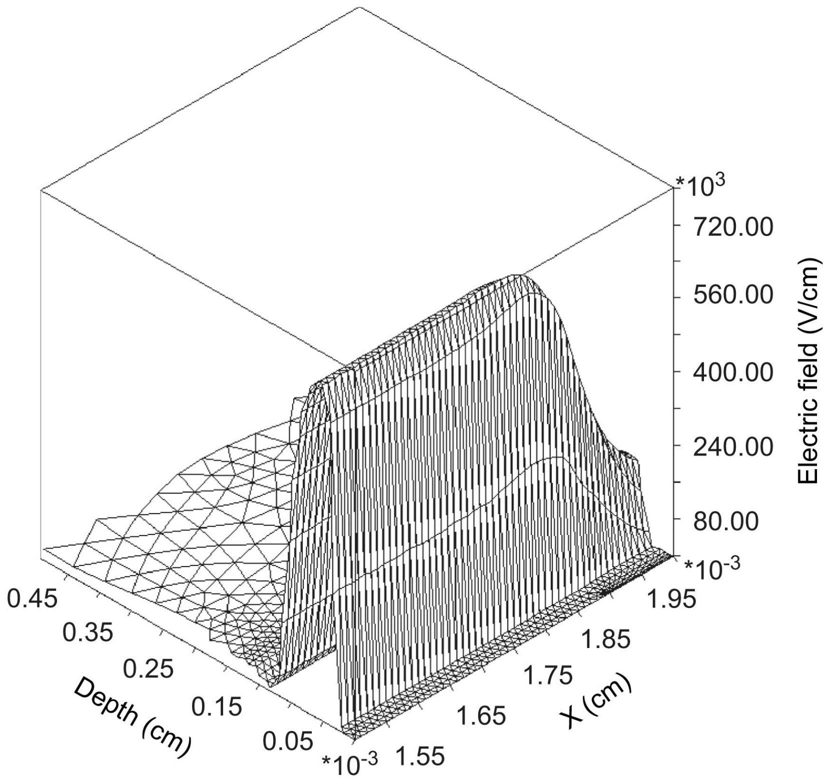

Figure 4.4: Simulated electric field distribution in the edge area of a micro-cell. Homogeneous high field regions without electric field peaks at the edges seem achievable with simplified technology. Image adapted from [134].

4.2. Simulations for feasibility study

In order to demonstrate the feasibility of the SiMPl approach, extensive simulations have been performed at the semiconductor laboratory[2] with the aim to specify and investigate basic technological process steps and device parameters. Common semiconductor 2-D device simulation tools, as described in Sec. 3.1, were used for these studies (DIOS, TeSCA).

Important parameters and characteristics for the SiPM are:

- the homogeneity of the electric field in the avalanche region
- the sidewards depletion from the gap regions
- the IV characteristics of the resistors
- the recovery time of the cells
- the signal strength of the device output.

The utilised simulation procedure is very similar to the detailed simulations of a second prototype, explained in more detail later in Sec. 5.2.1. Based on the requirement of a high detection efficiency, a cell size in the order of 100 µm has been aimed for. First simulations, based on the available wafer material (bulk doping around $2.5 \cdot 10^{12}$ cm^{-3}), already showed

---

[2] by Rainer Richter

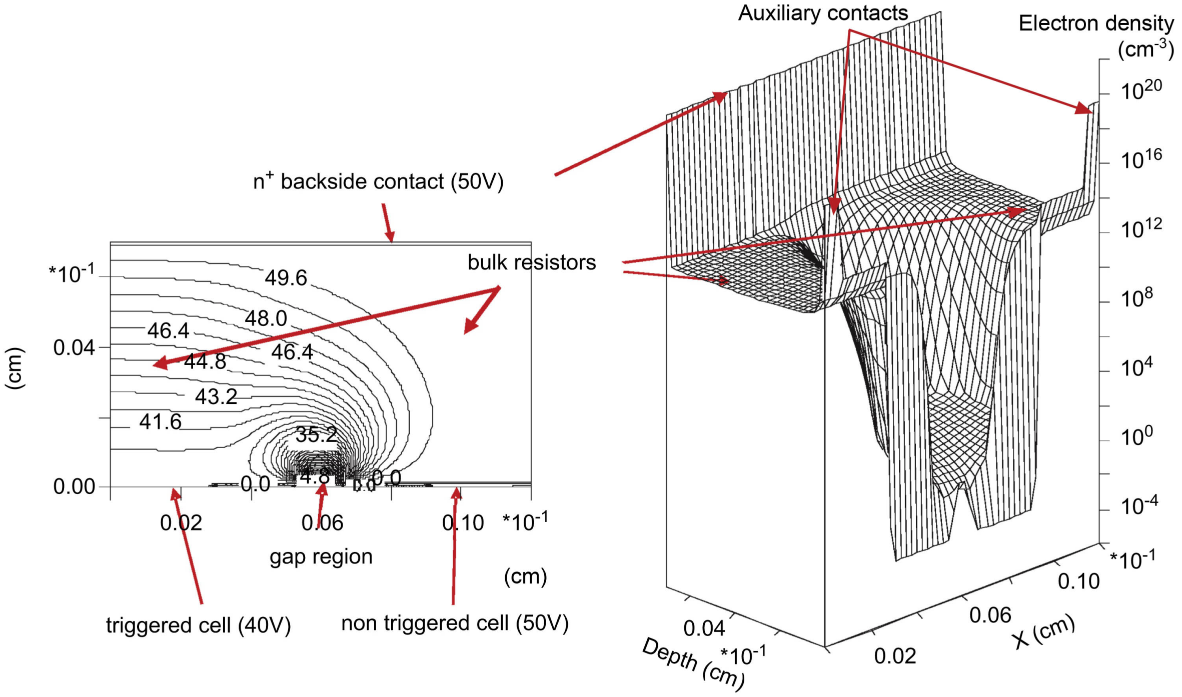

Figure 4.5: Simulation of potential distribution (left) and electron density (right) of a cell with 120 µm pitch and 14 µm gap (plotted upside down). With auxiliary contacts the internal anode of the right cell is kept at $V_{bias} = 50$ V whereas for the left cell the internal anode dropped to $V_{bd} = 40$ V. The non-depleted bulk regions, clearly visible in the right plot, indicate the quench resistors. Image adapted from [134].

that a wafer thickness of about 70 µm is required to meet the quench condition and to avoid pinch-off at once [136]. For this reason, the further simulations mainly focussed on this thickness and exhibited encouraging results [134].

Some general conclusions can be drawn from these studies. In Fig. 4.4, the electric field distribution in the edge region of the device is plotted. No distinct local field maxima in the edges of the high field region, which could cause early edge breakdown, are visible suggesting that simplified technology can be used to obtain a homogeneous electric field in the avalanche region.

The special property of the SiMPl approach is the integration of the quench resistors into the bulk. Therefore, the electron density distribution in the bulk with applied bias voltage is of interest. An example for a structure with 120 µm pitch and 14 µm gap is shown in Fig. 4.5. Two neighbouring cells with auxiliary contacts are plotted upside down (cf. Fig. 5.13 in Sec. 5.2.1). The additional contacts allow to simulate the state after an avalanche breakdown. On the left hand side, the electrostatic potential distribution is shown. While the internal anode of the non-triggered cell (right) is at the bias voltage (50 V) the internal anode of the left cell dropped to the breakdown voltage (40 V). On the right hand side of the picture, the electron density is plotted. The non-depleted regions correspond to the bulk resistors. The depletion extending from the gap to the bulk is clearly visible.

By changing the potential of the internal anode, it is possible to simulate the IV characteristic of the bulk resistors. An example of a result from this study is presented in Fig. 4.6. It shows the IV curves for three different bulk doping levels as a function of the voltage

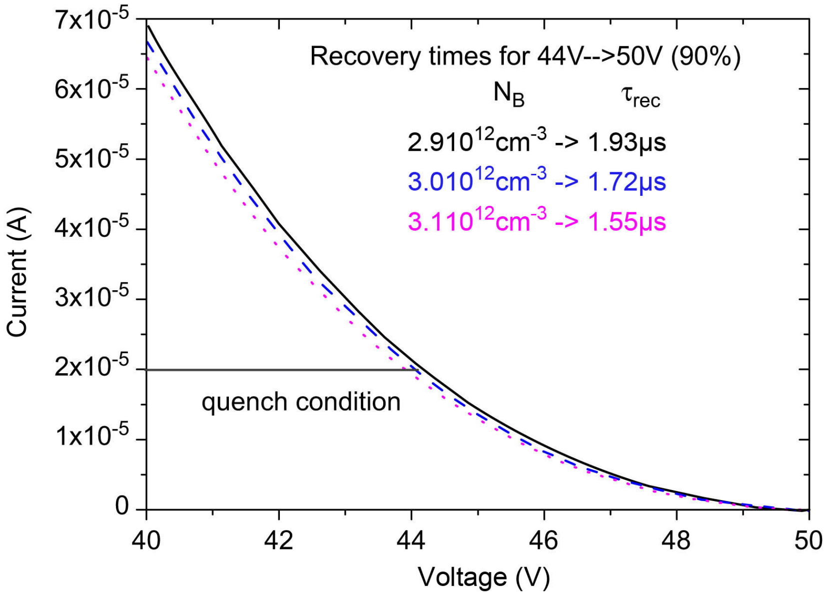

Figure 4.6: Non-linear IV curve of resistance R_Q due to parasitic JFET behaviour. As a result, longer recovery times can be expected, illustrated for three different bulk dopings (adapted from [134]). A variation of 3% in the doping level leads to a change of roughly 200 ns in the recovery time.

at the internal anode. A quench condition of 20 µA was assumed [101], which in this case allows an overbias voltage of 6 V. The quench resistor shows the expected non-linear (JFET-like) behaviour as discussed earlier. Also shown in Fig. 4.6 are the recovery times for three different bulk dopings N_B extracted from the IV curves (see Sec. 5.2.1). Compared to conventional polysilicon resistors, 3–4 times longer recovery times can be expected according to simulations, assuming the same quench conditions (20 µA at $V_{ob} = 6$ V).

Finally, the signal strength which depends on the discharge of the coupling capacitance C_Q can be studied by transient simulations (see Sec. 5.2.1). The result of the integrated charge is shown in Fig. 4.7. Below 1 ns the charge integral is associated with the signal formation, whereas the slow part corresponds to the recovery. From this result it can be concluded that the output signal of the device is sufficiently high and does not require any sophisticated amplifiers.

4.3. Advantages and drawbacks

In comparison to conventional SiPM devices, the novel approach of integrating the quench resistor to the silicon bulk brings some advantages for this kind of photon detectors but also implicates a few drawbacks.

The main advantages of the novel concept come with avoiding polysilicon. Since the resistor is integrated in the bulk, as well as due to the thereby allowed common p$^+$ implantation of the top layer, there is no need for polysilicon and a metal grid within the sensitive area. This allows to place the readout contact at the edge of the device outside of the sensitive area, which leads to a free and unstructured entrance window for light. Thus, it can be easily adapted to a specific wavelength with antireflective coatings to minimise reflection

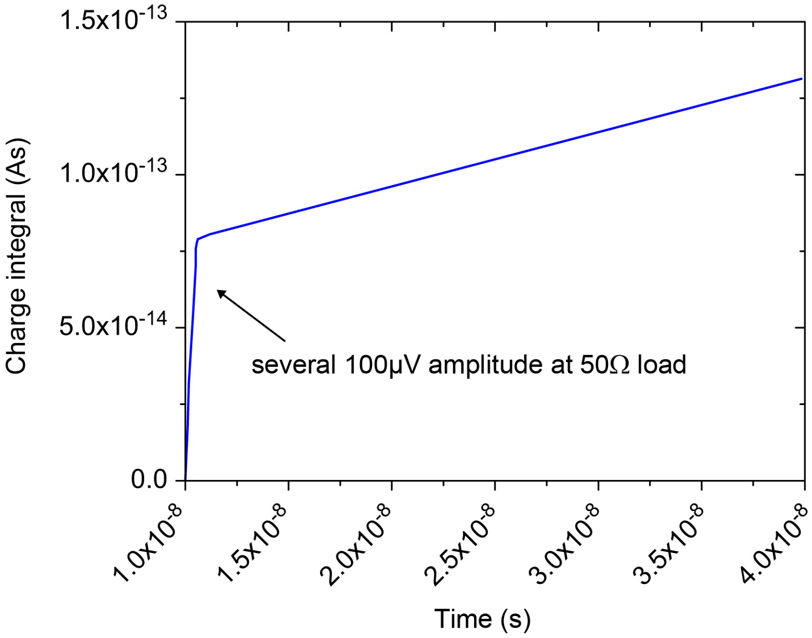

Figure 4.7: Integrated charge from simulation. The signal formation is described by the charge integral within the first nanosecond after triggering the breakdown at $t = 10$ ns. The slower tail corresponds to the recovery of the cell. Image adapted from [134].

losses. It also allows an easy combination with bump bonding techniques (see Sec. 6.1). With the absence of polysilicon and the metallic grid, the maximum fill factor of a SiPM and therefore its PDE can be increased. A limitation in the FF is only given by the separation of the G-APDs and the suppression of optical cross talk, which is, up to now, controlled by absorption via the size of the gap between neighbouring cells. Therefore, the SiMPl detectors promise higher PDE values ($\approx$ 60–70% PDE estimated) compared to conventional SiPMs. Furthermore, the absence of the metallic grid results in a very small parasitic capacitance C_g and thus promises optimum conditions for fast timing properties. In addition, the fabrication of the devices is simplified by reducing production steps. This fact should lower the costs once it comes to mass production.

A further advantage is the suppression of optical cross talk. By implementing a second pn-junction in conventional SiPMs, minorities from the bulk, generated thermally or by the absorption of hot carrier emission photons [121], are prevented from entering the avalanche region and from potentially triggering a neighbouring cell (see Sec. 3.2.2.7). In the design of SiMPl, the deep n-implant results in a diffusion barrier against minorities from the bulk and thus corresponds to the second pn-junction in a standard device. Due to the potential barrier at the n-implant, holes from the bulk prefer to move in the direction of the gap region and thus are not amplified by an avalanche breakdown. According to simulations, less than one hole reaches the high field region, with 1000 e-h-pairs created in the bulk. Therefore, the slow component of optical cross talk should be suppressed. Since this diffusion barrier is an inherent property of the SiMPl design, it does not require additional process steps.

The novel approach also has the potential to offer better radiation hardness compared to conventional SiPMs. Ionising radiation creates trapped positive charges in the oxide layer close to the Si-SiO$_2$ interface which induces the accumulation of electrons below the silicon

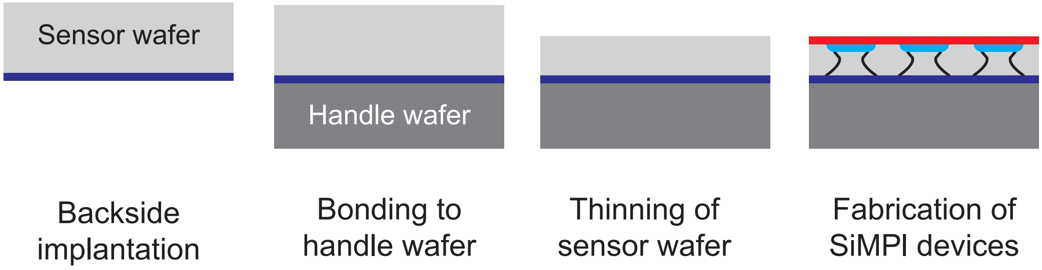

Figure 4.8: Fabrication process of SOI-wafer material and SiMPl devices. In a first step the backside of the sensor wafer is implanted. Subsequently, the sensor wafer is bonded to the handle wafer material and afterwards thinned down to the desired thickness. On this material the fabrication of the SiMPl device itself is performed. The wafer bonding process itself was carried out by industrial partners.

surface [84]. In combination with a structured p^+ top layer, this accumulation would lead to high lateral electric fields between the p^+ areas and the accumulated electrons in the intermediate gap regions (n-bulk), which can result in additional breakdowns (dark counts). In the SiMPl concept, the highly doped p^+ top layer is unstructured and covers the whole Si-SiO$_2$ interface of the device. The doping is chosen properly, so that the accumulation of electrons at the interface is negligible. Thus, the formation of high lateral fields caused by effects of surface radiation damage should be suppressed. The bulk damage is the same as for standard SiPMs but in the end the device can profit from the thin SOI material. Although the operation of irradiated devices is most probably limited by the increase of the dark count rate with the dose [137], it has to be taken into account that type inversion in the bulk can become an issue by using high resistivity wafers (bulk doping $\mathcal{O}(10^{12}\ \mathrm{cm}^{-3})$). According to Refs. [127, 138, 139], high ohmic silicon can tend to type inversion at lower equivalent doses, assuming otherwise identical bulk material (Czochralski or Float-Zone).

The drawbacks of the novel approach are basically limited to two facts. As shown in Eq. (4.2) in the previous section, the resistance depends on a parameter space of bulk resistivity, bulk thickness and cell dimension. Therefore, it is not possible to use standard wafer material with a thickness of ca. 450 µm due to bad resistor matching. Specific material is needed and requires modern wafer bonding technique or epitaxial growth of thin wafers. For the production of the SiMPl prototypes, the wafer bonding technique[3] was used to get the basic Silicon-on-Insulator (SOI) raw material. In Fig. 4.8, the production process for the SOI-wafers is illustrated. As an additional result of Eq. (4.2), it also prevents to produce devices with a significant change in cell size on the same wafer material. This would lead to either quenching problems (small resistance) or pinch-off. Again, the matching of the resistor requires a change of the thickness with the cell size.

The second drawback is the JFET-like behaviour of the internal resistor. The value of R_Q is a function of the overbias voltage at the internal anode and therefore the resistance changes during the recovery of the cell. This, in turn, will lead to an elongated recovery time of a micro-cell compared to conventional polysilicon resistors.

---

[3] The SOI technique was chosen because of the established technology in the laboratory. Epitaxial growth is a well established technology in semiconductor industry and is much easier and cheaper in comparison. Since doping levels in the order of $10^{13}\ \mathrm{cm}^{-3}$ become available, this technology could be the material of choice, in particular for small cell sizes [136].

It is therefore necessary to distinguish between the resistance value, which is responsible for the quenching of the avalanche and the resistance during the recovery process. The first is determined by the reduced lateral bulk depletion in the breakdown condition and corresponds to the smallest resistance value of the SiPM operation loop (cf. Fig. 2.10b). This value determines the current flowing after the avalanche breakdown and sets the limit for the maximum overbias voltage. Thus, a rather high resistor value would be preferred regarding passive quenching. While the cell is recovering, the depletion region in the bulk returns to its original shape, due to the change of the voltage at the internal anode. As a result, the resistance R_Q is increasing during the recovery and strictly speaking it is not correct to speak of a resistor in that case. This property complicates an exact analytical description of the resistance and is unfavourable in terms of a fast recovery time, since this would require small resistor values. Moreover, it leads to a time-dependent "time constant" and the recovery is different from a simple RC element.

5. Results

In order to demonstrate the feasibility of integrating the quench resistor of SiPMs into the silicon bulk, prototypes based on technology and device simulations have been produced. The aim was to specify and investigate basic technological process steps and to characterise the device parameters. The combination of simulations and measurements helps to understand the properties of the device and allows to draw conclusions for an optimisation.

For the novel SiPM approach, a proof of principle was achieved with a first prototype production (SiMPl 1), whereas a second prototype (SiMPl 2) allowed a full characterisation of the device. SiMPl 3 is a technology focussed test iteration on standard wafer material with the aim to improve device characteristics like dark counts and edge breakdown. In the following the results of the individual prototypes will be discussed in more detail.

5.1. First prototype

For the evaluation of the first test production, several pitch-gap combinations have been tested with TCAD simulations regarding quench condition and recovery time. On one hand, the resistance should allow an overbias voltage of ca. 5 V to maximise the trigger efficiency. On the other hand, pinch-off should be avoided and the recovery time of the cell should not exceed a maximum of a few µs. The thickness of the SOI-material was fixed to 70 µm. A summary of the room temperature simulations for several pitch-gap combinations, and a bias voltage which is set to 50 V, is plotted in Fig. 5.1. The dashed red lines in the plot illustrate the recovery time to 90% for the specific pitch-gap combinations. The solid black lines are associated with the maximum overbias voltage which can be applied to fulfil the 20 µA quench condition. In accordance with Eq. (4.1), an increase of the gap at a fixed pitch size corresponds to an increase of the resistance and thus a higher overbias voltage can be applied. In turn, the recovery time of the SiPM cell increases too. It is the same trade-off like for conventional devices but due to the JFET-behaviour of the SiMPl approach the problem is exacerbated (see Sec. 4.3). The results preferred a pitch size in the range of 120–140 µm with gap sizes in the range of 10–16 µm. These combinations allow overbias voltages in the range of 5 V, whereas the recovery time is around 2 µs. In order to investigate the limiting effects for operation and to take into account uncertainties in the simulations and inhomogeneities of the bulk doping, a variation of the pitch size between 90–160 µm in combination with varying gaps was chosen for the prototype production. Also a special pitch-gap combination with a pitch of 130 µm and gap of 20 µm was produced with the focus on achieving a working quench mechanism at high overbias voltages (high quench resistance).

For the layout of the micro-cells, a hexagonal shape has been chosen to allow a better approximation by the cylindrically symmetric simulations. The honeycomb arrangement of the cells is shown on the left hand side in Fig. 5.2. Within the top contact metallisation, which is located outside of the matrix, the whole array is covered by the common cathode implant (not shown for reasons of clarity) resulting in a free entrance window for light. An additional n-region (high field implant) outside of the matrix was added to compensate for

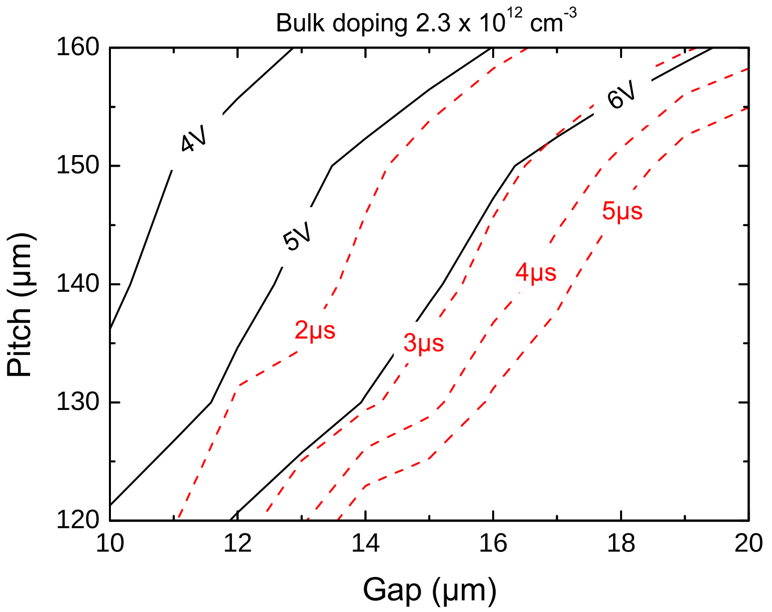

Figure 5.1: Summary of SiMPl prototype simulations for $N_B = 2.3 \cdot 10^{12}$ cm^{-3} at room temperature for pitch and gap size variations (pitch and gap as defined in Fig. 5.2). The bias voltage of the device was set to 50 V. The black solid lines in the plot indicate the maximum overbias voltage to meet a quench current of 20 µA whereas the red dashed lines specify the recovery time to 90% of V_{ob}. Results of simulations by Rainer Richter.

missing neighbouring cells at the edge of the device. However, the gap size at the peripheral areas differs slightly from the one within the array. For this reason, the lateral bulk depletion of cells at the edges is increased and thus cells behave slightly different. As shown on the right hand side, the different pitch-gap combinations are arranged in chip structures. Each chip has a dimension of 6 mm × 6 mm and contains a substructure of arrays of different size (single cells, arrays of 6, 19, 100 (10 × 10), and 900 (30 × 30) cells). In addition to the hexagonal shape, a few pitch-gap combinations of devices with square cells were fabricated as well.

Based on the results of the simulations, a production of first prototypes was performed [140]. For the preferred cell size of around 120–130 µm, the sensor wafer material from TOPSIL[1], with a bulk doping of ca. $2.7 \cdot 10^{12}$ cm^{-3}, has been chosen. The wafer bonding and the subsequent thinning to a thickness of 70 µm were done at ICEMOS[2]. With the resulting SOI material the production of the SiMPl devices was mainly performed in the semiconductor laboratory of the Max Planck Society.

The first step in the device production is the isolation of the silicon bulk with oxide. Afterwards the ion implantation of the internal anode (phosphorus implant) is performed. This process step requires high ion beam energies to achieve the necessary depth of penetration. In turn, this generates the most severe damage to the silicon crystal which has to be annealed by appropriate high temperatures, in order to reduce the defect density leading to a low dark count rate and less afterpulsing. However, high temperature scenarios affect the doping

---

[1] Topsil Semiconductor Materials A/S, Denmark

[2] Icemos Technology Ltd., Northern Ireland

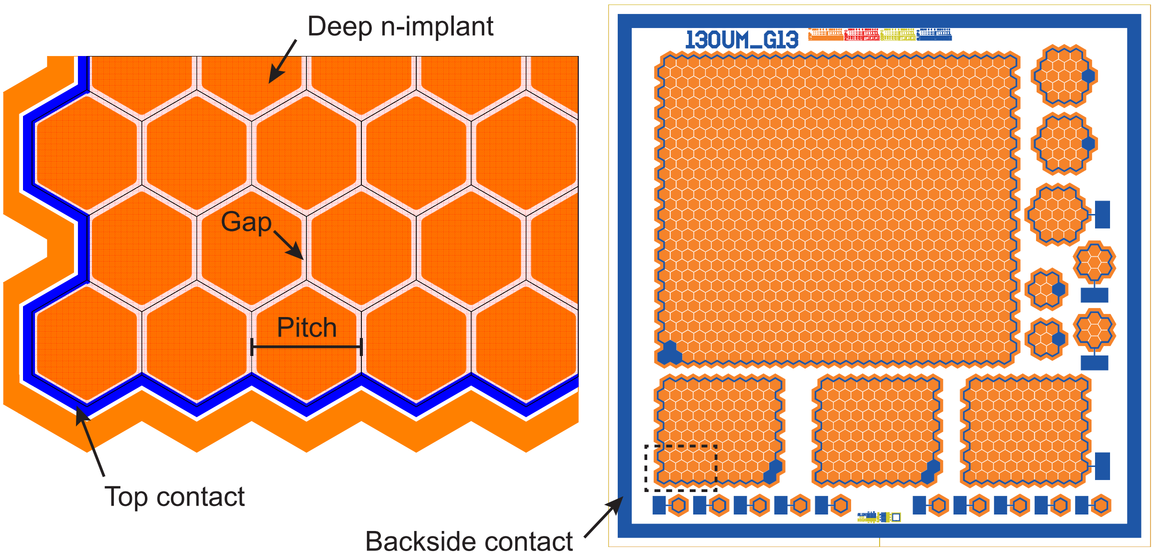

Figure 5.2: Layout for the prototype production of SiMPl. The hexagonal shape was chosen for a better approximation of the simulation results (cylindrical symmetry) to the produced sensors. The left hand side shows a magnified part of a 10 × 10 array with the deep n-implants (orange) and the metal contacts (blue), which are only located at the edge of the device. The common cathode (not shown) covers the whole area including the metal contact. The different pitch-gap combinations are arranged within chips which contain different sized arrays (right). The backside is contacted via the cutting edge of the chip. The lines appearing at the cell boundaries are just virtual lines drawn for clarity and do not appear in the masks.

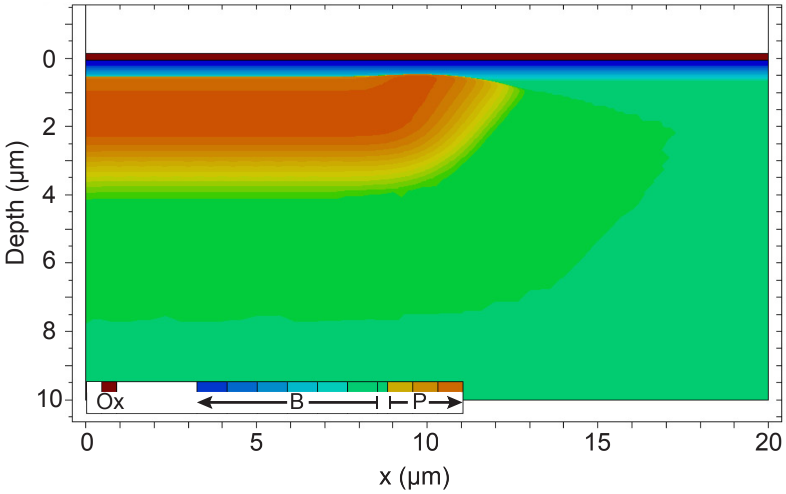

Figure 5.3: Doping profile of the final high field and gap region in the SiMPl production. Bluish colours correspond to the boron concentration (B) whereas phosphorus (P) is displayed by yellow to orange. The fabrication of the contacts is not shown in the simulation. The results are obtained using the DIOS tool.

profile by dopant diffusion, which has influence on the homogeneity of the electric field of the G-APD. During the implantation, the gap regions between the individual cells are covered by photoresist with a thickness of approximately 4 µm. The edge of the photoresist has an angle of roughly 60°. After the implantation the resist is removed and the wafer is annealed. The high field implant and the annealing were not done in-house, since the required equipment was not available at the semiconductor laboratory.

In the next step, the common cathode is formed with a shallow p^+ implantation of boron. Within the array no lithographic structuring is necessary, since the cathode is common for the whole matrix. After the second implantation, the structure is also annealed but at lower temperature and for a shorter amount of time. In a further mask step, the re-opening of the oxide at the positions of the contacts is realised. For the final metallisation, aluminium is sputtered and then structured. A doping profile of the final high field and gap region is depicted in Fig. 5.3.

Pictures of a processed six inch wafer are shown in Fig. 5.4. In addition to the SiPM chips, dedicated test structures for investigating the bulk doping and the quality of high field implantation are implemented as well. In particular, these are test diodes either processed with or without the deep n-implant. Some of the diodes without high field implant have a constant area of 1 mm^2 but different circumferences (4 mm, 5 mm, 8.5 mm, 16.25 mm) and can be used to determine the bulk leakage current.

The micrograph in the lower right demonstrates the advantage of the SiMPl approach. No metallic grid to contact the individual cells is necessary inside of the array due to the common cathode implant. Thus, free and unstructured entrance windows (here 4×4 mm^2) can be realised.

5.1.1. Characterisation of SiMPl 1

The characterisation of the first prototype production revealed diverse technological problems. Although the quality of this production was rather poor, it nevertheless allowed a proof of

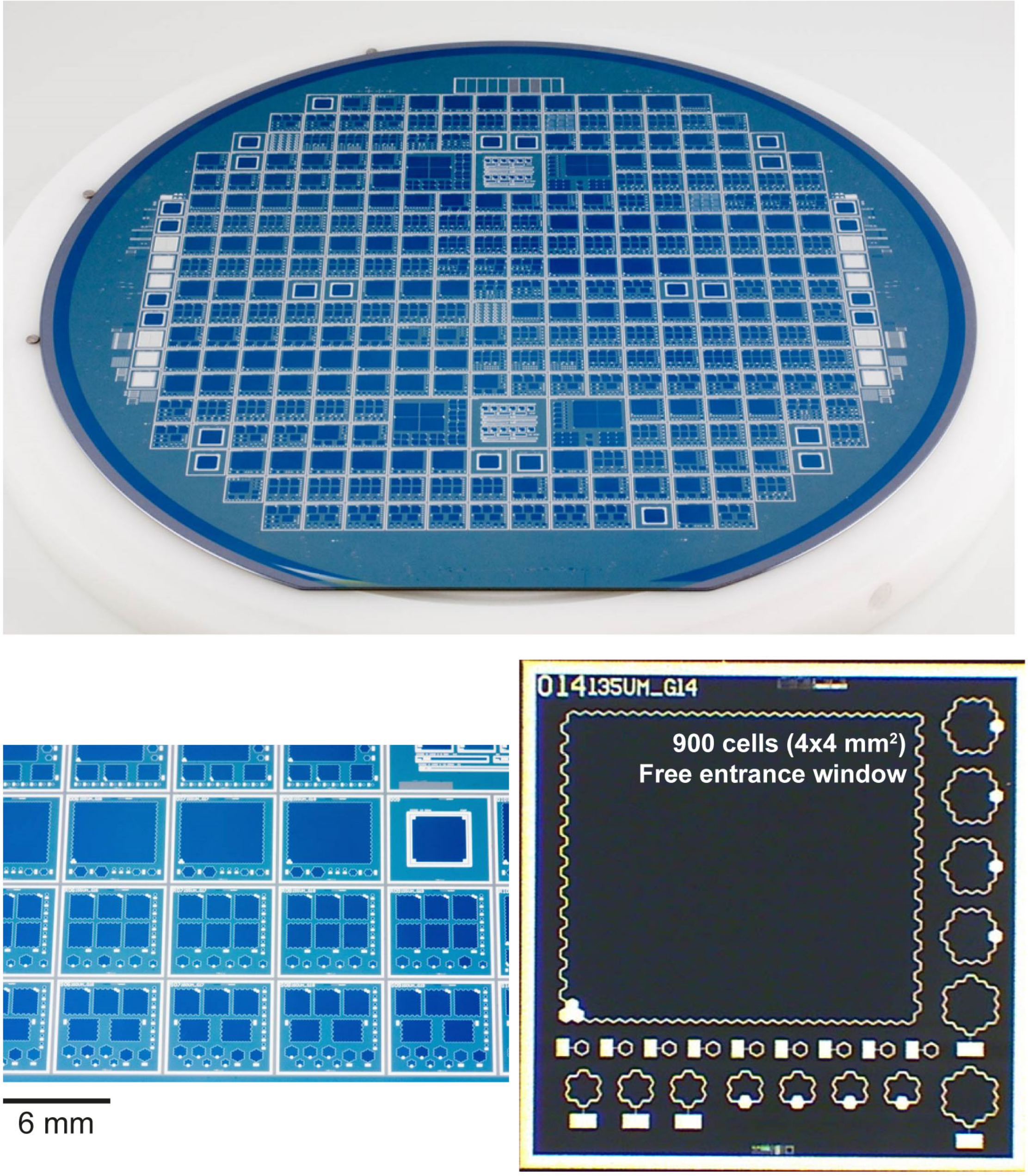

Figure 5.4: Picture of a SiMPl prototype. The devices were produced on a 6 inch SOI-wafer. Each chip of 6 mm × 6 mm contains one pitch-gap combination. Within one chip different array sizes from single cell up to 30 × 30 cells exist. The lower right picture shows a chip for a pitch of 135 µm and a gap of 14 µm. The arrays illustrate the free and unstructured entrance window with the metal contact only at the edge of the device.

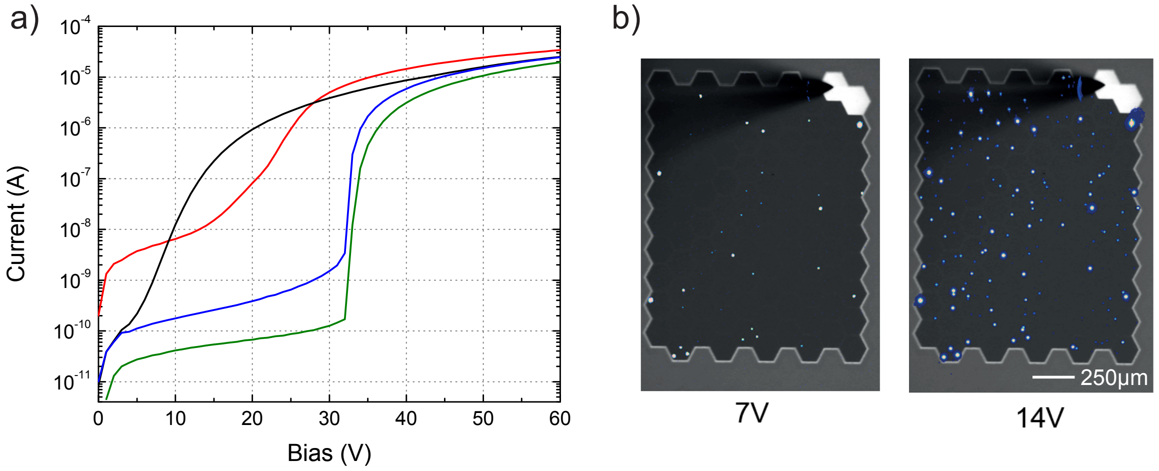

Figure 5.5: IV measurement of devices with a pitch of 120 µm. Different breakdown voltages due to technological problems in the fabrication process were obtained. For more details see text.

principle. In the following, the main results and conclusions from SiMPl 1 are described in more detail.

In order to get information about the leakage current and the breakdown voltage, measurements of the IV characteristics were performed on the wafer level. The influence of the high field implantation and the annealing process on the leakage current can be studied by comparing the current values of the previously mentioned test structures with and without a deep n-implant (see also Fig. 5.9). A significant increase of the current (up to 3–4 orders of magnitude) for the diodes with the high field implant was observed [140], which indicates problems concerning this process step. In order to distinguish between contributions from the bulk and the edges to the current, the test diodes with an area of 1 mm^2 and different circumferences were used. By extrapolating from the obtained leakage current results to a circumference of zero, a value of about 70 pA/mm^2 was determined for the contribution of the bulk. A detailed investigation of the influence of different annealing scenarios on the leakage currents was not possible because it could not be distinguished if the current is caused by the non-optimised annealing of the bulk damage or a surface contamination, which will be discussed below.

The technological problems also affected the functionality of the devices, as a measurement of the SiPM IV characteristics in Fig. 5.5a shows. The results can be divided into two dominant IV curves: devices with a breakdown voltage in the range of 30 V and devices which break down already at 10 V and below.

In combination with the SiMPl 1 results from the photon emission microscopy, which are shown in Fig. 5.5b, the following conclusions can be drawn: Particles, which were present on the surface during the deep phosphorus implantation, acted as shielding and led to local shallower doping profiles. This results in local peaks of the electric field which in turn cause point-like early breakdowns within the array at bias voltages around 10 V. Since the particle dimensions and densities vary, also the breakdown characteristics of these local peaks can vary. Thus, the surface contamination during the fabrication process explains the early breakdown of the SiPMs at very low bias voltages.

For devices with a breakdown voltage in the range of 30 V another effect is observed. The emission microscope pictures for those devices reveal increased emission of the edge regions

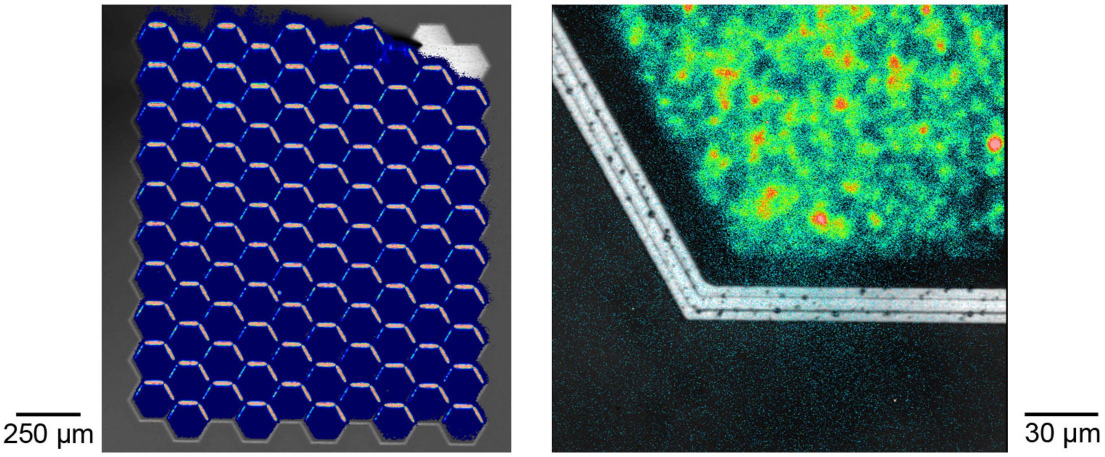

Figure 5.6: Emission microscope picture of SiMPl 1 with severe edge breakdown. The emission is dominated by the edge breakdown at two of the edges due to the tilt angle of the implant (left). On the right hand side a picture with a higher magnification is shown which illustrates that also the rest of the cell is emitting light but with lower intensity.

(see Fig. 5.6, left), which corresponds to a local maximum in the electric field and thus to a lower breakdown voltage compared to the inner part of the cell. Although, it was observed that at $V_{bias} = 40$ V the rest of the cell becomes active too, as illustrated on the right hand side in Fig. 5.6, the overall performance of the device is still dominated by the edge breakdown. It is striking, that only two sides of the hexagon show this effect. The reason can be found in the wafer orientation (tilt and rotation angle) during the implantation of the internal anode. The tilt angle indicates the angle between the ion beam and the wafer surface normal. For a complete description of the direction of the incident ion beam, the wafer rotation angle is necessary too. This angle is defined by the rotation of the wafer around its surface normal and is measured between the connecting line from the wafer centre to the primary flat and the plane containing the ion beam and the wafer normal (see Fig. C.1). Usually both angles are set to values, in which the direction of the incident ion beam does not coincide with a crystal axis in order to avoid ion channeling.

The doping profile in the edge regions depends on the relation of the tilt angle to the angle of the photoresist edge [93]. For this prototype, the internal anode was implanted with a tilt angle of 7°, while the angle of the resist was measured to be around 60°. In order to evaluate the influence on the electric field in the edge regions, the problem was simulated in the post processing phase with TCAD tools and the result is shown in Fig. 5.7. If the incident ion beam and the edge of the photoresist have opposite directions like in Fig. 5.7a, the ions penetrate through the thinner part of the resist edge which leads to a shift of the doping peak towards the wafer surface and thus towards the top boron layer. As a result of the higher doping concentration, the width of the depletion region in this area is reduced. This leads to a local maximum in the electric field which can result in early edge breakdown. On the opposite site of the hexagon which corresponds to the situation shown in Fig. 5.7b, the resist edge and the ion beam have the same orientation which results in a fast increase of the effective resist thickness in the edge region (shielding). Therefore, less dose is implanted in this region towards the surface and the peak concentration is significantly reduced in comparison to the previous case, with the result that no local field maximum is present in the edge region of

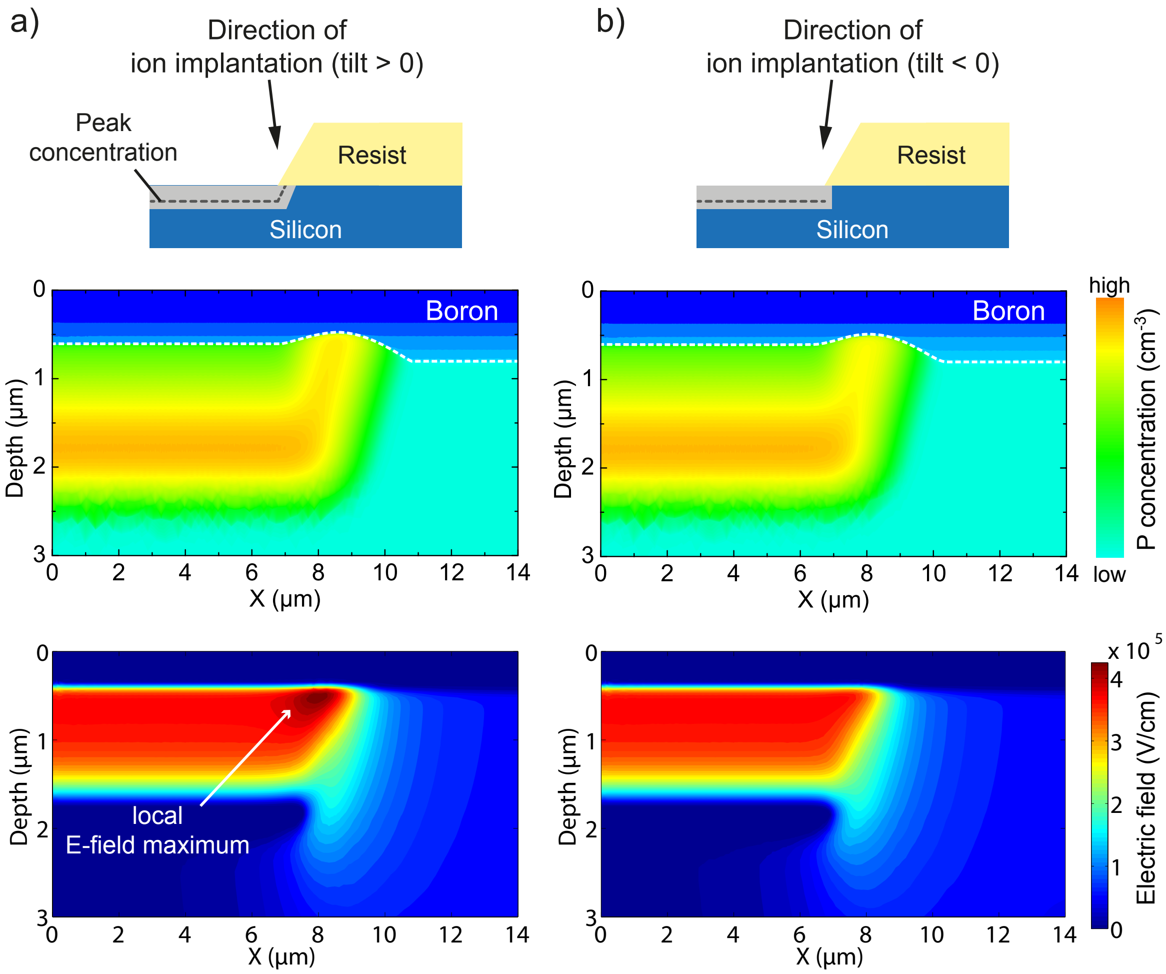

Figure 5.7: TCAD simulation results for a study of edge breakdown in SiMPl 1. The tilt angle of the phosphorus (P) implantation affects the doping profile in the edge region of the photoresist. a) if the tilt angle and the edge of the photoresist are in opposite direction, the resulting doping profile (centre) leads to a local maximum of the electric field (bottom). b) the implantation is additionally shielded in the edge regions due to the negative tilt angle. As a result, less dose is implanted and no peak in the electric field is visible. Thus, edge breakdown is related to the relative orientation of tilt angle with respect to the resist edge (see Sec. 5.3.1). The top blue regions in the centre plots are associated with the boron doping and the white dashed lines mark the junction to the n-region.

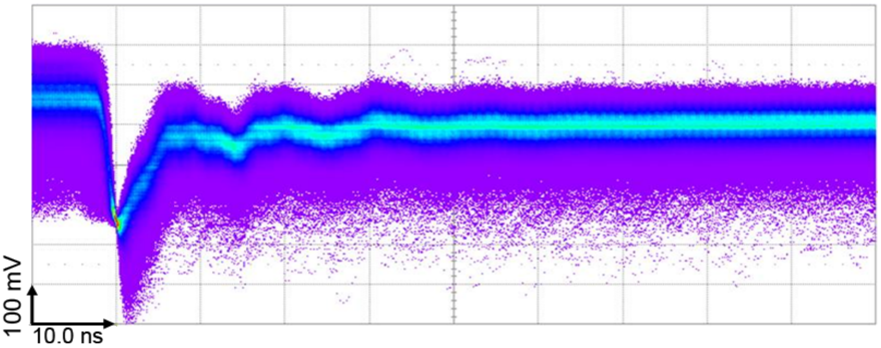

Figure 5.8: Proof of principle for quenching mechanism with bulk-integrated resistor.

the high field structure. Based on the results it can be concluded that the tilt angle has to be reduced in order to suppress the formation of electric field maxima.

As a result of the unforeseen technological difficulties concerning surface contamination and implantation, this prototype production did not provide any properly working SiPMs. Nevertheless, first pulses of the SiMPl approach were measured using devices with edge breakdown (Fig. 5.8), as it is not important for checking the quench mechanism where the avalanche is initiated. The persistence mode of the oscilloscope reveals the noisy characteristics of the first prototype by a distinct shift of the baseline. Nevertheless, the mean value demonstrates a clearly visible pulse shape with a working quench mechanism which can be taken as a proof of principle.

5.2. Second Prototype

With the experience from the first prototype production, solutions to improve the technology were elaborated. In order to avoid the spot-like early breakdowns special attention was paid to the surface cleanliness before the high field implant and as a measure against edge breakdown the tilt angle for the second prototype production was changed to $(0 \pm 2)^\circ$. A modification of the photoresist angle required a longer optimisation of the technology and the installation of new equipment. Furthermore, DIOS simulations revealed that a tilt angle of 0° could solve the problem even with a 60° photoresist angle. Therefore, a change of the resist angle was not applied in the second prototype. All other parameters as well as the layout were the same as in the production before. It should be mentioned that the high field implantation and the subsequent different annealing scenarios were not performed at the semiconductor laboratory. Thus, the exact parameters, especially for the annealing, were not under control.

First tests showed that the surface contamination problem was solved. The IV characterisation of the SiMPl 2 test diodes was used to preselect the different annealing scenarios for further characterisation. In addition, the wafers were tested for edge breakdown with the emission microscope. The IV characteristics of the test diodes as well as an emission microscopy measurement are shown in Fig. 5.9, in order to illustrate the improvements compared to SiMPl 1. The wafer with the hottest and longest annealing turned out to be the most promising candidate regarding the IV curves. The diode current after the high field implant is comparable to the diodes without. The breakdown voltage is in the expected range of 36 V. Additionally, the devices of this wafer showed the best results with respect to edge breakdown. Therefore, this wafer was chosen for further characterisations and in the follow-

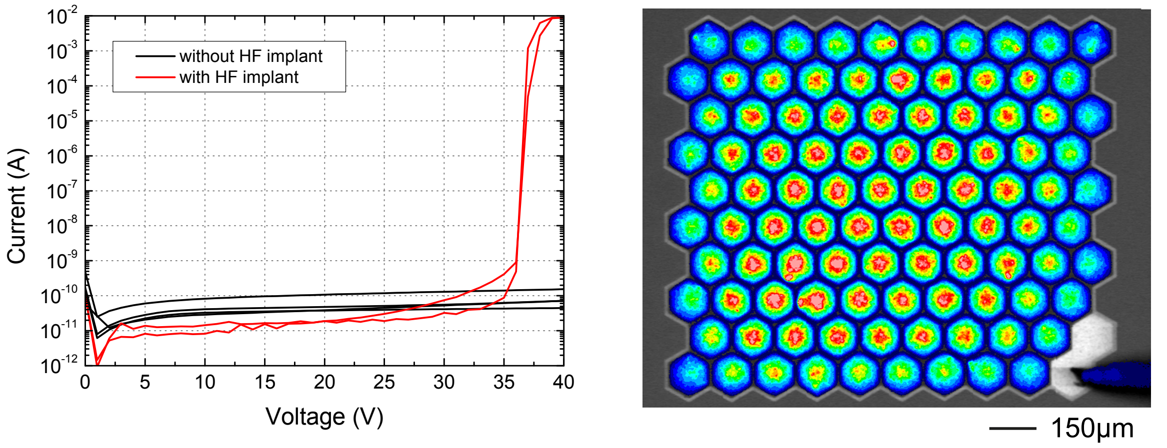

Figure 5.9: IV characteristics and emission microscopy measurements for test diodes of the second prototype production. The leakage current level of the diodes with HF implant is comparable to diodes without. The plot shows the results for the hottest and longest annealing. For comparison with SiMPl 1, an emission micrograph of the same wafer is shown on the right hand side as well. A homogeneous emission over the high field region without edge breakdown is observed.

ing all presented results are based on measurements of devices from this wafer. However, it should be mentioned already at this point, that the high dark count rate at room temperature (see Sec. 5.2.3.4) prevented a reasonable operation of the devices without cooling.

5.2.1. Detailed simulation of SiMPl 2

The main difference between conventional SiPMs and the SiMPl approach is the integration of the quench resistor into the silicon bulk. As a result, the resistance is defined by the resistivity and the thickness of the SOI wafer material, the size of the individual cells as well as the sidewards depletion from the gap regions. This initially large parameter space is reduced by requirements on the IV curve of the resistor concerning the capability to quench the avalanche and the recovery behaviour of the cell.

The capability of quenching the avalanche is given by the current flowing through the device after the breakdown. If the current exceeds a value of approximately 100 µA, the avalanche is no longer quenched by statistical fluctuations. As reported in Refs. [101,113,141,142], also the time for quenching the avalanche increases with approaching this current level from below. Cova stated as a rule of thumb a value of 20 µA to be safe on quenching [101]. Therefore, the resistance R_Q defines the maximum overbias via Eq. (2.32). Taking into account the voltage dependence of the trigger efficiency, the resistance should be designed to allow a maximum overbias of $V_{ob} \approx 0.15\,V_{bd}$ without $I_f > 20$ µA, in order to be able to achieve a high PDE without quenching problems.

In contrast to the proof of principle studies, which were performed with TeSCA assuming a bias voltage of 50 V and operation at room temperature, the detailed simulations of the SiMPl 2 prototype were implemented with the TCAD tools of Synopsys. The simulations allow to check and further optimise the predictions for the device properties by comparing the results with measurements (e.g. at $V_{bias} \approx 37$ V). As already mentioned in Sec. 3.1, Synopsys offers the opportunity to use MC tools for the implantations taking into account channeling effects which result in more realistic doping profiles, as well as an easier access to the characteristics of the internal anode, especially for transient simulations. Since the production of the prototypes was not entirely done at the semiconductor laboratory, not all parameters have been under control. Thus, for this parameters the technology simulations have been implemented with best possible assumptions. However, they can differ from reality which results in deviations in the doping profiles influencing other parameters too.

Because of the necessity to cool the SiMPl 2 devices for measurements and the fact that they were designed for room temperature operation, the influence of the change in the mobility with temperature was considered in the new simulations as well. The dependency for common silicon around 300 K is [143]:

$$\mu_e \propto T^{-2.4} \qquad \text{and} \qquad \mu_h \propto T^{-2.2}. \tag{5.1}$$

Since the depletion of the bulk depends on the applied bias voltage, the temperature dependence of V_{bd} was also taken into account in the simulations and adjusted to the values obtained from measurements.

All generation-recombination processes, except for SRH were disabled in the simulations. In particular, the deactivation of electron-hole pair generation due to impact ionisation (avalanche) is necessary in order to avoid a constant avalanche current in the device and to realise the meta-stable condition at bias voltages above breakdown.

5.2.1.1. Stationary simulations

The study of the IV curves with respect to the parameter space was performed with the devices with auxiliary contacts by using different combinations of pitch, gap, and temperature. For illustration the basic sequence is plotted in Fig. 5.10a. In order to simulate the current after the breakdown as a function of the overbias voltage, the device was put in an initial state by applying 0 V to the cathode and V_{bd} to the anode and the auxiliary contacts R1 and R2. Afterwards, the voltage at the anode and R2 is simultaneously increased while R1 is kept at V_{bd}. This corresponds to the situation of a fired cell at different bias voltages, taking into account the change of the depletion region in the bulk. For the IV curve of the quench resistor, the current between R1 and the anode is recorded as a function of the anode voltage which corresponds to $I(V_{ob})$. As a general result, the non-linear behaviour of the quench resistor, unlike for standard resistors in conventional SiPMs, can be observed (Fig. 5.11a). As already mentioned in Sec. 4.1 the behaviour is similar to that of a JFET with a changing resistance depending on the different potentials at the nodes (cathode, anode, internal anode). The accurate shape of the IV curve strongly depends on the dimensions of the non-depleted volume in the bulk which, in first order, is defined by the pitch, the gap and the geometrical shape of the cell. Further influences arise from second order effects like temperature dependence of the mobility and bulk doping variations.

The second important characteristic is the recovery time of the cell. Since the time constant is given by the product of the quenching resistor and the cell capacitance, a small resistance is needed for a fast recovery. In turn, this would result in a device which cannot be operated at a high overbias as discussed in the last paragraph. By inspecting the IV curve from the stationary simulation, it is already possible to rule out some pitch-gap combinations due to the pinch-off effect. In this case the recovery would be dominated by thermal generation and would therefore last several µs up to ms. Additionally, the applied voltage would already drop across the depleted bulk and result in a reduced V_{bias}. To estimate the recovery time

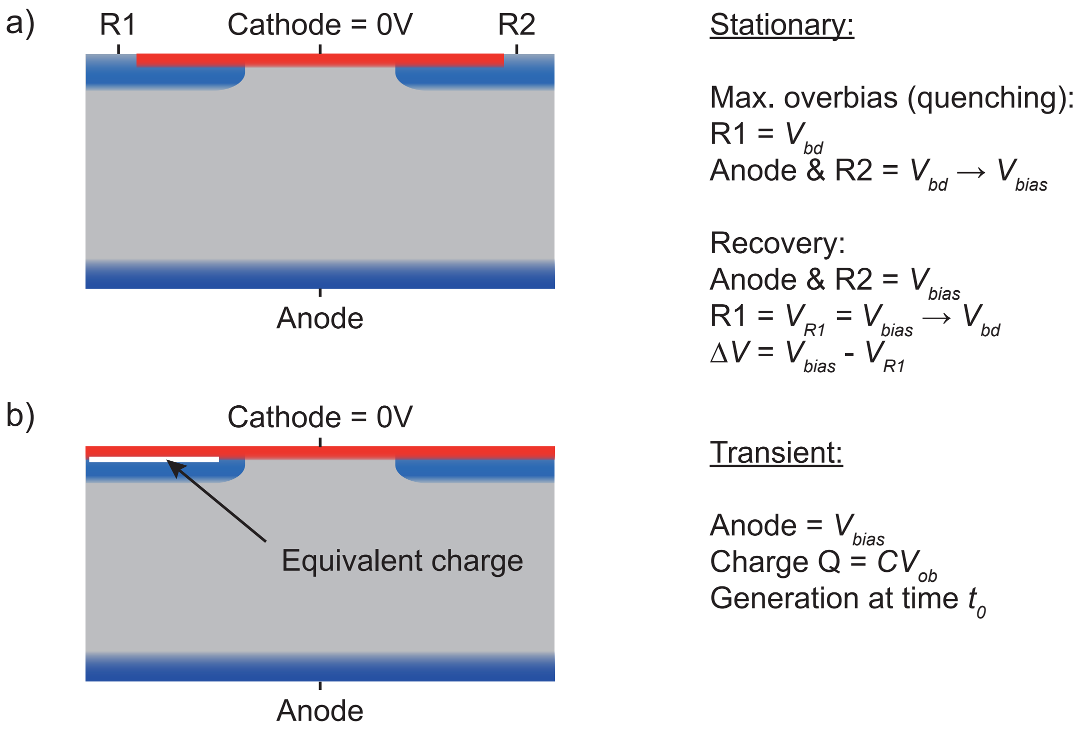

Figure 5.10: Sketch for the basic sequences of stationary and transient TCAD simulations of the prototype. In the stationary simulations (a)) the maximum overbias can be estimated with the IV behaviour between R1 and the anode at different bias voltages with the quenching condition by Cova [101]. The IV curve during the recovery at a fixed overbias can be simulated too which allows to determine the recovery time (see Eq. (5.2)). The transient simulations allow to simulate the recovery time and the signal output of the cells as a function of time. A charge which is equivalent to the avalanche is generated within the high field region (b)).

the stationary simulation of the IV characteristic has to be slightly modified. The anode and the auxiliary contacts R1 and R2 are set to a fixed bias voltage V_{bias} while the cathode is set to 0 V. To obtain the IV curve during recovery, the potential of contact R1 (V_{R1}) is decreased to V_{bd} and the current $I(\Delta V) = I(V_{bias} - V_{R1})$ between R1 and the anode is simulated (see also Fig. 5.10a). Since the depletion region in the bulk is different for every bias voltage a different IV curve, and thus recovery time, for every overbias is expected. Results for three different overbias voltages are shown in Fig. 5.11b.

With the resulting IV characteristics the recovery time can be estimated by using the displacement current relation

$$I(\Delta V) = \frac{dQ}{dt} = C_D \frac{dV}{dt}. \tag{5.2}$$

$I(\Delta V)$ and the diode capacitance C_D are known from the simulations. Thus, the time for a small voltage step dV at a given $I(\Delta V)$ can be calculated using Eq. (5.2). The summation of all voltage steps to a recovery of 90% ($\equiv 0.1\Delta V$) of the overbias voltage allows to estimate the recovery time of the cell from the static IV characteristics. For infinitesimal steps, it can be written as

$$\tau_{rec} = \int_{\Delta V}^{0.1\Delta V} C_D \frac{dV}{I(\Delta V)}. \tag{5.3}$$

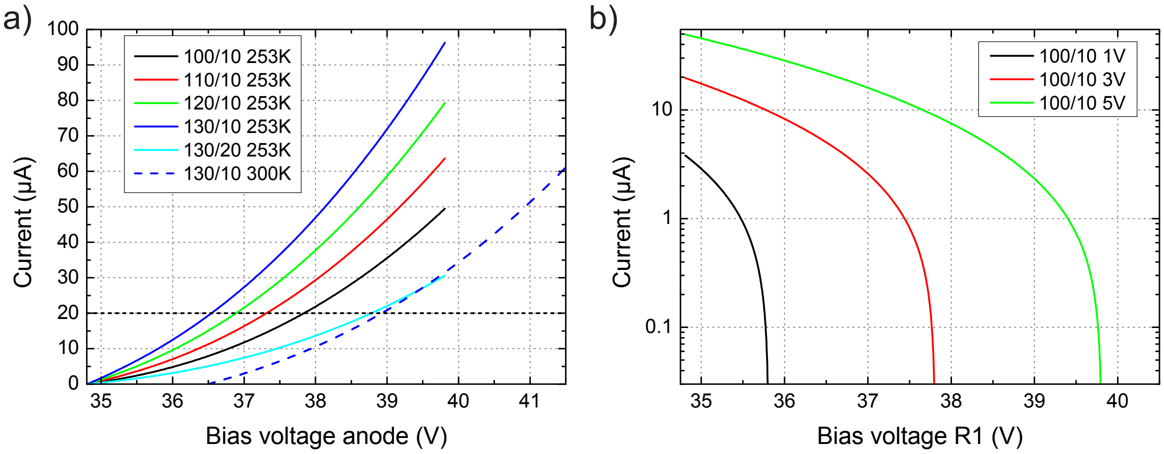

Figure 5.11: IV characteristics obtained from the static simulations. The JFET-like IV curves for different pitch-gap combinations are plotted in a) up to an overbias voltage of 5 V (V_{bd} = 34.8 V). The maximum overbias is estimated by meeting the quench condition of 20 µA [101]. The influence of the temperature on the shape of the IV curve and the breakdown voltage is illustrated as well (dashed line). In b) the IV curves of one combination are shown for three different operating voltages. Since the depletion region depends on the external bias voltage, the IV characteristics slightly differ. These curves were used to calculate the recovery time of the cell according to Eq. (5.3).

Since there is no accurate analytic expression for $I(\Delta V)$, the recovery time was calculated via numerical integration with a fixed voltage step of $dV = 1$ mV.

The different devices were investigated concerning the overbias voltage at a current of 20 µA and the recovery time versus the overbias voltage. The results of the simulations are discussed with the measurement results in the respective subsections.

5.2.1.2. Transient simulations

For the transient simulation the real structure without auxiliary contacts is used (see Fig. 5.10b). Since the calculations in the TCAD tools are based on carrier densities, the statistic process of the avalanche quenching cannot be simulated with an activated avalanche generation (see also Sec. 3.1.3). As a solution to this problem, the generation by impact ionisation is disabled and a charge (electron-hole pairs), which is equivalent to the product of the diode capacitance and the applied overbias (according to Eq. (3.10)), is generated inside of the depletion region of the SiPM cell within a period of a few picoseconds based on a Gaussian time distribution (σ = 2 ps). This time scale is comparable to the build up time of an avalanche breakdown in a G-APD [102]. The approach of a locally and temporally limited charge generation corresponds to an avalanche breakdown with subsequent quenching.

During the transient simulation, the currents at the external contacts and the potential of the internal anode are recorded as a function of time. This allows to obtain the signal output of the SiPM, the recovery time of the cell and extracting of parameters like C_D, which is important to estimate the gain and the recovery time of the individual cells, and the coupling capacitance C_Q which defines the signal strength of the G-APDs and is therefore related to the requirements on amplifiers.

C_D can be obtained from the ratio of the generated charge (electron-hole-pairs) and the resulting voltage drop V_{IA} at the internal anode. The maximum of V_{IA} corresponds to the

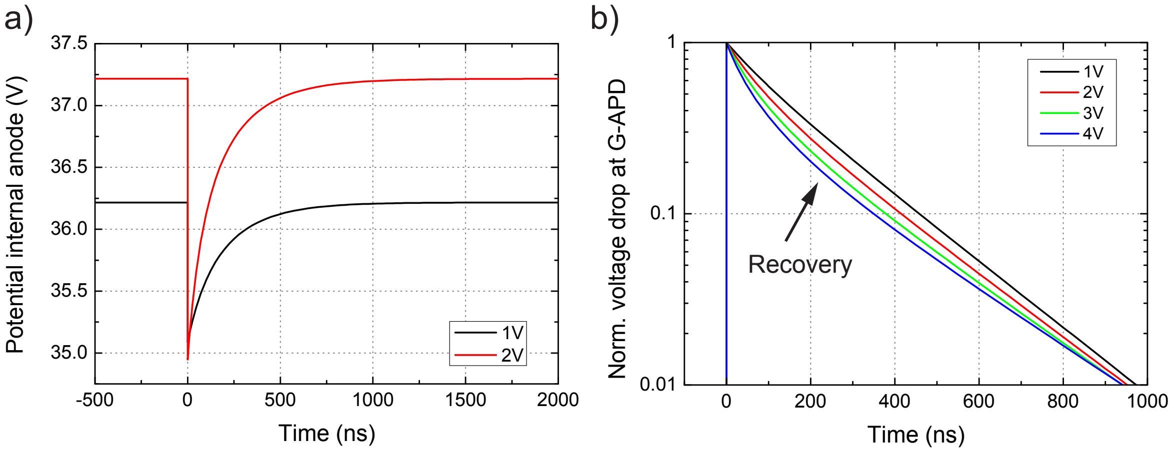

Figure 5.12: Results for the internal anode potential obtained from transient simulation. In a) the potential at the internal anode of the G-APD is plotted as a function of the time for two different voltages ($V_{bd} \approx 34.9$ V). At the avalanche breakdown the voltage at the internal anode drops and starts to recover once the avalanche is quenched (full equivalent charge is generated). b) shows the relative voltage difference between V_{bias} and the potential at the internal anode. This allows comparison of the recovery time to 90% for different V_{ob}. The influence of the JFET behaviour is visible since the recovery of standard RC elements would result in a straight line in a semilogarithmic plot.

applied overbias voltage V_{ob}. The coupling capacitance can be determined by integration of the displacement current signal $I(t)$ at the external contact over time. The charge within approximately the first nanosecond after the avalanche corresponds to the known voltage drop V_{IA} at C_Q. The discharge of this capacitance is associated with the fast contribution in the pulse shape of the SiPM (cf. Fig. 5.24). The recovery time is measured by looking for the time stamp when 90% of the overbias at the internal anode is restored. As mentioned in Sec. 3.1.2, the device simulation of Synopsys allows to log the potential at the internal anode and thus the recovery time can easily be determined. Fig. 5.12a shows the time curve of the potential of the internal anode for two different overbias voltages. The breakdown voltage in both cases is around 34.9 V and the avalanche breakdown occurs at $t = 0$. The recovery of the cell is clearly visible. Since the IV curve shows a non-linear behaviour (JFET) and the depletion region in the bulk depends on V_{bias}, the recovery time of SiMPl – in contrast to the standard RC-circuit in conventional SiPMs – is a function of the overbias voltage and does not meet the simple exponential decay ($\exp(-t/\tau_{rec})$). In order to compare the recovery time for different overbias voltages, each voltage drop $V_{IA}(t)$, which is calculated from the time-dependent electrostatic potential at the internal anode, is normalised to one and the time at the 10%-level crossing is recorded (equivalent to a 90% recovered cell). This is illustrated in Fig. 5.12b, where the normalised voltage drop over the avalanche diode is plotted as a function of the time. The deviation from a standard RC element is already implicated by the non-linearity of the recovery in the semilogarithmic plot. The shape of the curves indicates as well that the recovery time to 90% decreases with increasing overbias voltage. This is caused by the JFET-like behaviour and the change of the bulk depletion with the potential at the internal anode. The voltage drop results in a decrease of the depleted volume and thus a smaller resistance. During recovery the depletion region is restored to its initial dimension and the resistance increases again. The curves come close again at 99% which is also due to

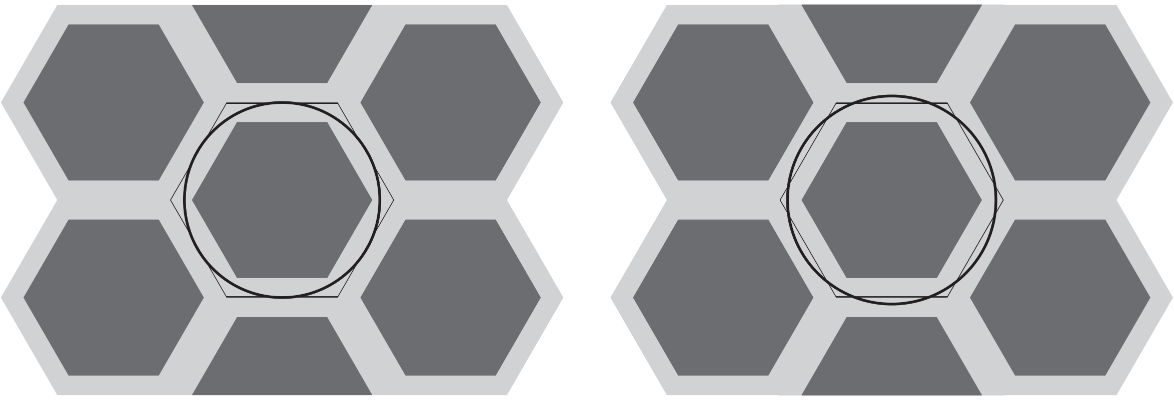

Figure 5.13: Illustration of the different simulation regimes (left: in-circle approximation, right: equivalent area approximation) used for the quasi-3-D device simulations.

the fact that the depletion region depends on the bias voltage. Looking at the static IV curves it is obvious that in the beginning of the recovery the current is larger for higher overbias. For the last 10% the initial depletion region, which is larger for higher overbias voltages, is dominant leading to a higher resistance in comparison.

5.2.1.3. Geometrical considerations

As already mentioned in the proof of principle studies, a hexagonal shape was chosen for the main cell structure since it allows a better approximation with the quasi-3-D cylindrical simulations. The two different approximations used for the simulations are highlighted in Fig. 5.13. The in-circle approximation corresponds to the pitch definition of the layout as shown in Fig. 5.2 but underestimates the area of the cell and thus C_Q and C_D, whereas the cylindrical approximation with the equivalent area of a hexagon does not[3]. As will be shown in the results of 3-D simulations, the drawback of the latter approach is the underestimation of the bulk resistor, which is more complex to correct for. The area ratios of the different approximations compared to the hexagonal cell (A_{hex}) are (cf. Eq. (5.7)):

$$\frac{A_{in}}{A_{hex}} = \frac{\pi}{2\sqrt{3}} \approx 0.907, \qquad \frac{A_{eq}}{A_{hex}} = 1, \tag{5.4}$$

where A_{in} is the area of the in-circle and A_{eq} the equivalent area.

In order to study the influence of the geometrical shape of the cell, first real 3-D simulations of SiMPl structures have been implemented. For reasons of comparison three different shapes have been studied: a cylindrical cell (in-circle and equivalent area) to get a comparison to the 2-D results, a hexagonal cell to see the difference in prototype devices from cylindrical approximation, and a square cell. In all simulations the characteristics of the SiPM cell have been studied in the presence of neighbouring cells in the array. To be able to simulate the quasi-stationary IV curve, in order to obtain the dependence on the geometrical shape, the same approach with the auxiliary contacts was used. The main focus in this investigation is the influence of the geometrical shape on the depletion region in the bulk which defines the quench resistor and therefore affects the recovery time and the maximum overbias. To

---

[3] In the real layout the corners of the hexagon are rounded which slightly decreases the area compared to an ideal hexagon.

reduce the processing time, the simulation regime was minimised according to the symmetry of the devices. Therefore, usually only a quarter of the full structure was used and the results obtained from the simulations have to be scaled to the full device dimension afterwards.

The simulation covers the same pitch for all devices. Hence, the pitch size of the cylindrical approximation corresponds either to the in-circle ($A_{cyl,in}$) or the same area ($A_{cyl,eq}$) of the hexagon, whereas the hexagon (A_{hex}) and the square (A_{sq}) cells have the same pitch as defined in the layout. Thus, they differ in the area and scale as follows:

$$\frac{A_{cyl,in}}{A_{hex}} = \frac{\pi}{2\sqrt{3}}, \qquad \frac{A_{cyl,eq}}{A_{hex}} = 1 \qquad \text{and} \qquad \frac{A_{sq}}{A_{hex}} = \frac{2}{\sqrt{3}} \approx 1.15 \tag{5.5}$$

A simulation result of the 3-D hexagonal and square structure is shown on the left hand side in Fig. 5.14. The graph depicts the electron density distribution in the bulk close to the bulk doping level of $N_B = 2.7 \cdot 10^{12}$ cm^{-3}, which in turn corresponds to the plotted isosurface. The depletion region expanding from the gap regions into the bulk is clearly visible. The right hand side in Fig. 5.14 shows a cross-section of the electron distribution at a depth of 10 µm (illustrated by the white lines) for a device with cylindrical shape (in-circle) and the hexagonal and square structure, respectively. Although small deviations are visible, the cylindrical in-circle approximation is in good agreement to the hexagonal cell shape, whereas the difference to the square cell shape is clearly visible. This is even more evident by comparing the IV characteristics of different shapes, which are plotted in Fig. 5.15 as a function of the bias voltage of the auxiliary contact R1 (corresponds to the potential at the internal anode). The purpose of this comparison was to check the accuracy of the quasi-3-D simulations in cylindrical symmetry. Real 3-D simulations are time consuming and require a lot of computational power and are therefore not suitable for comprehensive parameter studies. From the results obtained by the 3-D simulations, it can be concluded that the hexagonal structure is better described by the in-circle approximation (Fig. 5.13). In contrast, the results assuming an equal area in the cylindrical approximation seem to overestimate the current flowing through the resistor after a breakdown event. They are apparently closer to the square cells although the area of the square cell is again larger than the hexagon one.

For a cross-check of the results, the in-circle structure was simulated in two and three dimensions. The result is also plotted in Fig. 5.15 and it can be observed that both IV curves coincide with an uncertainty in the range of 1%. Consequently, the IV characteristics of the hexagonal structures are well described by the in-circle approach in the quasi-3-D simulations. However, the area of the high field region is smaller, according to Eq. (5.4). Thus, the values of the capacitances obtained from transient simulations have to be scaled by a correction factor which takes into account the different areas. This approach is preferable to the equal area approach, since the scaling of the capacitance is more accurate than correcting for the difference in the IV curves, which shows a strong dependence on several parameters as mentioned in Sec. 4.1. Therefore, the quasi-3-D in-circle approximation was applied for the studies of the hexagonal cells.

5.2.1.4. Model comparison and parameter variations

The high field implantation was calculated with MC tools as well as the analytical model of DIOS to be able to investigate possible differences. Besides the model of the implantation, both structures experienced the same processing in terms of energy, ion density and annealing scenario. Afterwards, stationary and transient simulations have been performed, as previously

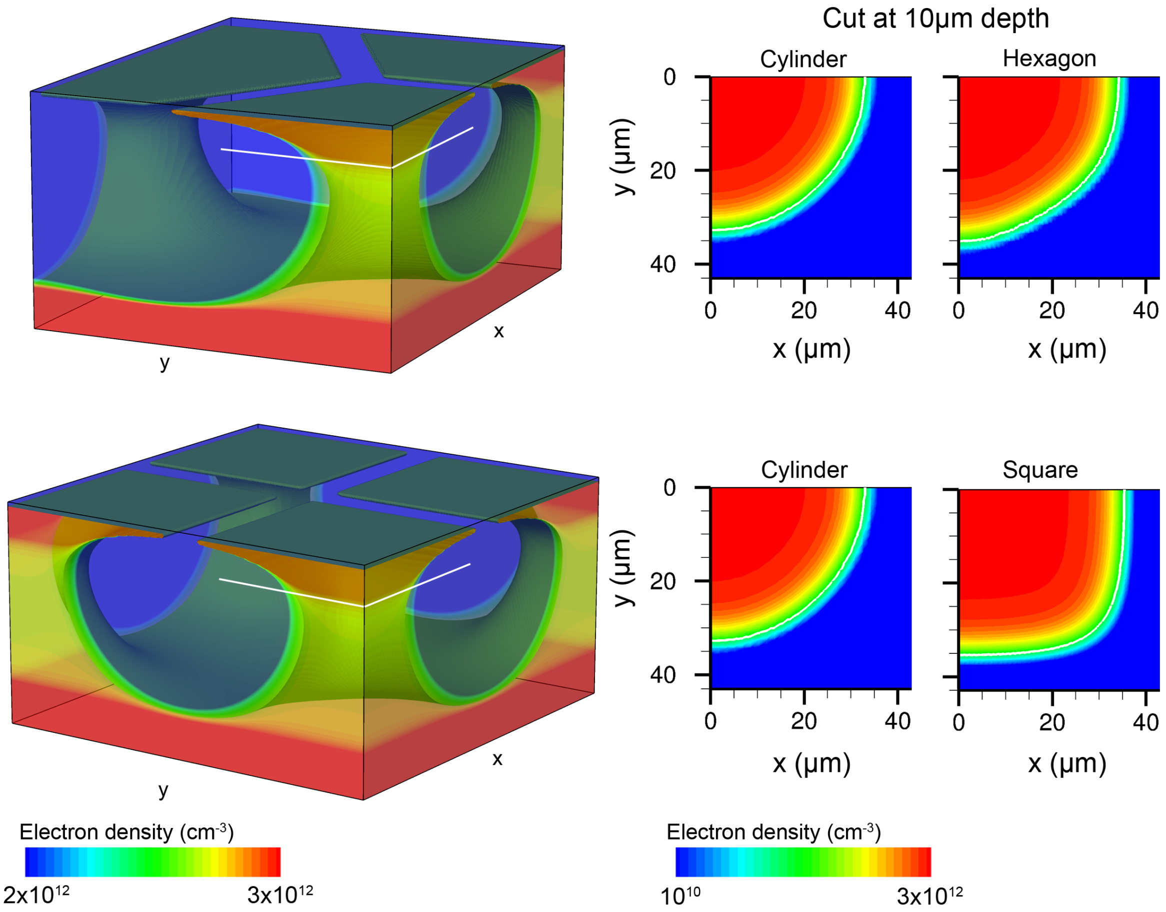

Figure 5.14: Comparison of real 3-D simulations of hexagonal and square micro-cells with the cylindrical approximation. In all graphs the electron density is shown. The isosurface on the left plots corresponds to the bulk doping level. On the right hand side a cut of the hexagonal and the square structure is shown at a depth of 10 µm in comparison to the cylindrical structure. For the hexagonal devices the cylindrically symmetric approximation seems to be legitimate.

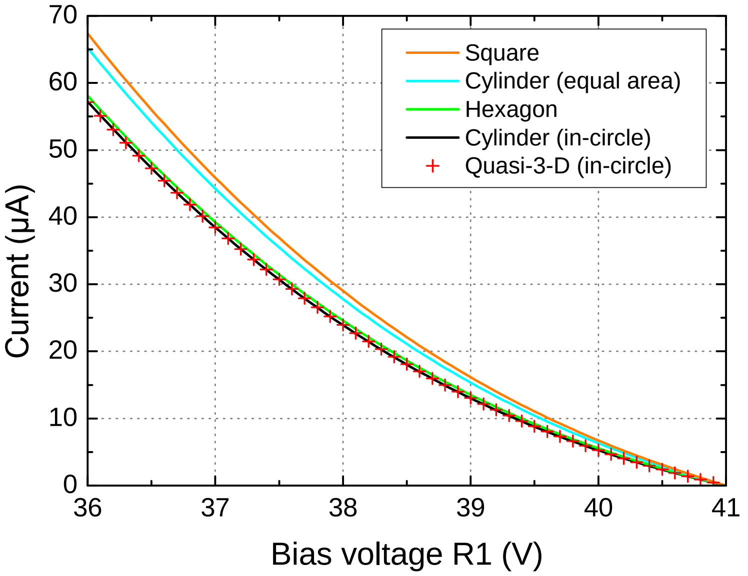

Figure 5.15: Comparative TCAD study of the geometrical shape with respect to the IV characteristics. The bias voltage of the device was set to 40 V whereas the internal anode is ramped from 36 V to 40 V. The in-circle cylinder approach seems to be a good approximation of the hexagonal cell structure, whereas the equal area results in an overestimation. The in-circle structure was also simulated in quasi-3-D, in order to cross-check reliability and comparability of the 3-D results. 2-D and 3-D simulations fit within an uncertainty of approximately 1%.

described, to investigate differences in the electric field distribution, breakdown voltage, diode capacitance, recovery time, etc.

Fig. 5.16 shows a 1-D comparison of the two implantation models with respect to the net doping concentration and the resulting electric field. From the doping profiles it is apparent that the concentration in the diffusion tail towards the bulk for the analytical DIOS model is less compared to Monte Carlo. By taking into account the channeling process in the MC model, a part of the doping concentration is shifted to deeper values and thus missing in the peak value (see also Sec. 5.3.1). This difference in the doping profile leads to a change of the depletion width and thus affects other parameters as can be seen in the electric field. The width of the depletion region is defined by the doping concentrations in the n- and p-region. Since the concentration of donors for DIOS is slightly higher, the depletion width is smaller which leads to an increased electric field at the same bias voltage as well as to a larger capacitance. The change in the electric field distribution in turn results in a change of the breakdown voltage since the ionisation integral is changed as well (see Eqs. (2.28) and (2.29) as well as Fig. 5.44).

The parameters of the diode capacitance and the recovery time can be determined by the analysis of the dynamic and stationary simulation results as described above. For illustration, a few representative parameters are shown in Table 5.1. Comparing the capacitances of the G-APDs, a deviation of about 3% is observed which can be explained by the difference in the doping profiles as mentioned above. From the simulations a depletion width of ca. 1.44 µm

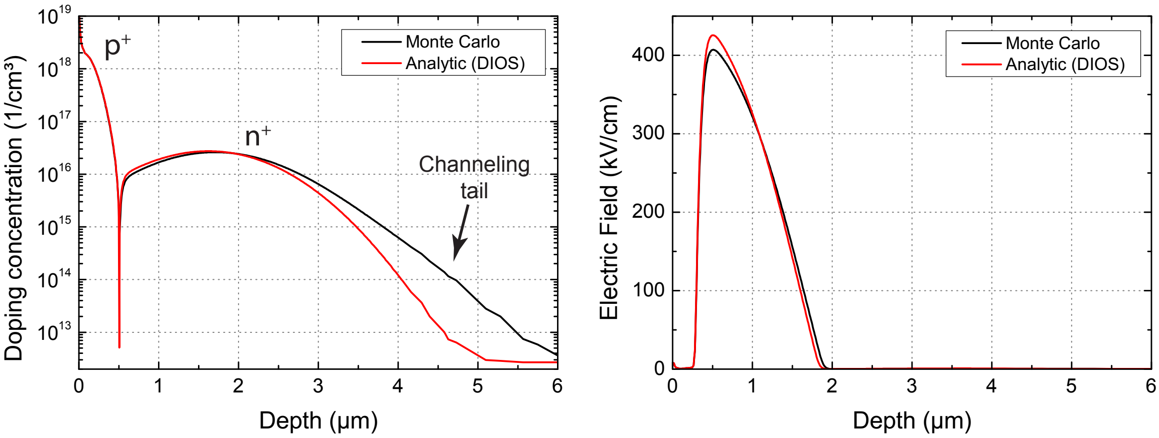

Figure 5.16: Net doping distribution and electric field obtained from TCAD simulation at the same bias voltage $V_{bias} = 40$ V. The left graph shows a comparison of the distribution of the doping concentrations resulting from the MC model (black) and the analytical model in DIOS (red). Due to the channeling, taken into account by the MC method, the doping level at higher depths is increased. In turn, the concentration is lower in the area of the pn-junction. This affects the electric field distribution which is plotted on the right hand side. The difference of the electric field as a function of the depth caused by the different doping concentrations is visible. The electric field has also influence on other parameters like breakdown voltage, Geiger efficiency, etc., as discussed in the text.

(DIOS) and 1.48 µm (MC) can be estimated. The values for the coupling capacitance C_Q showed no significant change with the different models.

In addition to the capacitance, the channeling tail also has significant influence on the recovery time. First, it can be seen that for both models the values correlate with the pitch-gap combination, since the remaining non-depleted bulk volume, which defines the resistance, depends on the pitch/gap ratio. By comparing the simulation results of both models, it can be observed that the values for the DIOS-based profile are larger. The reason for this behaviour can be found by taking a look at the sidewards depletion in the bulk for both cases, shown in Fig. 5.17. The expansion of the depleted area based on the DIOS implant is larger than for the MC profile. This effect can be traced back to the higher doping concentration in greater depths due to channelled dose. The increased donor concentration in the channeling tail shields the sidewards depletion from the gap region according to Eq.(2.15) and results in a smaller depleted area and thus a smaller quench resistance. This, in turn, leads to a faster recovery time of the cell. In general, devices which are approximating pinch-off (100/10 and 130/20) result in a higher model dependency, since the electron density in the non-depleted region, which forms the vertical resistor, gets affected by the sidewards depletion and may start to be slightly reduced. Thus, not only the cross-sectional area is decreasing but also the effective bulk doping which results in an additional change in the resistance. Hence, a precise knowledge of the doping profile is essential in order to increase the accuracy of the simulations.

Also shown in Table 5.1 is a comparison of the recovery times, obtained by the transient simulations as well as calculated from static IV characteristics via Eq. (5.3). From the results it can be concluded that the stationary method is a good approximation to estimate the recovery time of the cell. The smaller values from the stationary simulations can be explained

Pitch/Gap	MC			DIOS		
	C_D	$\tau_{90\%}$ trans.	$\tau_{90\%}$ stat.	C_D	$\tau_{90\%}$ trans.	$\tau_{90\%}$ stat.
(µm)	(fF)	(ns)	(ns)	(fF)	(ns)	(ns)
100/10	487	361	349	503	478	466
130/10	868	226	217	894	283	256
130/12	838	293	275	865	339	328
130/20	730	825	802	756	1044	1038

Table 5.1: Variation of TCAD results (diode capacitance C_D and recovery time) by using different implantation models. Also shown is the difference between the recovery time obtained from transient simulations ($\tau_{90\%}$ trans.) and the estimation via the stationary results according to Eq. (5.3) ($\tau_{90\%}$ stat.). All values are at $V_{ob} = 2$ V and $T = 253$ K. A good agreement is observed between the values from transient and static recovery time estimation as well as to the measurement results (e.g. Pitch/Gap: 130/10, $C_D \approx 855$ fF, $\tau_{90\%} \approx 300$ ns), as will be discussed in more detail in Sec. 5.2.3.

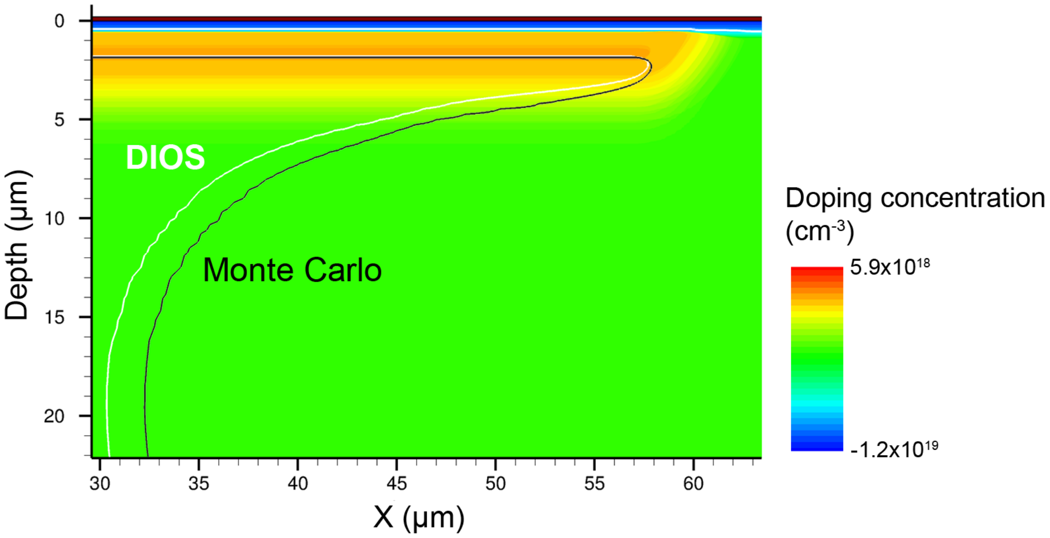

Figure 5.17: Comparison of DIOS and MC doping concentration with respect to the bulk depletion. The missing channeling tail in the DIOS doping profile leads to an increased sidewards depletion (indicated by the black and white curves) from the gap which results in a higher resistance and a longer recovery.

	$N_B = 2.6 \cdot 10^{12}$ cm^{-3}				$N_B = 2.7 \cdot 10^{12}$ cm^{-3}			
Pitch/Gap	MC		DIOS		MC		DIOS	
(µm)	V_{max} (V)	$\tau_{90\%}$ (ns)	V_{max} (V)	$\tau_{90\%}$ (ns)	V_{max} (V)	$\tau_{90\%}$ (ns)	V_{max} (V)	$\tau_{90\%}$ (ns)
100/10	3.2	376	3.6	509	3.1	349	3.5	466
125/10	2.0	241	2.2	290	1.9	228	2.2	272
130/10	1.8	230	2.0	273	1.8	217	2.0	256
130/12	2.2	294	2.5	351	2.1	275	2.4	328
130/20	4.2	903	4.5	1188	4.0	802	4.4	1038
135/15	2.6	387	2.9	462	2.5	358	2.8	427

Table 5.2: Influence of bulk doping variation on maximum overbias voltage (V_{max}) and recovery time ($\tau_{90\%}$) for TCAD models MC and DIOS. The values for V_{max} are obtained at a temperature of 253 K. The recovery time corresponds to an overbias of 2 V. Deviations of up to 150 ns (130/20) can be observed.

by neglecting the coupling capacitance in the calculation. The contribution from C_Q is in the range of ca. 3% which is in good agreement with the deviations between stationary and transient results. The advantage of the stationary simulations is that they are less time consuming and thus simplify comprehensive studies.

Taking into account the difference in the depletion region and the resulting change in the quench resistance, also a difference in the maximum overbias voltage $V_{max} = V(20\ \mu\text{A})$ is expected. The influence of the implantation model on this parameter is illustrated in Table 5.2, which additionally shows in comparison the results for a variation of the bulk doping by $0.1 \cdot 10^{12}$ cm^{-3}. For a constant bulk doping, V_{max} scales with the pitch-gap combination in the same way as the recovery time. This is due to the usual trade-off for SiPMs with passive quenching: a high overbias requires a high resistance and thus results in a slow recovery (cf. Sec. 2.3.3). As previously discussed, the dependency on the model is increasing for pitch/gap ratios close to pinch-off (130/20). The difference in the maximum overbias voltage for those devices is in the range of 0.4 V, whereas other SiPMs show only a discrepancy of 0.2 V.

A variation of the bulk doping also results in a change of V_{max} and the recovery time. In addition to the higher bulk resistivity, the lower doping concentration has the consequence that the depletion regions extends more into the bulk leading to a higher quench resistance. As already seen in the comparison of the models, the closer the situation in the bulk is to pinch-off, the more the properties are affected by changes in the depleted volume. As a results, the recovery time can vary up to 150 ns (average: 20–40 ns). According to the simulations, the contribution from the bulk doping variation to the uncertainty in the maximum overbias voltage is in the order of 0.2 V.

Additional uncertainties can by caused by variations in the wafer thickness of the SOI material and the relation between the resist and the tilt angle in the implantation which influences the doping distribution and thus the sidewards depletion.

Taking into account all uncertainties in the simulation, deviations in the range of 50–70 ns and 0.3 V have to be considered for the recovery time and the maximum overbias voltage, respectively.

5.2.2. Static characterisation of SiMPl 2

The first characterisation of the devices is the measurement of the IV curve in reverse bias and in dark condition. With this first simple measurement, informations about the quality of the production can be obtained. The leakage current of the diode is an indication for the damage and defects within the crystal structure which are responsible for the dark counts in the Geiger-mode operation of the detector. Another indication is the value of the breakdown voltage to define broken devices with early breakdowns.

On the wafer level a full IV mapping at room temperature was performed to obtain information about the yield and the homogeneity of the devices. Although the test diodes and the emission microscope pictures showed promising results, the wafer mapping revealed a low yield of working devices in the upper half of the wafer whereas the lower half showed better characteristics (homogeneous IV curves within 5 mm distance [140]).

The mapping was used to preselect working structures of the wafer for further characterisation. After bonding the devices to a ceramic, the IV curves of the bonded structures were measured again using finer steps in the voltage sweeps. A result of the measurements for a device with 130 µm pitch and 11 µm gap is shown in Fig. 5.18. On the left hand side the full IV characteristic at different temperatures is plotted. A typical IV curve for a SiPM, as well as the temperature dependence of the leakage current and the breakdown voltage, can be observed (cf. MPPC, Fig. 3.6). Increasing the bias voltage leads to a slow increase of the leakage current. Once the breakdown condition is fulfilled the current shows a strong increase. For the SiMPl devices, the breakdown voltage is in the range of 36 V at room temperature. Also the temperature dependence of the leakage current and the breakdown voltage is visible in Fig. 5.18. The situation in the regime around the breakdown voltage is plotted on the right hand side as a zoom of the marked area for better visualisation. From the IV curves, a temperature coefficient for V_{bd} of 36 mV/K can be extracted (MPPC: 55 mV/K). The second increase in the IV characteristics at bias voltages around 38–40 V already indicates where the non-quenching and pile-up regime starts (cf. Sec. 5.2.3.8).

The values for the total capacitance of the devices were obtained by CV measurements with a standard frequency of 1 MHz. Various pitch-gap combinations and arrays with different numbers of cells were measured and the results are shown in Fig. 5.19. On the left hand side, the capacitance is shown as a function of the bias voltage for different pitch-gap combinations of 10×10 arrays. By increasing the size of the gap, the area of the active region, which defines the capacitance, is accordingly reduced. This results in different capacitances of the arrays as illustrated in the plot. The difference in the results of the hexagonal and squared device with the same pitch-gap combination can be explained by the specification of the pitch (see Fig. 5.2) which results in a different area. Around a bias voltage of $V_{bias} = 30$ V, the SiMPl devices have a capacitance in the order of 40–75 pF. As shown on the right hand side of Fig. 5.19, the capacitance of the SiPMs scales with the number of cells due to their parallel connection. Decreasing the number of cells results in a decrease of the overall capacitance. This was already observed for MPPCs in Sec. 3.2.1.2, with the difference that the change in the area of the cells for two different pitches was compensated by their increasing number. The ratio of the measured capacitance values for the arrays with 100 and 19 cells, at $V_{bias} = 30$ V and 1 MHz, is

$$\frac{C_{100}}{C_{19}} = 4.55, \tag{5.6}$$

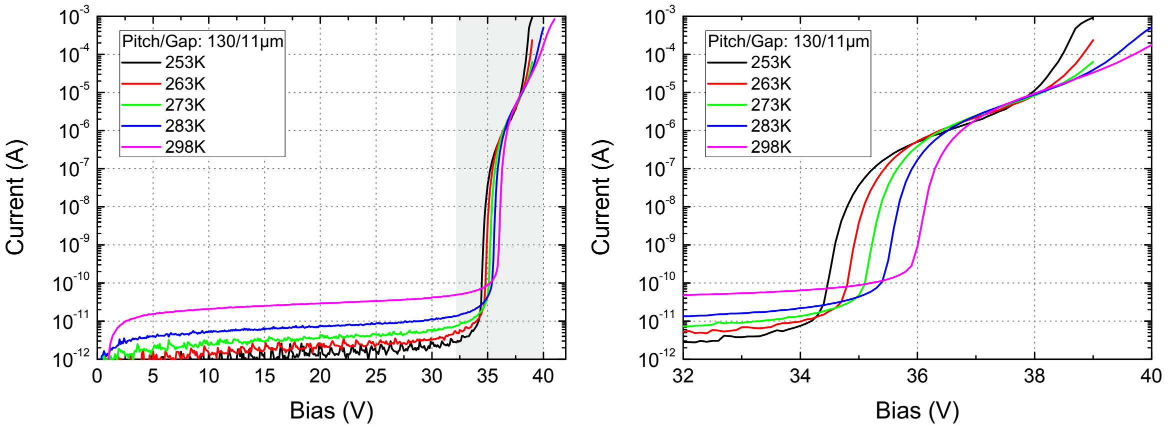

Figure 5.18: Temperature series of dark current IV curve of 130 µm pitch device with a gap of 11 µm. From the full IV characteristic (left) it can be seen that the leakage current is increasing with temperature. The noisy results at lower temperatures are measurement artefacts from the setup. The plot on the right hand side is a magnification of the marked area in the left graph. The temperature coefficient of V_{bd} was determined to be 36 mV/K. The temperature dependence of the bulk resistivity explains the difference in the behaviour for high overbias voltages.

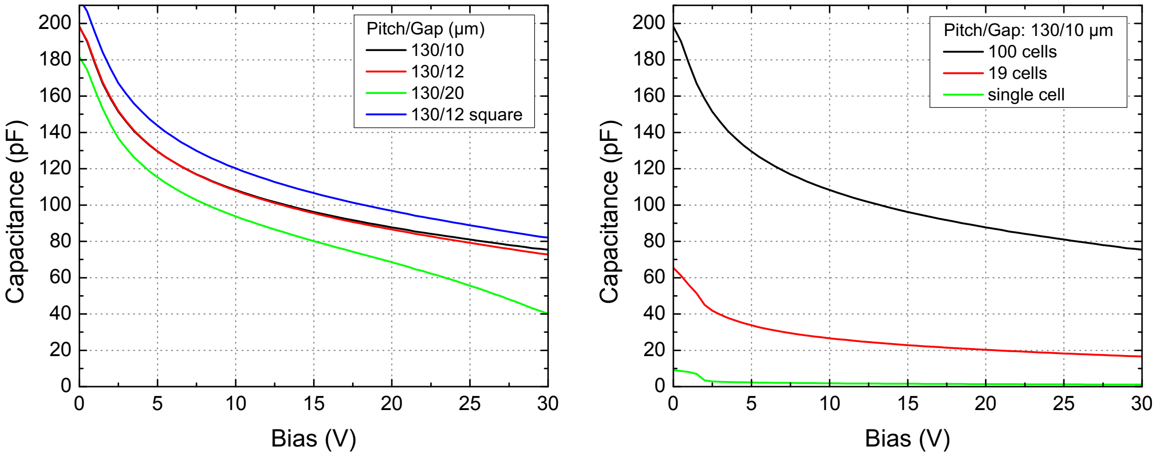

Figure 5.19: Results of CV measurements of SiMPl 2. In the left graph the capacitance as a function of the voltage is shown for different pitch-gap combination of 10 × 10 arrays which leads to different C_D. The device with square cells has a larger capacitance since they have a larger area (and therefore a larger capacitance, see Eq. (5.5)). In the right graph, the CV characteristic is plotted for arrays with a different number of cells. The capacitance of the SiPM increases with the number of cells.

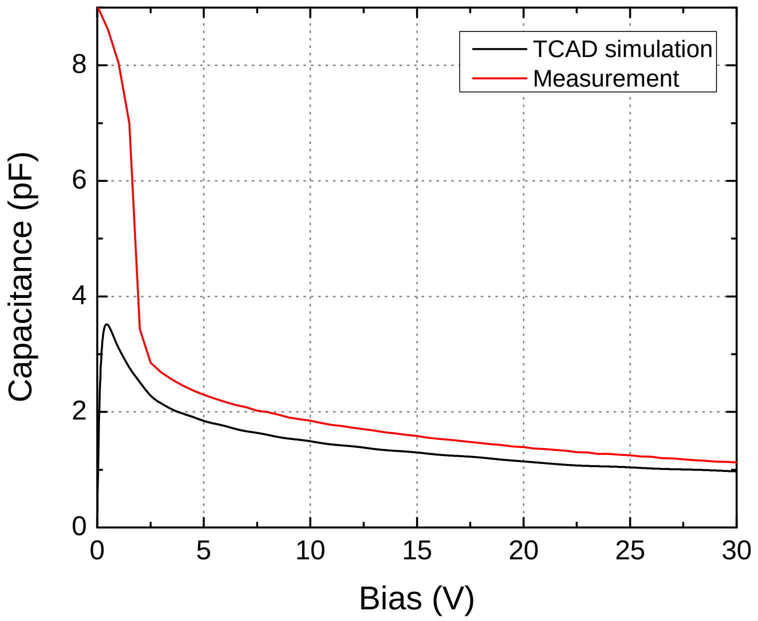

Figure 5.20: Comparison between simulation and measurement of the capacitance for a single cell with pitch 130 µm and gap 10 µm. Qualitatively a good agreement is observed in the high voltage regime. Even close to V_{bd}, the capacitance is still significantly changing due to the doping profile. The values from the simulation were calculated via the displacement current.

which is slightly different from the theoretically expected value of $100 : 19 \approx 5.26$ due to scaling of the array size. This can be explained by the different characteristics of the boundary cells (larger C_{cell}). By increasing the size of the array, the percentage of these cells in the device, and thus their contribution to the total capacitance, is decreased.

In contrast to the MPPCs, as shown in Fig. 3.8, a less pronounced plateau in the capacitance of SiMPl devices was observed. Even close at V_{bd} the capacitance is still significantly decreasing. This behaviour can be observed for all measured devices on the wafer. One difference to the MPPCs is the gap region and its resulting (sidewards) depletion which is necessary for the lateral definition of the bulk integrated quench resistor. This depletion region leads to an additional capacitance and, due to the dimension and doping distributions in the final device, this capacitance does not reach full depletion at voltages typical for operation of SiMPl detectors. However, the contribution of this capacitor (in the range of fF) to the overall capacitance is much smaller than that of the diode capacity C_D and cannot explain the behaviour of the CV measurements. A possible explanation can be found in the phosphorus doping profile.

To investigate this issue, the capacitance as a function of the bias voltage has been estimated via simulations of the displacement current (see Eq. (5.2)) for a single cell. The comparison of the measured and simulated result is plotted in Fig. 5.20. Both show the same qualitative behaviour with respect to the bias voltage. For small values, the discrepancy between measurement and simulation can be attributed to deviations of the simulated doping profile from the fabricated structure as well as parasitic capacitances of the measurement setup, which are not present in the simulation. For higher values of the bias voltage, even the quantitative value of the capacitance is in good agreement to the measurements. From these results it can be concluded that the doping concentration in the maximum of the internal anode implant is apparently not high enough to reach a distinct saturation in the capacitance characteristics. Therefore, the depletion width is still increasing with the bias voltage of the device, even in the doping peak. Due to this effect the capacitance of the diode changes and results in the observed behaviour. Smaller deviations from the simulation and the measurements in this regime can be explained by the difference in geometry (in-circle) and uncertainties of the doping profile. In order to minimise this change in the capacitance, the doping concentration in the doping peak has to be increased which is realised by a higher dose for the deep n-implantation in the next prototype production.

The devices were also measured at different temperatures (253–300 K) and frequencies from 1 kHz to 1 MHz. In both cases no significant dependencies of the capacitance were observed.

5.2.3. Dynamic characterisation of SiMPl 2

The dynamic measurements of the device are important to obtain information about the characteristics during operation and reveal problems which cannot be determined by static IV or CV measurements.

5.2.3.1. Gain and capacitance

The gain G of the SiMPl devices was measured using the *SiPM Evaluation Kit* described in Sec. 3.2.2.2. As shown in Eq. (3.10), the gain of a G-APD is a linear function of the overbias voltage V_{ob}. This linear dependency is clearly visible in the measurement results of the devices from the second prototype, which are plotted versus V_{ob} in Fig. 5.21. The slope of the linear fit function corresponds to the cell capacitance which is dominated by the capacitance of the avalanche diode C_D ($C_{cell} = C_D + C_Q$, with $C_D : C_Q \approx 35 : 1$). The gain for different devices at $V_{ob} = 1$ V is summarised in Table 5.3. In addition, the fill factors (ca. 80–85%) and the capacitance values, calculated from the measurements, are shown. Furthermore, the table includes the results from device simulations with the Synopsys tool. The capacitance was calculated from the transient simulations via the voltage drop V_{ob} for a given generated charge. As can be seen, the results extracted from the gain measurements are in good agreement with the values obtained from the TCAD simulations. The simulation results in Table 5.3 are based on the MC model for the implantation, since they fit better to the measurements than the results of the analytical model used in DIOS. The deviations between measurements and simulations can be explained by uncertainties in the simulation of the exact doping profile as well as in the accurate cell dimension (e.g. the exact position of the resist edge may slightly differ from the one assumed in the simulation). The former contributes to the deviation from the measurements by differences in the depletion width which defines the distance of the plate capacitor. The latter affects C_D via different areas. Assuming an uncertainty of 0.5 µm in the gap size and of 25 nm in the depletion width already results in a deviation of around 2% in the capacitance. In addition, a small contribution can be derived from the fact that the corners of the hexagons are rounded. Thus, the actual active area of the cell is slightly smaller than a perfect hexagon which also decreases the capacitance.

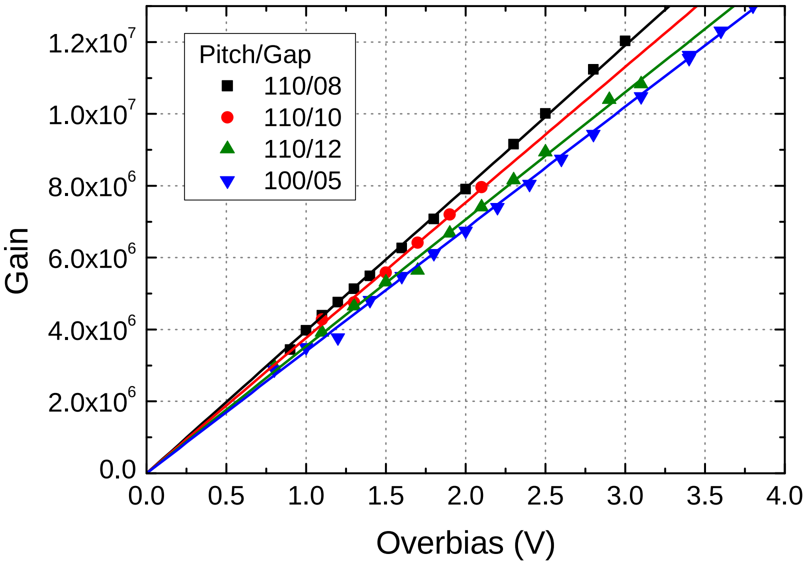

Figure 5.21: The gain of the SiMPl device as a function of overbias voltage. According to Eq. (3.10), a linear dependency can be observed. The breakdown voltage is given by the value of $G = 0$.

Pitch (µm)	Gap (µm)	FF	Gain at 1 V ($\times 10^6$)	Capacitance (fF)	Cap. (sim.) (fF)	Comment
110	8	0.86	3.97 ± 0.09	611 ± 17	639 ± 13	10x10 hex.
110	10	0.83	3.77 ± 0.36	578 ± 68	614 ± 11	10x10 hex.
110	12	0.79	3.53 ± 0.17	539 ± 32	589 ± 10	10x10 hex.
120	9	0.86	4.44 ± 0.08	682 ± 15	755 ± 13	10x10 hex.
130	11	0.84	5.26 ± 0.10	844 ± 17	855 ± 10	10x10 hex.
120	12	0.84	5.19 ± 0.45	797 ± 73	835 ± 12	10x10 sq.
100	5	0.90	3.40 ± 0.09	520 ± 18	558 ± 10	1x1 hex.

Table 5.3: Overview of gain measurement results. The values are given for 10×10 hexagonal arrays, one single hexagonal cell and one 10×10 square array, as indicated in the comment column. The measurements were performed at $T = 253$ K, except for the single cell, which was done at room temperature. For the measurements, the gate width was in the range of 1 µs. The capacitance is calculated from the measurement results. From the CV measurements, capacitance values in the order of 800 fF were obtained for devices with pitch 130 µm. The simulated value of the capacitance was obtained from transient device simulations. The high fill factors illustrate one advantage of the SiMPl approach. For more details see text.

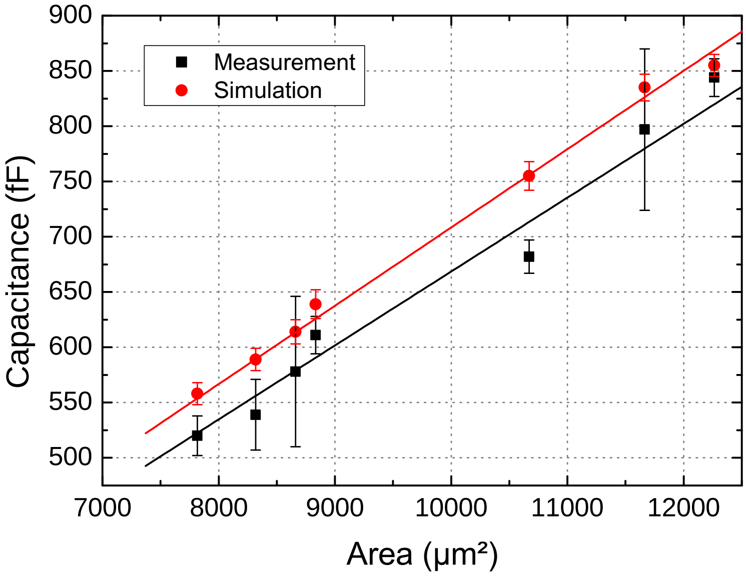

Figure 5.22: Capacitance of the SiMPl devices from Table 5.3 as a function of the active area. The linear dependence, expected from Eq. (2.19), is visible. The errors in the simulation result from the uncertainty in the width of the depletion region. All values were extracted at 1 V overbias.

For comparison, the value of the capacitance can also be estimated via Eq. (2.19), where the depletion width in the stationary simulations is found to be approximately $W = (1.48 \pm 0.01)$ µm (MC method), while the active area A_a of the hexagonal cells is given by

$$A_a = \frac{\sqrt{3}}{2}(Pitch - Gap)^2. \tag{5.7}$$

As an example, Eq.(5.7) returns for a pitch of 110 µm and a gap size of 10 µm a value for the diode capacitance of $C_D = 606$ fF, which is in good agreement to the values obtained from the measurements as well as the transient simulations.

According to Eq. (2.19), the capacitance also scales linearly with the active area of the G-APD. This is illustrated in Fig. 5.22, where the capacitances from Table 5.3 (measured and simulated) are plotted as a function of the active area. In both cases, the data are fitted with a straight line which is in good agreement to the measurement results of the prototype. A pinch-off effect could not be observed in any of the measurements. Therefore, the gain of the devices with other pitch-gap combinations can be scaled according to the ratio of the cell active area.

5.2.3.2. Breakdown voltage

The linear fit of the gain measurement values is a further possibility to determine the breakdown voltage of the device, which is defined as the voltage at $G = 0$. The breakdown voltage of G-APDs depends on the operating temperature. For four different devices with a pitch size of 130 µm, V_{bd} as a function of the temperature between 223 K and 273 K is shown in Fig. 5.23. Within the measured range a linear dependency is observed. The temperature

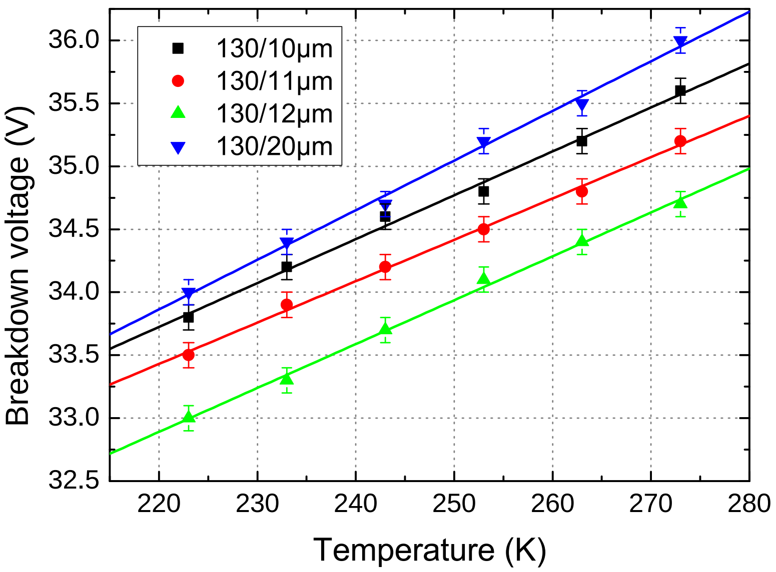

Figure 5.23: Temperature dependency of the breakdown voltage for devices with pitch 130 µm. Due to less phonon scattering V_{bd} decreases with decreasing temperature. The slope of the linear fit returns the temperature coefficient.

Pitch (µm)	Gap (µm)	$\partial V_{bd}/\partial T$ (mV/K)
130	10	35 ± 1
130	11	33 ± 1
130	12	35 ± 1
130	20	39 ± 1

Table 5.4: Temperature coefficient of the breakdown voltage for SiMPl devices.

coefficient of the SiMPl devices is given by the slope of the linear fit. Table 5.4 lists the results for the devices shown in the plot. This effect is caused by the reduction of phonon scattering of charge carriers in the avalanche process [84]. The mean free path of the charge carriers is thus increased and they can gain more energy to impact ionise further electron-hole pairs which is equivalent to an increase of the ionisation coefficients α and β. The value of the temperature coefficient depends, amongst others, on the width of the avalanche region. Changing the ionisation coefficients also changes the electric field strength which is necessary to fulfil the breakdown condition (cf. Eqs. (2.28)-(2.29)). This shift in the electric field has to be compensated by a change in the bias voltage of which amplitude depends on the width of the high field depletion region [100]. In average, the temperature coefficient for the SiMPl prototype is $\partial V_{bd}/\partial T = 36$ mV/K, which is in agreement with the value obtained by the IV measurements. In comparison, the MPPCs from Hamamatsu have a temperature coefficient of 56 mV/K and a breakdown voltage of approximately 70 V. This is consistent with the simple assumption that the temperature coefficient of the breakdown voltage depends on the

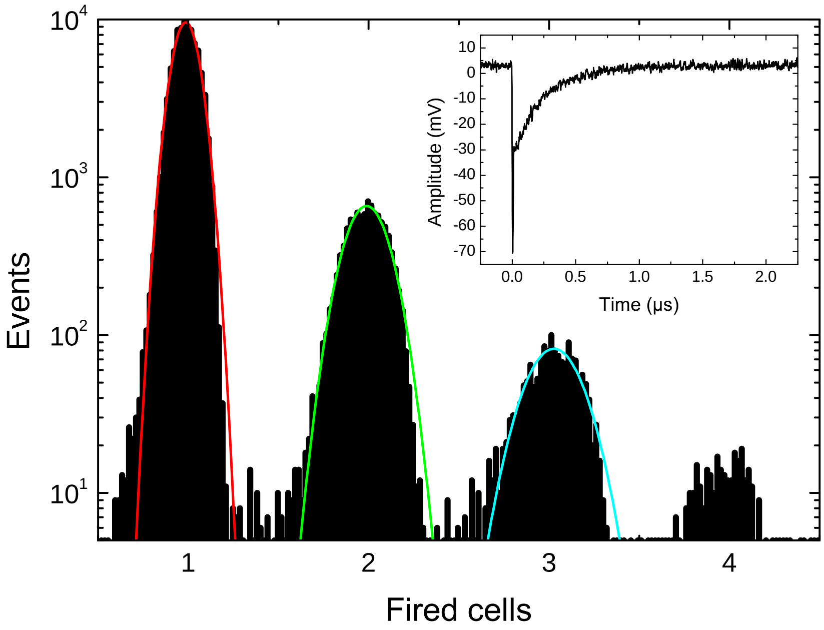

Figure 5.24: Dark count spectrum of a SiMPl device. Pitch is 135 µm with a gap size of 16 µm. Only dark counts at a temperature of $T = 253$ K were measured. Distinct peaks are visible and in good agreement with Gaussian fits. The inset graph shows a standard output pulse of the device.

depletion width of the high field region. MPPCs, which show roughly twice the breakdown voltage also have a higher dependency on the temperature compared to SiMPl.

The measurements in Fig. 5.23 show also a spread in the breakdown voltage of the devices in the range of 1 V which is a result of inhomogeneities over the wafer during the prototype production.

5.2.3.3. Amplitude spectrum

The signal amplitude provides important information on the device performance. Inhomogeneities of the gain within the array or edge breakdown lead to a broadening of the photoelectron peaks. These effects are not visible in the IV characteristics and require an amplitude histogram.

The amplitude spectrum is very similar to the charge spectrum which was used for the gain measurements, but it is less affected by afterpulsing and dark counts from other cells in the array, since the measurement window can be very small. Fig. 5.24 shows a dark count amplitude spectrum of a SiMPl 10×10 array at 253 K. The spectrum was recorded using a digital oscilloscope with a noise filter. Due to the clear separation of the peaks a good homogeneity within the array can be assumed. Furthermore, the peaks are in good agreement to a Gaussian fit (see Eq. (2.35)). On the left hand side of the peaks a small shoulder can be recognised which has two contributions. First, the trigger threshold is set to a level of 0.5 p.e. which still allows detection of afterpulses with a smaller amplitude. Second, the cells at the edge of the matrix are designed slightly different. Thus, those cells in turn contribute with a different amplitude to the spectrum. The inset in Fig. 5.24 depicts a standard output pulse of the device on the oscilloscope. It shows that the signal consists of a fast and a slow

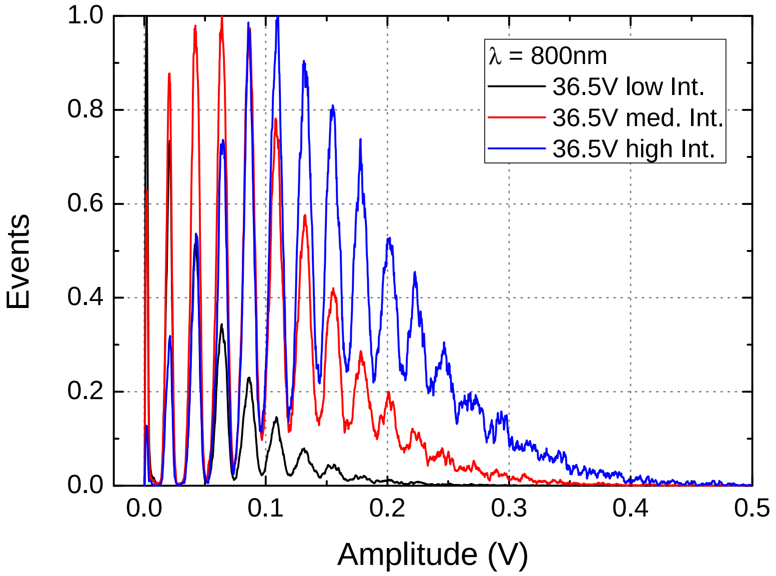

Figure 5.25: Normalised amplitude spectrum of a SiMPl device, illuminated with a pulsed laser source ($\lambda = 800$ nm) using three different intensity levels.

contribution, where the latter corresponds to the recovery of the G-APDs through the bulk resistor.

The response of the device to a pulsed laser source with a wavelength of $\lambda = 800$ nm is shown in Fig. 5.25. All amplitude spectra of the device were recorded with the same overbias voltage $V_{ob} = 2$ V. For a better comparison, the maxima of the spectra were normalised to one. By increasing the light intensity a shift of the mean value of the Poissonian-like photoelectron distribution is clearly visible which indicates the positive response of the SiPM to the laser. From the spectrum with the highest intensity a resolution up to 12 p.e. peaks can be observed. For improvements of the single photon resolution an optimisation of the device characteristics, especially the homogeneity of the array and the suppression of edge breakdown, is necessary.

5.2.3.4. Dark count rate

A low dark count rate (DCR) is important for the detection of single photons, since the signal of an avalanche initiated by a thermally generated charge cannot be distinguished from a pulse caused by the absorption of a photon. To avoid cooling of the devices, the dark count rate at room temperature should be as small as possible (depending on the expected background level). As already mentioned, the leakage current of the devices is increased compared to the leakage current of the bulk material itself, which can be explained by the crystal damage caused by the implantation of the deep n-implant. This is a process step with a high energy implant and not all defect states can be removed by the annealing process afterwards. The resulting energy states in the band gap cause increased electron-hole pair production (SRH generation) and the avalanche can also be triggered by these thermally generated charge carriers. Due to this fact the dark count rate depends on an optimised technology with a low defect density.

The high dark count rate of the SiMPl detector prevents a reasonable operation of the devices at room temperature. At this conditions a DCR of a few MHz/mm^2 was measured (see Fig. 5.26). Since the dark counts originate from thermal generation of electron-hole pairs, the generation rate can be reduced by cooling the device. This results in a decrease of the dark count rate by approximately a factor of two every 7 K, according to Eq. (3.14). This behaviour is shown in Fig. 5.26, where the dark count rate is plotted as a function of the overbias voltage for different temperatures ($T = 253 \ldots 298$ K). The measurements were performed with a frequency counter using a threshold level of 0.5 p.e. While the DCR is increasing with the bias voltage, since the trigger probability for an avalanche breakdown is also increasing with V_{bias}, a decrease of the dark count rate with the temperature is clearly visible. The steeper increase of the DCR at higher overbias voltages is caused by pile-up effects (afterpulsing) and the transition to the non-quenching regime. The cooling has also the consequence that the carrier mobility, and thus the resistivity of the bulk changes. By lowering the temperature, the resistivity is decreased according to Eq. (5.1) due to less phonon scattering. Thus, also the value of R_Q, which defines the maximum overbias via the quenching condition is reduced (see Eq. (4.1)). As a result, the SiMPl devices, which were designed for room temperature operation, may not be operated in the full saturation regime of the Geiger efficiency, since the required overbias is usually above the 20 µA rule of thumb. However, the onset of a saturation was already observes as will be shown later.

In order to investigate the origin of the dark counts an Arrhenius plot of the DCR at a constant overbias voltage (by taking into account the voltage shift of V_{bd} with temperature) is shown in Fig. 5.27. The data were fitted with an exponential curve to determine the activation energy E_A of the defects causing the dark counts. From the fit parameters an activation energy of $E_A = 0.55$ eV, which is approximately $E_g/2$, can be determined and confirms the origin of the thermal dark counts by SRH from energy states in the mid of the band gap.

By increasing V_{ob} also the dark counts are increasing. This is due to the effect that the trigger probability for an avalanche breakdown is increasing with the overbias voltage. In addition, the probability that an afterpulsing event triggers a breakdown is increasing, too. This leads to a steep increase of the DCR at high V_{ob} and sets a limitation of the operation range of the SiPM (also for conventional devices). In the second prototype production, this effect, in combination with optical cross talk, was rather the limiting factor than the limitation of quenching the avalanche.

By plotting the dark count rate as a function of the trigger threshold, the staircase structure can be observed. The form of the staircase allows also conclusions on the single photon resolution of the SiPM as well as the optical cross talk and thus the DCR at higher p.e. thresholds. An inhomogeneous device would result in indistinct steps due to the broadening and overlap of the Gauss peaks in the amplitude spectrum. A comparison between the staircase obtained from DCR measurements and calculated from a dark count amplitude spectrum is shown in Fig. 5.28. In both plots the staircase structure can be observed. The left graph shows the DCR as a function of the trigger threshold in values of photoelectron equivalents (p.e.). In agreement to Fig. 5.26, an increase of the overbias results in an increase of the DCR and of the ratio between the levels of 0.5 p.e. and 1.5 p.e threshold. On the right hand side the normalised staircase, calculated from the amplitude spectrum, is plotted. It shows the same behaviour as the DCR plot but the staircase is more distinct. This can

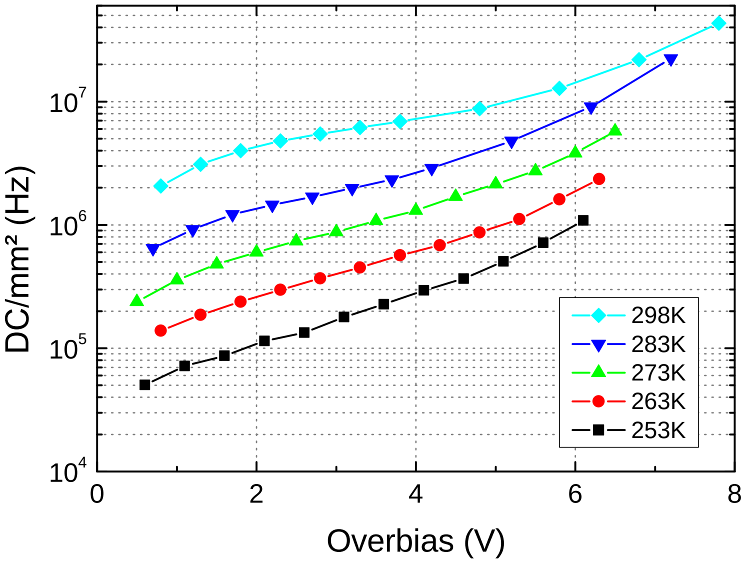

Figure 5.26: Dark counts/mm^2 at different temperatures as a function of the overbias voltage. The increase of the dark count rate with the overbias, due to the increased trigger probability, can be observed. On the other hand, the DCR decreases with the temperature, since the thermal generation of e-h-pairs depends on T (see Eq. (3.14)).

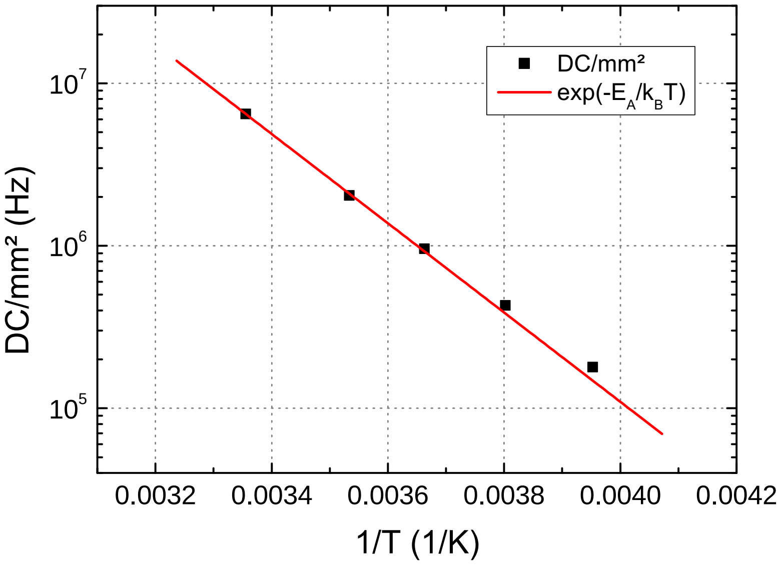

Figure 5.27: Arrhenius plot of dark count rate. All values were measured at the same overbias. From the fit an activation energy of $E_A = 0.55$ eV can be determined which corresponds well to the mid of the band gap in silicon.

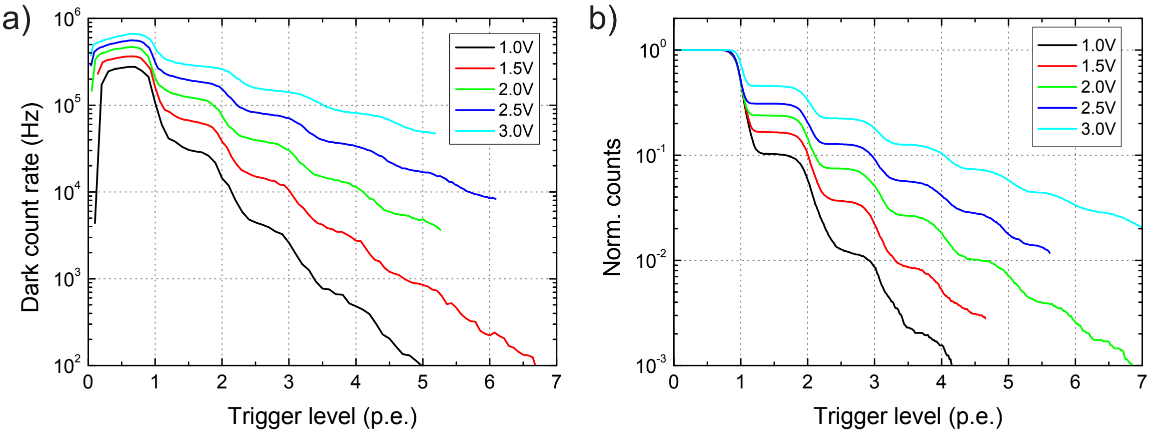

Figure 5.28: Comparison of staircase plots obtained from DCR measurements (a) and an amplitude spectrum (b). In both graphs the staircase structure is clearly visible. For the DCR the increase of the count rate with V_{ob} is visible. The staircase from the amplitude spectrum was normalised so the optical cross talk value is given at 1.5 p.e. Because of the noise filters used in the measurements of the amplitude spectrum, the staircase is of better quality. From both plots can be concluded that the OCT rate is increasing with the overbias voltage.

be explained by the noise filters used for the measurement of the amplitude spectrum. In addition, the DCR measurements are more affected by afterpulsing which is not the case for the amplitude spectrum. Thus, the steps in the staircase can be easily determined and allow a good estimation of the optical cross talk.

5.2.3.5. Optical cross talk

The optical cross talk (OCT) in SiPMs can be measured by the ratio of the DCR at a threshold level of 1.5 p.e. amplitude to 0.5 p.e. amplitude (see Eq. (3.16)). Because of the reasons mentioned above, the OCT was determined from the staircase of the amplitude spectrum. Fig. 5.29 shows the results of the measurements for devices with a pitch of 130 µm and three different gap sizes. For all devices a non-linear increase of the OCT with the bias voltage can be observed. As discussed in Sec. 3.2.2.7, this can be explained by the increase of the gain and the trigger probability with V_{ob}. Due to the increasing number of charge carriers, crossing the junction in an avalanche breakdown, more photons are emitted in average, which may be absorbed in neighbouring cells and trigger an additional breakdown. Furthermore, the probability that the absorbed photon triggers an avalanche breakdown is also increasing with the overbias voltage (Geiger efficiency, see Fig. 5.42).

The SiMPl prototype with its different pitch-gap combinations gives the possibility to study the cross talk behaviour. However, the small yield and the inhomogeneity reduces the number of comparable structures significantly.

In Table 5.5, the results of the OCT measurements are summarised for devices with varying pitch and gap size. The OCT for each device was measured at an overbias voltage of $V_{ob} = 2$ V. For a pitch size of 130 µm the values are in a range of 15% to 30%, depending on the gap. It should be mentioned that for the prototypes no additional measures for cross talk suppression were implemented. It can be observed that the OCT is decreasing if the gap size is increased for a fixed pitch. By increasing the distance between the active areas of neighbouring cells the probability of absorption within this "inactive" region is also increasing and leads to lower

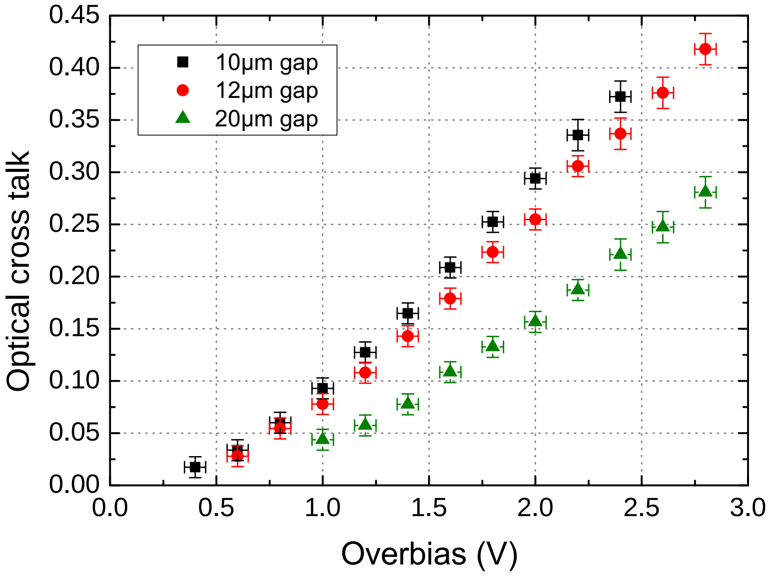

Figure 5.29: Optical cross talk of SiMPl devices with pitch size of 130 µm and various gap. The OCT is increasing with the overbias voltage. A bigger gap results in a lower fill factor, gain and therefore cross talk (cf. Ref. [144]).

Pitch/Gap (µm)	Comment	Fill Factor (%)	OCT (%)
135/15	10x10 hex.	79.0	24
130/10	10x10 hex.	85.2	29
130/11	10x10 hex.	83.8	27
130/12	10x10 hex.	82.4	25
130/20	10x10 hex.	71.6	15
120/12	10x10 hex.	81.0	24
110/12	10x10 hex.	79.4	23
130/12	10x10 sq.	82.4	30

Table 5.5: Optical cross talk at an overbias of $V_{ob} = 2$ V for different devices with high fill factors. By increasing the gap size the OCT value shows a decrease. The squared device has the same FF as the hexagonal one but a higher gain what can explain the increased OCT. For more details see text.

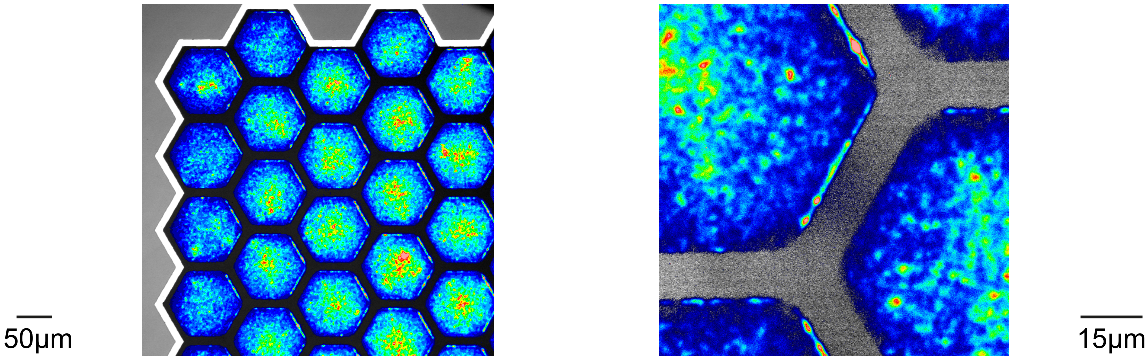

Figure 5.30: Increased light emission at the cell edges of device from the SiMPl 2 wafer chosen for characterisation.

OCT values. As this is associated with a lower fill factor, the photon detection efficiency is also reduced. Since the device with the square cells has a larger area compared to the hexagonal structures with the same pitch, the gain is also higher. Amongst others, the increased gain explains the higher cross talk probability for this device.

In order to compare the devices with the same pitch-gap combination of 130/12 µm but a different geometrical shape, the excess noise factor (ENF) was determined, as described in Sec. 3.2.2.3. At $V_{ob} = 2$ V, the device with hexagonal cells shows a number of 1.41 fired cells in average whereas the square cell device has an ENF value of 1.49. The increased number could be an indication that it is more likely for an array with square cells to trigger more than one neighbouring cell in an OCT event, since there are eight next neighbours while for a honeycomb structure only six directly adjacent cells exist. However, the increase could also be due to the higher gain or by enhanced emission in the edge region and should be a subject of further studies.

It has to be taken into account that optical cross talk is a complex process, since it is a combination of the gain which scales with the area, the fill factor ($\propto$ gap^2) and the absorption probability for the emitted photons, which increases exponentially with the distance and is also a function of the wavelength. In addition, the contribution from the trigger probability, which is a function of the overbias voltage, has to be considered. Furthermore, it was shown that reflections within the silicon bulk can result in a significant contribution to OCT [145].

As a general remark concerning the cross talk measurements, it has to be mentioned that some of the devices showed enhanced light emission at the edge of the cells as observable in the emission microscopy pictures in Fig. 5.30. For example all of the square structures had visible edge emission characteristic. This could explain deviations in the cross talk measurements, since the influence of such enhanced emissions on OCT is difficult to estimate. A new prototype with a high yield of homogeneous devices would allow further and more reliable studies of the cross talk properties of SiMPl.

For comparison, also the OCT of three MPPCs (S10362-11 series with 25/50/100 µm) were determined for an overbias voltage of one and two volts. The recommended operating overbias voltage for the MPPCs with a pitch size of 100 µm is usually in a range of $V_{ob} = 1$ V. A further increase of the voltage to an overbias of 1.5–2 V leads to a the signal which is dominated by cross talk and afterpulses. Thus, the maximum overbias voltage is limited to rather low values for a breakdown voltage of ca. 70 V (relative overbias $V_{ob}/V_{bd} \approx 2\%$ compared to a rule of thumb of 15% for saturation of the detection efficiency). The results for the MPPCs

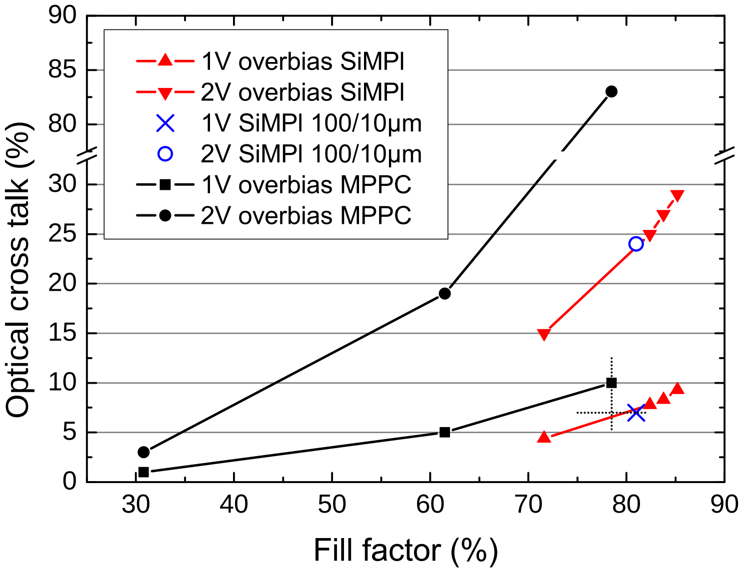

Figure 5.31: Comparison between optical cross talk of Hamamatsu MPPCs and SiMPl devices (130 µm and 100 µm pitch) as a function of the fill factor (see Ref. [144]). No special OCT suppression technology was applied for the prototype production (just intrinsic property of SiMPl devices).

are shown in Fig. 5.31 as a function of the fill factor, together with the values obtained with SiMPl devices of pitch size 130 µm and different gaps. These devices were chosen because they showed the best performance. From the data it can be concluded that with SiMPl devices very high fill factors can be achieved and the optical cross talk is still lower than for the commercial devices. The values for the MPPC with 100 µm are even higher than the values for the SiMPl device with a pitch size of 130 µm. With a fill factor of 78.5%, taken from the data sheet [146], a gap size of the MPPC-100 of ca. 11 µm can be assumed and the corresponding SiMPl device was chosen. In order to compare the SiPMs, the results of a SiMPl detector with pitch 100 µm and gap 10 µm (FF: 81%) were "scaled down" to a fill factor of 78.5%, keeping the OCT value constant. With this assumption, the value is already lower than for the commercial device although the gain is comparable and the fill factor of SiMPl is higher. An explanation could be found in the inherent diffusion barrier present in SiMPl devices (deep n-implant) which strongly suppresses the slow component of the OCT. The minority charge carriers, generated in the bulk by absorption of photons, emitted during the avalanche process, do not reach the sensitive high field region to potentially trigger a neighbouring cell, but rather diffuse towards the gap region due to the built-in potential.

However, it should be mentioned, that the devices from Hamamatsu were fabricated some years ago. In the meanwhile, commercial manufacturers presented demonstration devices with optical trenches, which can reduce the cross talk up to one order of magnitude (see in Sec. 3.2.2.7 and Refs. [147–149]). Similar approaches are applicable for SiMPl devices as well and will be discussed in Sec. 6.2.

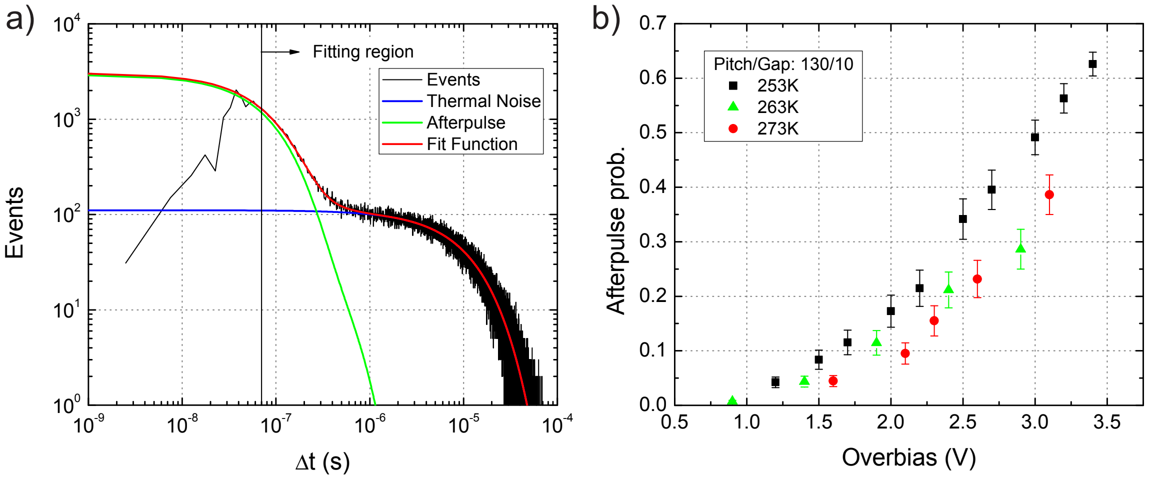

Figure 5.32: Afterpulsing results of Simpl 2. a) Time spectrum of an afterpulsing measurement at $T = 253$ K and 2 V overbias. The fits show the different contributions from afterpulsing and thermal counts. b) Afterpulse probability as a function of the bias voltage. With increasing bias voltage a higher afterpulse probability can be observed because of the increase in gain and trigger efficiency. By decreasing the temperature, the recovery time of SiMPl and the emission rate of the traps is decreasing which has an influence on the afterpulsing measurements.

5.2.3.6. Afterpulsing

As well as optical cross talk, also afterpulsing in SiPMs contributes to the correlated noise and reduces the single photon resolution of the device. Trapped charge carriers during the avalanche process, which are released with a certain delay time τ, can trigger the cell again and result in an additional charge contribution in the measurements. Depending on the emission time of the traps and the recovery time of the cell, their contribution is more or less pronounced (see Sec. 3.2.2.8). For SiMPl, the probability of afterpulse events was measured as a function of the overbias voltage at different temperatures, using the method as described in Sec. 3.2.2.8. The results for a device with 130 µm pitch and 10 µm gap are shown in Fig. 5.32. On the left hand side, the time spectrum of the SiMPl device is plotted at a temperature of 253 K and an overbias voltage of $V_{ob} = 2$ V (room temperature measurements require new prototypes with better performance). Like for the MPPCs in Fig. 3.17, the data are in good agreement with the exponential fits which are associated with thermal (blue) and afterpulsing (green) events. The fitting range for the analysis of the measurements was set to a minimum time difference of 70 ns. From the fitting of the results at 253 K, an average time constant of $\tau_{apf} = (73 \pm 5)$ ns for the fast afterpulse contribution and $\tau_{aps} = (254 \pm 30)$ ns for the slow afterpulse contribution can be derived. Further values as a function of the temperature are shown in Table 5.6. With increasing temperatures, the emission time of the traps, especially

Temperature (K)	τ_{apf} (ns)	τ_{aps} (ns)
253	73 ± 5	254 ± 30
263	65 ± 5	167 ± 54
273	67 ± 15	108 ± 20

Table 5.6: Average time constants for afterpulsing at different temperatures.

of the slow contribution, is decreasing as can be expected from Eq. (3.22) due to the higher thermal energy (k_BT). Also the time constant of the fast contribution is reduced for lower temperatures but the effect is less pronounced. This could be an effect of the limitation of the measurement setup. Since the minimum time difference is set to 70 ns the determination of the fast contribution was less accurate. Fast afterpulses may not be detected with the pulse finding method from Sec. 3.2.2.8 due to their small amplitude which leads to uncertainties in the time spectra. Thus, also the parameters extracted from the data varies, leading to inconclusive results of the determination of the time constants.

Because of these problems the time distribution was tentatively fitted with only one exponential term for afterpulsing. The agreement of the fit with the data was worse compared to the fit with a fast and a slow contribution. This indicates the presence of two dominant time constants in the measurement and is in turn in good agreement with Ref. [125].

The afterpulse probability as a function of the overbias voltage is plotted in Fig. 5.32b. By increasing V_{ob}, the probability of aferpulsing increases too. It shows the same qualitative behaviour as was measured for the MPPC of Hamamatsu in Fig. 3.18. The increased gain results in an increased probability that traps are filled with charge carriers and the increased Geiger efficiency results in an increased probability that the released charge triggers another avalanche breakdown. By decreasing the temperature the afterpulse probability is slightly increasing. This could be a result of the increased emission time of the traps at lower temperatures. In addition, the recovery time for SiMPl is decreasing with the temperature due to the fact that the resistivity of the bulk material is decreasing. Thus, the cell becomes more sensitive to the fast contribution of afterpulsing.

At the same V_{ob}, the SiMPl devices of the second prototype showed less afterpulsing in comparison to the afterpulse probability of MPPCs with 100 µm pitch (1 V: MPPC 50%, SiMPl 3%). This could be a result of the different recovery times. MPPCs have a recovery time to 90% of $\tau_{90\%} = 100$ ns whereas SiMPl devices are in the range of 300 ns to 500 ns depending on the pitch-gap combination, as will be shown in the next section. Thus, a larger amount of afterpulses is suppressed by the slow recovery of the cell in the SiMPl approach. On the other hand, this also means that the cell is not fully active for a longer time.

5.2.3.7. Recovery time and quench resistor

Since the quench resistor for the SiMPl detector is integrated to the bulk material, the resistance is defined by the lateral and vertical depletion from the gap regions. As discussed in Sec. 4.1 this depletion depends on a parameter space which includes the pitch/gap ratio and the (over)bias voltage. Taking this into account it is obvious that the quench resistor in the SiMPl approach is defined only in reverse bias. If a voltage in forward bias is applied to the device, the depletion regions in the bulk do not exist. For this reason, the method described in Sec. 3.2.1.1 which is used for devices with conventional resistors is inapplicable. Furthermore, the potential of the internal anode changes during the recovery of a cell, which results in a variation of the corresponding depletion region and leads to the JFET-like characteristics. These are associated with a non-linear IV curve for R_Q due to the varying resistance with V_{ob}. As a result, no time "constant" for the recovery can be defined for the SiMPl device, since $\tau_{rec}(t) = R_Q(V(t))\,C_D$ is a function of the time. Due to the variation of τ_{rec} with time, it is also inaccurate to describe the slow decaying part of the signal with an exponential decay function as for standard RC elements (as mentioned in Sec. 3.2.2.6).

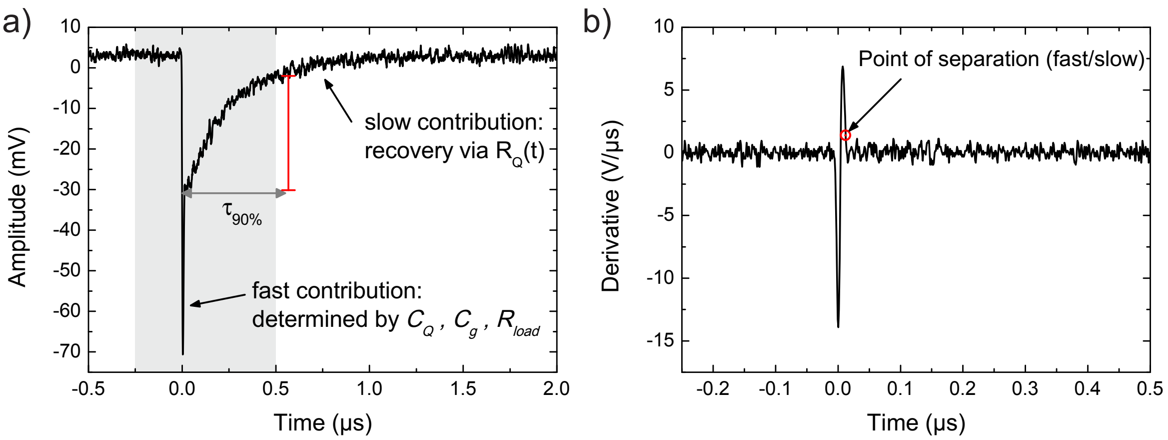

Figure 5.33: Measurement method developed to determine the recovery time of SiMPl. a) shows a common signal of the SiMPl device. The fast contribution in the signal falling edge is determined by the coupling capacitance C_Q, the grid capacitance C_g and the value of the load resistor R_{load}. The slow decaying part is defined by the recharging of the cell via the quench resistor and is therefore associated with the recovery time. b) In order to separate the two time contributions, the derivative of the signal was calculated and the point of separation was defined. Afterwards the recovery time to 90% was measured. More details are given in the text.

Because of these properties, the recovery time of the SiMPl devices has to be measured in a different way. For the determination of the recovery time to 90% ($\tau_{90\%}$), dedicated analysis of the pulse shape was used. As shown in Fig. 5.33a, the decaying part of SiPM signals consists of a fast contribution, determined by the coupling capacitance C_Q, the parasitic grid capacitance C_g and the load resistor R_{load} (see Fig. 2.13), which is followed by the slow part, associated with the recovery of the cell via R_Q. Therefore, only the slow part of the pulse was considered for the measurements of the recovery time. By using an oscilloscope (LeCroy WaveRunner 610Zi), the SiPM waveforms were preselected and recorded. In order to eliminate the influence of dark counts and afterpulses on the determination of the recovery time, only events without additional breakdowns within the measurement window of the oscilloscope were saved. This was realised by differentiation of the signal, which leads to significant peaks due to the fast rising edge, as illustrated in Fig. 5.33b, and allows to detect also afterpulses with small amplitudes (see also Sec. 3.2.2.8). In addition, the signal was also filtered to reduce the noise by using a bandwidth filter of 200 MHz and a digital filter (3 bits). For every V_{ob} and temperature step about one thousand waveforms were recorded.

The data were analysed offline using a MATLAB[4] code, in order to separate the fast and the slow contribution of the signal. In a first step the derivative was calculated. Afterwards, the time stamp of the maximum of the derivative was determined. The point of separation between the fast and the slow component was defined by the point in time at which the derivative drops again to a value of 20% of the maximum (see Fig. 5.33b). With the remaining slow part of the waveform, the time to reach 10% of the amplitude (which corresponds to 90% recovery, see Eq. (3.15)) was measured. For each voltage and temperature step in the study, a mean value and the corresponding standard deviation was calculated.

Due to the JFET-like behaviour of the quench resistor in the SiMPl devices and the resulting non-linear IV curve, the recovery time to 90% of V_{ob} is a function of the overbias voltage,

---

[4] MATLAB R2012a, www.mathworks.com/products/matlab

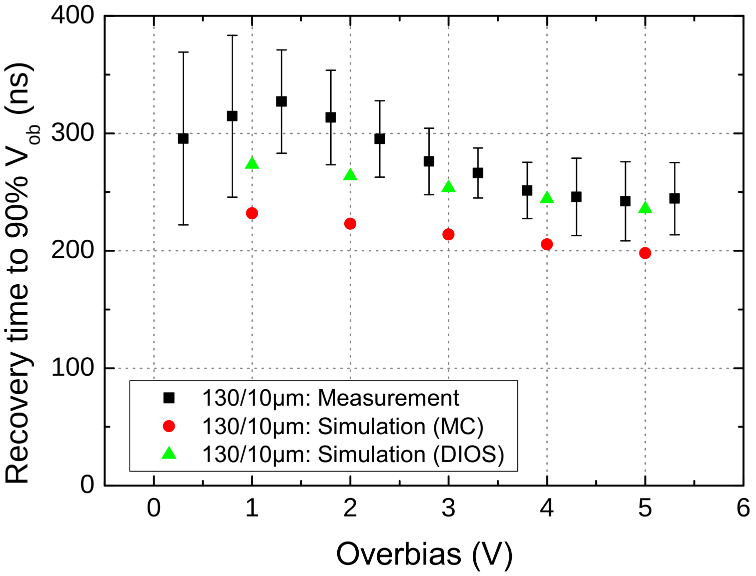

Figure 5.34: Recovery time of SiMPl as a function of the overbias voltage. The time to recover to 90% of V_{ob} is decreasing with increasing voltage due to the non-linear IV curve of the SiMPl devices. Results obtained from TCAD simulations (implant based on MC and DIOS) are plotted for comparison. Within the uncertainties, a good qualitative agreement is achieved. The discussion is given in the text.

which is depicted in Fig. 5.34. For comparison, the results from the TCAD simulations (MC and DIOS) are plotted too. By increasing the overbias voltage, the 90% recovery time of the device is reduced. The explanation of this effect is the shift of the voltage drop V_{IA} at the internal anode corresponding to a recovery of 90% (e.g. $V_{ob} = 1$ V $\rightarrow V_{IA}(90\%) = 0.1$ V, $V_{ob} = 4$ V $\rightarrow V_{IA}(90\%) = 0.4$ V, cf. Sec. 5.2.1.1). As previously discussed in Sec. 5.2.1.2, by increasing the overbias voltage, the part of the non-linear IV characteristics which corresponds to the highest resistance, and therefore longest time steps, becomes more and more negligible. As a result, the 90% recovery time decreases (also illustrated in Fig. 5.12b).

The decrease of the measured $\tau_{90\%}$ for overbias voltages below 1 V can be attributed to the noise in the measurements. At voltages above 1 V overbias the recovery time starts to decrease with the overbias and finally reaches a constant value. The latter can be explained by the transition to the non-quenching regime. The time to quench the avalanche is increasing [142, 150], which also increases the recovery time.

The results, obtained from the TCAD simulations are plotted for comparison. They show a qualitative agreement in a decreasing characteristic with the overbias voltage, although it seems to be less pronounced. It can be seen that the values of the Monte Carlo and the DIOS implant differ by roughly 50 ns, whereas in contrast to the gain measurements the DIOS implant seems to agree better. This variation is due to the different depletion in the bulk region. In the Monte Carlo method the channeling effect is taken into account which results in a tail in the doping concentration, as shown on the left hand side in Fig. 5.16. This leads to a less extended depletion region in the bulk, which defines the quench resistor. This effect was already discussed in more detail in Sec. 5.2.1. Remarkably, the values for the recovery

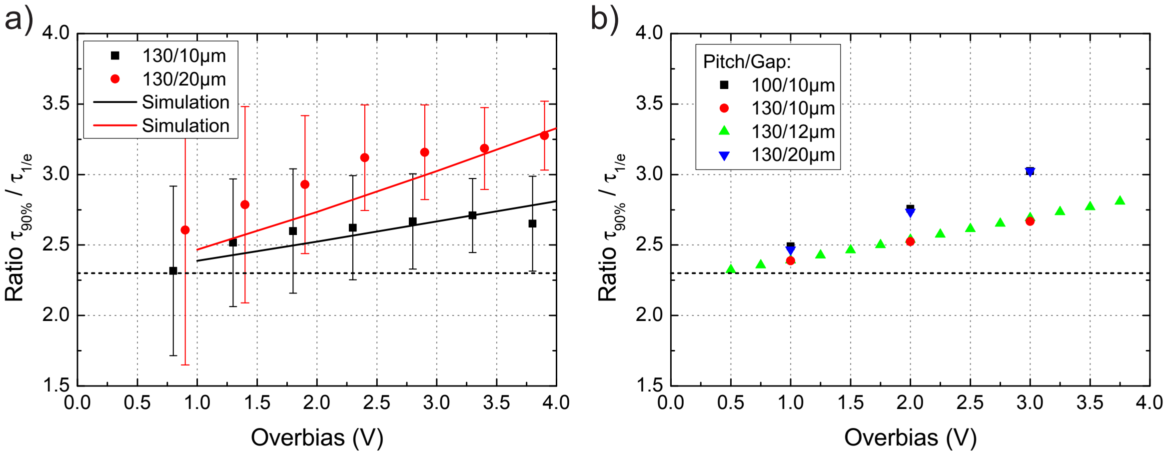

Figure 5.35: Ratio of the recovery times $\tau_{90\%}$ and $\tau_{1/\mathrm{e}}$. A standard RC element shows a ratio of approximately 2.3, independent from the overbias (dashed line). a) comparison of measured and simulated values of the time ratio for devices with pitch 130 µm. With increasing overbias the difference to the RC value increases too. b) simulation results for different pitch-gap combinations. A difference in the dependence on the overbias voltage for different sizes of active areas can be observed.

time in the simulations are smaller compared to the measurements. A possible explanation can be that the real depletion in the bulk is more extended than calculated in the simulations. As shown by the difference in the simulation results, small variations in the doping profile or bulk doping concentration have already an influence of 50 ns on the recovery time of the device. Therefore, the deviation of the measurements and the simulation results are most probably due to the uncertainties in the simulation with respect to the real parameters of the device (see Tables 5.1 and 5.2). Furthermore, the geometry of the real device is different to the quasi-3-D cylindrical approximation. However, real 3-D simulations showed that the IV characteristic in quasi-stationary simulations is in good agreement to the inner circle quasi-3D approximation. By changing the tilt angle of the implantation from positive to negative (cf. Fig. 5.7), an additional uncertainty of 10 ns is obtained. Thus, within the accuracy of the simulation the recovery time is well reproduced. The transition to the non-quenching regime at high overbias voltages cannot be taken into account in the simulations, since the statistical fluctuations require particle-based models (see Sec. 3.1.2).

The deviation from the standard RC behaviour can be estimated by calculating the time required to recover to a value of $(1-1/\mathrm{e})V_{ob} \equiv \tau_{1/\mathrm{e}}$ and $0.9\,V_{ob} \equiv \tau_{90\%}$, based on Eq. (3.15)[5]. For a standard RC element, the ratio is given by

$$\frac{\tau_{90\%}}{\tau_{1/\mathrm{e}}} = \frac{\ln(0.1)}{\ln(1/\mathrm{e})} = 2.30\ldots \tag{5.8}$$

In the case of a time-dependent resistance $R_Q(V(t))$, the ratio differs from this value. The amount of the deviation of the ratio is a measure for the non-linearity of the IV characteristic. The greater the deviation, the more JFET-like is the resistor. The results obtained from the measurements are shown in Fig. 5.35a. By increasing the overbias voltage, the deviation from the standard RC element value is increasing too. This behaviour is in good agreement to the

---

[5] In other words: At $\tau_{1/\mathrm{e}}$, the voltage drop across the G-APD due to the avalanche breakdown has reached a value of 1/e of the maximum, which corresponds to a recovery of about 63%.

results from the simulations, which are also shown for comparison. The level of deviation depends on the pitch-gap combination of the cell as illustrated in Fig. 5.35b. A large size with a small gap tends to be closer to a standard RC element than a cell with the same size but a larger gap or the same gap but a smaller size. The reason for this behaviour can be found in the change of the bulk depletion during the recovery of the cell, which leads to the non-linearity of the IV curve. The amount of change in the depletion, and thus the resistance, is more pronounced for smaller active areas (small pitch, large gap) and increases with the applied overbias voltage.

To verify the described method for the estimation of the recovery time, a MPPC device from Hamamatsu was also characterised. For the recovery time $\tau_{90\%}$, a value of 103 ns was determined. Both characteristic times, $\tau_{90\%}$ and $\tau_{1/\mathrm{e}}$, are given in Table 5.7 and result in a ratio of around 2.3 ± 0.1, which is in good agreement to the expected value for a standard RC element (Eq. (5.8)). Furthermore, the influence of afterpulses and dark counts on the recovery time measurements was tested. Waveforms with and without these parasitic effects within the measurement window were recorded and analysed. The comparison is also shown in Table 5.7. By not correcting on the parasitic effects the recovery time is increased, since the 10% of the signal level is reached later in time and the standard deviation is larger too. The value without parasitic effects is in good agreement to the values obtained in Sec. 3.2.2.6 from the waveform analysis.

Parameter	with rejection (ns)	without rejection (ns)
Mean value $\tau_{90\%}$	103	122
Standard deviation $\tau_{90\%}$	6	32
Mean value $\tau_{1/\mathrm{e}}$	44	44
Standard deviation $\tau_{1/\mathrm{e}}$	3	11

Table 5.7: Determination of MPPC (100 µm) recovery time. Rejecting waveforms with detected parasitic effects leads to improved measurement results.

Due to the fact that the mobility in the bulk changes with the temperature, the recovery time is also expected to be temperature-dependent. In Fig. 5.36a the recovery time is plotted as a function of the overbias voltage at different temperatures. It can be observed that the time is increasing with the temperature, which is due to the fact that the resistivity of the bulk material is increasing. Fig. 5.36b shows the recovery time measurements at $V_{ob} = 2$ V as a function of the temperature in comparison to the values obtained from simulations. The results are in good qualitative agreement. A function is fitted to the data in Fig. 5.36b taking into account the temperature dependence of the mobility ($\propto T^{-2.4}$). Within the errors the data fit quite well to the expected behaviour. Taking also into account the dependency of the breakdown voltage on the temperature, an increased temperature dependence is expected for the recovery time since the depletion region in the bulk depends on the potential difference between external anode and gap. This is visible by the small deviation of the simulation results from the fit.

Additionally, the dependence of the recovery time on the geometrical dimension (pitch-gap combination) was studied. The measured and simulated results for devices with a pitch size of 130 µm and different gaps are shown in Fig. 5.37 as a function of the cell active area. By increasing the gap size which corresponds to decreasing the sensitive region, the non-depleted volume in the bulk is decreased resulting in a higher resistance. On the other hand,

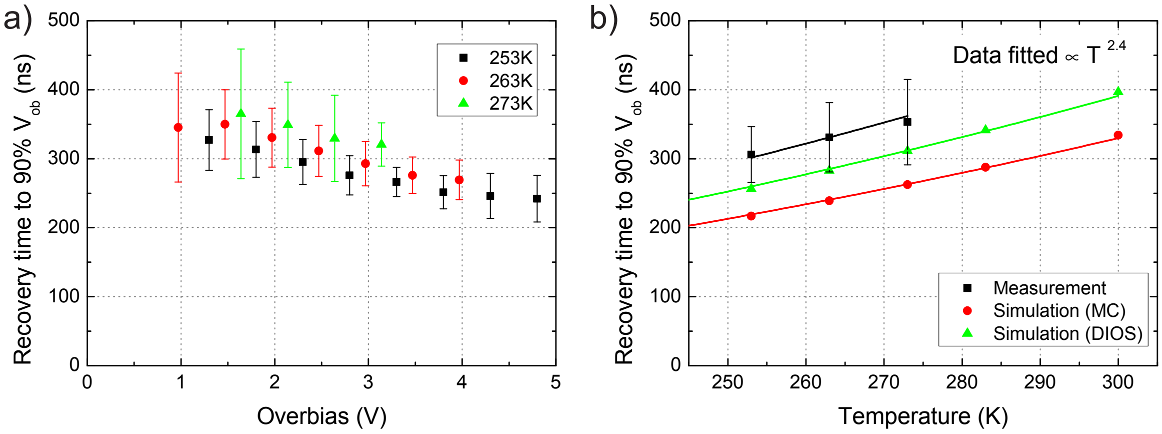

Figure 5.36: Recovery time as a function of the temperature (device with pitch/gap 130/10 µm). Due to the decreasing resistivity of the bulk for lower temperatures also the recovery time is decreasing. This is shown in a) as a function of the overbias for different temperatures. b) recovery times from measurement and simulation plotted versus the temperature and fitted with a function proportional to $T^{2.4}$, which corresponds to the change in the mobility [143]. All values for $V_{ob} = 2$ V.

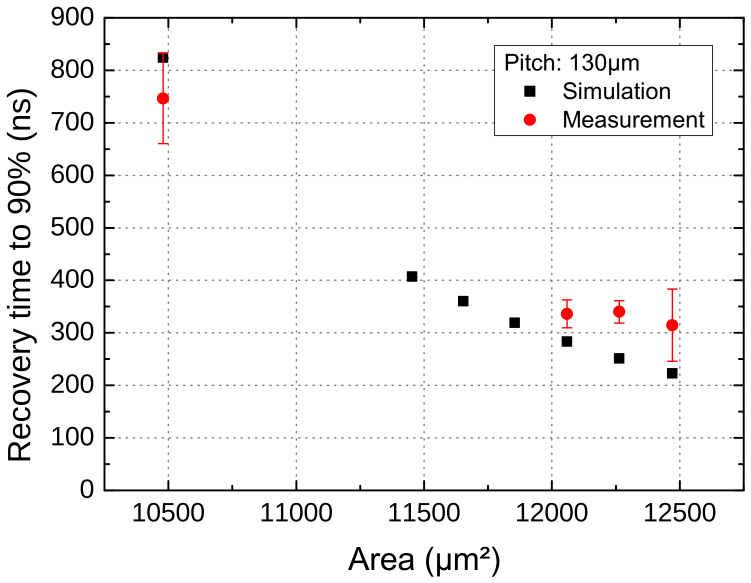

Figure 5.37: Recovery time versus sensitive area for pitch 130 µm at $V_{ob} = 2$ V. By reducing the area via increasing the gap size, the recovery time at a constant bias voltage is increasing due to fact that the non-depleted volume, which corresponds to the quench resistor is decreased. A smaller area also results in a smaller capacitance which should compensate the difference in R_Q. The increasing recovery time indicates that the change of the resistance is larger.

Overbias voltage (V)	2.0	2.2	2.4	2.6	2.8	3.0	3.2	3.4	3.6	3.8	4.0
ENF	1.4	1.5	1.7	1.9	2.0	2.6	3.0	3.6	4.2	4.9	6.1

Table 5.8: Excess noise factors of SiMPl detector as a function of the overbias voltage.

the capacitance of the cell is decreasing since the area becomes smaller with a bigger gap size, which should compensate in first approximation the increase in resistance according to

$$\tau = R \cdot C = \varrho \frac{l}{A} \cdot \varepsilon_0 \varepsilon_r \frac{A}{W} = \varrho\, \varepsilon_0 \varepsilon_r \frac{l}{W}, \tag{5.9}$$

with R defined by Eq. (4.1) and C defined by Eq. (2.19). The gain measurements confirm the linear dependency of the cell capacitance on the area (see Fig. 5.22). Since the recovery time in Fig. 5.37 shows an increase by reducing the area, it can be concluded that the change in the resistance, as a result of the varying sidewards depletion in the bulk, is larger than the change in the capacitance.

5.2.3.8. Determination of SiPM operating range

By using the optical cross talk in combination with the dark count rate and the measurement of the dark current, a new method to determine the recommended operating range of a SiPM was developed (see Ref. [151]). The basic idea is to compare the measured dark current of a SiPM with a calculated current value based on the dark count rate taking into account the OCT contribution. A deviation from the calculated current value indicates a discrepancy of the normal operation.

The dark current of a G-APD is defined by the charge per second flowing through the junction. Thus, for an ideal avalanche photo diode the current is given by the product of dark counts per second (DCR) and charge per pulse [152], whereas latter is determined by the elementary charge e multiplied by the gain G of the device. Therefore, the ideal dark current is

$$I_{ideal} = DCR \cdot G \cdot e. \tag{5.10}$$

By measuring the dark count rate, only the number of events above the trigger level (here 0.5 photon equivalent, p.e.), but not the number of simultaneously fired cells due to optical cross talk in the array is obtained. For SiPMs, the value of dark counts has to be corrected by the excess noise factor, given by N_X, which takes into account the parasitic contribution of optical cross talk. The method to calculate N_X was described in Sec 3.2.2.3 and is equivalent to the average number of fired cells per dark count event. The ENF for a SiMPl device at different overbias voltages is given in Table 5.8.

Thus, Eq. (5.10) changes to an OCT corrected dark current for SiPMs, which can be written as:

$$I_{OCT} = DCR \cdot N_X \cdot G \cdot e. \tag{5.11}$$

Based on this assumption, the ratio r of the measured dark current and the one calculated with Eq. (5.11) for an ideal device in normal operation is expected to be $r = 1$. With increasing the overbias voltage, problems in quenching should be identified by a disproportional enhancement of the measured current due to the self-sustaining avalanche process [142], leading to a high increase of r. Ideal in this context means that the contribution of surface leakage currents to the dark current measurements is neglected. In reality, an additional contribution of leakage currents results in a ratio r, which is slightly larger than one. However, since these currents are not amplified by the avalanche process, this contribution is only relevant for small overbias voltages and can usually be neglected (see Fig. 5.38).

In order to use the temperature coefficient of the quench resistor for the variation of R_Q, and thus the quenching condition (see Eq. (2.32) in Sec. 2.3.3) the devices were placed in a light-tight climate chamber.

Using this new method, the characteristics and relations of dark current and dark counts of devices from Hamamatsu, MEPhI-Pulsar and SiMPl were analysed in a comparative study. In Fig. 5.38, the ratio of measured and calculated current for a SiMPl device is shown as a function of the overbias voltages. A ratio of $r \approx 1$ for all estimated resistor values at low bias above breakdown voltage implies that the measured current is well predicted by the theoretical value. Small deviations are expected due to parasitic effects and can be minimized by improving the measurement setup. By increasing the bias voltage up to 4 V above breakdown, an increase of the ratio by a factor of 5–10 can be observed. According to Refs. [101, 142], the initiation of this increase depends on the value of the quench resistor via the quenching time, which is a function of the quench current I_f (see Eq. (2.32)). Thus, for a smaller resistance the quenching of the avalanche should get problematic at smaller values of V_{ob}. In order to compare different measurements, the overbias voltage needed to obtain a ratio of $r = 2$ was chosen. For a resistor value of $R_Q = 115$ kΩ, a voltage of 3.2 V above breakdown was measured, whereas for $R_Q = 160$ kΩ the overbias can be increased to 3.6 V, leading to quench currents of $I_f = 28$ µA and $I_f = 23$ µA, respectively (see Table 5.9)[6]. Since the quench resistor in the SiMPl approach, as mentioned earlier, is formed by the non-depleted bulk material, the mobility of charge carriers is increased by decreasing the temperature, thus leading to a positive temperature coefficient of the resistance [153]. Additionally, the breakdown voltage is decreasing with lower temperatures. Hence, the bias voltage for applying a certain overbias is decreasing too, which results in a slightly smaller lateral bulk depletion and reduces the value of R_Q. Furthermore, the change of the resistance with the overbias voltage has to be taken into account (JFET-like IV curve).

For comparison, the same measurement of a Hamamatsu MPPC with 50 µm pixel size is shown in Fig. 5.39. Also with this device, the measured value is in good agreement with the calculated one for small overbias voltages, which is indicated by the ratio of $r \approx 1$. At 2.75 V for $R_Q = 139$ kΩ ($I_f = 20$ µA), respectively 2.95 V for $R_Q = 183$ kΩ ($I_f = 16$ µA) the value of r starts to increase about one order of magnitude, showing the same qualitative behaviour as measured for SiMPl. Conventional SiPMs with polysilicon resistors have a negative temperature coefficient $\partial R/\partial T$ (non-linear behaviour, see Ref. [115]), leading to an inverted temperature dependence in comparison with SiMPl. Due to this different behaviour of the measurements with respect to the temperature and the opposite temperature coefficients, it can be assumed that the effect is related to the change in the resistance and thus the quenching of the avalanche breakdown.

In Table 5.9, the pitch size, the temperature T with the corresponding breakdown voltage V_{bd}, R_Q, and the determined current corresponding to $r = 2$ are listed for all devices tested in the study. The respective overbias, which has to be applied to obtain a ratio of $r = 2$, is shown in Fig. 5.40 for comparison. For the MEPhI-Pulsar device, at $T = 273$ K and $T = 253$ K, only a ratio of $r = 1.4$ was feasible due to the unstable performance of its measurements. The points, plotted in the graph, are therefore extrapolated values to $r = 2$. Except the SiMPl detector most of the devices tend to reach the regime of problematic operation at a current level which is below $I_f = 20$ µA. Since the resistor value of the SiMPl device

---

[6] Values recalculated compared to Ref. [151]

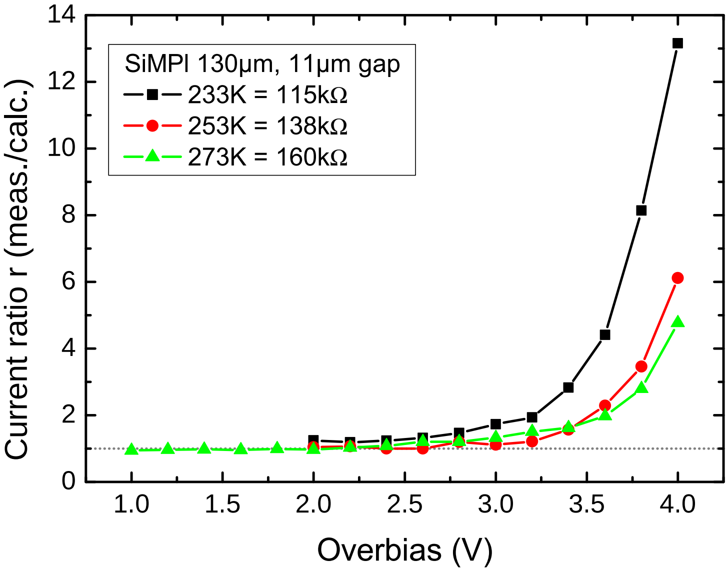

Figure 5.38: Ratio of currents for SiMPl device (pitch 130 µm, gap 11 µm) as a function of overbias voltage. The dotted line indicates a ratio of $r = 1$. A resistor dependent start of the increase of r can be observed.

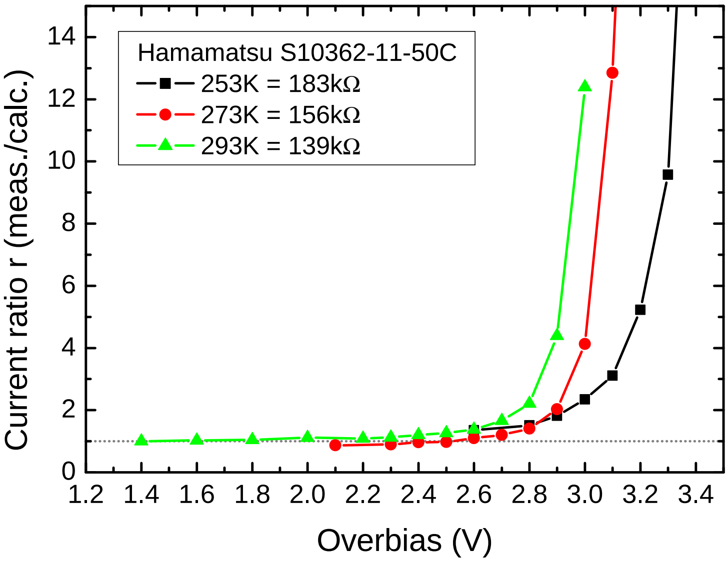

Figure 5.39: Ratio of currents for a MPPC with 50 µm pitch as a function of overbias voltage. The measurements show the same qualitative dependence on R_Q as measured for the SiMPl device.

Device	Pitch size (μm)	T (K)	V_{bd} (V)	R_Q (kΩ)	$I_f(r=2)$ (μA)
MPPC	25	293	69.4	332	17
	25	273	68.4	371	16
	25	253	67.5	417	15
	50	293	70.1	139	20
	50	273	68.9	156	19
	50	253	67.6	183	16
	100	300	70.2	125	13
	100	273	68.7	145	12
	100	253	67.6	163	10
	100	233	66.5	190	9
MEPhI	35	293	77.5	700	9
	35	273	76.2	855	8
	35	253	74.9	1030	7
SiMPl	130	273	35.2	160	23
	130	253	34.5	138	25
	130	233	33.9	115	28

Table 5.9: Pitch size, temperature, corresponding breakdown voltage V_{bd}, resistance R_Q and current I_f at $r = 2$ of all devices in this study. The sensor area was ca. 1 mm^2. For conventional SiPMs the values of R_Q were determined by IV measurements in forward bias. For SiMPl, R_Q was estimated by recovery time measurements and simulations. It has to be taken into account that the SiMPl resistance changes with the overbias voltage. Values recalculated compared to Ref. [151].

changes during the recovery process, an accurate determination of the quenching resistance is difficult. However, it should be noted, that this value of I_f is only a rule of thumb. The fact that the results do not fit to one straight line indicates that the quenching process seems to be influenced by other SiPM parameters (breakdown voltage, electric field distribution, temperature, etc.), too. More precise predictions require further studies with an optimised setup in order to eliminate parasitic effects.

In general, the measurements demonstrated that the dark current in normal operation is well described by the dark count rate and a coarse prediction of the operating range is already possible by measuring the dark current and identifying a disproportional increase. The accuracy of the determination is improved by measuring the dark count rate, taking into account the influence of optical cross talk. On the other hand, in combination with a known gain, the measurement of the dark current characteristics already allows an estimation of the range and the increase of the SiPM dark count rate via Eq. (5.10), due to the DCR-dark current correlation.

5.2.3.9. Photon detection efficiency

The photon detection efficiency of the devices was measured using the method explained in Sec. 3.2.2.9. Due to the high dark count rate, all devices were cooled down for the measurements to a temperature of $T = 253$ K. Thus, the DCR is reduced but the value of the quench resistor also decreases, which limits the maximum overbias voltage. The repetition

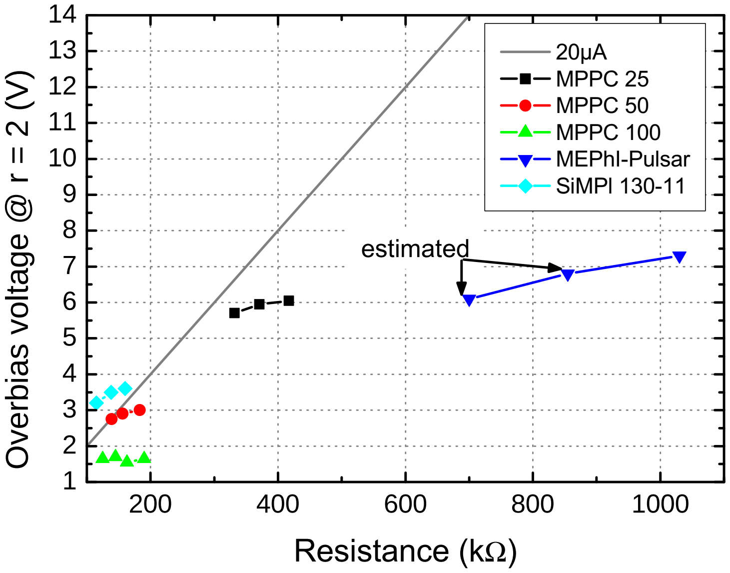

Figure 5.40: Overbias to obtain a ratio of $r = 2$ for different devices as a function of resistance. Due to the unstable operation of the MEPhI device only a ratio of $r = 1.4$ was achievable in the measurements at 253 K and 273 K. Therefore, those two points in the graph were extrapolated values to $r = 2$. The solid line represents the 20 µA rule of thumb, according to Ref. [101].

rate of the ps-light pulses was set to 300 kHz, providing sufficient time for the cells to recover between two consecutive pulses and to avoid effects of afterpulses.

The dependency of the PDE on the overbias voltage is plotted in Fig. 5.41. At 4 V overbias a PDE of 36% was measured for a wavelength of 405 nm. In the near UV (342 nm) still a PDE of 22% was obtained in the measurements. As shown in Eq. (3.23), the PDE is a product of the fill factor (FF), the quantum efficiency (QE) and the Geiger efficiency (ε_G). In contrast to the first two parameters, the Geiger effficiency depends on the voltage, and therefore also the detection efficiency changes with the applied overbias voltage. The dependency is clearly visible for both wavelengths plotted in Fig. 5.41. Up to a voltage of approximately 2.5 V (7% relative overbias) the PDE shows a strong, almost linear increase with V_{ob}. For higher voltages, the rise in the PDE is decreasing and a saturation effect is observed, which could be attributed to a saturation behaviour of the trigger efficiency (discussion below). As a rule of thumb, an overbias of $V_{ob} \approx 0.15 \cdot V_{bd}$ is required to reach the regime of full PDE saturation [129]. Assuming this value, the SiMPl devices should reach this situation at about 5 V overbias. In the measurements, the maximum applicable overbias was 4.5 V. An increase of the overbias beyond this value was not feasible due to pile-up events and quenching problems which can be traced back to the cooling of the device (lower resistor value).

Based on the results obtained by the TCAD simulations of the second prototype, the Geiger efficiency of the SiPM was simulated with the MC tool (see Sec. 3.1.3), in order to compare the voltage dependence with the characteristics of the PDE in the measurements. The electric field distributions, obtained from the two doping profiles (MC, DIOS), were transferred to the MC simulation tool which calculates the trigger efficiency depending on the applied bias voltage. Fig 5.42a depicts the Geiger efficiency for different temperatures as a function of the

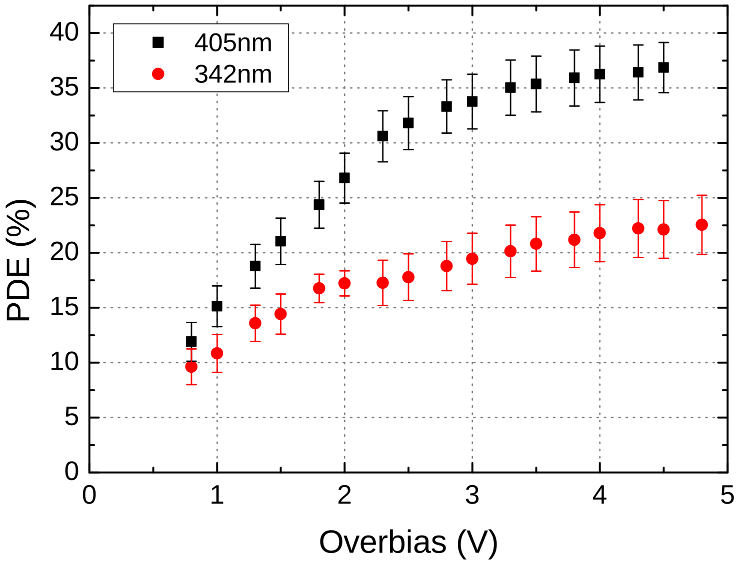

Figure 5.41: Photon detection efficiency of a SiMPl device with a pitch of 100 µm and 10 µm gap size as a function of the overbias voltage. For low overbias an increase is visible. A saturation behaviour sets in at around 3 V overbias. The measurement temperature was 253 K, which results in a breakdown voltage of $V_{bd} = 34.2$ V.

bias voltage based on the doping profiles obtained with DIOS, whereas Fig 5.42b illustrates the same results for the MC model. The generation of the electron-hole pair in both cases was assumed close to the surface which leads to electron dominated avalanche triggering. The breakdown voltage of the two models varies by about 2 V (at room temperature MC: 38 V, DIOS: 36 V). The temperature coefficient of V_{bd} in both simulations is (50 ± 12) mV/K. A comparison with the measured values ($V_{bd} = 36.5$ V, $\partial V_{bd}/\partial T = 36$ mV/K) shows that the breakdown voltage of the devices is between the results of the simulations, whereas the temperature dependence is overestimated by the MC tool. Within the uncertainties, which are discussed below, the breakdown voltage of the DIOS implant is in good agreement with the measurement results.

Differences can be observed in the steepness, and thus the saturation of the curves. From the simulated efficiencies, a value of 90% is reached at an overbias of roughly 9 V (27% relative overbias) which is in contrast to the rule of thumb and the trend of the PDE measurements in Fig. 5.41 where a saturation behaviour is reached at much lower voltages.

For comparison, the results for an ideal homogeneous electric field distribution with a depletion width of 1 µm is additionally plotted in Fig. 5.42a-c. Due to the smaller depletion width, the breakdown voltage at room temperature is reduced by 2 V and 4 V, respectively. The Geiger probability increases much faster ($\varepsilon_G = 90\%$ at 15% rel. overbias in good agreement with rule of thumb) compared to the field distributions obtained from the SiMPl 2 device simulations. This is illustrated in Fig. 5.42c, where the Geiger efficiencies, obtained from the simulations, are compared as a function of the relative overbias. In addition, ε_G values, which were converted from PDE measurements, are plotted. The conversion was performed on the basis of two different assumptions. On one hand, a Geiger efficiency of 85% at an overbias

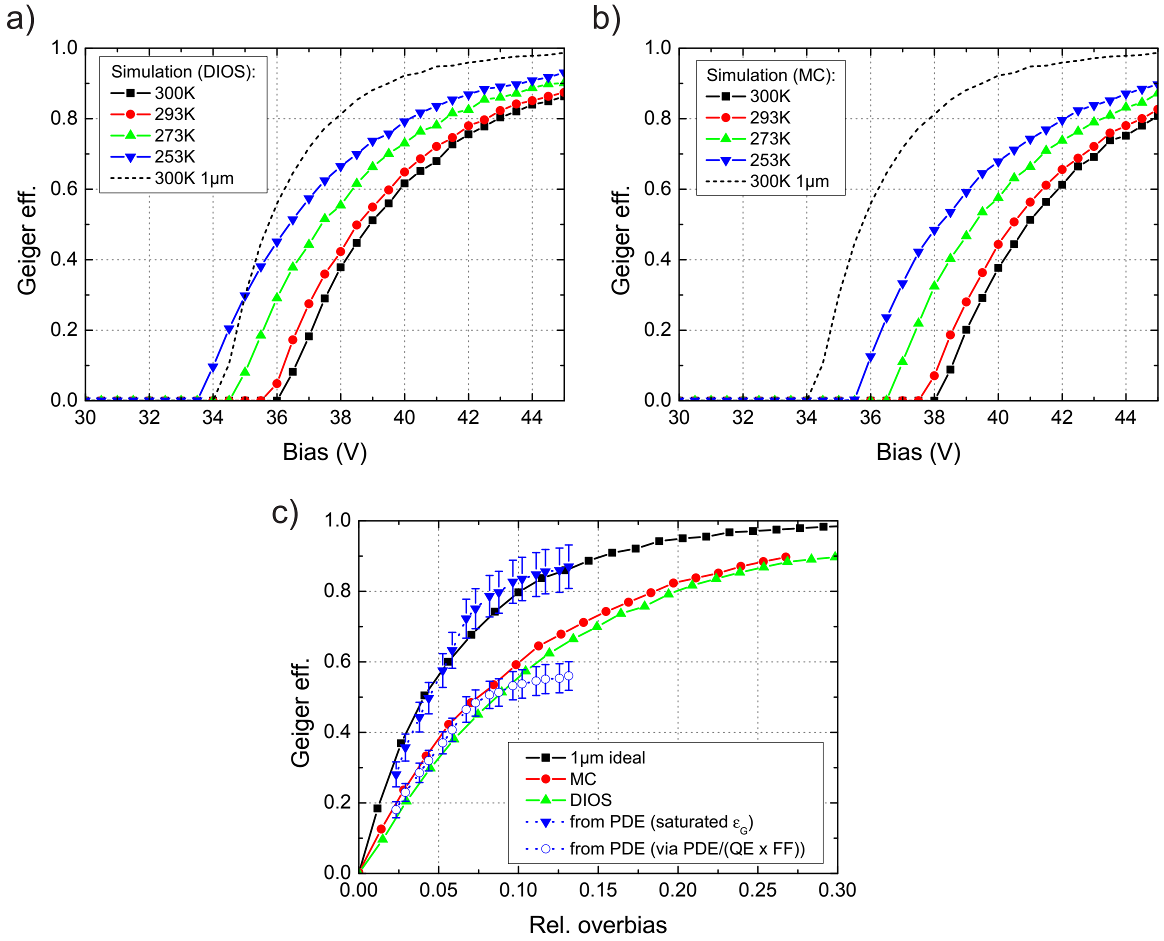

Figure 5.42: MC results for the Geiger efficiency as a function of overbias and temperature. a) results obtained with the high field implant based on the DIOS model, b) the corresponding values for a Monte Carlo model based implant (technology parameters based on SiMPl 2). The absorption was assumed to be close to the surface and is thus dominated by electrons. The decrease of the breakdown voltage with decreasing temperature is included in the model. The discussion can be found in the text. For comparison the result for a homogeneous electric field of 1 µm width is shown. c) Comparison of Geiger efficiency (ε_G) from simulations (DIOS, MC and test structure) to PDE measurements assuming on one hand $\varepsilon_G = 85\%$ for $V_{ob} = 4.5$ V (saturated ε_G). On the other hand, the measurements are scaled with respect to the value from Eq. (5.12) which results in a saturation behaviour at roughly 56%. Details are given in the text.

voltage of 4.5 V is assumed, which corresponds to the 15% overbias rule of thumb. On the other hand, based on a measured PDE of 36% an equivalent ε_G value of a device with a QE of 80% (see below) and a pitch/gap ratio of 100/10 is calculated via (cf. Eq. (3.23))

$$\varepsilon_G = \frac{PDE}{FF \cdot QE} = \frac{0.36}{0.81 \cdot 0.80} \approx 0.56\,. \tag{5.12}$$

Afterwards the PDE values from the measurement are scaled with respect to this data point.

If the saturation in the PDE is only due to the saturation of ε_G (first assumption, blue triangles), the good agreement of the PDE data and the simulated Geiger efficiency would implicate an ideal electric field in the depletion width. Since this is rather unlikely, the saturation effect in the PDE is most probably influenced by additional effects. The data obtained from the second assumption (white circles) is in good agreement with the values from the TCAD simulations, except the saturation at 15% relative overbias. This saturation effect at around 56% could arise from an increasing dark count rate, optical cross talk and afterpulsing with the overbias voltage. Thus, more and more cells are not fully recovered when the photons arrive which corresponds to a reduced effective bias voltage at the cells and could explain the PDE saturation at lower Geiger efficiency values.

It also has to be taken into account that the implantation and annealing models in the simulation tool can result in inaccuracies in the doping profiles compared to the fabricated structures, which in turn affect the electric field distribution and thus the Geiger efficiency. As shown in the comparison between DIOS and MC, a difference of 50 nm in the depletion region results in a difference of 2 V in the breakdown voltage. Like V_{bd}, the slope of the efficiency curve is also strongly related to the exact shape of the electric field distribution [154]. Maybe the electric field in the device is more homogeneous than obtained from the simulations, and thus closer to the ideal case. An additional contribution to the discrepancy could arise from the simplicity of the MC model, since an avalanche breakdown is a complex process. However, promising results have been obtained with similar MC models [102, 113].

For more accurate simulations and to distinguish between the two sources of errors, new prototypes for tuning the simulations to doping profiles obtained by e.g. SIMS[7] measurements are required. Thus, a higher precision in the prediction of the electric field and the trigger probability should be possible. Unfortunately, only test implants but no new devices could be provided in the time frame of this thesis.

As already mentioned in Sec. 3.2.2.9, the PDE is also a function of the energy of the incident photons. The wavelength dependence of the detection efficiency is shown in Fig. 5.43 for the same device as previously described. The overbias voltage in the comparison is set to $V_{ob} = 4$ V. The peak wavelength of the PDE is in the blue regime around 405 nm and is decreasing for longer wavelengths. This is a result of the p-on-n structure of the SiMPl device. With increasing wavelength, the absorption depth of the photons increases too. Therefore, the trigger probability is more and more dominated by hole injection. This behaviour is illustrated in Fig. 5.44, where the Geiger efficiency is plotted as a function of the single photon absorption depth. Also shown is the corresponding electric field distribution for $V_{bias} = 44$ V (DIOS). The two black curves show the results for two different bias voltages. In the simulations the absorption of a single photon corresponds to the generation of one electron-hole pair, where electrons move in positive direction. The maximum efficiency is obtained for absorption close to the surface. In this case the primary electron, which has a higher ionisation coefficient

---

[7] Secondary Ion Mass Spectrometry: Secondary ions from a sample, formed by a sputtering process with a primary ion beam, are analysed using a mass spectrometer [155].

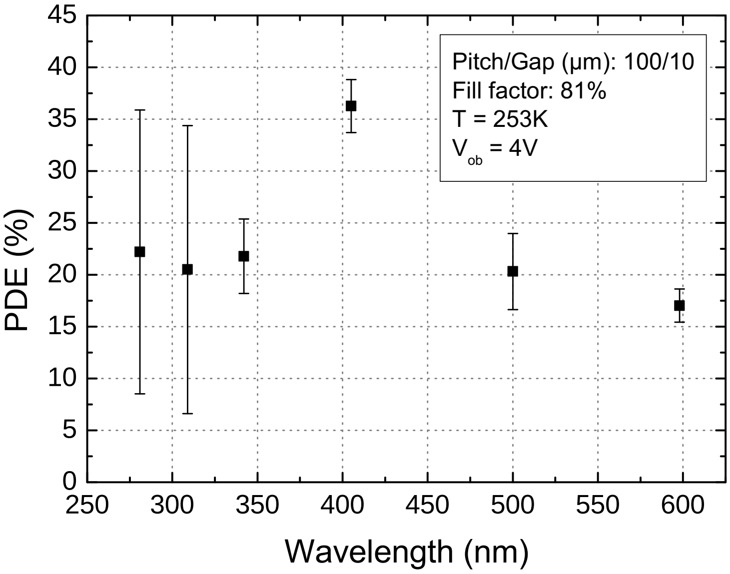

Figure 5.43: PDE as a function of wavelength. The highest efficiency was measured around $\lambda = 405$ nm. For longer wavelengths the PDE decreases due to the increasing avalanche initiation by holes. The PDE also decreases for shorter wavelengths but sensitivity in the UV range was measured. The large error bars are a result of the low quantum efficiency of the reference diode in the measurement setup (see Appendix B).

than holes, drifts through the whole high field region. With increasing absorption depth, the distance covered by the initial electron in the high field region becomes smaller and smaller. Once this electron does no longer drift through the entire area with an electric field above the critical field strength for impact ionisation ($>$ 300 kV/cm), the Geiger efficiency starts to decrease. From this point, the ionisation probability of electrons declines and the overall trigger probability is more and more dominated by the ionisation coefficient for holes. At about 1.25 µm the efficiency reaches a second plateau, corresponding to pure hole injection. In this region, the electric field strength is no longer sufficient for impact ionisation of electrons. With these results, the effective high field region where impact ionisation takes place can be reduced to an area between 0.35 µm and 1.25 µm, which corresponds to a field strength larger than 300 kV/cm. This is in good agreement to the values given in the literature [84].

The capability of detecting photons in the UV regime is an important requirement, especially for Cherenkov light detectors (cf. Sec. 1.2.2). Although the efficiency drops by nearly 50% from 405 nm to 342 nm, still a PDE of 22% was measured. Below 340 nm the QE of the reference diode in the measurement setup collapses (see Appendix B), which explains the large error bars for the measurements in this wavelength range. However, clear coincidence events could be observed on the oscilloscope which indicates sensitivity down to 280 nm.

Assuming a homogeneous quantum and Geiger efficiency for all devices, the PDE is only a function of the fill factor. A comparison of measured devices and the theoretical scaled values, normalised on the device with a pitch/gap ratio of 100/10 µm is shown in Table 5.10. Within the accuracy of the measurements a good agreement is achieved.

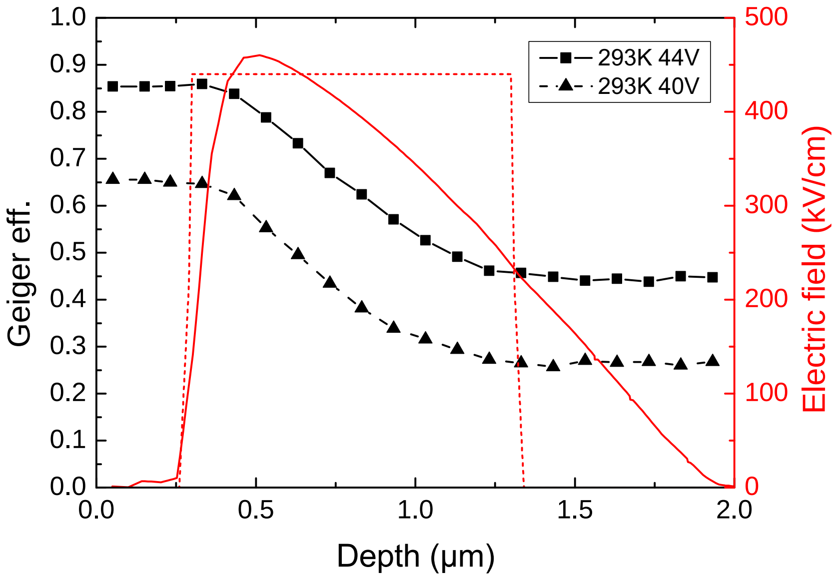

Figure 5.44: MC results for Geiger efficiency as a function of single photon absorption depth for two different bias voltages ($V_{bd} = 35.5$ V). Electrons move in positive direction. With increasing absorption depth the initial charge carrier, which triggers the avalanche, changes from electron to hole. Due to the lower ionisation coefficients of the holes the efficiency drops. Also shown (red scaling) are the electric field distributions from the simulation (DIOS) and the ideal homogeneous test field at $V_{bias} = 44$ V.

Pitch (µm)	Gap (µm)	Fill factor	PDE (norm.) (%)	PDE (meas.) (%)
100	10	0.81	14	14 ± 2
130	12	0.82	14	15 ± 2
130	20	0.72	12	13 ± 2
170	25	0.72	13	13 ± 2

Table 5.10: PDE of different pitch-gap combinations at $\lambda = 500$ nm and $V_{ob} = 2$ V. The normalised PDE values are scaled with respect to the device with a pitch/gap ratio of 100/10 µm. Within the errors a good agreement with the measured PDE is obtained.

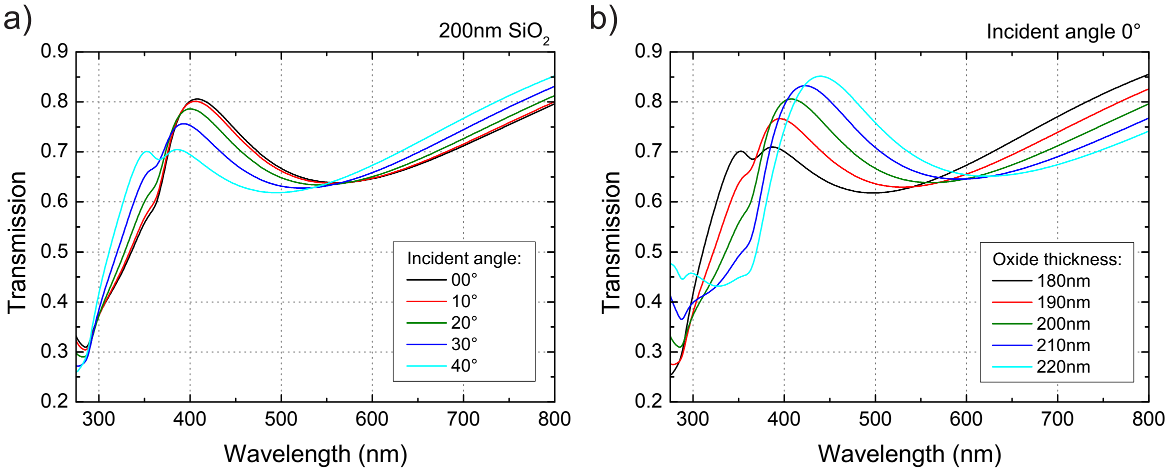

Figure 5.45: Simulated transmission to the silicon bulk for SiMPl 2. a) the transmission through 200 nm SiO_2 as a function of the wavelength. The incident angle with respect to the surface normal is varied. b) the variation of the transmission versus wavelength taking into account uncertainties of the oxide layer thickness (shown for perpendicular light incidence).

It should be noted that the devices of the second prototype were not optimised for UV sensitivity with respect to the shallow p^+ implant (see Sec. 3.2.2.9). Also no antireflective coatings were implemented to reduce the reflection of the Si/SiO_2-air interface for a specific wavelength. Thus, a certain amount of light is reflected from the surface due to the differences in the refractive indices. Instead, the silicon surface of the devices used for PDE measurements was covered with a layer of approximately 200 nm of SiO_2. The transmission to the silicon bulk, which has influence on the internal quantum efficiency, was calculated by using the simulation tool *OpenFilters* [128] with respect to variation of the incident angle and oxide layer thickness. The results for a layer of 200 nm of SiO_2 on a silicon wafer are plotted in Fig. 5.45a. It shows the transmission into the silicon for incident angles up to 40°. The transmission depends significantly on the wavelength of the incident light, whereas the dependency on the incident angle is less pronounced within the simulated regime. For the PDE measurements, most probable the light impinges in a cone of 0–15°. As can be seen, the maximum transmission is in the bluish region with a value of around 80%. By increasing the wavelength to 550 nm the transmission drops to 64% while a decrease of the wavelength to the ultraviolet region (300 nm) reduces the transmission by roughly 50%.

Taking also into account variations of the thickness of the SiO_2 layer, the change of the transmission is shown in Fig. 5.45b for an incident angle of 0°. It highlights how the values are changed by 10% of oxide thickness variations. A shift of the maximum in the blue regime and a drop of the transmission in the UV can be observed. Those non-optimised parameters limit the PDE of the present devices.

In summary, the first PDE measurements of SiMPl devices showed promising results taking into account that no optimised optical entrance window was implemented in the second prototype production. For devices with high fill factors (FF: 80%), antireflective coatings ($\approx$ 95% transmission) and operation in the saturation regime of the trigger efficiency ($\varepsilon_G \approx$ 90%) peak PDE values in the range of 65–70% should be achievable.

Pitch/Gap	Fill factor	Size	V_{max}			Recovery		
			Meas.	DIOS	MC	Meas.	DIOS	MC
(µm)	(%)		(V)	(V)	(V)	(ns)	(ns)	(ns)
100/10	81.0	10 × 10	5.0	3.5	3.1	430	466	349
110/08	86.0	10 × 10	2.7	2.2	2.0	312	242	196
110/10	82.6	10 × 10	3.2	2.9	2.5	415	352	280
110/12	79.4	10 × 10	4.0	3.5	3.2	540	526	406
120/10	84.0	10 × 10	3.0	2.4	2.1	444	292	241
130/10	85.2	10 × 10	3.3	2.0	1.8	300	256	217
130/11	83.8	10 × 10	3.6	2.2	2.0	350	290	244
130/12	82.4	10 × 10	3.8	2.4	2.1	330	328	275
130/20	71.6	10 × 10	5.0	4.4	4.0	750	1038	802
135/13	81.7	10 × 10	2.7	2.3	2.1	360	340	288
135/15	79.0	10 × 10	3.3	2.8	2.5	460	427	358
135/16	77.7	10 × 10	3.5	3.0	2.7	520	480	401
170/25	72.8	10 × 10	3.5	2.5	2.3	495	482	423
120/12	81.0	10 × 10 sq.	2.7	2.4	2.2	456	395	330
130/12	82.4	10 × 10 sq.	2.4	2.1	2.0	360	362	305
130/16	76.9	10 × 10 sq.	2.7	2.8	2.6	560	528	445
100/05	90.3	1 × 1	6.0	4.1	3.7	600	747	573
130/10	85.2	1 × 1	4.0	2.9	2.7	450	457	390
130/12	82.4	1 × 1	4.5	3.2	2.9	512	530	448
130/13	81.0	1 × 1	4.0	3.3	3.1	625	573	482
130/14	79.6	1 × 1	4.5	3.5	3.2	700	622	520
130/20	71.6	1 × 1	6.0	4.5	4.2	970	1155	907

Table 5.11: Comparison of measured maximum overbias voltage (V_{max}) and recovery time with simulation results. All values correspond to a temperature of 253 K. For the recovery measurements, an overbias of 2 V was applied. The maximum overbias voltage from the simulations is based on a 20 µA quench condition. An uncertainty of the maximum voltage measurements of ca. 0.5 V and 30–50 ns for the recovery time measurements has to be considered.

5.2.3.10. Process window for operating devices and validation of simulations

An equally important aspect in the evaluation of the prototype production of the SiMPl approach is the process window which allows normal operation of the detector. In this context, also a cross-check of the prediction accuracy of the simulations is of interest for future optimisations. For this purpose, the measurement results of the maximum operating voltage and the recovery times are listed in Table 5.11. In addition, the results obtained by the simulations (DIOS and MC) are stated as well.

Concerning the quenching of the avalanche, all devices showed a higher maximum overbias voltage than expected from the simulation results (with varying deviations). On one hand, this is caused by uncertainties in the simulation regarding the resistance value, as discussed in Sec. 5.2.1.4. On the other hand, the quench condition of 20 µA is only a rule of thumb, and hence sufficient quenching is also possible for higher current values. The measurements indicate that the current limit in the quench condition for obtaining operable devices could be increased to higher values (ca. 30 µA). However, a cross-check and fine tuning with measurements of an improved prototype are required. Although the SiPMs were designed for room temperature operation and aimed for a pitch size of 120 µm, all devices in Table 5.11 allow overbias voltages up to roughly 3 V at temperatures of 253 K. For many devices, the main limiting factors were rather optical cross talk and pile-up effects. In none of the tested structures pinch-off was detected, which is in agreement to the expectations from the simulation results. The device which is closest to pinch-off has a pitch of 100 µm and a gap of 10 µm. For an array of these cells, pinch-off does not occur below 40 V which is beyond a feasible normal operation due to dark counts, afterpulsing, optical cross talk and non-quenching. Even for a single cell element, which has the larger lateral bulk depletion, pinch-off would occur at bias voltages around 40 V.

Deviations are also determined for the recovery time of the cells. Depending on the applied implantation model the depleted volume in the bulk changes, and hence also the recovery time. On average, the recovery times are longer compared to the simulation which suggests that the quench resistance is higher than assumed in the simulations (consistent with results for V_{max}). However, the deviations are in an acceptable range and thus qualified for predicting the device parameters.

By comparing the hexagonal structures to the square cells, it can be observed that the maximum overbias voltage for the square device is reduced due to the fact that the area of the cell, and also the non-depleted volume of the bulk, is larger (see Sec. 5.2.3). The smaller resistance is compensated by a larger capacitance, so that the differences in the recovery time are less pronounced.

In contrast, the bulk depletion for single cells is increased due to the missing neighbouring cells, and thus the maximum overbias and the recovery times are increased compared to the values obtained from the array structures.

In summary, it can be concluded from the results of the characterisation that the SiMPl approach for achieving high PDE values (big SiPM cells) allows a sufficient process window for working devices, taking into account variations of parameters like pitch, gap, thickness or bulk doping. Most promising results at 253 K were obtained for a pitch around 130 µm. However, the design was based on a bias voltage of 50 V at room temperature. A new prototype would allow to further investigate the dimensional limits for operating devices by "worst case" layouts, which permit to reach both, the pinch-off and the non-quenching regime.

5.3. Third prototype

In parallel to the characterisation of the second prototype, new studies concerning improvements of the technology, especially the reduction of the dark count rate to allow room temperature operation and the suppression of edge breakdown were started. In addition, the feasibility of a cell size in the range of 20–50 µm was evaluated. Within the time frame of this thesis, a production of new prototypes could not be started. Therefore, this section is limited to simulation results and preliminary test structure measurements. As shown above, those simulation results may still contain uncertainties. To minimise this issue, the production of the third prototype is planned to be done in-house (except the high field implant), which gives better control over all the parameters in the fabrication and allows more accuracy in setting up the TCAD simulations.

5.3.1. Improvement of technology

In the first prototype production, severe edge breakdown of the devices was observed by emission microscope pictures (see Fig. 5.6). However, it only occurred on two of the six sides of the hexagons. As explained in Sec. 5.1.1, the reason for this was the orientation of the wafer in the implanter (see Fig. C.1), which resulted in a tilt angle of 7° for the implant of the internal anode. A detailed discussion about the wafer positioning is given in Ref. [110]. Based on this information, the tilt angle in the second prototype was set to $(0 \pm 2)^{\circ}$ because DIOS results suggested that with the given photoresist angle the edge breakdown effect can be minimised. As the results of the second prototype showed the edge breakdown in this iteration was reduced, but to all appearances the implantation was not performed at an angle of 0°. Considering the results of the MC simulation for an implant with a tilt angle of 0°, as shown by the red curve in Fig. 5.46, it can be recognised that the doping distribution is smeared out by the channeling effect (not considered by the implantation model in DIOS). For zero tilt, the main peak of the doping concentration is almost in the same order of magnitude as the second peak, which is caused by channeling. The lower peak concentration at the internal anode would result in an increase of the depletion width and, as a result, the breakdown voltage would increase significantly as well. Since this behaviour was not observed in the measurements of SiMPl 2, it indicated that the implantation was performed with a non-zero tilt angle. Furthermore, the slight edge breakdown in some devices also indicates a tilt angle larger than zero.

By deviating from a perpendicular implantation, the situation improves as can be observed in Fig. 5.46 too. For tilt angles, slightly different from zero, the amount of channelled dose is reduced (blue curve). However, for a wafer rotation angle like in variant *Rot A* the ion beam is still close to one of the crystal axis and the channeling peak is in the order of 10% of the peak concentration. If the rotation of the wafer is changed as well, such that the difference between the crystal axis and the ion beam is increased (*Rot B*), channeling can be further reduced even for tilt angles close to zero. This is shown by the green curve in Fig. 5.46.

A test implant was produced with the same parameters as were chosen for the green curve. The doping profile obtained from a SIMS measurement is in good agreement with the simulation result which leads to the conclusion that the implant can be well reproduced by the TCAD tool (also for parameters beyond standard CMOS specifications). However, significant deviations have been discovered, i.e. for implantation energies above 10 MeV as well as for thick oxide layers[8]. Furthermore, in order to improve the predictions of e.g. the electric field by the simulation tools, also measured doping profiles of annealed wafers are required.

An additional approach to improve the edge breakdown suppression is to decrease the amount of doping concentration in the transition regions of the deep n-implants by increasing the steepness of the resist angle. Thus, the effective resist thickness for the ion beam is increasing much faster at the edge of the resist resulting in less doping concentration in this region (comparable to the situation in Fig. 5.7a), which also reduces the local electric field maximum in this part of the Geiger cell.

The third parameter is the annealing scenario which is also connected to the reduction of the leakage current of the device. In order to activate the doping material and to remove the crystal damage which occurred during the high energy ion implantation, the wafer is heated up to a high temperature for a certain amount of time. The associated diffusion of

---

[8] private communication with Rainer Richter and Stefan Aschauer

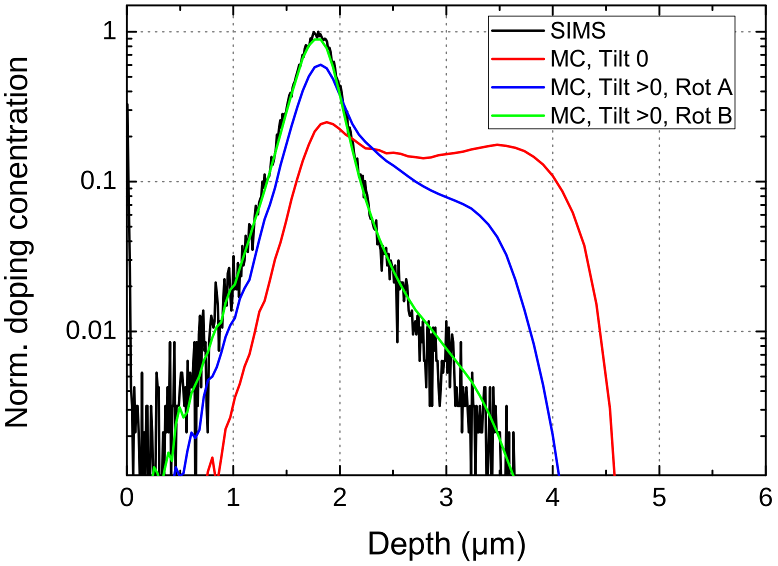

Figure 5.46: SIMS profile in comparison with TCAD simulations with different tilt and rotation angles. The green curve corresponds to a simulation with the same parameters as used for the implantation and shows very good agreement with the SIMS measurement. For a tilt angle of 0°, the primary concentration peak is similar to the channeling peak. By increasing the tilt angle, channeling is reduced but still significant since rotation *Rot A* is still close to one of the crystal axes. By changing also the rotation to *Rot B*, the channeling is minimised. The values for the doping concentration are normalised to the maximum of the SIMS profile.

the dopants can help to attenuate the peak concentrations in the edge of the high field region of the device and thus avoiding early breakdowns. On the other hand, the diffusion also changes the doping distribution in the avalanche region which may result in an increasing inhomogeneity of the electric field.

The suppression of edge breakdown by additional guard ring structures, as described in Ref. [135], was not considered in the technology improvements for the third prototype. A guard ring implementation would lead to additional process steps in the device fabrication (mask steps, implantation, annealing), whereas the idea of the SiMPl approach is to minimise the production steps for a SiPM.

Based on 2-D TCAD simulations, intensive studies concerning the doping profiles, electric fields and breakdown properties were performed to investigate the influence of tilt and resist angle as well as time, temperature and atmosphere (reactive, inert) of annealing scenarios. Detailed technology parameters cannot be given.

The general results are plotted in Fig. 5.47. The graphs show the Geiger efficiency as a function of the bias voltage. In each plot, a comparison between a result obtained for a charge trajectory in the centre of the SiPM cell and at the position of the local electric field maximum is illustrated (cf. Fig. 3.3 in Sec. 3.1.3). In Fig. 5.47a, the Geiger efficiency is compared for two different tilt angles, whereas *Tilt A* > *Tilt B*. In both cases, the devices have severe edge breakdown ($\Delta V_{bd} \approx 4$ V). By changing the resist angle to *Type2* > *Type1*, while keeping the other parameters constant, the situation improves drastically as can be seen in Fig. 5.47b. The difference in the breakdown voltages seems to be smaller than 0.5 V.

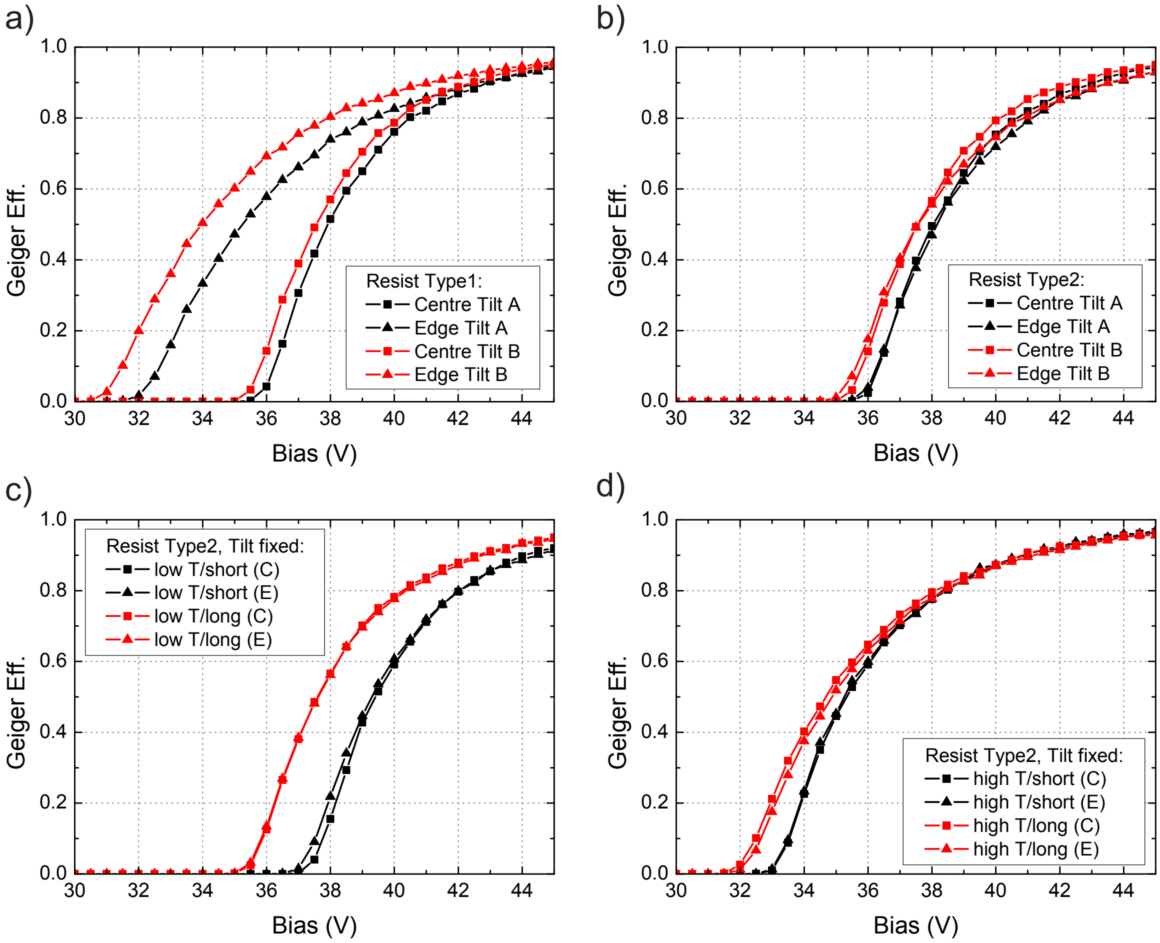

Figure 5.47: Comparison of different technological approaches to suppress edge breakdown in G-APDs. a) Geiger efficiency at centre (squares) and edge (triangles) position for two tilt angles (*Tilt A* > *Tilt B*). The resist angle in this case was *Type*1. Edge breakdown is clearly observable by the reduced breakdown voltage at local maximum of the electric field at the edge. b) change to a resist angle of *Type2* > *Type1* in comparison to a). The difference in the breakdown voltages is significantly reduced. c-d) Resist and tilt angle are fixed but the annealing scenarios differ. Diffusion of the doping concentration leads to changes in V_{bd}. Edge breakdown seems to be completely suppressed.

Thus, a steep photoresist edge is desirable to increase the tolerances of the fabrication process and minimise edge breakdown effects. Figs. 5.47c+d illustrate a comparison of the situation for different annealing scenarios. In both cases the resist and tilt angles are fixed. While a long annealing time at low temperatures seems to be sufficient to avoid edge breakdown, the effect is not completely suppressed by annealing with the same temperature but for a shorter time. Increasing the temperature reveals that edge breakdown can be also suppressed for short annealing times, as shown in the lower right. This is caused by the diffusion of the dopants and thus the reduction of the local electric field maximum in the edge region.

Concerning the breakdown suppression, no significant differences could be observed by changing the annealing scenario from reactive to inert atmosphere (assuming a steep resist angle), except from the change in the breakdown voltage itself. For very long and hot annealing, the steepness of the increase in the Geiger efficiency starts to change, which is already indicated in Figs. 5.47c+d. The reason is the increased diffusion with higher temperature and time. The doping diffusion by such an annealing scenario also leads to a more inhomogeneous electric field distribution in the centre of the cell, as illustrated in Fig. 5.48. The plot on the left hand side already indicates that, in comparison to an inert ambient (same time and temperature), an annealing under a reactive atmosphere increases the diffusion of the deep n-implant profile by injecting point defects into the silicon (oxidation enhanced diffusion, [156]). This results in a smaller depletion width[9] and a less homogeneous electric field profile. However, the shapes of both depicted distributions are still comparable. By increasing the temperature ($Temp1 < Temp2 < Temp3$), as plotted in Fig. 5.48b, the shape of the electric field starts to change, which is even more developed by increasing the time as well.

In summary, simulation results of different resist, tilt and wafer rotation angles in combination with different annealing scenarios lead to the following conclusions:

- the amount of dose channeling depends on the tilt and rotation angle of the wafer during implantation
- for edge breakdown suppression a tilt angle of 0° is preferred (independently from the resist angle) but results in a distinct channeling of dopant ions (decrease in peak concentration by a factor of five). As shown in Sec. 5.2.1, the channelled dose also influences the sidewards depletion from the gap into the bulk and thus the value of the quench resistor. This effect has an even more severe influence for smaller cells on thin wafers.
- a steep resist angle allows to increase the tilt angle as well as to reduce edge breakdown. The steeper the resist edge, the larger is the tolerance of the tilt angle.
- edge breakdown suppression benefits from hot annealing scenarios via diffusion. In turn, the homogeneity of the electric field distribution in the avalanche region is affected. The more homogeneous the electric field in the avalanche region, the smaller is the relative overbias for achieving a Geiger efficiency of 90%.

In general, the simulations revealed that the resist and the tilt angle are the crucial parameters for achieving a guard-ring free device without edge breakdown.

---

[9] It has to be taken into account that the oxidation consumes silicon from the substrate. As a result, the Si/SiO_2 interface is shifted towards the doping concentration peak. In combination with the subsequent boron implantation this influences the resulting pn-junction and thus the electric field distribution.

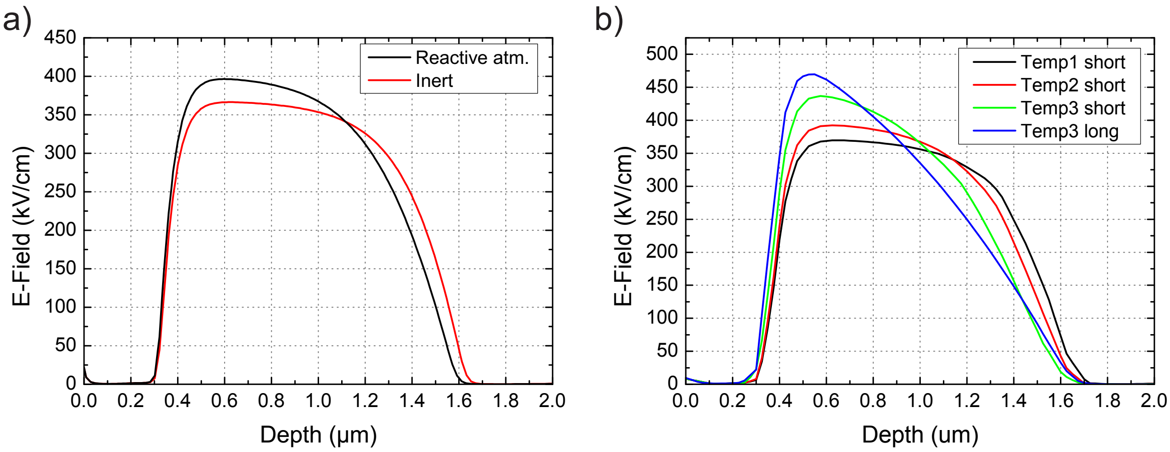

Figure 5.48: Electric field distributions for different annealing scenarios. a) comparison of electric fields obtained from an annealing with and without a reactive atmosphere (same temperature and time). The increased diffusion under the presence of a reactive gas leads to a smaller depletion width and a more inhomogeneous electric field profile. b) electric fields for different temperatures (*Temp1* < *Temp2* < *Temp3*). Increasing the temperature leads to a higher diffusion and results in a less homogeneous electric field. The same is true for increasing the annealing time as is also shown in b), where the field is approximating a triangular shape. The applied bias voltage for all structures is $V_{bias} = 38$ V.

Since the technology to realise photoresist edges with the required steepness is now available at the semiconductor laboratory, test structures, based on the simulation results, have been produced on standard wafer material for investigation of the technology parameters on the leakage currents and the edge breakdown. Fig. 5.49a depicts preliminary IV measurements from five different annealing scenarios. The annealing time for all wafers is the same. Very low leakage currents in the order of 10 pA and a well defined breakdown voltage at 35 V can be observed for the device from the wafer at *Temp3* (highest temperature) under a reactive atmosphere. Decreasing the temperature of the annealing process results in an increase of the leakage current. By changing the scenario to inert atmosphere conditions, an additional small increase of the leakage current is measured. The influence of the annealing on the breakdown voltage is visible too. The different diffusion of the dopants results in a change of the electric field distribution (see Fig. 5.48) and thus in the breakdown voltage. The annealing scenario still has to be optimised, since a long annealing results in a further increase of the leakage current as illustrated in Fig. 5.49b, where the IV characteristics of devices annealed with same temperature but different times are compared. This effect could be caused by diffusion of impurities from the atmosphere into the silicon during the long high temperature process.

Concerning the edge breakdown, the preliminary results showed a small change of the edge breakdown characteristics over the wafer for all annealing scenarios. This is most probably caused by inaccuracies in the wafer position in the implanter and the tilt angle variation over the wafer. Therefore, annealing scenarios are preferred which can reduce the effects of these uncertainties as far as possible. It was observed that good results with respect to the edge breakdown suppression were achieved with all inert annealing scenarios, but as previously discussed the leakage current is increased compared to the reactive atmosphere scenario. As emission microscopy pictures from the wafer with the highest temperature (*Temp3*) under reactive atmosphere indicate (Fig. 5.49c), devices without edge breakdown and low leakage

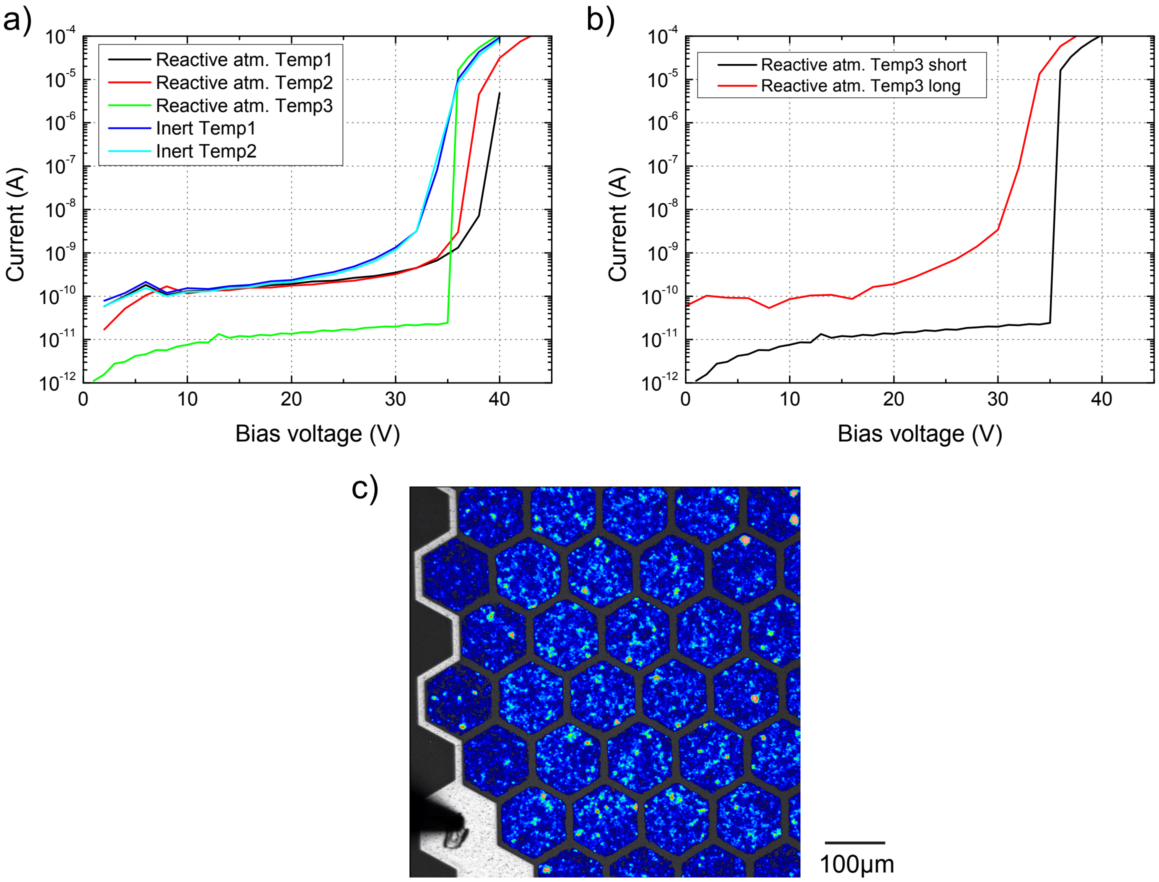

Figure 5.49: Preliminary results of SiMPl 3 test structures. a) IV curves of devices from five wafers with different annealing scenarios. The annealing time for all plotted wafers was the same. The best result concerning the leakage current is achieved with the highest temperature under reactive atmosphere. b) Current voltage measurements for the same temperature but different time. The leakage current for long annealing is increasing again. c) emission microscope picture of the wafer with reactive atmosphere, *Temp3* and short annealing time (lowest leakage current option plotted in a)). No edge breakdown is observed.

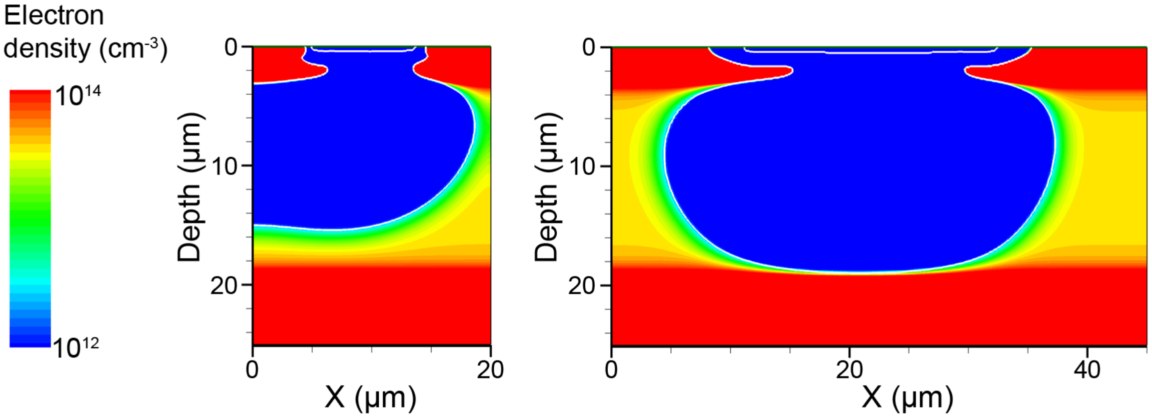

Figure 5.50: Electron density distribution for two different pitch-gap combinations of SiMPl devices with small cell size (stationary simulation including auxiliary contacts). On the left hand side a device with pitch 20 µm and the minimum gap size of 5 µm is shown. The depletion region extends to the full area below the cell (pinch-off). By increasing the pitch (45 µm), pinch off is avoided, as can be seen on the right hand side, and the quench condition becomes the limiting factor.

currents can be realised by using this annealing scenario. However, as already mentioned, the presented results are preliminary. A detailed characterisation of all test wafers will be a subject of further studies and allows a deeper understanding of the process with more precise conclusions.

5.3.2. Studies for devices with small cell size

For the next production, also the fabrication of devices with small cells (pitch of 20–50 µm) is planned. Because of the lower fill factor, these SiPMs have a lower PDE compared to devices with pitches in the range of 100 µm, but they offer a higher dynamic range and are thus of interest for applications like calorimetry in future linear colliders. Since the quench resistor depends on the cell dimension and the gap size (see Eq. (4.2)), a change of SOI material is needed[10]. In particular, the thickness and the resistivity of the sensor wafer have to be adjusted to avoid pinch-off and to provide a sufficient resistor value (20 µA rule of thumb, [101]). This requires new simulations in order to find the parameter space for a working device, as it was done for the first prototype production in Sec. 4.2. For the small cells a stronger influence on the technology parameters is expected because the doping diffusion affects the resistivity of the bulk to a greater extent than for the big cells with a thicker SOI material. Both, the diffusions from the internal anode and the back side contact have to be considered, since they define the remaining amount of volume at bulk doping level. The improvements and customisations of the simulation tools, which are one of the achievements of this thesis, allowed reliable studies of those devices.

Extensive simulations showed that a thickness of 25 µm is the most promising candidate for a specified bulk resistivity of 400 Ωcm. For the feasibility study, the structures with the auxiliary contacts were used, in order to determine the IV characteristics and to estimate the

---

[10] SOI technique for prototyping is used because of the established technology in the laboratory. As was shown in Ref. [157], a realisation of devices with small cells on epitaxially grown material is also possible and offers an easier and cheaper mass production.

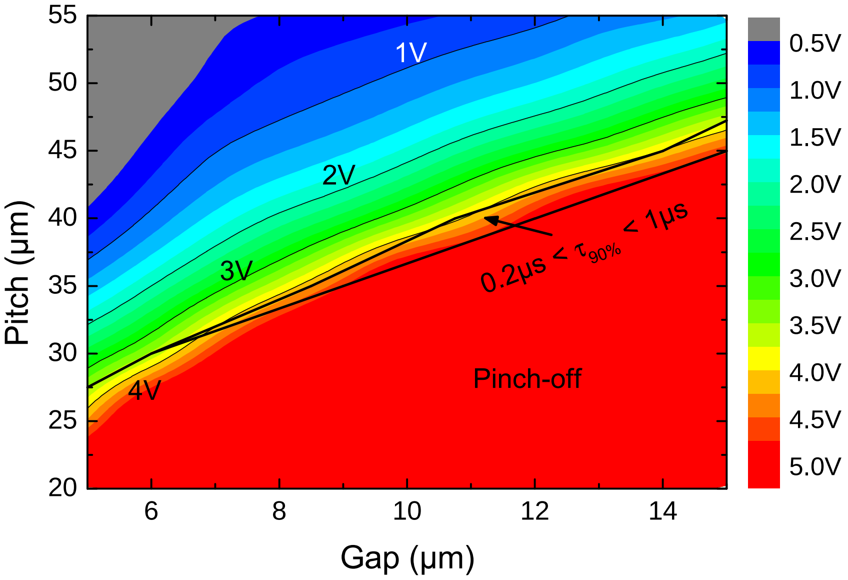

Figure 5.51: Overview of maximum overbias and recovery time for small cell size. A SOI material of 25 µm thickness with a bulk resistivity of 400 Ωcm was assumed. The results suggest a minimum cell size of 35 µm. In first approximation, the transition from normal operation to pinch-off corresponds to the isoline for a maximum overbias voltage of $V_{ob} = 4$ V, whereas pinch-off can be associated with the red area.

recovery time. For illustration, the obtained electron density distributions for two different pitch-gap combinations are shown in Fig. 5.50. The left half of the simulated structure corresponds to the investigated cell (cylindrical symmetry). The right half emulates the influence of an adjacent cell in an array but with different boundary conditions, which explains the asymmetry in the results (i.e. different behaviour of left and right cell). In the plot on the left hand side (pitch/gap: 20/5 µm) the depletion region from the gap extends to the full area below the internal anode, even for the minimum gap size. Structures which show this pinch-off effect are ruled out because of the voltage drop across the bulk resistor. As a result, the potential of the internal anode is reduced and the G-APD is not fully biased. The pinch-off effect can be avoided by increasing the pitch of the cell, as shown on the right hand side in Fig. 5.50 for a device with 45 µm pitch and a gap of 12 µm. On the other hand, the resistor matching for passive quenching devices requires sufficient resistor values to allow operation at a relative overbias in the range of 15% of the breakdown voltage (trigger efficiency). Since the thickness of the SOI material is small, the cross-section of the non-depleted bulk area has to be small as well, according to Eq. (4.2).

With the TCAD tool of Synopsys automated simulations were developed in order to cover wide range of device parameters. An overview of the results for different pitch-gap combinations with respect to the maximum overbias voltage and the recovery time is shown in Fig. 5.51. Due to technological restrictions the minimum gap size of the devices is set to 5 µm. The pitch size was studied between 20 µm and 55 µm.

From the results, based on the current technology, it can be concluded that a realistic minimum cell size is in the range of 35 µm with a gap of 7 µm (FF: 64%). For all devices with a pitch below 30 µm, pinch-off was observed assuming a breakdown voltage of ca. 35 V. This behaviour was already illustrated in Fig. 5.50. By increasing the cell size, the pinch-off state is shifted to a larger gap distance resulting in an increased process window for working pitch-gap combinations. For devices with 50 µm pitch, no pinch-off was observed up to a gap of 15 µm (FF: 49%). On the other hand, a large pitch/gap ratio is associated with a small resistance and thus a low maximum overbias voltage due to the quench condition in passively quenched G-APDs (20 µA rule of thumb).

As long as pinch-off is avoided, small cells offer fast recovery times (10–100 ns) due to their small capacitances. This operating range corresponds to the blue and green areas in Fig. 5.51. Also illustrated is the narrow transition regime ($0.2\ \mu s < \tau_{90\%} < 1\ \mu s$) from normal operation to pinch-off within an increase of 1–2 µm in gap size for a given pitch. As indicated by the results of the simulations the maximum overbias voltage is limited to roughly 4 V which is already close to pinch-off and thus corresponds to a recovery time in the range of 200 ns to 400 ns. This voltage value is already in the range of roughly 10% relative overbias assuming a breakdown voltage of 35 V. Since a high PDE is not a goal of devices with a small cell size, a lower relative overbias voltage can be afforded. However, the temperature dependence of the SiPM response decreases for devices in full PDE saturation.

According to the simulations, the small cell production offers only a small process window, with the most promising pitch-gap combinations close to the isoline of 3 V overbias. The influence on doping variations should be smaller compared to the big cell structures, since the uncertainties in the doping variation increases with the resistivity of the bulk material [136].

In order to proof the feasibility of the concept for small cells, a prototype production with a variation in pitch-gap combinations is necessary, which will also allow further investigations of the characteristics and a cross-check of the simulation results. It should be mentioned that significant changes in the technology (i.e. the annealing scenario) affect the depleted volume as well as the effective bulk resistivity and thus may lead to different results.

If the SiPM is used for particle tracking, single cell readout is required (see Sec. 6.1.1). Thus, the limitation for the quench resistor can be loosened by the implementation of an active quenching circuit for the individual cells [101,158,159].

6. Future concepts

In order to further explore different application areas, first ideas for the next SiMPl generation were developed and will be discussed in brief in the following chapter. First, two approaches for single cell readout focussed on particle and photon detection, respectively, are presented. Afterwards, the suppression of optical cross talk by implementing trenches is discussed and in the final section the feasibility of operating SiMPl devices at cryogenic temperatures is studied.

6.1. Single cell readout

The aim of high precision measurements with future LC machines, in particular the need to separate bottom and charm vertices (flavour tagging for e.g. branching fractions of a Higgs boson), results in challenging requirements for the innermost part of the detector, the vertex tracking system. Main goals which should be met by the detector are a hit resolution of 5 µm and a single bunch time resolution to suppress background [15]. In order to achieve less than 0.3% radiation length per layer, a low power consumption of the detector (and readout electronics) is required. Thus, thin devices with small cell size, fill factors close to one, fast read-out possibilities and low power consumption have to be developed.

Since for tracking applications the detection of a particle hit does not require a signal proportional to its charge, G-APD arrays have the potential to be utilised for measuring particle tracks in a vertex detector. Furthermore, they have a large signal amplitude and the fast build-up time of the avalanche (sub-ns) results in good timing properties which fit the bunch crossing times in future colliders (i.e. ILC: ca. 300 ns bunch crossing separation [16]). The SiMPl concept offers the advantage of a fast signal due to the avalanche process as well as a high fill factor and reduced material budget due to the thinned SOI approach. Of course, the application in tracking systems requires the implementation of a substructure readout of the array down to single cells. However, this implies a readout line for all the individual cells which could be achieved by either increasing the dead space within the array for contact lines and integration of the readout electronics or by the introduction of flip-chip bonding or 3-D integration [160, 161].

In single cell readout mode a distinction between a signal generated by photon absorption or by thermal generation is not possible and thus the high dark count rate becomes problematic. For suppression of dark count trigger events, either a sum-trigger threshold above 1 p.e. can be defined or the G-APDs are operated in gated mode [162]. By keeping the diodes only active ($V_{bias} > V_{bd}$) for a short period of time, the dark count rate is drastically reduced and afterpulsing is mostly avoided (with dedicated off times in the order of few 100 ns). However, this requires applications where the arrival of the signal is known in advance and the on-state of the cells can be synchronised with the event.

In addition to the tracking of MIPs, also a single cell readout concept for the use of SiPMs in the detection of low light signals with spatial resolution (single photon imager, [163]) is under development.

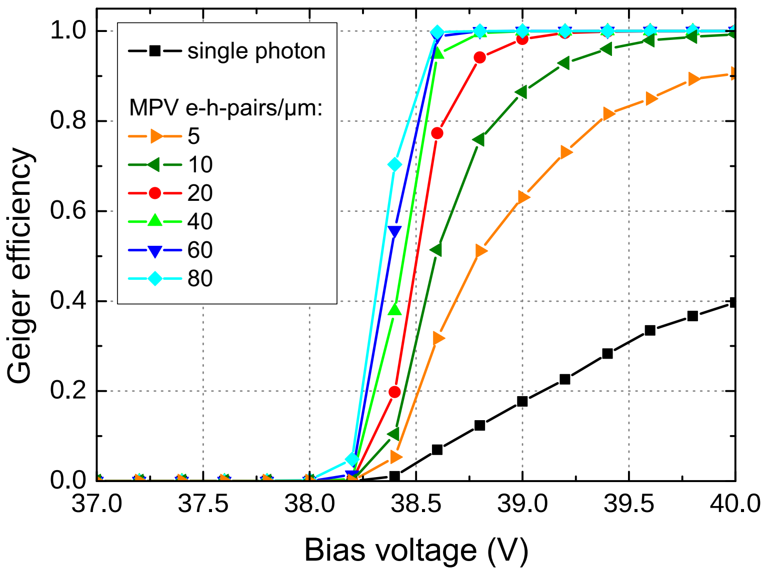

Figure 6.1: MC simulation of Geiger efficiency for MIP detection under the assumption of normal incidence and various most probable values (MPV) for e-h generation in comparison to single photon absorption. The width of the depletion region is approximately 1.4 µm (doping profile from SiMPl 2).

6.1.1. Particle detection

A minimum ionising particle looses a predictable amount of energy while passing through a semiconductor of a given thickness (Bethe-Bloch formula). The number of generated electron-hole-pairs is proportional to the amount of deposited energy. Due to momentum conservation, the energy to create an e-h-pair in silicon is 3.6 eV. The most probable value of the Landau distribution of the deposited energy for a MIP is approximately 270 eV/µm, which corresponds to the generation of ca. 80 e-h-pairs per µm while propagating through silicon [13]. However, this value is averaged over several micrometres and on short distances or thin material variations, also from the Landau distribution, are expected.

Since the number of MIP-generated e-h-pairs in the depletion region is much higher than for single photon absorption, the probability to trigger an avalanche is significantly increased. For this kind of applications, the devices can be operated with a smaller overbias voltage compared to single photon detection. The results from the MC simulations of the trigger probability, assuming different most probable values for the electron-hole generation by the MIP, are shown in Fig. 6.1. In the MC tool the e-h-pairs are randomly distributed over the depletion region of the G-APD to take into account the spatially distributed charge generation by the MIP. As can be seen, even for a value of 20 e-h-pairs/µm the trigger probability at 1 V overbias is almost equal to one. The situation improves even more if the number of generated e-h-pairs is increased to 80. According to the simulations the overbias can be reduced to $V_{ob} = 0.5$ V. In comparison, the trigger probability for single photon absorption, which corresponds to a single e-h-pair, is significantly smaller. Thus, the results suggest that the SiPM can be operated at a relative overbias of 1–3%. Measurements of the accurate MIP detection efficiencies with SiPMs are a subject of further studies.

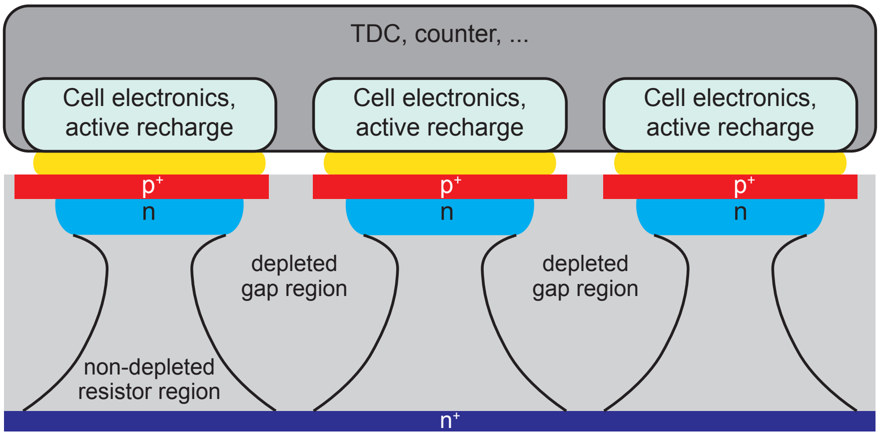

Figure 6.2: SiMPl approach for particle detection in vertex tracking detectors. By structuring the common cathode implant, individual cell readout can be realised by bump-bonding to the surface. As a consequence, the device is optically blind.

The decrease of the overbias voltage is associated with a reduction of dark count events and afterpulsing as well as OCT. Since the trigger efficiency for a single electron-hole pair is reduced compared to the standard overbias range in light detection (ca. 10–15% of V_{bd}), the DCR is reduced by roughly one order of magnitude. The correlated noise (afterpulsing and optical cross talk) is further reduced by decreasing the overbias due to the fact that the gain is a function of V_{ob}. Less charge carriers in the avalanche result in less emission of photons as well as a lower probability of filling charge traps during the avalanche breakdown.

An advantageous aspect of the SiMPl approach is that for the adaptation to particle tracking no fundamental changes of the basic structure are necessary. In order to electrically separate the individual cells, a structuring of the common cathode is required. This can be achieved without additional effort, by using a different structured mask compared to the common cathode lithography step for the standard SiMPl approach. Additional mask steps are only necessary to add an under bump metallisation (copper). All other process steps are the same as for the standard device. Afterwards, the cells have to be individually connected via bump-bonding techniques on the free and flat surface of the SOI wafer, which is one advantage of the SiMPl concept. As a result, these arrays cannot be used for photon detection, since such a device is optically blind. A general sketch of the particle tracking approach is shown in Fig. 6.2. Via the bump-bonds appropriate cell electronics for the readout, and optional active quenching, can be connected as well as further electronics like time-to-digital converters, counters, etc.

In order to proof the general feasibility of the concept, such a structure was simulated with TCAD tools and the result is plotted in Fig. 6.3. On the left hand side, the electron density for a cell size of 35 µm with a gap of 7 µm at a bias voltage of 37 V is shown. The distance between the two individual boron implants (p^+) is 4 µm. The depletion of the bulk from the cathode which forms the vertical resistor is also visible for the approach with the structured cathode. The amount of depleted volume is slightly smaller compared to the standard SiMPl device with a common cathode, which is caused by the missing acceptor concentration in the gap region. On the right hand side in Fig. 6.3, the electric field of two neighbouring cells is illustrated for an enlarged view of the gap region. The avalanche regions of the G-APD structures are clearly visible. The transition region of the structured cathodes to the bulk

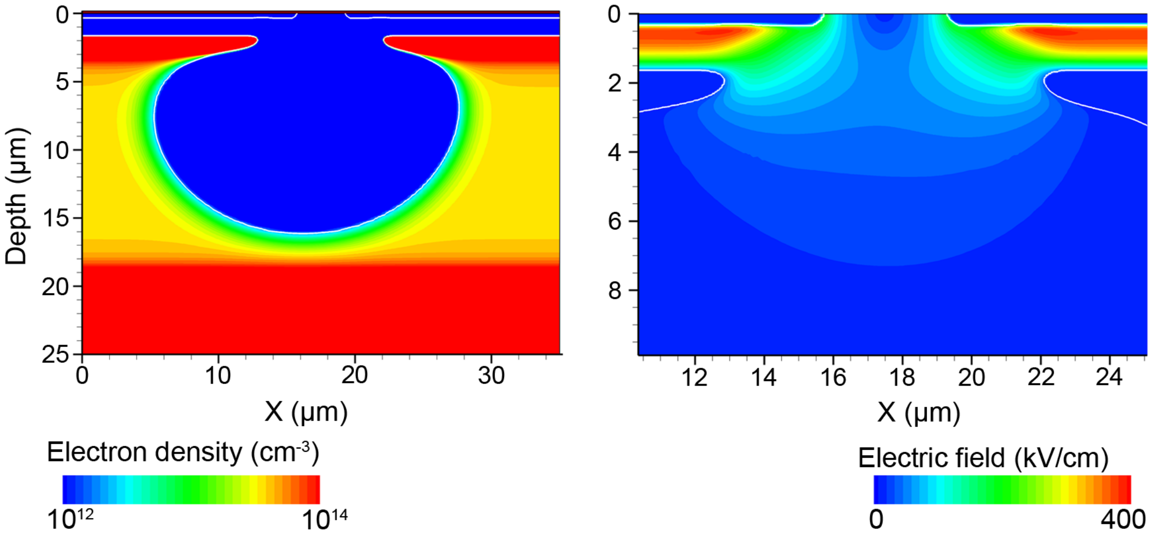

Figure 6.3: TCAD study of the particle detection concept for the next SiMPl generation. On the left hand side the electron density distribution is plotted for a pitch-gap combination of 35/7 µm. The depletion region is also formed with structured cathode implants. On the right hand side the electric field distribution in a magnification of the gap region is shown. No guard ring structures are required, since the structured cathode implant does not result in edge breakdown problems.

shows values for the electric fields in the range of 200 kV/cm, but no edge breakdown is observed. Thus, no guard ring structures which would decrease the fill factor (here 64%) are necessary. To achieve the required fill factors of larger than 90%, the effective dead space can be further reduced by using multiple shifted layers.

According to Eq. (1.1) a single point resolution of 10 µm can be achieved with a pitch size of 35 µm, whereas the tracking detector systems of future collider machines require a resolution better than 5 µm. This corresponds to a pitch size in the range of 20 µm which is not achievable with passively quenched devices based on the current SiMPl technology, as was shown in Sec. 5.3.2. However, it is also worth mentioning that by using active quenching [101], the requirements for the bulk-integrated quench resistance are less strict, which allows to change the parameters of the thickness, bulk doping and pitch/gap ratio for optimisation.

Up to now the minimum pitch of the bump-bonds is the limiting factor for the cell size (ca. 40 µm). Further development is ongoing in order to reduce this number. In addition, the connection of the bumps to the avalanche region, the so-called under bump metallisation, and its influence on the device characteristics has to be developed and studied.

6.1.2. Photon detection

For the realisation of a SiMPl device with single cell readout which is still sensitive to photons, a more ambitious version is required. In order to keep the surface of the SiPM as a free entrance window for light, the contacts for the individual cells have to be mounted on the backside of the sensor. A basic sketch of the photon sensitive device is shown in the upper part of Fig. 6.4. In contrast to the approach for particle tracking, the separation of the cells has to be realised in the first step of the fabrication by structuring the phosphorus implantation of the backside contact before the SOI-wafer bonding. In order to guarantee the electrical separation, the depletion region in the bulk has to reach the backside of the sensor wafer.

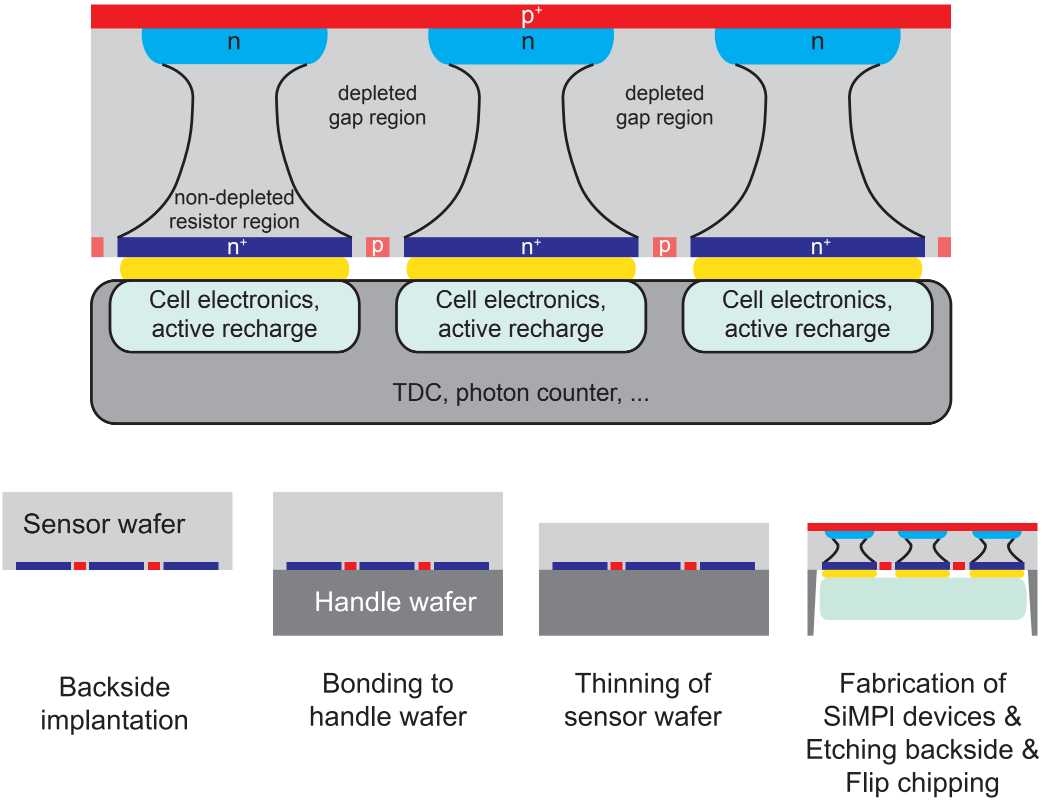

Figure 6.4: SiMPl approach for photon sensitive single cell readout. In contrast to the particle approach in Fig. 6.2, the contacts have to be attached to the backside in order to keep a free entrance window for light. As a result, the implant for the back contact has to be structured before the wafer bonding which is sketched in the lower part. Finally, the handling wafer has to be removed at the detector locations by anisotropic etching.

An additional floating p-implant has to be introduced between adjacent back contacts to avoid short-circuiting of the cells by accumulation of electrons at the Si/SiO_2 interface of the depleted backside (due to positive oxide charges). After the fabrication of the remaining parts of the SiMPl device, the handle wafer has to be thinned down to the contact layer at the location of the detectors e.g. by deep anisotropic wet etching, which stops at the oxide layer between the two wafers [164]. This is followed by the removal of the oxide layer and thereafter, the sensor wafer can be connected to the readout electronics via bump-bonding. The individual steps are sketched in the lower part of Fig. 6.4.

One possible problem of this method could be the high temperature step for the bonding of the sensor and the handle wafer. The high temperature leads to a high diffusion of the implanted atoms in the order of several µm until the bulk doping level is reached (both laterally and in depth). To prevent the diffusion of the backside contacts into each other, sufficient gap space between the n-implants has to be provided in order to ensure the contacting of a single cell. The conductive channel is determined by the depleted volume of the bulk region which has to guarantee that the current of the avalanche is limited to one readout contact and no electrical cross talk occurs. The mandatory full depletion to the backside requires simulations to adjust the thickness of the SOI material to the cell dimensions and the expected operating voltage.

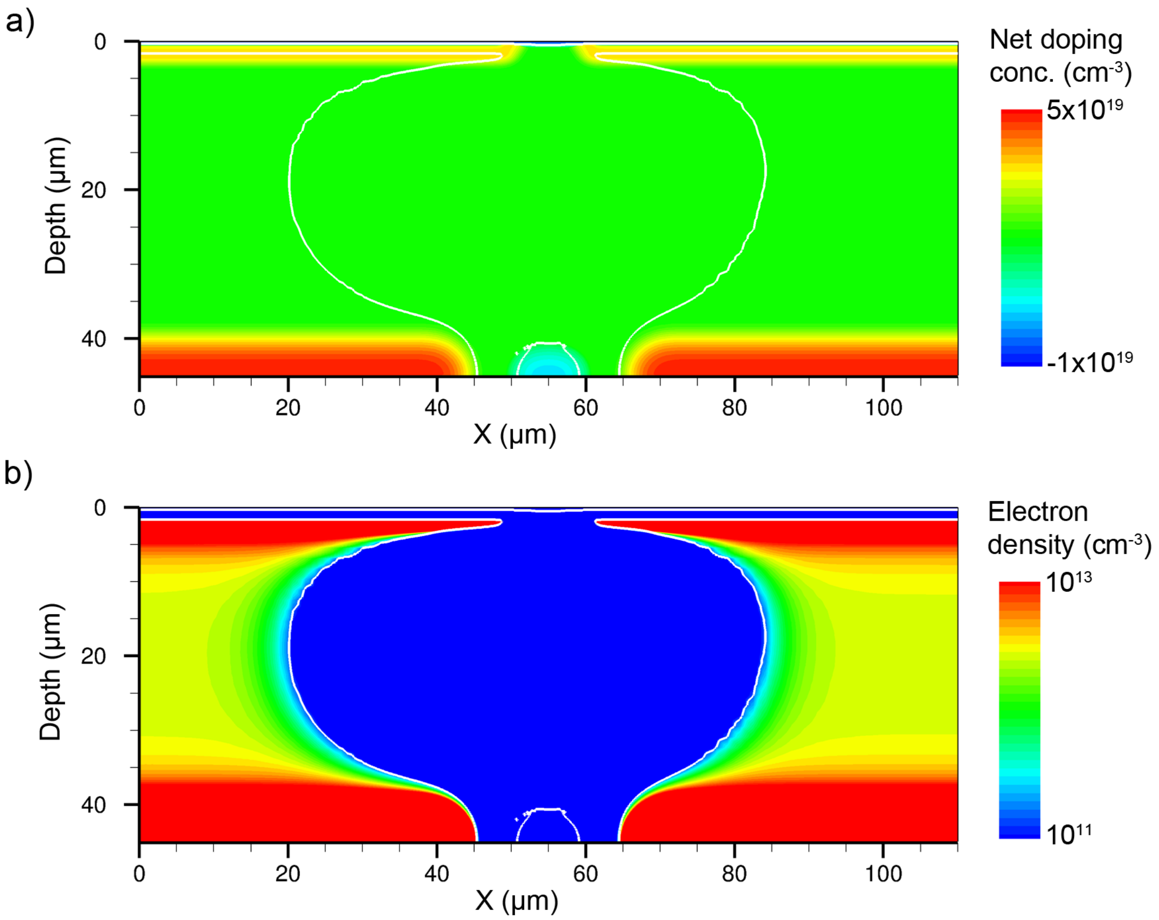

Figure 6.5: TCAD study for SiMPl photon detector with single cell readout. Shown is the net doping concentration (a)) and the electron density distribution in the bulk (b)) for a device with pitch 110 µm and a gap of 10 µm ($V_{bias} = 40$ V). The photoresist-covered distance between the backside contact n-implants is 30 µm wide. A short-circuit of the backside contacts, due to accumulation of electrons at the interface, is prevented by an intermediate boron implantation. The depletion region extending from the gap to the backside of the sensor wafer guarantees the electrical separation of the individual cells. Assuming the current material and device parameters, the thickness has to be reduced to roughly 45 µm. The white lines illustrate the depleted area. The asymmetry in the electron density can be attributed to the cylindrically symmetric approximation.

First feasibility studies with TCAD simulations were implemented and Fig. 6.5 shows a result of the obtained electron density for a device with 110 µm pitch and 10 µm gap size (FF: 83%) at $V_{bias} = 40$ V. The distance between the backside n-implants which is covered with photoresist is 30 µm wide, but can be varied, independent from the gap size of the top structures, to a minimum distance of 20 µm. The electrical separation by a depletion extending from the gap region to the backside of the sensor wafer is achievable, but with the current technology and a breakdown voltage of ca. 35 V the sensor wafer has to be thinned down to roughly 45 µm. By using appropriate cell electronics an active quenching mechanism can be introduced which allows smaller resistance values, since the 20 µA quench condition becomes obsolete. Thus, parameters like thickness, bulk doping, and pitch-gap ratios can be re-adjusted and optimised.

Since the photon sensitive approach requires a removal of the handle wafer, a technological solution for the support of the sensors during the bump-bonding has to be found.

6.2. Optical cross talk suppression

Optical cross talk is one of the major drawbacks of SiPMs. Cross talk events lead to additional fake counts of the device which deteriorate the single photoelectron spectrum. Moreover, a high cross talk probability results in a high dark count rate even at thresholds larger than 1.5 p.e. (see Fig. 5.28). The voltage dependence of this effect leads to the result that optical cross talk is especially pronounced in the operating range of high overbias voltages which is required for maximum PDE values (high trigger probability, high gain). Therefore, this property of SiPMs is an important characteristic for cameras of IACT systems, since the dark count rate defines the trigger level, and hence the minimum energy threshold. Although there is already an inherent suppression of the slow component of OCT in the SiMPl approach (see Sec. 4.3), the values are still in a range of 40% for a relative overbias of 10%. Optical trenches between the cells reduce also the fast component of cross talk and result in OCT probabilities of 1–10% [149]. Additionally, the fill factor can be further increased, since the optical separation allows to reduce the gap region to the technological minimum. However, it is obvious that the introduction of optical trenches implies that the advantage of the unstructured entrance window cannot be fully maintained.

In order to study the possibilities of realising optical trenches, TCAD simulations were implemented. One technological challenge is to keep a common cathode for the parallel readout of the SiPM. Two basic principles were investigated and the results with respect to doping concentration, electric field, and electron density are shown in Fig. 6.6a-c, respectively. On the left hand side the anisotropic plasma etching approach is illustrated. The process steps are exactly the same as for standard devices. In a final step, the optical trenches between the active regions of the SiPM are etched down to a larger depth than the extension of the avalanche region (Fig. 6.6a, left). For the realisation of the common cathode, parts in the corners of the micro-cells are omitted in the etching process. The minimum opening of the trench is limited by the technology, i.e. the minimum structure size achievable by the lithography and the maximum aspect ratio of the plasma etching. In the presented studies a width of 4 µm was assumed with a distance of 2 µm from the high field regions, which results in a fill factor of 85%. By optimising the technology even values of about 90% should be achievable.

By taking a look at the electric field distribution no problems concerning local field maxima can be observed with this approach. The electric field is dominated by the high field regions of the G-APD (Fig. 6.6b, left). One possible issue could be the plasma-induced damage of the silicon [165,166], which leads to increased leakage currents and may affect the dark count rate of the SiPM. A suppression of this process requires an additional oxidation and p-implant at the etched region.

The removal of a part of the cathode implant in the gap region affects the electron density distribution in the silicon bulk (Fig. 6.6c, left). The depleted volume is much smaller compared to a standard device and results in a smaller quench resistance. This, in turn, is also reducing the maximum overbias voltage in passively quenched SiPMs. This issue could be

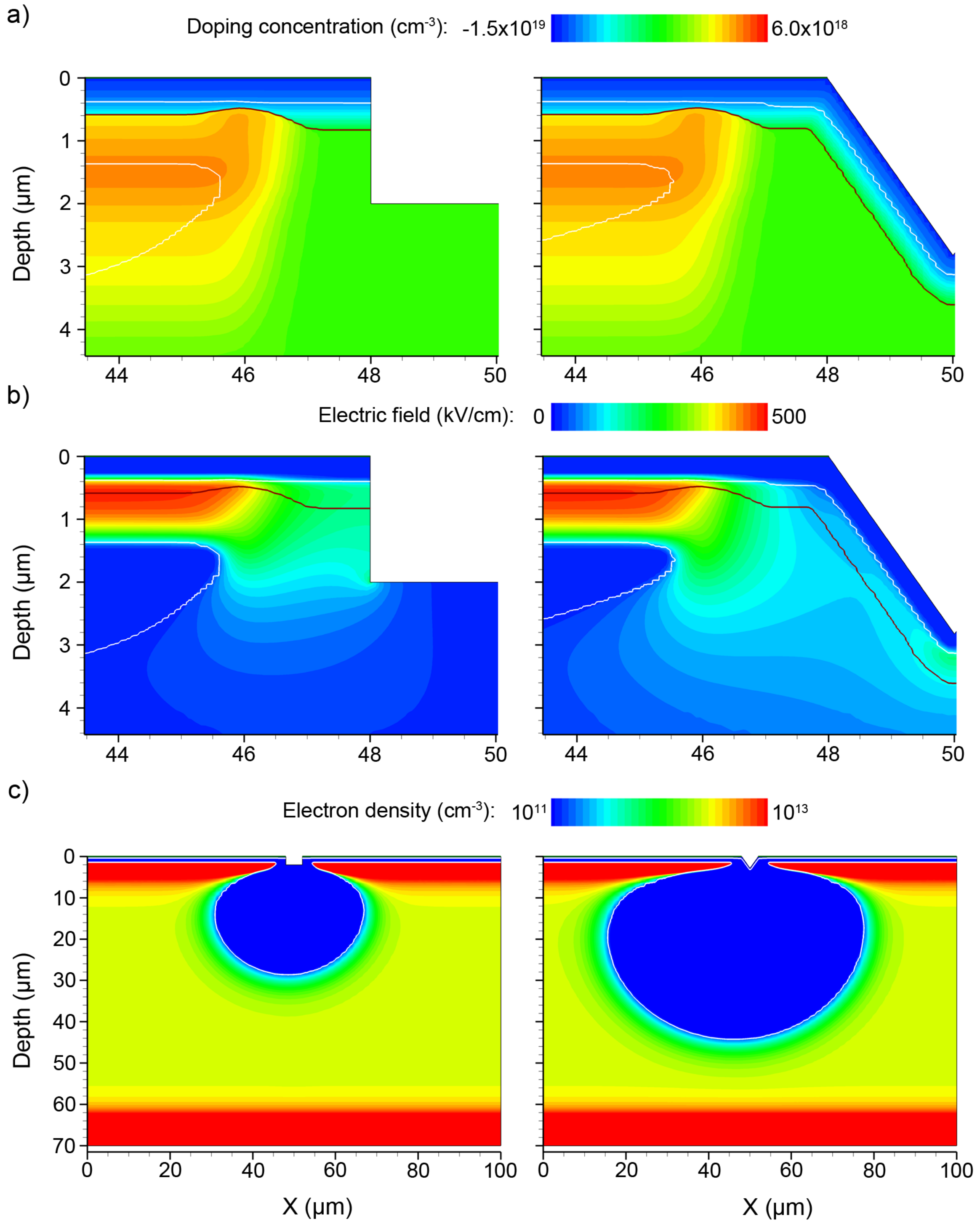

Figure 6.6: TCAD study for implementation of optical trenches. On the left hand side the approach with anisotropic plasma etching (idealised) is plotted whereas on the right hand side orientation-dependent wet etching of silicon is used. The doping concentration (a)), the electric field distribution (b)) and the electron density distribution in the bulk (c)) are shown. The white lines represent the profile of the depletion region, the dark lines mark the pn-junction. The scaling of the y-axis left and right in one row is identical. The label of the x-axis for all plots is located at the lowermost plots.

optimised by technology developments for high aspect ratio etching processes which reduce the amount of the removed cathode implant.

The second approach is to use the property of silicon that some crystal planes are etched much faster than other ones, which results in orientation-dependent etching rates. A commonly used etch for silicon is mixture of tetramethylammonium hydroxide (TMAH) with water [167], which etches the (100)-plane at much higher rates compared to the (110)- and (111)-planes. Etching of a <100>-oriented silicon results in a V-shaped trench at an angle of 54.7° with respect to the surface [168]. This concept would of course require square devices and a corresponding alignment of the structures to the wafer orientation. In addition, the opening angle of the trench leads to a minimum width D of the gap given by

$$D = 2\,l \cot 54.7^{\circ}, \tag{6.1}$$

where l is the etched depth.

The process sequence of this approach is slightly changed since the etching of the silicon is performed prior to the implantation of the common cathode. Thus, the boron implant corresponds to the profile of the surface, as illustrated on the right hand side in Fig. 6.6a. The use of this approach has the advantage that the common cathode is realised without any precautions in the etching process and fill factors around 85% seem to be easily feasible. For the opening of the etching mask the same value of 4 µm, as for the plasma etching process, was considered, resulting in a deeper etching. Since the depth of the high field region is less then 2 µm, also the depth of the trench can be reduced which, in turn, results in a smaller width. As a result, the fill factor of this approach can be increased to roughly 90%.

Concerning the electric field (Fig. 6.6b, right) a small increase is visible at the apex of the V-shaped etch but still much smaller than the values in the high field region and the critical field strength of 300 kV/cm. Thus, it can be concluded that the etching does not introduce additional edge breakdown problems. A further advantage of this approach is the high doping density throughout the etched area which should improve the leakage currents from the surface.

In the plot of the electron density a clearly developed depletion region in the bulk material is visible. Its extension is close to the ideal case where the depletion reaches the backside n^+ implant. Hence, no cell-to-cell coupling should be existent (Fig. 6.6c, right).

In both presented concepts, the trenches are filled with opaque material to avoid the propagation of photons to neighbouring cells. For this purpose aluminium can be used to suppress the transmission. In this case the connection between the readout and the cells will improve as well. Otherwise, the spread resistance of the p^+ layer limits the timing properties of the SiPM (time for the holes to reach the metal contact).

The results show that with a small additional technological effort SiMPl devices with 90% fill factor and reduced optical cross talk are achievable. Since the wet chemical processing of silicon wafers is well established in the in-house research and development laboratory, and due to the avoidance of depleted areas at the surface, this method is preferred for the first prototype production with optical trenches.

6.3. Low temperature devices

As previously discussed in Sec. 1.3, low light level photon detectors are also of interest for low temperature applications with liquid noble gas detectors like dark matter detection (XENON [67]) and neutrino studies (EXO-200 [52], ICARUS [169]). Up to now, these experiments use

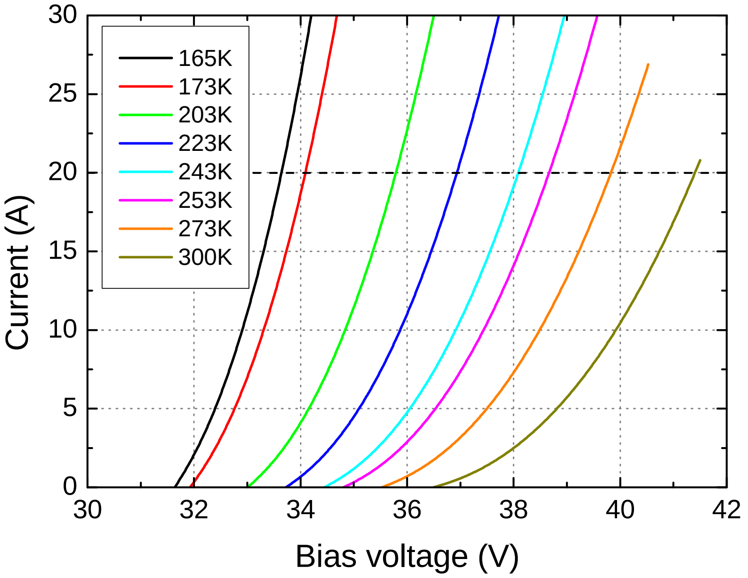

Figure 6.7: TCAD simulations for operation of the SiMPl device at cryogenic temperatures. The simulations cover the temperature range down to $T = 165$ K. The temperature dependence of the breakdown voltage was taken into account. The reduction of the maximum overbias, defined by the 20 µA condition (dashed line), is clearly visible (see also Table 6.1).

photomultiplier tubes, but it turned out that they are one of the main sources of background [78, 79]. Therefore, SiPMs with the capability to be operated at cryogenic temperatures (liquid xenon: 165 K, liquid argon: 87 K) are promising candidates to replace the PMTs, due to their low radioactivity. The scintillation of noble gas detectors is typically in the vacuum UV range (below 200 nm) which is a problematic regime for SiPMs, but it can be shifted via chemical wavelength shifters into the sensitive spectral region of the detector [77].

The advantage of operating SiPMs in this temperature regime is the mainly exponential decrease of the dark count rate. On the other hand, the probability of afterpulses is increasing since the emission time for the charged traps is increasing too [170]. The negative temperature dependence of the polysilicon resistors in conventional SiPMs leads to an increase of the recovery time as well. As already mentioned in Sec. 4.1, the bulk integrated resistor of the SiMPl concept is related to the carrier mobility in silicon which is a function of the temperature [143]. Thus, by cooling the device the resistivity of the bulk is decreasing. This results in a faster recovery of the cell but also in a reduction of the quench resistor value and sets a limitation to the maximum overbias voltage. Additionally, the decrease of the breakdown voltage with lower temperatures has to be considered, which further decreases the depletion region in the bulk.

Since the temperature dependence of the carrier mobility in silicon and of the breakdown voltage are known, the design of the devices can be optimised by simulations for cryogenic conditions. The IV characteristics for temperatures between 165 K and 300 K, obtained from first TCAD simulations, are shown in Fig. 6.7. The decrease of the breakdown voltage was taken into account and results in a maximum difference of $\Delta V_{bd} \approx 4.9\ V$. Clearly visible is also the difference in the slope of the IV curve with respect to the overbias voltage. With

Temperature (K)	165	173	203	223	243	253	273	300
V_{max} (V)	2.0	2.2	2.8	3.2	3.6	3.9	4.3	4.9
$\tau_{90\%}$ (ns)	156	183	282	366	465	521	648	854

Table 6.1: Study of maximum overbias and recovery time as a function of the temperature for a device with pitch 100 µm and a gap of 11 µm. The SOI thickness is set to 70 µm and a bulk doping of $N_B = 2.7 \cdot 10^{12}$ cm^{-3} is assumed.

decreasing temperature the slope steepens due to the decrease in the resistivity of the bulk. An overview of the values for the maximum overbias voltage V_{max} at a current of 20 µA and the estimated recovery time versus the temperature is given in Table 6.1. For the given material parameters the overbias decreases by 3 V, whereas the recovery time of the cell is reduced by a factor of more than five.

In order to reach the saturation of the PDE, the value of 2 V for the overbias at 165 K could be too low. However, the detection efficiency could benefit from the temperature dependence of the ionisation parameters [171], and from the fact that the breakdown voltage is reduced with decreasing temperature. Moreover, special designs for cryogenic temperatures are possible. With those the applicable overbias and PDE could be further increased, but as a consequence those devices would not be operable at 300 K and would require characterisation at cryogenic temperatures.

Since the leakage current of SiPMs decreases by cooling the detector, the area of the devices can be increased to meet the requirements of the experiments.

The first results of studies for applications at cryogenic temperatures are encouraging. Optimisations of the material parameters and device dimensions are required but seem feasible. The confirmation of the simulation results and a fine tuning of the models by comparison to measurements will be a subject of further studies.

7. Summary and outlook

The aim of this thesis was the development and characterisation of prototypes for a novel concept of silicon photomultipliers. The approach is based on the idea to integrate the quench resistors for the individual cells into the high-ohmic silicon bulk material. In contrast to conventional devices, this integration allows to remove light absorbers such as the polysilicon and metal elements within the sensitive area of the detectors and results in a free entrance window for light. Thus, the geometrical fill factor is only limited by the need for suppression of optical cross talk which should increase the photon detection efficiency of the device. In addition, the fact that polysilicon can be omitted reduces the number of process steps and should lower the costs in the case of mass production, which is quite an important criterion for large detector areas in future experiments. Furthermore, this novel concept offers an inherent diffusion barrier for minority charge carriers generated in the bulk which decreases the slow component of optical cross talk in SiPMs.

First, the basic feasibility of the approach was studied by process and device simulations with respect to electric field distributions, electrical separation of individual cells and IV characteristics. It turned out that the devices require fabrication on a thin wafer material in order to match the resistor values for passive quenching and to prevent cell-to-cell coupling. Because of the well established technology in the semiconductor laboratory silicon on insulator material was chosen for the realisation of a prototype. Since the resistor in the bulk material is formed by sidewards depletion extending from the gap regions between adjacent cells, a non-linear IV characteristic for the resistance is obtained which increases the recovery time compared to conventional polysilicon resistors. Those first simulations also indicated that the signal strength of the devices is sufficiently large and no sophisticated and expensive amplifiers are required.

In a comprehensive simulation study, several pitch-gap combinations were investigated regarding the recovery time and the maximum overbias voltage, which meets a quench current of 20 µA. Based on the results, the layout and the process window for a first prototype production were defined. A hexagonal cell shape was chosen, in order to achieve a better approximation to the results of the cylindrically symmetric simulation.

A key element in the development of a novel sensor is the measurement and understanding of the device characteristics. This is also of importance for a precise interpretation of results from an application in an experimental setup. Within the scope of this thesis a full characterisation chain for SiPMs was developed, allowing all relevant static and dynamic measurements for the investigation of the prototype properties. In a first prototype iteration, a surface contamination during the high field implantation resulted in point-like early breakdowns. Other devices showed significant edge breakdown of the cells which was traced back to the tilt angle of the ion beam during the high field implantation process. Because of these technological problems, the first prototype did not yield properly working devices preventing a full characterisation. Nevertheless, first signals showed a working quenching mechanism and thus demonstrated the feasibility of the concept.

Using the results of the first iteration, the problem of the surface contamination was solved in a second prototype production. In addition, the tilt angle of the implantation was changed and a few different annealing scenarios were used, in order to improve the edge breakdown suppression. Test diode measurements revealed improvements compared to the first prototype, but a high dark count rate at room temperature indicated a non-optimised process sequence. The wafer with the most promising characteristics concerning leakage current and edge breakdown was chosen for a further characterisation.

Because of the high dark count rate, the devices had to be cooled down to 253 K for the measurements. One of the achievements of this thesis is the first full prototype characterisation of the SiMPl detector concept, which showed promising results and additionally contributed to the improvements of the simulations. A breakdown voltage of the devices in the range of 34.5 V, with a temperature dependence of 36 mV/K was obtained, which is comparable to commercially available devices. Clearly separated photoelectron peaks were observed in amplitude spectra, which proves the electrical separation between the individual cells and the homogeneity within the array. For all measured devices a linear gain-overbias dependence up to 3 V overbias was observed which indicates that pinch-off was not reached in any of the pitch-gap combinations. Hence, a sufficient process window of operating devices is available. The optical cross talk probability at 2 V overbias is in the range of 30%. In comparison to commercial devices without optical cross talk suppression mechanisms, the SiMPl concept showed lower values at higher fill factors which could be explained by the inherent diffusion barrier against contributions from the bulk. Afterpulsing at the same overbias voltage is at a level in the range of 15% and increases to a value of 50% for an overbias voltage of 3 V. This is much lower compared to commercial devices from Hamamatsu used in this thesis, which could be a result of the slower recovery time leading to a suppression of fast afterpulsing contributions. Improvements in the technology emerging from the characterisation results of the prototypes should reduce the afterpulse probability as well as the dark count rate in future iterations and allow room temperature operation. The recovery time of the SiMPl devices to 90% of the overbias voltage is a factor of 3–5 longer compared to MPPCs from Hamamatsu (in the range of 300–500 ns depending on the pitch-gap combination). The analysis of the measurements also confirmed the deviations of the recovery behaviour from a standard RC element due to the JFET-like behaviour of the bulk-integrated quench resistor. This IV characteristic exacerbates the trade-off, which is common for all passively quenched devices, between a low resistance for a fast recovery time and a high resistance for quenching the avalanche breakdown at high overbias voltages (high PDE). According to the results, it can be concluded that the lower limits for the recovery time of passively quenched devices with a cell size in the order of 100 µm, designed for low light level applications, are in the range of 450 ns assuming a resistance for high overbias voltage operation at room temperature. In PDE measurements, a maximum value of about 35% (λ = 405 nm) for a device with a fill factor of 81% was achieved. These results are comparable to most commercially available SiPMs. However, it has to be taken into account that no optimised entrance window was engineered for this prototype production. The simulations performed in this thesis revealed a surface reflection of the devices of roughly 20–40% between 350 nm and 700 nm. Due to the inverted structure of the SiPM, sensitivity was also observed in the ultraviolet regime down to 280 nm which is especially important for the detection of Cherenkov light but also in applications utilising liquid noble gas scintillation. A comparison of parameters between commercial MPPCs and SiMPl devices is given in Table 7.1.

Parameter	Hamamatsu MPPC	SiMPl prototype	SiMPl optimised
Breakdown voltage (V)	69	37	35
Typ. relative overbias (%)	2	5	15
Fill factor (%)	78	81	87
Gain	10^6	10^6	10^7
Dark count rate (MHz/mm^2)	0.1	5	0.3
Optical cross talk			
- without trenches (%)	35	24	
- with trenches (%)	< 10		< 10
Afterpulsing (%)	< 10	15	< 10
Recovery time to 90% (ns)	165	550	500
Photon detection efficiency (%)	35	35	70

Table 7.1: Comparison of parameters between commercially available Hamamatsu MPPCs (S12571, [172]) and the current SiMPl prototypes (both for a pitch size of 100 µm and room temperature). Also shown are estimations for an optimised SiMPl device. MPPC demonstration devices with trenches have been presented but they are not yet commercially available. Gain, cross talk, afterpulsing, dark count rate and detection efficiency (PDE) depend on the applied overbias voltage and are given for the typical relative overbias. The PDE estimation of the optimised SiMPl device assumes a fill factor of 87%, a trigger efficiency of roughly 90% and surface reflection losses below 10%. All numbers are approximate values.

Furthermore, within the scope of this thesis a new method to determine the operating range for SiPMs, by comparing the dark current to the cross talk corrected dark count rate, was developed. As long as the dark current is well described by the corrected dark count rate, the ratio between both of them is close to one and the device is in normal operation. A deviation of the ratio from a value of one indicates the transition to problematic quenching. In a comparative study of different devices, the expected relation to the quench resistance was observed. Hence, the method provides an easy way of estimating the SiPM operation regime already on the wafer level by measuring the IV characteristics. Future investigations will allow fine tuning and optimisation of the developed method, by taking into account further parasitic effects like afterpulsing.

By means of the measurement results obtained from the prototype characterisation, the process and device simulations were customised and improved resulting in a reliable description of the SiMPl device. Detailed TCAD studies revealed a dependency of the obtained results from device simulations on the utilised implantation models (DIOS, Monte Carlo), which can be explained by the consideration of the channeling effect in the Monte Carlo model. This effect has influence on both the depletion region in the G-APD and the bulk. The resulting reduction of the depleted volume in the bulk leads to a lower resistance which in turn affects the recovery time of the cell in the order of 30 ns. Considering also a five percent uncertainty in the bulk doping level, an additional deviation of about 30 ns is obtained. Comparing the maximum overbias for meeting the quench condition, higher values were observed in the characterisation. One explanation can be found in the uncertainty regarding the depletion region in the bulk which is consistent with the longer recovery times in the measurements, but it is also worth mentioning that the assumed quench condition of

20 µA is only a rule of thumb. Within these uncertainties, the measurements are in good agreement with the simulations.

A further achievement of this thesis was that for the first time real 3-D simulations of SiMPl devices were performed which enabled studies of various geometrical shapes as well as the verification of the cylindrically symmetric approach in the 2-D simulations. This is an important fact, since comprehensive device studies are not feasible with time-consuming real 3-D simulations and require the 2-D approach. The results confirmed that the in-circle approximation is in good agreement with the IV curve obtained from the real 3-D hexagonal structure. Therefore, it can be concluded that the simulations provide reliable results, allowing them to be utilised to predict device characteristics and define operating windows for future productions.

Due to the achieved advances in the simulations, studies of technological improvements were made possible, which are required for further optimisations of the SiMPl device characteristics. The tilt and resist angles were optimised by extensive TCAD simulations, in order to suppress edge breakdown in a new SiMPl prototype. Furthermore, different annealing scenarios were tested using reactive and inert atmospheres. The insights from these simulations influence the production process of new prototypes. First preliminary results of a test production showed that devices with low leakage currents and no edge breakdown can be fabricated. According to the emission microscope pictures inert annealing seems to be preferable for edge breakdown suppression. Lowest leakage currents were achieved with short annealing under reactive atmosphere and high temperature. A detailed investigation of the test structures was not possible within the time frame of this thesis and will be a subject of further studies.

In addition, the feasibility for implementing trenches for optical cross talk suppression was studied. According to the simulations, V-shaped trenches can be realised by well established anisotropic wet chemical etching, without resulting in edge breakdowns. Based on the current technology, the introduction of optical trenches in the next SiMPl generation can easily increase the fill factor of the devices up to 85% for a pitch of 100 µm. Therefore, by additional optimisation of the entrance window, low cross talk devices with PDE values in the order of 60–70% in the blue wavelength regime are achievable. Hence, the SiMPl device could become an interesting candidate for future Cherenkov telescope cameras.

The improvements in the simulations also allowed the implementation of first investigations with respect to possible applications of SiMPl devices in future detectors. For the next SiMPl generation, feasibility studies were performed concerning small cell size devices, single cell readout and low temperature application. For a reasonable operation window with respect to the passive quenching concept (trade-off between applicable overbias voltage and pinch-off avoidance), a minimum cell size of 30–35 µm seems achievable and thus allows the fabrication of high dynamic range devices. This expands the possibility of application of the SiMPl detectors to the readout of scintillators. Since a high PDE is not the main focus of these devices, the maximum overbias voltage for PDE saturation is not the decisive property. Thus, the current technology limits the minimum gap size for these devices to roughly 6 µm which results in fill factors in the order of 65%. Based on these results, a first iteration of devices with a small cell size for a high dynamic range is planned.

The simulations also showed promising results for the realisation of arrays with single cell readout. In both presented approaches for particle tracking and photon detection applications, a full electrical separation of the individual cells without local electric field maxima is possible which indicates the feasibility of the concepts. For a realisation of those sensors, technological developments of bonding techniques and readout electronics are required. The associated implementation of active quenching will also loosen the requirements on the bulk resistor. With this development, SiMPl devices also become an interesting alternative to current technology options (e.g. CMOS Pixel Sensors, DEPFETs) for vertex detectors.

In connection with the particle detection by SiPMs a Monte Carlo tool was developed which takes into account the charge generation by minimum ionising particles. This tool enabled studies of the trigger efficiency for a particle passage through a G-APD at low overbias. According to the results, a trigger efficiency close to one can be achieved for overbias voltages around 1 V. As a result, the noise contribution from optical cross talk and dark counts will be significantly reduced. The simulations have to be confirmed by further investigations and measurements of the SiPM detection efficiency for minimum ionising particles. The application in vertex detectors also requires detailed studies about the radiation hardness of those novel sensors.

First simulations performed for low temperature operation also showed that the SiMPl detector is a potential candidate for cryogenic applications like rare event searches. Devices for those applications can be realised by taking into account the temperature dependence of the bulk resistivity and its influence on the quenching of the avalanche in the design.

In summary, the characterisation of first SiMPl prototypes revealed promising results regarding the realisation of low cost devices with a high detection efficiency. However, in order to meet the requirements for future detectors, further optimisations in particular with respect to dark counts (one order of magnitude), optical cross talk and entrance window are still necessary and a subject of an ongoing process (see Table 7.1). With the developments for the next SiMPl generation, the concept is prepared for a wide field of potential applications in high energy physics and beyond.

A. Derivation of PDE

The photon detection efficiency of the SiPM can be derived from the measurements described in Sec. 3.2.2.9 as followed: The light intensity in the setup is defined by

$$\Im = \frac{\bar{N}_\gamma \, \hbar\omega \, \nu}{A}, \tag{A.1}$$

with $\bar{N}_\gamma / A$ the average number of photons per laser pulse and unit area, $\hbar\omega$ the photon energy and ν the laser pulse frequency. Due to the diffusive reflector it is assumed that the intensities at the location of the pin-diode and the SiPM are equal:

$$\Im_{SiPM} = \Im_{PD}. \tag{A.2}$$

The current of the pin-diode is related to $\bar{N}_\gamma$, the average number of photons per pulse hitting the detector area. Since only a fraction, given by QE, is converted, the photo current is given by

$$I_{PD} = \bar{N}_\gamma \cdot QE \cdot e \cdot \nu, \tag{A.3}$$

where e is the elementary charge. For the SiPM, the mean number of photo electrons n_{pe} is given by N_γ and the photon detection efficiency which results in

$$\bar{n}_{pe} = PDE \cdot \bar{N}_\gamma. \tag{A.4}$$

Replacing $\bar{N}_\gamma$ in Eq. (A.2) with Eqs. (A.3) and (A.4) and taking into account the different areas of the pin-diode A_{PD} and the SiPM A_{SiPM} results in

$$\frac{\bar{n}_{pe} \cdot \hbar\omega \cdot \nu}{PDE \cdot A_{SiPM}} = \frac{I_{PD} \cdot \hbar\omega \cdot \nu}{QE \cdot e \cdot \nu \cdot A_{PD}}. \tag{A.5}$$

This results in the equation for the PDE of the SiPM (see Eq. (3.26)):

$$PDE = \frac{\bar{n}_{pe} \, e \, \nu}{I_{PD}} \cdot QE_{PD} \cdot \frac{A_{PD}}{A_{SiPM}} \tag{A.6}$$

B. pin-diode data

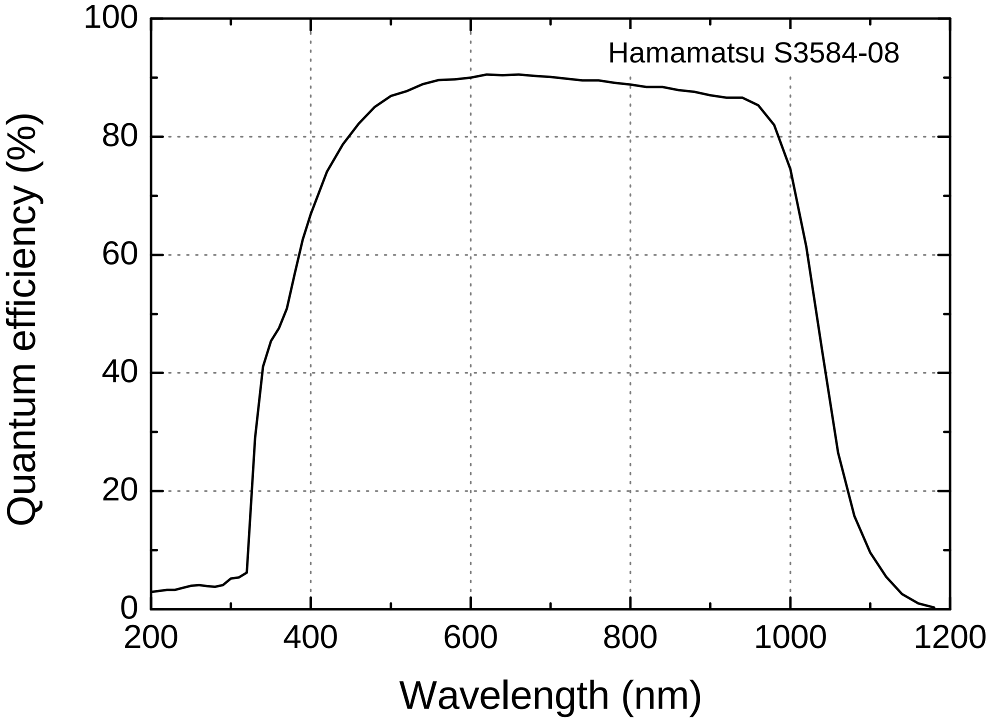

Figure B.1: The quantum efficiency of the calibrated pin-diode S3584-08 from Hamamatsu with a sensitive area of 28 × 28 mm^2.

C. Wafer positioning

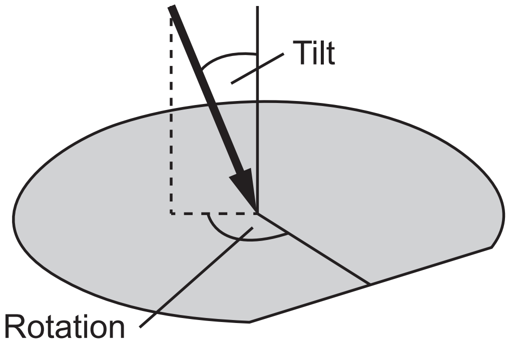

Figure C.1: Direction of the ion beam with respect to the wafer surface defined by tilt and rotation angle.

In order to avoid the ion channeling effect during the implantation of crystalline silicon, the ion beam is turned via tilt and rotation angle to a direction, which does not coincide with one of the crystal axes. The tilt angle indicates the angle between the ion beam and the wafer surface normal (Fig. C.1). The wafer rotation angle is defined by the rotation of the wafer around its surface normal and is measured between the connecting line from the wafer centre to the primary flat and the plane containing the ion beam and the wafer normal. The primary flat defines the orientation of the silicon crystal. In a 100-oriented wafer it is aligned to a <110> direction. Thus, the direction of the ion beam with respect to the orientation of the silicon crystal structure is completely determined. A detailed discussion of the wafer orientation, in particular with respect to the TCAD simulations, is given in Ref. [173].

Bibliography

[1] S. L. Glashow. Partial-symmetries of weak interactions. *Nuclear Physics*, 22(4):579–588, 1961. `doi:10.1016/0029-5582(61)90469-2`.

[2] S. Weinberg. A Model of Leptons. *Physical Review Letters*, 19(21):1264–1266, 1967. `doi:10.1103/PhysRevLett.19.1264`.

[3] A. Salam. Weak and Electromagnetic Interactions. In N. Svartholm, editor, *Proceedings of the 8th Nobel Symposium: Elementary Particle Theory*, pages 367–377, Stockholm, Sweden, 1968.

[4] G. Aad, T. Abajyan, B. Abbott *et al.* Observation of a new particle in the search for the Standard Model Higgs boson with the ATLAS detector at the LHC. *Physics Letters B*, 716(1):1–29, 2012. `doi:10.1016/j.physletb.2012.08.020`.

[5] S. Chatrchyan, V. Khachatryan, A. Sirunyan *et al.* Observation of a new boson at a mass of 125 GeV with the CMS experiment at the LHC. *Physics Letters B*, 716(1):30–61, 2012. `doi:10.1016/j.physletb.2012.08.021`.

[6] J. E. Brau, R. M. Godbole, F. R. Le Diberder *et al.* ILC submissions — 2012 European strategy for Particle Physics: The Physics Case for an e+e- Linear Collider: CLIC-Note-949, 2012. Online: `https://indico.cern.ch/abstractDisplay.py/getAttachedFile?abstractId=69&resId=0&confId=175067`.

[7] G. Weiglein, T. Barklow, E. Boos *et al.* Physics interplay of the LHC and the ILC. *Physics Reports*, 426(2-6):47–358, 2006. `doi:10.1016/j.physrep.2005.12.003`.

[8] H. Baer, T. Barklow, K. Fujii *et al.* The international linear collider - Technical Design Report: Volume 2, 2013. Online: `arXiv:1306.6352[hep-ph]`.

[9] R. D. Heuer, D. Miller, F. Richard, and D. Zerwas, editors. *TESLA Technical Design Report - Part III.* DESY, Hamburg, 2001.

[10] D. Dannheim, P. Lebrun, L. Linssen *et al.* CLIC e+e- Linear Collider Studies, 2012. Online: `arXiv:1208.1402[physics.acc-ph]`.

[11] P. Lebrun, L. Linssen, A. Lucaci-Timoce *et al.*, editors. *The CLIC Programme: towards a staged e+e– Linear Collider exploring the Terascale: CLIC Conceptual Design Report.* CERN-2012-005.

[12] J. Kühn and G. Rodrigo. Charge Asymmetry in Hadroproduction of Heavy Quarks. *Physical Review Letters*, 81(1):49–52, 1998. `doi:10.1103/PhysRevLett.81.49`.

[13] J. Beringer, J. Arguin, R. Barnett *et al.* Review of Particle Physics. *Physical Review D*, 86(1), 2012. `doi:10.1103/PhysRevD.86.010001`.

[14] K. Seidel, F. Simon, M. Tesař, and S. Poss. Top quark mass measurements at and above threshold at CLIC. *The European Physical Journal C*, 73(8), 2013. `doi:10.1140/epjc/s10052-013-2530-7`.

[15] T. Behnke, J. E. Brau, P. Burrows *et al.* The international linear collider - Technical Design Report: Volume 4, 2013. Online: `arXiv:1306.6329[physics.ins-det]`.

[16] C. Adolphsen, M. Barone, B. Barish *et al.* The international linear collider - Technical Design Report: Volume 3.II, 2013. Online: `arXiv:1306.6328[physics.acc-ph]`.

[17] CLIC. Test Facility CTF3. Online: `http://ctf3.home.cern.ch/ctf3/CTFindex.htm`.

[18] H. Braun, R. Corsini, J. Delahaye *et al.* CLIC 2008 Parameters (CLIC-Note-764). 2008.

[19] M. Aicheler, P. Burrows, M. Draper *et al.*, editors. *A Multi-TeV linear collider based on CLIC technology: CLIC Conceptual Design Report.* CERN-2012-007, 2012.

[20] CLIC. The Compact Linear Collider Study: Design & Parameters. Online: `http://clic-study.web.cern.ch/CLIC-Study/Layout/OverallCLIC3.html`.

[21] T. Behnke, J. E. Brau, B. Foster *et al.* The international linear collider - Technical Design Report: Volume 1, 2013. Online: `arXiv:1306.6327[physics.acc-ph]`.

[22] Linear Collider Collaboration Webpage. Online: `http://www.linearcollider.org/images/`.

[23] M. Thomson. Particle flow calorimetry and the PandoraPFA algorithm. *Nuclear Instruments and Methods in Physics Research Section A: Accelerators, Spectrometers, Detectors and Associated Equipment*, 611(1):25–40, 2009. `doi:10.1016/j.nima.2009.09.009`.

[24] C. Adloff, Y. Karyotakis, J. Repond *et al.* Construction and commissioning of the CALICE analog hadron calorimeter prototype. *Journal of Instrumentation*, 5(05):P05004, 2010. `doi:10.1088/1748-0221/5/05/P05004`.

[25] V. Morgunov and A. Raspereza. Novel 3D Clustering Algorithm and Two Particle Separation with Tile HCAL, 2004. Online: `arXiv:physics/0412108[physics.ins-det]`.

[26] F. Simon. Studies of Scintillator Tiles with SiPM Readout for Imaging Calorimeters. *Journal of Physics: Conference Series*, 293:012074, 2011. `doi:10.1088/1742-6596/293/1/012074`.

[27] C. Soldner. Scintillators with silicon photomultiplier readout for timing measurements in hadronic showers. In *2011 IEEE Nuclear Science Symposium and Medical Imaging Conference (2011 NSS/MIC)*, pages 2060–2062.

[28] H. Spieler. *Semiconductor Detector Systems.* Oxford University Press, USA, 2005.

[29] E. Graugés, A. Comerma, L. Garrido *et al.* Study of Geiger avalanche photo-diodes (GAPDs) applications to pixel tracking detectors. *Nuclear Instruments and Methods in Physics Research Section A: Accelerators, Spectrometers, Detectors and Associated Equipment*, 617(1-3):541–542, 2010. `doi:10.1016/j.nima.2009.10.022`.

[30] J. Hinton and W. Hofmann. Teraelectronvolt Astronomy. *Annual Review of Astronomy and Astrophysics*, 47(1):523–565, 2009. `doi:10.1146/annurev-astro-082708-101816`.

[31] C. Weniger. A tentative gamma-ray line from Dark Matter annihilation at the Fermi Large Area Telescope. *Journal of Cosmology and Astroparticle Physics*, 2012(08):007, 2012. `doi:10.1088/1475-7516/2012/08/007`.

[32] J. Ballet and T. H. Burnet. The Fermi LAT Third Source Catalog. In *33rd International Cosmic Ray Conference*, 2013. Online: `http://www.cbpf.br/~icrc2013/papers/icrc2013-1153.pdf`.

[33] NASA Goddard Space Flight Center. The Fermi Science Support Center. Online: `http://fermi.gsfc.nasa.gov/ssc/`.

[34] M. Punch, C. W. Akerlof, M. F. Cawley *et al.* Detection of TeV photons from the active galaxy Markarian 421. *Nature*, 358(6386):477–478, 1992. `doi:10.1038/358477a0`.

[35] M. Actis, G. Agnetta, F. Aharonian *et al.* Design concepts for the Cherenkov Telescope Array CTA: an advanced facility for ground-based high-energy gamma-ray astronomy. *Experimental Astronomy*, 32(3):193–316, 2011. `doi:10.1007/s10686-011-9247-0`.

[36] B. Giebels. Status and recent results from H.E.S.S, 2013. Online: `arXiv:1303.2850[astro-ph.HE]`.

[37] A. de Angelis. Status of MAGIC and recent results. *Advances in Space Research*, 51(2):280–285, 2013. `doi:10.1016/j.asr.2011.12.005`.

[38] N. Galante. Status And Highlights Of VERITAS, 2012. Online: `arXiv:1210.5480[astro-ph.HE]`.

[39] CTA collaboration. CTA observatory website. Online: `http://www.cta-observatory.org/`.

[40] D. Paneque Camarero. *The MAGIC Telescope: development of new technologies and first observations.* PhD thesis, Technische Uiversität München, Munich, 2004.

[41] A. Bouvier, L. Gebremedhin, C. Johnson *et al.* Photosensor characterization for the Cherenkov Telescope Array: silicon photomultiplier versus multi-anode photomultiplier tube. In *SPIE Optical Engineering + Applications*, SPIE Proceedings, pages 88520K–88520K–17. SPIE, 2013.

[42] H. Anderhub, M. Backes, A. Biland *et al.* Design and operation of FACT – the first G-APD Cherenkov telescope. *Journal of Instrumentation*, 8(06):P06008, 2013. `doi:10.1088/1748-0221/8/06/P06008`.

[43] M. L. Knötig, A. Biland, T. Bretz *et al.* FACT - Long-term stability and observations during strong Moon light. In *33rd International Cosmic Ray Conference*, 2013. Online: `arXiv:1307.6116[astro-ph.IM]`.

[44] M. A. Hofmann. *Liquid Scintillators and Liquefied Rare Gases for Particle Detectors: Background-Determination in Double Chooze and Scintillation Properties of Liquid Argon.* PhD thesis, Technische Universität München, Munich, 2012.

[45] A. Morozov, T. Heindl, R. Krücken, A. Ulrich, and J. Wieser. Conversion efficiencies of electron beam energy to vacuum ultraviolet light for Ne, Ar, Kr, and Xe excited with continuous electron beams. *Journal of Applied Physics*, 103(10):103301, 2008. `doi:10.1063/1.2931000`.

[46] G. Plante. *The XENON100 Dark Matter Experiment: Design, Construction, Calibration and 2010 Search Results with Improved Measurement of the Scintillation Response of Liquid Xenon to Low-Energy Nuclear Recoils*. PhD thesis, Columbia University, New York, 2012.

[47] M. Thomson. *Modern particle physics*. Cambridge University Press, New York, 2013.

[48] A. Giuliani and A. Poves. Neutrinoless Double-Beta Decay. *Advances in High Energy Physics*, 2012(1):1–38, 2012. `doi:10.1155/2012/857016`.

[49] K.-H. Ackermann, M. Agostini, M. Allardt *et al.* The GERDA experiment for the search of $0\nu\beta\beta$ decay in ^{76}Ge. *The European Physical Journal C*, 73(3), 2013. `doi:10.1140/epjc/s10052-013-2330-0`.

[50] M. Agostini, M. Allardt, E. Andreotti *et al.* Results on Neutrinoless Double-β Decay of ^{76}Ge from Phase I of the GERDA Experiment. *Physical Review Letters*, 111(12), 2013. `doi:10.1103/PhysRevLett.111.122503`.

[51] N. Ackerman, B. Aharmim, M. Auger *et al.* Observation of Two-Neutrino Double-Beta Decay in ^{136}Xe with the EXO-200 Detector. *Physical Review Letters*, 107(21), 2011. `doi:10.1103/PhysRevLett.107.212501`.

[52] M. Auger, D. J. Auty, P. S. Barbeau *et al.* The EXO-200 detector, part I: detector design and construction. *Journal of Instrumentation*, 7(05):P05010, 2012. `doi:10.1088/1748-0221/7/05/P05010`.

[53] S. Elliott. Recent progress in double beta decay. *Modern Physics Letters A*, 27(07):1230009, 2012. `doi:10.1142/S0217732312300091`.

[54] E. Aprile, K. Arisaka, F. Arneodo *et al.* Dark Matter Results from 100 Live Days of XENON100 Data. *Physical Review Letters*, 107(13), 2011. `doi:10.1103/PhysRevLett.107.131302`.

[55] SNOMASS on the Mississippi (CSS 2013). DarkSide Whitepaper. Online: `http://www.snowmass2013.org/tiki-index.php?page=Darkside`.

[56] SNOMASS on the Mississippi (CSS 2013). SLAC Workshop Talk, XENON. Online: `http://www.snowmass2013.org/tiki-index.php?page=XENON`.

[57] McKinsey. : from DMTOOLS @ UCB, 2007.

[58] A. Minamino. XMASS experiment, 2004.

[59] A. Arbey, M. Battaglia, A. Djouadi, and F. Mahmoudi. An update of the constraints on the phenomenological MSSM from the new LHC Higgs results. *Physics Letters B*, 720(1-3):153–160, 2013. `doi:10.1016/j.physletb.2013.02.001`.

[60] C. Strege, G. Bertone, D. G. Cerdeno *et al.* Updated global fits of the cMSSM including the latest LHC SUSY and Higgs searches and XENON100 data, 2012. Online: `arXiv:1112.4192[hep-ph]`.

[61] V. Chepel and H. Araújo. Liquid noble gas detectors for low energy particle physics. *Journal of Instrumentation*, 8(04):R04001, 2013. `doi:10.1088/1748-0221/8/04/R04001`.

[62] R. Bernabei, P. Belli, A. Bussolotti *et al.* The DAMA/LIBRA apparatus. *Nuclear Instruments and Methods in Physics Research Section A: Accelerators, Spectrometers, Detectors and Associated Equipment*, 592(3):297–315, 2008. `doi:10.1016/j.nima.2008.04.082`.

[63] G. Angloher, M. Bauer, I. Bavykina *et al.* Commissioning run of the CRESST-II dark matter search. *Astroparticle Physics*, 31(4):270–276, 2009. `doi:10.1016/j.astropartphys.2009.02.007`.

[64] S. Cebrián, N. Coron, G. Dambier *et al.* First underground light versus heat discrimination for dark matter search. *Physics Letters B*, 563(1-2):48–52, 2003. `doi:10.1016/S0370-2693(03)00630-0`.

[65] J. Sander, Z. Ahmed, A. J. Anderson *et al.* SuperCDMS status from Soudan and plans for SNOLab. In *Workshop On Dark Matter, Unification And Neutrino Physics: CETUP* 2012*, AIP Conference Proceedings, pages 129–135. AIP, 2013.

[66] E. Armengaud, C. Augier, A. Benoît *et al.* Final results of the EDELWEISS-II WIMP search using a 4-kg array of cryogenic germanium detectors with interleaved electrodes. *Physics Letters B*, 702(5):329–335, 2011. `doi:10.1016/j.physletb.2011.07.034`.

[67] E. Aprile, K. Arisaka, F. Arneodo *et al.* The XENON100 dark matter experiment. *Astroparticle Physics*, 35(9):573–590, 2012. `doi:10.1016/j.astropartphys.2012.01.003`.

[68] D. Akimov, G. Alner, B. A. Araújo *et al.* The ZEPLIN-III dark matter detector: Instrument design, manufacture and commissioning. *Astroparticle Physics*, 27(1):46–60, 2007. `doi:10.1016/j.astropartphys.2006.09.005`.

[69] D. N. McKinsey, D. Akerib, S. Bedikian *et al.* The LUX dark matter search. *Journal of Physics: Conference Series*, 203:012026, 2010. `doi:10.1088/1742-6596/203/1/012026`.

[70] M. Laffranchi, A. Rubbia, and A. collaboration). The ArDM project: a Liquid Argon TPC for Dark Matter Detection. *Journal of Physics: Conference Series*, 65:012014, 2007. `doi:10.1088/1742-6596/65/1/012014`.

[71] K. Ueshima. *Study of pulse shape discrimination and low background techniques for liquid xenon dark matter detectors.* PhD thesis, University of Tokyo, Tokyo, 2010.

[72] K. Abe, K. Hieda, K. Hiraide *et al.* XMASS detector. *Nuclear Instruments and Methods in Physics Research Section A: Accelerators, Spectrometers, Detectors and Associated Equipment*, 716:78–85, 2013. `doi:10.1016/j.nima.2013.03.059`.

[73] D. Akimov. Techniques and results for the direct detection of dark matter (review). *Nuclear Instruments and Methods in Physics Research Section A: Accelerators, Spectrometers, Detectors and Associated Equipment*, 628(1):50–58, 2011. `doi:10.1016/j.nima.2010.06.283`.

[74] R. Acciarri, M. Antonello, B. Baibussinov *et al.* The WArP Experiment. *Journal of Physics: Conference Series*, 308:012005, 2011. `doi:10.1088/1742-6596/308/1/012005`.

[75] T. Alexander, D. Alton, K. Arisaka *et al.* DarkSide search for dark matter. *Journal of Instrumentation*, 8(11):C11021, 2013. `doi:10.1088/1748-0221/8/11/C11021`.

[76] E. Figueroa-Feliciano. Direct detection searches for WIMP dark matter. *Progress in Particle and Nuclear Physics*, 66(3):661–673, 2011. `doi:10.1016/j.ppnp.2011.01.003`.

[77] V. Boccone, P. K. Lightfoot, K. Mavrokoridis *et al.* Development of wavelength shifter coated reflectors for the ArDM argon dark matter detector. *Journal of Instrumentation*, 4(06):P06001, 2009. `doi:10.1088/1748-0221/4/06/P06001`.

[78] M. Carson, J. Davies, E. Daw *et al.* Neutron background in large-scale xenon detectors for dark matter searches. *Astroparticle Physics*, 21(6):667–687, 2004. `doi:10.1016/j.astropartphys.2004.05.001`.

[79] J. Hall. Low Background Materials for Direct Detection of Dark Matter, 2013. Online: `http://www.snowmass2013.org/tiki-download_file.php?fileId=89`.

[80] E. Popova, B. Dolgoshein, P. Buzhan *et al.* Evaluation of high UV sensitive SiPMs from MEPhI/MPI for use in liquid argon. *PoS(PhotoDet2012)034*, 2012.

[81] NIST. XCOM: Photon Cross Sections Database. Online: `http://www.nist.gov/pml/data/xcom/`.

[82] G. F. Knoll. *Radiation detection and measurement.* Wiley, New York, 3rd edition, 2000.

[83] B. Povh, K. Rith, C. Scholz, and F. Zetsche. *Teilchen und Kerne: Eine Einführung in die physikalischen Konzepte.* Springer, Berlin, 8th edition, 2009.

[84] S. M. Sze and K. K. Ng. *Physics of semiconductor devices.* Wiley-Interscience, Hoboken and N.J, 3rd edition, 2007.

[85] K. Kopitzki and P. Herzog. *Einführung in die Festkörperphysik.* Teubner, Wiesbaden, 6th edition, 2009.

[86] J. Singh. *Semiconductor devices: Basic principles.* Wiley, New York, 2001.

[87] R. Groß and A. Marx. *Festkörperphysik.* Oldenbourg, München, 2012.

[88] J. Chelikowsky and M. Cohen. Nonlocal pseudopotential calculations for the electronic structure of eleven diamond and zinc-blende semiconductors. *Physical Review B*, 14(2):556–582, 1976. `doi:10.1103/PhysRevB.14.556`.

[89] E. D. Palik, editor. *Handbook of optical constants of solids.* Academic Press, San Diego [etc.], 1985.

[90] C. Anderson and C. Crowell. Threshold Energies for Electron-Hole Pair Production by Impact Ionization in Semiconductors. *Physical Review B*, 5(6):2267–2272, 1972. `doi:10.1103/PhysRevB.5.2267`.

[91] M. E. Levinshtein, J. Kostamovaara, and S. Vainshtein. *Breakdown phenomena in semiconductors and semiconductor devices.* World Scientific, New Jersey and London, 2005.

[92] P. Wolff. Theory of Electron Multiplication in Silicon and Germanium. *Physical Review*, 95(6):1415–1420, 1954. `doi:10.1103/PhysRev.95.1415`.

[93] S. Selberherr. *Analysis and simulation of semiconductor devices.* Springer-Verlag, Wien and New York, 1984.

[94] R. van Overstraeten and H. de Man. Measurement of the ionization rates in diffused silicon p-n junctions. *Solid-State Electronics*, 13(5):583–608, 1970. `doi:10.1016/0038-1101(70)90139-5`.

[95] W. Maes, K. d. Meyer, and R. van Overstraeten. Impact ionization in silicon: A review and update. *Solid-State Electronics*, 33(6):705–718, 1990. `doi:10.1016/0038-1101(90)90183-F`.

[96] W. Grant. Electron and hole ionization rates in epitaxial silicon at high electric fields. *Solid-State Electronics*, 16(10):1189–1203, 1973. `doi:10.1016/0038-1101(73)90147-0`.

[97] A. Lacaita, F. Zappa, S. Bigliardi, and M. Manfredi. On the bremsstrahlung origin of hot-carrier-induced photons in silicon devices. *IEEE Transactions on Electron Devices*, 40(3):577–582, 1993. `doi:10.1109/16.199363`.

[98] A. N. Otte. *Observation of VHE Gamma-Rays from the Vicinity of magnetized Neutron Stars and Development of new Photon-Detectors for Future Ground based Gamma-Ray Detectors.* PhD thesis, TU München, Munich, 2007.

[99] D. Renker. Geiger-mode avalanche photodiodes, history, properties and problems. *Nuclear Instruments and Methods in Physics Research Section A: Accelerators, Spectrometers, Detectors and Associated Equipment*, 567(1):48–56, 2006. `doi:10.1016/j.nima.2006.05.060`.

[100] W. T. Tsang. *Lightwave communications technology: Part D: Photodetectors.* Academic Press, Orlando FLA, 1985.

[101] S. Cova, M. Ghioni, A. Lacaita, C. Samori, and F. Zappa. Avalanche photodiodes and quenching circuits for single-photon detection. *Applied Optics*, 35(12):1956, 1996. `doi:10.1364/AO.35.001956`.

[102] A. Spinelli and A. Lacaita. Physics and numerical simulation of single photon avalanche diodes. *IEEE Transactions on Electron Devices*, 44(11):1931–1943, 1997. `doi:10.1109/16.641363`.

[103] V. Golovin, Z. Sadygov, M. Tarasov, and N. Yusipov, Patent, #1644708 of Russia.

[104] G. Gasanov, V. Golovin, Z. Sadygov, and N. Yusipov, Patent, #1702831 of Russia.

[105] S. Seifert, H. T. van Dam, J. Huizenga *et al.* Simulation of Silicon Photomultiplier Signals. *IEEE Transactions on Nuclear Science*, 56(6):3726–3733, 2009. `doi:10.1109/TNS.2009.2030728`.

[106] A. Kolb, E. Lorenz, M. S. Judenhofer *et al.* Evaluation of Geiger-mode APDs for PET block detector designs. *Physics in Medicine and Biology*, 55(7):1815–1832, 2010. `doi:10.1088/0031-9155/55/7/003`.

[107] B. Dolgoshein, V. Balagura, P. Buzhan *et al.* Status report on silicon photomultiplier development and its applications. *Nuclear Instruments and Methods in Physics Research Section A: Accelerators, Spectrometers, Detectors and Associated Equipment*, 563(2):368–376, 2006. `doi:10.1016/j.nima.2006.02.193`.

[108] M. T. Robinson and O. S. Oen. The Channeling of Energetic Atoms in Crystal Lattices. *Applied Physics Letters*, 2(2):30, 1963. `doi:10.1063/1.1753757`.

[109] Synopsys. Sentaurus Device User Guide: Version G-2012.06, 2012.

[110] Synopsys. Sentaurus Structure Editor User Guide: Version G-2012.06, 2012.

[111] W. Oldham, R. Samuelson, and P. Antognetti. Triggering phenomena in avalanche diodes. *IEEE Transactions on Electron Devices*, 19(9):1056–1060, 1972. `doi:10.1109/T-ED.1972.17544`.

[112] R. McIntyre. On the avalanche initiation probability of avalanche diodes above the breakdown voltage. *IEEE Transactions on Electron Devices*, 20(7):637–641, 1973. `doi:10.1109/T-ED.1973.17715`.

[113] D. A. Ramirez, M. M. Hayat, G. J. Rees, X. Jiang, and M. A. Itzler. New perspective on passively quenched single photon avalanche diodes: effect of feedback on impact ionization. *Optics Express*, 20(2):1512, 2012. `doi:10.1364/OE.20.001512`.

[114] S. Ramo. Currents Induced by Electron Motion. *Proceedings of the IRE*, 27(9):584–585, 1939. `doi:10.1109/JRPROC.1939.228757`.

[115] E. Obermeier and P. Kopystynski. Polysilicon as a material for microsensor applications. *Sensors and Actuators A: Physical*, 30(1-2):149–155, 1992. `doi:10.1016/0924-4247(92)80210-T`.

[116] F. Corsi, A. Dragone, C. Marzocca *et al.* Modelling a silicon photomultiplier (SiPM) as a signal source for optimum front-end design. *Nuclear Instruments and Methods in Physics Research Section A: Accelerators, Spectrometers, Detectors and Associated Equipment*, 572(1):416–418, 2007. `doi:10.1016/j.nima.2006.10.219`.

[117] CAEN. Digital Pulse Processing for SiPM Kit: Preliminary User's Guide, 2010.

[118] P. Buzhan, B. Dolgoshein, A. Ilyin *et al.* An advanced study of silicon photomultiplier. *ICFA Instrumentation Bulletin*, 23, 2001.

[119] P. Eckert, R. Stamen, and H.-C. Schultz-Coulon. Study of the response and photon-counting resolution of silicon photomultipliers using a generic simulation framework. *Journal of Instrumentation*, 7(08):P08011, 2012. `doi:10.1088/1748-0221/7/08/P08011`.

[120] R. Newman. Visible Light from a Silicon p-n Junction. *Physical Review*, 100(2):700–703, 1955. `doi:10.1103/PhysRev.100.700`.

[121] R. Mirzoyan, R. Kosyra, and H.-G. Moser. Light emission in Si avalanches. *Nuclear Instruments and Methods in Physics Research Section A: Accelerators, Spectrometers, Detectors and Associated Equipment*, 610(1):98–100, 2009. `doi:10.1016/j.nima.2009.05.081`.

[122] J. Bude, N. Sano, and A. Yoshii. Hot-carrier luminescence in Si. *Physical Review B*, 45(11):5848–5856, 1992. `doi:10.1103/PhysRevB.45.5848`.

[123] P. Buzhan, B. Dolgoshein, A. Ilyin *et al.* The cross-talk problem in SiPMs and their use as light sensors for imaging atmospheric Cherenkov telescopes. *Nuclear Instruments and Methods in Physics Research Section A: Accelerators, Spectrometers, Detectors and Associated Equipment*, 610(1):131–134, 2009. `doi:10.1016/j.nima.2009.05.150`.

[124] P. Eckert, H.-C. Schultz-Coulon, W. Shen, R. Stamen, and A. Tadday. Characterisation studies of silicon photomultipliers. *Nuclear Instruments and Methods in Physics Research Section A: Accelerators, Spectrometers, Detectors and Associated Equipment*, 620(2-3):217–226, 2010. `doi:10.1016/j.nima.2010.03.169`.

[125] Y. Du and F. Retière. After-pulsing and cross-talk in multi-pixel photon counters. *Nuclear Instruments and Methods in Physics Research Section A: Accelerators, Spectrometers, Detectors and Associated Equipment*, 596(3):396–401, 2008. `doi:10.1016/j.nima.2008.08.130`.

[126] F. Retière, Y. Du, S. Foreman *et al.* Characterization of Multi Pixel Photon Counters for T2K Near Detector. *Nuclear Instruments and Methods in Physics Research Section A: Accelerators, Spectrometers, Detectors and Associated Equipment*, 610(1):378–380, 2009. `doi:10.1016/j.nima.2009.05.124`.

[127] M. Moll. *Radiation Damage in Silicon Particle Detectors - microscopic defects and macroscopic properties.* PhD thesis, Hamburg University, Hamburg, 1999.

[128] S. Larouche and L. Martinu. OpenFilters: open-source software for the design, optimization, and synthesis of optical filters. *Applied Optics*, 47(13):C219, 2008. `doi:10.1364/AO.47.00C219`.

[129] R. Mirzoyan, E. Popova, M. J. F. Digonnet, S. Jiang, and J. C. Dries. SiPM for atmospheric Cherenkov telescopes. In *SPIE OPTO*, SPIE Proceedings, pages 862106–862106–12. SPIE, 2013.

[130] H. Kellermann. Präzise Vermessung der fokussierten Reflektivität der MAGIC-Teleskopspiegel und Charakterisierung des hierfür verwendeten diffusen Reflektors. Diploma thesis, Munich University of Applied Sciences, Munich, 2011.

[131] M. L. Knötig. Light sensor candidates for the Cherenkov Telescope Array. Diploma thesis, Technische Universität München, Munich, 2012.

[132] M. M. Mandurah, K. C. Saraswat, C. R. Helms, and T. I. Kamins. Dopant segregation in polycrystalline silicon. *Journal of Applied Physics*, 51(11):5755, 1980. `doi:10.1063/1.327582`.

[133] L. Andriček, G. Lutz, and R. Richter, Avalanche photodiode for use in Avalanche radiation detector, has electrode arranged lateral to diode layer so that it depletes substrate laterally adjacent to layer, when resistance layer is shielded from diode layer opposite to electrode, Patent, DE 102007037020 B3.

[134] J. Ninković, L. Andriček, G. Liemann *et al.* SiMPl—Novel high QE photosensor. *Nuclear Instruments and Methods in Physics Research Section A: Accelerators, Spectrometers, Detectors and Associated Equipment*, 610(1):142–144, 2009. `doi:10.1016/j.nima.2009.05.182`.

[135] W.-S. Sul, J.-H. Oh, C.-H. Lee *et al.* Guard-Ring Structures for Silicon Photomultipliers. *IEEE Electron Device Letters*, 31(1):41–43, 2010. `doi:10.1109/LED.2009.2035829`.

[136] R. Richter. Private Communication.

[137] Y. Qiang, C. Zorn, F. Barbosa, and E. Smith. Neutron radiation hardness tests of SiPMs. In *11th Conference On The Intersections Of Particle And Nuclear Physics: (CIPANP 2012)*, AIP Conference Proceedings, pages 703–705. AIP, 2013.

[138] D. Pitzl, N. Cartiglia, B. Hubbard *et al.* Type inversion in silicon detectors. *Nuclear Instruments and Methods in Physics Research Section A: Accelerators, Spectrometers, Detectors and Associated Equipment*, 311(1-2):98–104, 1992. `doi:10.1016/0168-9002(92)90854-W`.

[139] E. Fretwurst, N. Claussen, N. Croitoru *et al.* Radiation hardness of silicon detectors for future colliders. *Nuclear Instruments and Methods in Physics Research Section A: Accelerators, Spectrometers, Detectors and Associated Equipment*, 326(1-2):357–364, 1993. `doi:10.1016/0168-9002(93)90377-T`.

[140] J. Ninković, L. Andriček, G. Liemann *et al.* SiMPl—An avalanche diode array with bulk integrated quench resistors for single photon detection. *Nuclear Instruments and Methods in Physics Research Section A: Accelerators, Spectrometers, Detectors and Associated Equipment*, 617(1-3):407–410, 2010. `doi:10.1016/j.nima.2009.10.025`.

[141] M. A. Itzler, X. Jiang, B. M. Onat, and K. Slomkowski. *Progress in self-quenching InP-based single photon detectors: Proceedings of SPIE.* SPIE, 2010.

[142] R. H. Haitz. Model for the Electrical Behavior of a Microplasma. *Journal of Applied Physics*, 35(5):1370, 1964. `doi:10.1063/1.1713636`.

[143] C. Jacoboni, C. Canali, G. Ottaviani, and A. Alberigi Quaranta. A review of some charge transport properties of silicon. *Solid-State Electronics*, 20(2):77–89, 1977. `doi:10.1016/0038-1101(77)90054-5`.

[144] C. Jendrysik, L. Andriček, G. Liemann *et al.* Characterization of the first prototypes of Silicon Photomultipliers with bulk-integrated quench resistor fabricated at MPI semiconductor laboratory. *Nuclear Instruments and Methods in Physics Research Section A: Accelerators, Spectrometers, Detectors and Associated Equipment*, 718:262–265, 2013. `doi:10.1016/j.nima.2012.10.093`.

[145] I. Rech, A. Ingargiola, R. Spinelli *et al.* In-depth analysis of optical crosstalk in single-photon avalanche diode arrays. In W. Becker, editor, *Optics East 2007*, SPIE Proceedings, pages 677111–677111–10. SPIE, 2007.

[146] Hamamatsu Photonics. MPPC latest information: Presentation at SiPM Advanced Workshop 2013, 2013.

[147] P. Bérard, M. Couture, F. Laforce *et al.* Characterization of an SiPM dedicated at analytical, life science, and medical imaging. In *SPIE OPTO*, SPIE Proceedings, pages 86211D–86211D–10. SPIE, 2013.

[148] KETEK GmbH. SiPM PM3350 STD Trench Datasheet, 2013. Online: `http://www.ketek.net/products/sipm-technology/microcell-construction`.

[149] Hamamatsu Photonics. MPPC data sheet: S10362-11 series, 2013. Online: `http://www.hamamatsu.com`.

[150] D. Ramirez. *Modeling and Engineering Impact Ionization in Avalanche Photodiodes for Near and Mid Infrared Applications.* PhD thesis, University of New Mexico, Albuquerque, NM, USA, 2012.

[151] C. Jendrysik, L. Andriček, G. Liemann *et al.* New method for the determination of non-quenching regime for silicon photomultipliers: A comparative study. *Nuclear Instruments and Methods in Physics Research Section A: Accelerators, Spectrometers, Detectors and Associated Equipment*, 695:226–228, 2012. `doi:10.1016/j.nima.2011.10.007`.

[152] C. Piemonte, R. Battiston, M. Boscardin *et al.* Characterization of the First Prototypes of Silicon Photomultiplier Fabricated at ITC-irst. *IEEE Transactions on Nuclear Science*, 54(1):236–244, 2007. `doi:10.1109/TNS.2006.887115`.

[153] J. Ninković, L. Andriček, C. Jendrisyk *et al.* The first measurements on SiPMs with bulk integrated quench resistors. *Nuclear Instruments and Methods in Physics Research Section A: Accelerators, Spectrometers, Detectors and Associated Equipment*, 628(1):407–410, 2011. `doi:10.1016/j.nima.2010.07.012`.

[154] G. Collazuol. The silicon photo-multiplier physics and technology: a review: Presentation at International Workshop on New Photon-detectors, 2012. Online: `https://indico.cern.ch/contributionDisplay.py?contribId=72&confId=164917`.

[155] A. Benninghoven, F. G. Rüdenauer, and H. W. Werner. *Secondary ion mass spectrometry: Basic concepts, instrumental aspects, applications, and trends*, volume 86 of *Chemical analysis*. J. Wiley, New York, 1987.

[156] P. M. Fahey, P. B. Griffin, and J. D. Plummer. Point defects and dopant diffusion in silicon. *Reviews of Modern Physics*, 61(2):289–384, 1989. `doi:10.1103/RevModPhys.61.289`.

[157] G. Zhang, X. Hu, C. Hu *et al.* Demonstration of a silicon photomultiplier with bulk integrated quenching resistors on epitaxial silicon. *Nuclear Instruments and Methods in Physics Research Section A: Accelerators, Spectrometers, Detectors and Associated Equipment*, 621(1-3):116–120, 2010. `doi:10.1016/j.nima.2010.04.040`.

[158] T. Frach, G. Prescher, C. Degenhardt *et al.* The digital silicon photomultiplier - Principle of operation and intrinsic detector performance. In *2009 IEEE Nuclear Science Symposium and Medical Imaging Conference (NSS/MIC 2009)*, pages 1959–1965, 2009.

[159] E. Vilella and A. Diéguez. A gated single-photon avalanche diode array fabricated in a conventional CMOS process for triggered systems. *Sensors and Actuators A: Physical*, 186:163–168, 2012. `doi:10.1016/j.sna.2012.01.019`.

[160] M. Lozano, E. Cabruja, A. Collado, J. Santander, and M. Ullán. Bump bonding of pixel systems. *Nuclear Instruments and Methods in Physics Research Section A: Accelerators, Spectrometers, Detectors and Associated Equipment*, 473(1-2):95–101, 2001. `doi:10.1016/S0168-9002(01)01127-5`.

[161] K. Banerjee, S. Souri, P. Kapur, and K. Saraswat. 3-D ICs: a novel chip design for improving deep-submicrometer interconnect performance and systems-on-chip integration. *Proceedings of the IEEE*, 89(5):602–633, 2001. `doi:10.1109/5.929647`.

[162] E. Vilella, A. Comerma, O. Alonso, D. Gascon, and A. Diéguez. Gated Geiger mode avalanche photodiode pixels with integrated readout electronics for low noise photon detection. *Nuclear Instruments and Methods in Physics Research Section A: Accelerators, Spectrometers, Detectors and Associated Equipment*, 695:218–221, 2012. `doi:10.1016/j.nima.2011.12.026`.

[163] S. Bellisai, D. Bronzi, F. A. Villa *et al.* Single-photon pulsed-light indirect time-of-flight 3D ranging. *Optics Express*, 21(4):5086, 2013. `doi:10.1364/OE.21.005086`.

[164] L. Andricek, G. Lutz, M. Reiche, and R. Richter. Processing of ultra-thin silicon sensors for future e+e- linear collider experiments. *IEEE Transactions on Nuclear Science*, 51(3):1117–1120, 2004. `doi:10.1109/TNS.2004.829531`.

[165] H. Jansen, H. Gardeniers, M. d. Boer, M. Elwenspoek, and J. Fluitman. A survey on the reactive ion etching of silicon in microtechnology. *Journal of Micromechanics and Microengineering*, 6(1):14–28, 1996. `doi:10.1088/0960-1317/6/1/002`.

[166] H. Abe, M. Yoneda, and N. Fujiwara. Developments of Plasma Etching Technology for Fabricating Semiconductor Devices. *Japanese Journal of Applied Physics*, 47(3):1435–1455, 2008. `doi:10.1143/JJAP.47.1435`.

[167] MicroChemicals. Ätzen von Silizium: Version: 2012-02-11, 2012. Online: `http://www.microchemicals.de/technische_infos/silizium_aetzen.pdf`.

[168] S. M. Sze. *Semiconductor devices, physics and technology.* Wiley, New York, 2 edition, 2002.

[169] C. Rubbia, M. Antonello, P. Aprili *et al.* Underground operation of the ICARUS T600 LAr-TPC: first results. *Journal of Instrumentation*, 6(07):P07011, 2011. `doi:10.1088/1748-0221/6/07/P07011`.

[170] G. Collazuol, M. Bisogni, S. Marcatili, C. Piemonte, and A. Del Guerra. Studies of silicon photomultipliers at cryogenic temperatures. *Nuclear Instruments and Methods in Physics Research Section A: Accelerators, Spectrometers, Detectors and Associated Equipment*, 628(1):389–392, 2011. `doi:10.1016/j.nima.2010.07.008`.

[171] C. R. Crowell and S. M. Sze. Temperature Dependence Of Avalanche Multiplication In Semiconductors. *Applied Physics Letters*, 9(6):242, 1966. `doi:10.1063/1.1754731`.

[172] Hamamatsu Photonics. MPPC data sheet: S12571 series, 2014. Online: `http://www.hamamatsu.com`.

[173] Synopsys. Sentaurus Process User Guide: Version G-2012.06, 2012.

List of Figures

1.1. The two main Higgs boson production processes at a linear collider 2
1.2. Cross-section for different production mechanisms for a 125 GeV Higgs boson 3
1.3. The International Linear Collider 6
1.4. The layout scheme of the Compact LInear Collider (CLIC) 7
1.5. View of ILD [15] (left) and SiD [22] (right) detector concepts for ILC. 8
1.6. CALICE prototype scintillator module 9
1.7. Sketch of imaging atmospheric Cherenkov technique 11
1.8. Full five year map of the Large Area Telescope 13
1.9. Possible layout for the Cherenkov Telescope Array with different telescope sizes 15
1.10. Cherenkov and night sky background spectra for IACTs 16
1.11. Emission spectra of noble gases 18
1.12. Schemes of standard and neutrinoless double beta decays 18
1.13. Measurement concept for single and dual phase xenon TPCs 20
1.14. WIMP cross section limit versus particle mass for different experiments . . . 21
1.15. Schematic view of the XMASS detector 22

2.1. Light-matter interactions in solid states 26
2.2. Energy level of single atom and in crystal structure 28
2.3. Band structure and unit cell of silicon 29
2.4. Principle of doping in semiconductors 30
2.5. Absorption spectrum of direct and indirect semiconductors 31
2.6. Shockely-Read-Hall process and trapping 32
2.7. Schematic overview of an abrupt pn-junction 34
2.8. Impact ionisation in semiconductors 36
2.9. Ionisation rates of silicon 37
2.10. Different operating principles of photo diodes 38
2.11. Basic passive quenching circuit with current-mode readout 39
2.12. G-APD versus SiPM 40
2.13. Structure and equivalent circuit of a SiPM 41
2.14. Typical time behaviour of diode voltage and current of a SiPM micro-cell in limited Geiger-mode 42
2.15. Theoretical charge spectrum for an ideal device 44

3.1. Interaction principle of technology and device simulations 48
3.2. Remeshing principle for trajectory calculation 50
3.3. Calculation of charge trajectory for MC simulations of the breakdown probability 51
3.4. Random distribution of e-h-pairs as starting condition for MIP trigger probability simulation 52
3.5. Setup for IV and CV measurements 53

3.6. Example of an IV measurement in reverse bias of a Hamamatsu MPPC with 100 µm pitch size at three different temperatures 54
3.7. Measurement of the quenching resistor for conventional SiPMs 54
3.8. CV measurements of Hamamatsu MPPCs 56
3.9. Gain of Hamamatsu MPPCs with different pitch 57
3.10. Custom-made readout board for SiPMs 58
3.11. Amplification versus frequency of the readout boards 58
3.12. Amplitude spectrum and resulting normalized dark count rate of a Hamamatsu MPPC with 50 μm pitch 59
3.13. Average response of three different array sizes of SiPMs. 60
3.14. Dark count rate of a MPPC at different temperatures 61
3.15. Optical cross talk: process and suppression 63
3.16. Basic readout and analysis for afterpulsing measurements of SiPMs 65
3.17. Time distribution of MPPCs with 100 µm pitch size 66
3.18. Voltage and temperature dependence of afterpulsing for MPPCs 67
3.19. Comparison between p-on-n and n-on-p structures 69
3.20. Schematic of the PDE measurement setup 70
3.21. Photon emission microscope images 71

4.1. Conventional SiPM 73
4.2. Equivalent circuit and cross-section for SiMPl 74
4.3. Thick wafer exclusion for SiMPl 76
4.4. Simulated electric field distribution in the edge area of a micro-cell. 77
4.5. Simulation of potential distribution (left) and electron density (right) 78
4.6. Non-linear IV curve of resistance R_Q due to parasitic JFET behaviour 79
4.7. Integrated charge from simulation 80
4.8. Fabrication process of SOI-wafer material 81

5.1. Summary of SiMPl prototype simulations 84
5.2. Layout for the prototype production of SiMPl 85
5.3. Doping profile of the final high field and gap region in the SiMPl production 86
5.4. Picture of a SiMPl prototype 87
5.5. IV measurement of devices with a pitch of 120 µm 88
5.6. Emission microscope picture of SiMPl 1 with severe edge breakdown 89
5.7. TCAD simulation results for a study of edge breakdown in SiMPl 1 90
5.8. Proof of principle for quenching mechanism with bulk-integrated resistor. . . 91
5.9. IV characteristics and emission microscopy measurements for test diodes of the second prototype production 92
5.10. Sketch for the basic sequences of stationary and transient TCAD simulations of the prototype 94
5.11. IV characteristics obtained from the static simulations 95
5.12. Results for the internal anode potential obtained from transient simulation . 96
5.13. Illustration of the different simulation regimes 97
5.14. Comparison of real 3-D simulations of hexagonal and square micro-cells with the cylindrical approximation 99
5.15. Comparative TCAD study of the geometrical shape with respect to the IV characteristics 100

5.16. Net doping distribution and electric field obtained from TCAD simulations at the same bias voltage . . . 101
5.17. Comparison of DIOS and MC doping concentration with respect to the bulk depletion . . . 102
5.18. Temperature series of dark current IV curve of 130 µm pitch device . . . 105
5.19. Results of CV measurements of SiMPl 2 . . . 105
5.20. Comparison between simulation and measurement of the capacitance . . . 106
5.21. The gain of the SiMPl device as a function of overbias voltage . . . 108
5.22. Capacitance of the SiMPl devices as a function of the active area . . . 109
5.23. Temperature dependency of the breakdown voltage . . . 110
5.24. Dark count spectrum of a SiMPl device . . . 111
5.25. Normalised amplitude spectrum of a SiMPl device, illuminated with a pulsed laser source ($\lambda = 800$ nm) using three different intensity levels. . . . 112
5.26. Dark counts/mm^2 at different temperatures as a function of the overbias voltage 114
5.27. Arrhenius plot of dark count rate . . . 114
5.28. Comparison of staircase plots obtained from DCR measurements (a) and an amplitude spectrum (b) . . . 115
5.29. Optical cross talk of SiMPl devices . . . 116
5.30. Increased light emission at the cell edges of device from the SiMPl 2 wafer chosen for characterisation. . . . 117
5.31. Comparison between optical cross talk of Hamamatsu MPPCs and SiMPl devices as a function of the fill factor . . . 118
5.32. Afterpulsing results of Simpl 2 . . . 119
5.33. Measurement method developed to determine the recovery time of SiMPl . . . 121
5.34. Recovery time of SiMPl as a function of the overbias voltage . . . 122
5.35. Ratio of the recovery times $\tau_{90\%}$ and $\tau_{1/\mathrm{e}}$ . . . 123
5.36. Recovery time as a function of the temperature (device with pitch/gap 130/10 µm) 125
5.37. Recovery time versus sensitive area for pitch 130 µm . . . 125
5.38. Ratio of currents for SiMPl device (pitch 130 µm, gap 11 µm) as a function of overbias voltage . . . 128
5.39. Ratio of currents for a MPPC with 50 µm pitch as a function of overbias voltage 128
5.40. Overbias to obtain a ratio of $r = 2$ for different devices as a function of resistance 130
5.41. Photon detection efficiency of a SiMPl device with a pitch of 100 µm and 10 µm gap size as a function of the overbias voltage . . . 131
5.42. MC results for the Geiger efficiency as a function of overbias and temperature 132
5.43. PDE as a function of wavelength . . . 134
5.44. MC results for Geiger efficiency as a function of single photon absorption depth 135
5.45. Simulated transmission to the silicon bulk for SiMPl 2 . . . 136
5.46. SIMS profile in comparison with TCAD simulations with different tilt and rotation angles . . . 140
5.47. Comparison of different technological approaches to suppress edge breakdown in G-APDs. . . . 141
5.48. Electric field distributions for different annealing scenarios . . . 143
5.49. Preliminary results of SiMPl 3 test structures . . . 144
5.50. Electron density distribution for two different pitch-gap combinations of SiMPl devices with small cell size . . . 145
5.51. Overview of maximum overbias and recovery time for small cell size . . . 146

6.1. MC simulation of Geiger efficiency for MIP detection 150
6.2. SiMPl approach for particle detection in vertex tracking detectors 151
6.3. TCAD study of the particle detection concept for the next SiMPl generation 152
6.4. SiMPl approach for photon sensitive single cell readout 153
6.5. TCAD study for SiMPl photon detector with single cell readout 154
6.6. TCAD study for implementation of optical trenches 156
6.7. TCAD simulations for operation of the SiMPl device at cryogenic temperatures 158

B.1. The quantum efficiency of the calibrated pin-diode S3584-08 from Hamamatsu with a sensitive area of 28 × 28 mm^2. 169

C.1. Direction of the ion beam with respect to the wafer surface defined by tilt and rotation angle. 171

List of Tables

1.1. Basic design and beam parameters for the ILC 6
1.2. Basic design and beam parameters for CLIC 7
1.3. Candidate isotopes of experimental interest for neutrinoless double beta decay 19

2.1. Transition energies for different semiconductors at 300 K. 26
2.2. Ionisation energies for donors and acceptors in silicon 30
2.3. General comparison between SiPM and PMT. 44

3.1. Recovery times for Hamamatsu MPPCs 62
3.2. Extracted values from afterpulsing measurement of Hamamatsu MPPC . . . 66
3.3. Refraction index and surface reflection for silicon at different wavelengths for an incident angle of 90° [128]. 68

5.1. Variation of TCAD results (diode capacitance C_D and recovery time) by using different implantation models 102
5.2. Influence of bulk doping variation on maximum overbias voltage (V_{max}) and recovery time ($\tau_{90\%}$) for TCAD models MC and DIOS 103
5.3. Overview of gain measurement results 108
5.4. Temperature coefficient of the breakdown voltage for SiMPl devices. 110
5.5. Optical cross talk at an overbias of $V_{ob} = 2$ V for different devices 116
5.6. Average time constants for afterpulsing at different temperatures. 119
5.7. Determination of MPPC (100 µm) recovery time. Rejecting waveforms with detected parasitic effects leads to improved measurement results. 124
5.8. Excess noise factors of SiMPl detector as a function of the overbias voltage. . 126
5.9. Pitch size, temperature, corresponding breakdown voltage, resistance and current at $r = 2$ of all studied devices 129
5.10. PDE of different pitch-gap combinations at $\lambda = 500$ nm and $V_{ob} = 2$ V 135
5.11. Comparison of measured maximum overbias voltage (V_{max}) and recovery time with simulation results 137

6.1. Study of maximum overbias and recovery time as a function of the temperature for a device with pitch 100 µm and a gap of 11 µm 159

7.1. Parameter comparison of commercial MPPCs and SiMPl 163

List of Abbreviations

AGN	Active galactic nucleus
AP	Afterpulsing
ATLAS	A Toroidal LHC ApparatuS
CLIC	Compact LInear Collider
CMS	Compact Muon Solenoid
DCR	Dark count rate
EWSB	Electroweak symmetry breaking
FF	Fill factor
FWHM	Full width half maximum
G-APD	Geiger-mode avalanche photo diode
GE	Geiger efficiency (also: trigger efficiency)
IACT	Imaging Atmospheric Cherenkov Technique
ILC	International Linear Collider
ILD	International Large Detector
JFET	Junction field effect transistor
LC	Linear collider
LHC	Large Hadron Collider
MC	Monte Carlo
MIP	Minimum ionising particle
MPPC	Multi Pixel Photon Counter
MPV	Most Probable Value
OCT	Optical cross talk
p.e.	Photon equivalent
PDE	Photon detection efficiency
phe	Photoelectron

PMT	Photomultiplier tube
QE	Quantum efficiency
SiMPl	Silicon MultiPixel light detector
SIMS	Secondary Ion Mass Spectrometry
SiPM	Silicon Photomultiplier
SM	Standard model
SNR	Signal-to-noise ratio
SOI	Silicon-on-Insulator
SRH	Shockley-Read-Hall
TCAD	Technology Computer Aided Design
WIMP	Weakly Interacting Massive Particle

List of Publications

Journals and proceedings

- C. Jendrysik, et al., ”New method for the determination of non-quenching regime for silicon photomultipliers: A comparative study”, *Nuclear Instruments and Methods in Physics Research A*, Vol. 695, p. 226-228 (2012)
- C. Jendrysik, et. al., ”Characterization of the first prototypes of Silicon Photomultipliers with bulk-integrated quench resistor fabricated at MPI semiconductor laboratory”, *Nuclear Instruments and Methods in Physics Research A*, Vol. 718, p. 262-265 (2013)
- C. Jendrysik, ”Silicon Photomultiplier - Concepts, Characteristics, Prospects”, *Proceedings of Science*, PoS(Vertex 2013)043
- J. Ninković, et al., ”The first measurements on SiPMs with bulk integrated quench resistors”, *Nuclear Instruments and Methods in Physics Research A*, Vol. 628, p. 407-410 (2011)
- M. Tesař, et al., ”Study of detection efficiency distribution and areal homogeneity of SiPMs”, `arXiv:1211.6330` [physics.ins-det]

Poster presentations

- ”New method for the determination of non-quenching regime for silicon photomultipliers: A comparative study”, *New Developments in Photodetection*, Lyon, France, 2011

Oral presentations

- ”SiMPl - High efficient silicon photomultipliers with integrated bulk resistor”, *DPG Frühjahrstagung*, Bonn, Germany, 2010
- ”Silicon photomultipliers with bulk-integrated quenching resistor: first results of characterization”, *DPG Frühjahrstagung*, Karlsruhe, Germany, 2011
- ”Characterization of the first prototypes of Silicon Photomultipliers with bulk-integrated quench resistor fabricated at MPI semiconductor laboratory” (Young Scientist Award), *12th Pisa Meeting on Advanced Detectors*, Elba, Italy, 2012
- ”Performance studies of Silicon Photomultipliers with quench resistors integrated to silicon bulk”, *PhotoDet 2012 - International Workshop on New Photon-detectors*, Paris, France, 2012

- ”Studies of Silicon Photomultipliers with Bulk Integrated Quench Resistor Fabricated at MPI Semiconductor Laboratory”, *IEEE Nuclear Science Symposium, Medical Imaging Conference*, Anaheim, USA, 2012
- ”SiPMs with bulk integrated quench resistors - Properties and perspectives”, *15th International Workshop on Radiation Imaging Detectors*, Paris France, 2013
- ”Silicon Photomultiplier - Concepts, Characteristics, Prospects” (invited), *22nd International Workshop on Vertex Detectors*, Berg, Germany, 2013

Acknowledgements

Over the past few years, I received helpful support from many people. Therefore, I want to thank everybody who contributed to the success of this thesis. My special thanks go to:

Prof. Siegfried Bethke for supervising this thesis.

Jelena Ninković for introducing me to the field of silicon photomultiplier, her open door in case of problems in the lab, the critical discussion of results and for pushing forward the SiMPl project during a very difficult period of time. Thank you also for the proofreading of the thesis.

Hans-Günther Moser, who gave me the possibility to work at the semiconductor lab.

Rainer Richter for sharing his immense knowledge in the fields of semiconductors and electronics, the introduction to the simulation tools and so many helpful discussions, which made this thesis possible. I do not want to forget to thank also for the proofreading of a major part of this thesis.

the **MAGIC group** at the MPI for Physics, in particular **Razmik Mirzoyan**, **Max Knötig**, **Uta Menzel**, **Priyadarshini Bangale** and **Jürgen Hose**, for their help with the detection efficiency measurements, interesting discussions about SiPMs and their characteristics as well as the introduction to gamma-ray astronomy.

the **CALICE group** at the MPI for Physics, especially **Frank Simon**, **Michal Tesař** and **Christian Soldner**, for fruitful discussions about SiPMs and the introduction to linear colliders.

Carina Schlammer and **Danilo Mießner** for the bonding and re-bonding of all devices.

Christian Koffmane who gave me an introduction to the fields of electronics, SPICE simulations and designing circuit boards.

Eva Vilella Figueras for her contribution to the development of an electronic model of the SiMPl device.

Paola Avella who proofread important parts of this thesis and gave helpful suggestions.

all colleagues in my office for so many interesting, fruitful and entertaining discussions about physics and beyond. I really appreciated the great atmosphere in the office; especially the ”social seminars” during the last year. In particular, I have to thank **Stefan Aschauer** for the introduction to the TCAD tools from Synopsys as well as the discussions about their bugs, **Henning Ryll** for the Matlab support and **Stephan Schlee** for sharing his knowledge about fitting methods and statistics. I also do not want to forget **Stefan Petrovics** who put his health on the line for the critical proofreading of this thesis.

the **whole staff** of the semiconductor laboratory; first of all to the people who actually worked on the production of the SiMPl devices, but also to the IT crowd and the secretaries.

my **family** for many years of support. This dissertation is dedicated to my late father, **Dominik Jendrysik**.